

Polarizing Agents for High-Frequency Dynamic Nuclear Polarization – Development and Applications

by

Kan-Nian Hu

M.S., Chemistry (1998), National Taiwan University
B.S., Chemistry (1996), National Taiwan University

Submitted to the Department of Chemistry
in Partial Fulfillment of the Requirements for the Degree of

DOCTOR OF PHILOSOPHY IN CHEMISTRY

at the

MASSACHUSETTS INSTITUTE OF TECHNOLOGY

September 2006

© 2006 Massachusetts Institute of Technology

All rights reserved

ARCHIVES

Signature of Author.....

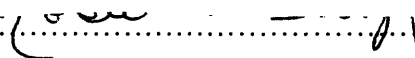
Department of Chemistry

August 14, 2006



Certified

by.....



Robert G. Griffin

Professor of Chemistry

Thesis Supervisor

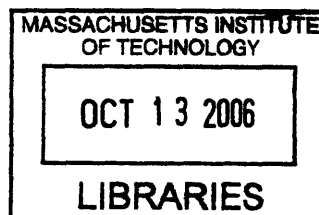
Accepted

by.....

Robert W. Field

Professor of Chemistry

Chairman, Departmental Committee on Graduate Students



Chairman, Departmental Committee on Graduate Students

This doctoral thesis has been examined by a Committee of the Department of Chemistry
as follows:

Professor Mouni G. Bawendi.....
Chairman

Professor Jeffrey I. Steinfeld.....

Professor Robert G. Griffin.....
Thesis Supervisor

POLARIZING AGENTS FOR HIGH-FREQUENCY DYNAMIC NUCLEAR
POLARIZATION – DEVELOPMENT AND APPLICATIONS

by

Kan-Nian Hu

Submitted to the Department of Chemistry
on August 14, 2006 in Partial Fulfillment of the Requirements for the
Degree of Doctor of Philosophy in Chemistry

ABSTRACT

Dynamic Nuclear Polarization (DNP) is utilized to enhance NMR signal intensities in systems including metals, ceramics, polymers and biological solids. The enhancement results from polarization transfers from unpaired electrons, usually carried by a polarizing agent such as TEMPO (2,2,6,6-tetramethylpiperidin-1-oxyl), to the target nuclei. In this thesis, polarizing agents were developed for efficient polarization mechanisms at 5 Tesla. DNP using biradicals yielded improvements of proton enhancement by about fourfold compared to an identical amount of monomeric TEMPO as used previously. The polarizing mechanism involved was the cross effect (CE), which relies on three-spin processes involving two electrons and one nucleus. Optimization of the CE requires the appropriate electron-electron interaction and the correct EPR frequency separation matching the nuclear Larmor frequency. Due to the relatively short inter-radical distance in interesting biradicals, multi-frequency EPR lineshape analyses are suitable to characterize the distance and relative g-tensor orientations between electrons, revealing spectral parameters that explain the improvement of DNP efficiency. Alternatively, radical mixtures of TEMPO and Trityl, methyl tris(8-carboxy-2,2,6,6-tetramethylbenzo[1,2-d:4,5-d']bis(1,3)dithiol-4-yl), improve the probability of the correct EPR frequency separation compared to TEMPO by itself. A 1:1 radical mixture produced a combined EPR spectrum with the required frequency separation and gave an improvement of the DNP enhancement by about threefold relative to TEMPO alone. In addition, a quantum mechanical theory of the CE was developed to provide sound explanations of the improved polarizing mechanism using the above polarizing agents.

The soluble biradical–TOTAPOL, yielding proton enhancements of 160-290–was developed and applied to a wide range of aqueous systems from amyloid peptide

nanocrystals to liquid samples. Polarizing nanocrystals relies on nuclear spin diffusion that transfers enhanced nuclear polarization from solvent into crystals that are isolated from paramagnetic species. This requires efficient polarizing agents that produce and maintain a high level of nuclear polarization surrounding the nanocrystals. In a second application, efficient polarizing agents that reduce the required radical concentration are important for temperature-jump DNP experiments involving a cycle of freezing, polarization, melting and observation of the liquid-state NMR spectrum of samples of interest. During melting, preservation of the nuclear polarization benefits from reduced paramagnetic relaxation at low radical concentrations.

Thesis Supervisor: Robert G. Griffin

Title: Professor of Chemistry

Director of the Francis Bitter Magnet Laboratory

Table of Contents

Polarizing Agents for High-Frequency Dynamic Nuclear Polarization – Development and Applications	1
Chapter 1 Introduction.....	11
Chapter 2 Background.....	17
2.1. Solid-state magnetic resonance.....	17
2.1.1. EPR spectroscopy.....	19
2.1.2. NMR spectroscopy.....	21
2.1.2.1. High resolution SSNMR.....	21
2.1.2.2. Improvement of NMR Sensitivity.....	23
2.2. Dynamic Nuclear Polarization.....	26
2.2.1. DNP mechanisms.....	28
2.2.1.1. Polarizing mechanisms in rotating frames.....	30
2.2.1.2. Polarizing mechanisms in the laboratory frame.....	33
2.2.2. Requirements for DNP at high magnetic fields.....	53
2.2.2.1. High power, high frequency microwave sources and transmission.....	55
2.2.2.2. Cryogenic MAS devices.....	61
2.2.2.3. Cryogenic RF circuitry—transmission line probes.....	62
2.2.2.4. Polarizing agents and cryoprotectants.....	64
Chapter 3 Dynamic Nuclear Polarization Using Biradicals.....	67
3.1. DNP with Biradicals Possessing a Polyethyleneglycol Tether.....	67
3.2. TOTAPOL – A Biradical Polarizing Agent for Dynamic Nuclear Polarization Experiments in Aqueous Media.....	73
3.2.1. Introduction.....	73
3.2.2. Experimental Section.....	74
3.2.2.1. Synthesis of TOTAPOL.....	74
3.2.2.2. EPR experiments.....	77
3.2.2.3. DNP enhanced NMR experiments with TOTAPOL.....	77
3.2.3. Results and discussion.....	78
3.2.4. Conclusions.....	87
Chapter 4 Improvement of High-Frequency Dynamic Nuclear Polarization Using Biradicals: A Multifrequency EPR Lineshape Analysis.....	89
4.1. Introduction.....	89
4.2. Theoretical Background.....	92
4.2.1. DNP mechanisms in solid dielectrics.....	92
4.2.2. Powder EPR lineshape of a biradical.....	95

4.3. Materials and Methods	101
4.3.1. Model biradicals	101
4.3.2. DNP experiments.....	102
4.3.3. Powder EPR spectra at 9 and 140 GHz	104
4.3.4. Multifrequency EPR lineshape fitting	105
4.4. Results	107
4.4.1. Solution EPR at 9 GHz.....	107
4.4.2. Powder EPR spectra at 9 and 140 GHz	110
4.4.3. Magnetic field dependence of DNP.....	117
4.4.4. DNP buildup during microwave irradiation	119
4.4.5. Radical concentration dependence of DNP	120
4.4.6. Microwave power dependence of DNP	122
4.5. Discussion	124
4.5.1. Designs of better polarizing agents.....	124
4.5.2. Optimization of DNP experimental conditions.....	126
4.6. Conclusions	129
Appendix A: Absence of the ^{15}N Zeeman interaction in 140-GHz EPR spectra	130
Appendix B: Diagonalization of a two-pseudo-spin-1/2 4×4 matrix.....	131
Chapter 5 High-Frequency Dynamic Nuclear Polarization Using Mixtures of TEMPO and Trityl Radicals	133
5.1. Introduction	133
5.2. Experimental Section.....	137
5.3. Results	138
5.4. Discussion	142
5.5. Conclusion.....	146
Chapter 6 Quantum Mechanical Theory of Dynamic Nuclear Polarization in Solid Dielectrics	147
6.1. An Analytical Approach.....	147
6.1.1. Introduction	147
6.1.2. Theory	150
6.1.2.1. Polarization transfer in a spin system	150
6.1.2.2. The SE in an electron–nucleus spin system.....	157
6.1.2.3. The CE in an electron–electron–nucleus spin system	163
6.1.3. Discussion.....	193
6.1.3.1. Frequency matching conditions for DNP	194
6.1.3.2. Influences of microwave field and external magnetic field strengths on DNP	197
6.1.4. Conclusions	198

Appendix I: Strong electron–electron interactions in the three-spin system	199
6.2. Simulation of Electron–Electron–Nucleus Spin Systems with Relaxation	201
6.2.1. Introduction	201
6.2.2. Stochastic Liouville equations in a three-spin system	203
6.2.3. Results and discussion	208
6.2.3.1. Frequency matching in the SE and the CE	208
6.2.3.2. Polarization buildup during microwave irradiation	212
6.2.3.3. Essential microwave field and inter-electron interaction for DNP	215
6.2.3.4. Relaxation effects on DNP	219
6.2.3.5. Influence of external magnetic field on DNP	228
6.2.3.6. Improvement of DNP using designer biradicals	232
6.2.4. Conclusions	233
6.2.5 Supporting Materials	234
Chapter 7 Applications of DNP using TOTAPOL	235
7.1. Dynamic Nuclear Polarization of Amyloidogenic Peptide Nanocrystals: GNNQQNY, a Core Segment of the Yeast Prion Protein Sup35p.....	235
7.1.1. Introduction	235
7.1.2. Theory	238
7.1.3. Experimental Section.....	243
7.1.3.1. Peptide nanocrystal samples	243
7.1.3.2. DNP experiments.....	244
7.1.3.3. Transmission Electron Microscopy	245
7.1.4. Results and Discussion	245
7.1.4.1. Enhanced NMR signal intensities of peptide nanocrystals	245
7.1.4.2. Polarized portions of fibril crystals.....	251
7.1.5. Conclusions	253
7.2. In situ Temperature Jump-High Frequency Dynamic Nuclear Polarization Experiments: Enhanced Sensitivity in Liquid State NMR Spectroscopy	255
7.2.1. Introduction	255
7.2.2. Experimental Section.....	257
7.2.3. Results and Discussion	260
7.2.4. Conclusions	267
References	269
Curriculum Vitae	274

Acknowledgement

My fruitful career at MIT could not be concluded without supports from my teachers, my friends and my family. First and foremost, I am thankful to my advisor, Prof. Griffin, who offered me enormous resources to do science and to lead my life. Particularly, I appreciate his support to my independent research works, attendances on many important conferences and opportunities to collaborate with excellent groups inside and outside the MIT community.

I am grateful to Prof. Swager for his insightful consults on biradical syntheses.

I want to thank my thesis committee, Prof. Bawendi and Prof. Steinfeld, for their guidance and verification of my thesis work.

I also want to thank Prof. Vega who enlightened me when I first time encountered the intricate spin dynamics involved in the theory of DNP using biradicals.

Many of my research works were accomplished through collaborations and discussions with some of my best friends, Bruce, Changsik, Yuan-Chung, Patty and Nine-Yuan; thank you all. I am also thankful to the others who enriched my life in Boston; “thank you” to Meng-Chuan, I-Hong, Hsuan-Sen, Juing-Jay, Jack, Linda, Charles, Pey-Gia, Hong-Ren, Jing-In and many others whom are missed.

In the laboratory, enormous intellectual and technical supports came from our scientists, Tony, Chris and Dave, our current and former postdocs, Chan Gyu, Patrick, Ramesh, Gael, Thorsten, Chris, Mike, Dinu, Claudiu, Vlad, Voker and Marina, our formal grads, Mikhail, Melanie, Gali, Chris and John, my colleagues, Xander, Matt, Vik, Malody, and our mighty techs, Jeff, Ron, AJ, Peter and Mike.

I also want to convey my gratitude to people in PSFC who involved in building gyrotrons for us. Specifically, I want to thank Prof. Temkin, Paul, Ivin, Jags, Michael, Colin and Malissa.

I always want to say “thank you” to my grand mother Chang-Tzen Pei-Chuan, my parents Hu Chao-Chan and Chang Chi-Hua, parents in law Jou I-Chang and Chou-Huang Pao-Chu, my sister Hu Shao-Ling and Sun Wei-Ching, and my better half Chou Yang-Ling. They provided me the steadiest supports which strengthened my spirit and led me through every single challenge in my research and my daily life. Not only do they share my unhappiness but also my successes.

Chapter 1 Introduction

Magic angle spinning (MAS) solid-state nuclear magnetic resonance (SSNMR) spectroscopy has become an important technique to investigate a variety of different systems—biological and synthetic polymers, inorganic porous materials, drugs, semiconductors, etc. However, NMR signal intensities are intrinsically low due to the small gyromagnetic ratios (γ_n) of the nuclei involved and, in many cases, the low natural abundance of the NMR active species. Thus, it is important to develop methods to enhance the sensitivity of SSNMR if its applicability is to be extended. Dynamic nuclear polarization (DNP) can be used to improve the sensitivity of SSNMR by 2 to 3 orders of magnitude, thereby dramatically reducing the acquisition time and/or sample quantity required for the experiments.

The high gain in sensitivity results from polarization transfer from endogenous or exogenous unpaired electrons to the nuclei and is commonly driven by microwave irradiation at or near the electron Larmor frequency via polarization mechanisms such as the Overhauser effect (OE), the solid effect (SE), the cross effect (CE) and thermal mixing (TM). Recent developments of DNP have advanced to high resolution SSNMR of samples with stable MAS at nitrogen-cooled temperatures (~90 K) and high magnetic fields (9 and 5 T), where the stable microwave irradiation with high frequency/power (250 GHz/25 W and 140 GHz/10 W for 9 and 5 T, respectively) is provided by gyrotrons. Multi-dimensional SSNMR experiments with constant enhanced nuclear polarization have become possible by employing DNP under stable sample rotation, temperature, and microwave power.

While developments in instrumentation for high-field DNP experiments are maturing, controls of the underlying polarization mechanisms are receiving more attention with the aim of increasing the current NMR sensitivity enhancement to values approaching the theoretical value of γ_e/γ_n (e.g., ~660 for ^1H or ~2600 for ^{13}C). Note that at 5 Tesla, a routine DNP experiment, using TEMPO (2,2,6,6-tetramethylpiperidin-1-oxyl) radicals as the source of electron polarization, can typically generate an enhancement by a factor of ~50 in the ^1H polarization via the polarization mechanism identified as the CE and TM. According to DNP theories in the literature, the primary mechanism of DNP processes is dependent on the size of the linewidth of electron paramagnetic resonance (EPR) of the polarizing agent relative to the nuclear Larmor frequency. We review this point in Chapter 2 which contains a brief description and comparison of classical polarization mechanisms as part of the background of this thesis work.

Of the polarization mechanisms listed above, the CE and TM have advantages over the SE and the OE for efficiently generating enhanced polarization at high magnetic fields. This is observed experimentally at a field larger than 5 T where the CE and TM are operative. For both mechanisms, the underlying physics is essentially described by a three-spin process that involves the coupling of two electrons whose frequencies, ω_{e1} and ω_{e2} in the EPR spectrum of the polarizing agent, are spaced at the nuclear Larmor frequency, ω_n . Since the introduction of the DNP technique 50 years ago, all experiments have relied on monomeric paramagnetic centers such as a nitroxide or metal ion as a source of polarization. However, the electron–electron dipole coupling is clearly an important parameter governing the efficiency of the three-spin CE and TM processes. Thus, we explore in Chapter 3 the possibilities to optimize the enhancements in DNP

experiments by constraining the distance between the two unpaired electrons – utilizing biradicals as polarizing agents.

As mentioned above, DNP results have a strong correlation with the EPR lineshape of the paramagnetic species used to provide the electron polarization. Thus, in Chapter 4 we discuss improved DNP enhancements using biradicals (composed of two TEMPO's) on the basis of multifrequency EPR lineshape analysis. Specifically, the nature of the tether in a biradical affects the inter-radical distance which is responsible for the inter-electron dipolar interaction, and the relative orientation of the g-tensors which contributes to the distribution of the EPR frequency separation in randomly oriented biradicals. The analysis of the EPR lineshapes of biradical polarizing agents allows measurement of several spectral parameters that explain the improved efficiency of DNP. This arises primarily because the efficient biradicals have relatively short intramolecular electron–electron distances.

After we clearly emphasized the importance of electron–electron dipole coupling in the CE and TM mechanisms, we focus on optimization of the other factor – the EPR frequency separation between two coupled electrons. This is discussed in Chapter 5, where we report improvements of the proton DNP enhancement by about threefold using mixtures of TEMPO (a nitroxide radical) and trityl (a triphenylmethyl based molecule) radicals. The improvements are due to the composite EPR spectrum of the radical mixture that provides greater probabilities of matching the EPR frequency separation of two electrons with the proton Larmor frequency. In addition, according to the theory of the CE, a difference in electron spin-lattice relaxation time in TEMPO and trityl may contribute to the improvement of the DNP enhancement. The DNP results from the

mixture (in 1:1 mole ratio) shed new light on improving biradical polarizing agents.

Until recently polarizing mechanisms were discussed in terms of classical pictures, where the master equations governing the spin polarizations are derived from thermodynamic properties of strongly correlated spin ensembles. However, a more complete description of DNP can be obtained when spin parameters determined from EPR spectra are used in a quantum mechanical description of the spin dynamics. Thus, in Chapter 6 we develop a new theory of the CE where the quantum dynamics of an electron–electron–nucleus three-spin system are calculated. In addition to describing the CE, the three-spin system, in the limit where one electron is weakly coupled, reduces to a two-spin system that describes the SE. The spin system can also be expanded to include additional electron spins to explain the TM mechanism, a topic that we leave for a future investigation. Using this formalism we derive analytical expressions describing both the CE and SE to verify the exact frequency matching conditions for polarization transfer in the CE and SE experiments, and to obtain the effective microwave Hamiltonian that transfers the polarization from the electrons to the nuclear spins. In addition, in calculations of the three-spin model, we use the steady-state DNP enhancement and buildup time constant to explain the DNP results that depend on EPR parameters such as the relaxation times, the electron–electron interaction, the external magnetic field strength, and finally the microwave field strength.

The effort to develop new polarizing agents has yielded a new designer water-soluble biradical, TOTAPOL, which produces an enhancement of up to 290 at 90 K and 5 T. Applications of TOTAPOL to DNP in various aqueous systems include nanocrystals of the amyloid peptide (GNNQQNY) and biological solution NMR, which are promising

and are described in Chapter 7. The feasibility of polarizing inhomogeneous crystal domains in the size ranging from nanometers to micrometers demonstrates the important role of homonuclear spin diffusion in DNP experiments, and accounts for the distribution of the enhanced nuclear polarization into the crystals through ^1H - ^1H spin diffusion. The experimental results show that the successful polarization of nanocrystals ($\epsilon \sim 120$) relies on efficient polarizing agents that produce high level of nuclear polarization in the matrix surrounding the nanocrystals. In the second application, a new approach to enhance NMR signals in liquid state is demonstrated in experiments employing freezing-DNP-melting cycles. Large enhancements of solution NMR signal intensities ($\epsilon^\dagger \sim 120-400$) can be obtained when the DNP-enhanced nuclear polarization is preserved through a rapid temperature jump in the sample. The success of such a technique relies on a polarizing agent that allows for a large DNP enhancement at a low electron concentration (< 10 mM), because the primary limitation of the melting part of the experiment is a loss of polarization due to a short nuclear T_1 which is usually aggravated by high radical concentrations.

Chapter 2 Background

Magnetic resonance spectroscopy, including electron paramagnetic resonance (EPR) and nuclear magnetic resonance (NMR), as a tool to probe molecular structures is introduced in the first part of this chapter. Relative to EPR, the signal intensities in NMR spectra are intrinsically low, limiting its application in studies of chemical sites with small numbers of spins. Alleviating the limitation demands increased signal-to-noise in NMR experiments. One option to enhance the NMR signal intensity is to raise the nuclear polarization involved through dynamic nuclear polarization (DNP), which transfers spin polarization from electrons to nuclei during microwave irradiation. Mechanisms for the polarization transfer discussed in the literature are briefly described in the second part of this chapter with an emphasis on the requirements for performing DNP at high magnetic fields.

2.1. Solid-state magnetic resonance

Magnetic resonance spectroscopy studies spin interactions within an ensemble of identical spins or a mixture of spin species. The total Hamiltonian for a spin system is composed of several terms such as

$$H = H_e + H_{ee} + H_{en} + H_n + H_{nn} + H_{RF}, \quad (1)$$

where H_e and H_n are the Zeeman interactions for electrons and nuclei, respectively, H_{ee} represents electron–electron interactions composed of exchange integrals and magnetic

dipolar interactions, H_{en} denotes electron–nuclear (hyperfine) interactions composed of scalar interactions and magnetic dipolar interactions, H_{nn} represents nucleus–nucleus interactions composed of scalar J-couplings and magnetic dipolar interactions, and H_{RF} denotes the interaction between the spins and electromagnetic wave irradiation.

Table 2.1. Spin interactions for electrons (**S**) and nuclei (**I**).

Interaction	Hamiltonian	Note
Zeeman	$H_e = \beta_e \mathbf{B} \mathbf{g} \mathbf{S}$	g : g-tensor, β_e : Bohr magneton, B : external magnetic field
Scalar Dipole	$H_{ee} = J \mathbf{S}_1 \mathbf{S}_2$ $\mathbf{S}_1 \mathbf{D} \mathbf{S}_2$	<i>J</i> : exchange integral between electrons D : e ⁻ -e ⁻ dipolar tensor $\propto \gamma_e^2 / r^3$; γ_e is the electron gyromagnetic ratio
Scalar Dipole	$H_{en} = a \mathbf{S} \mathbf{I}$ $\mathbf{S} \mathbf{D} \mathbf{I}$	<i>a</i> : isotropic hyperfine coupling constant D : e ⁻ -n dipole tensor $\propto \gamma_e \gamma_n / r^3$
Zeeman Quadrupole	$H_n = -\gamma_n \mathbf{B} \boldsymbol{\sigma} \mathbf{I}$ $\mathbf{I} \mathbf{Q} \mathbf{I}$	γ_n : gyromagnetic ratio, $\boldsymbol{\sigma}$: chemical shift tensor, B : external field Q : quadrupole tensor
Scalar Dipole	$H_{nn} = J \mathbf{I}_1 \mathbf{I}_2$ $\mathbf{I}_1 \mathbf{D} \mathbf{I}_2$	<i>J</i> : J-coupling constant between nuclei D : n-n dipole tensor $\propto \gamma_{n1} \gamma_{n2} / r^3$
Oscillating field	$H_{RF}^{(MW)} = 2\omega_1 I_x \cos(\omega t + \phi)$	ω , ω_1 , ϕ : oscillating frequency, field strength and phase, respectively

Table 2.1 lists Hamiltonian terms for common spin interactions; the details of these terms are discussed in text books (e.g., see the reference ¹³). Most of those interactions are proportional to the gyromagnetic ratio of the involved spin species, except for the electron exchange integral and nuclear quadrupole interaction which originate from static electric interactions between two charges (the former) and between the nuclear quadrupole moment and the electric field gradient (the latter). Note that the influence of nuclear quadrupole interaction is not presented in the NMR Hamiltonian of $I=1/2$ spins. Those interactions are useful to probe molecular structures as is mentioned in the following sections. The large difference between the gyromagnetic ratios of an electron

and a nucleus implies a correspondingly large difference between the associated resonance frequencies. While EPR experiments are usually performed with microwave frequencies in the gigahertz regime, NMR is employed with radiofrequencies in the megahertz range. Therefore, EPR and NMR spectra are usually discussed separately despite their possible integration into a single experiment.

2.1.1. EPR spectroscopy

EPR spectroscopy utilizes microwave transmission and reception techniques as well as control of the magnetic field, to detect perturbations of the transition energies associated with electron spins. EPR spectra are governed by Eq. 1 with truncation of some small Hamiltonian terms to simplify the derivation. For example, H_n and H_{nn} are usually omitted in discussions of EPR spectra since they are smaller than the remaining terms in an electron spin Hamiltonian and often unresolved in the typical EPR spectrum. All spin interaction terms – including H_e , H_{ee} and H_{en} – are anisotropic, and their intensities depend on the orientation of individual molecules with respect to the laboratory frame defined by the external magnetic field, B_0 . Expressing each of these anisotropic Hamiltonian terms in a tensor form (Table 2.1) leads to a standard definition of such an interaction in the principal axes frame. Subsequent transformation of the anisotropic Hamiltonian term into the laboratory frame simply involves routine algebra.

The spin interactions are associated with molecular structures. For examples, H_e reflects the chemical environment of an individual electron spin through its g-value (the electronic analogue of the chemical shift in NMR), H_{ee} indicates the electron–electron distance in a spin pair (e.g., in a biradical molecule), and H_{en} denotes the bonded nuclear

species and perhaps the electron–nuclear distance. However, poor spectral resolution due to a distribution of resonant frequencies in powder or polycrystalline samples complicates deconvolution of each spin interaction. Brownian motion of spins may average the anisotropic interactions to zero or an isotropic value, but this averaging is not complete until the motion is faster than anisotropic frequencies. A slow motion complicates the resonance lineshapes but can often be understood with stochastic models ¹⁴. Simplification of an EPR spectrum by fast motions eliminates all useful structural information carried by the anisotropic interactions but, nonetheless, can be partially recovered from the relaxation properties associated with the narrowed lineshapes.

EPR experiments are usually conducted with continuous-wave (CW) microwave irradiation at a low field (e.g., 9 GHz at 0.3 T). A theoretical CW EPR lineshape associated with molecular motions in the fast- and rigid-limits is obtained from the eigenvalues and eigenvectors of the stationary spin Hamiltonian (Eq. 1) in absence of microwave irradiation (e.g., see the reference ¹⁵). On the other hand, recent implementations of 9 GHz pulsed-EPR have found wide usage in investigations of transient electron spins and in filtering signals from different paramagnetic species with different relaxation times. Pulse-EPR also enables measurements of electron-electron distances in spin-labeled molecular systems ¹⁶. In addition, recent improvements in high-frequency (> 90 GHz) microwave instrumentation and switches for pulsed EPR at high magnetic fields (> 3 T) have demonstrated significant advantages in separating signals and simplifying spectra of paramagnetic metal ions (e.g., Mn-EPR ¹⁷) because of the dominance of the electron Zeeman interaction. The simplifications in high-field EPR spectra facilitate measurement and deconvolution of spin interactions that are often

essential for determining molecular structures.

2.1.2. NMR spectroscopy

The transition energies in a nuclear spin system can be perturbed and detected using radiofrequencies (RF). Modern NMR spectroscopy relies almost exclusively on pulsed- and Fourier-Transform techniques of time-domain signals, because nuclear relaxation rates are usually slower than the nutation frequency of typical RF pulse strengths (provided by a few hundred watts RF power). Explanations of NMR spectra again involve the general Hamiltonian in Eq. 1, usually without the presence of electron spins.

Molecular structures are again probed through interactions of nuclear spins¹⁸⁻²⁰ – the isotropic and anisotropic chemical shifts distinguishing signals from various chemical sites of a molecule. The nucleus-nucleus magnetic dipolar interaction is proportional to r^{-3} , where r is the distance between the coupled nuclei. Further, when any two chemical shift or dipolar tensors are correlated, the torsion angle of three adjacent chemical bonds can be determined. In addition, a nucleus with $I > 1/2$ interacts with the local electric field gradient (known as quadrupole interaction), which probes the local electronic structure and therefore the arrangement of neighboring atoms around the nucleus.

2.1.2.1. High resolution SSNMR

Solid-state NMR (SSNMR) spectra of static samples exhibit the anisotropic broadening effects from randomly oriented molecules in a powder sample, as all possible interactions contribute to the resonance lineshape. Two approaches are usually utilized to

improve the resolution of SSNMR spectra. First, if the sample forms a single crystal, the number of orientations is reduced from infinite to a discrete number, which yields narrow lines for each orientation. Alternatively, magic-angle-spinning (MAS)^{21, 22} was developed as an effective and general approach to average anisotropic interactions of any orientation to the projections on the axis that is tilted with respect to the external magnetic field by 54.74°. At that angle, all anisotropic magnetic resonance Hamiltonian terms which are second rank tensors are averaged to zero provided that the spinning frequency is much larger than the anisotropic coupling. This is a result that can be demonstrated theoretically using classical calculations or results from first order average-Hamiltonian theory²³. The exception to this statement is the second order quadrupole coupling which is a fourth rank tensor which requires spinning about two angles²⁴⁻²⁶ or multiquantum^{27, 28} experiments to attenuate the anisotropy.

While the spin interactions that are supposed to carry structural information are attenuated by MAS, they can be reintroduced selectively by a series of radiofrequency pulses whose amplitudes and phases are altered synchronously with the rotation frequency^{29, 30}. Those methodologies that restore the spin interactions averaged by MAS are known in the parlance of the trade as ‘recoupling’ techniques. Note that similar pulse sequences can eliminate residual spin interactions not removed by the averaging effect of MAS and are known as ‘decoupling’ techniques. The implementation of recoupling and decoupling sequences in MAS experiments is essential for solving molecular structures using SSNMR. In particular recoupling experiments are used to perform spectral assignments and to measure distance and torsion angles in MAS spectra, and the efficiency of decoupling determines the spectral resolution involved.

2.1.2.2. Improvement of NMR Sensitivity

The sensitivity of NMR experiments is determined by intrinsic nuclear polarization and extrinsic detection limits of probes and receiver circuits. NMR signals arise from the polarization of nuclear spins defined as the population difference between the up and down quantum states involved in an $I=1/2$ NMR transition. For the two spin-states split by an external magnetic field B_0 , the polarization in a thermal equilibrium is defined as

$$P_0 \equiv \frac{n_0^- - n_0^+}{n_0^- + n_0^+} = \frac{\exp(\frac{\gamma_n B_0}{2k_B T}) - \exp(-\frac{\gamma_n B_0}{2k_B T})}{\exp(\frac{\gamma_n B_0}{2k_B T}) + \exp(-\frac{\gamma_n B_0}{2k_B T})},$$

where n_0^- and n_0^+ are populations of down and up states at thermal equilibrium, γ_n is the gyromagnetic ratio of the nucleus, T is the temperature, and k_B is the Boltzmann constant. It is obvious that lower T and higher B_0 lead to larger P_0 which saturates at 100% below ~1 K at 5 T. However, for proton spins at 21 T (900 MHz NMR) and 300 K, the thermal equilibrium polarization is only 7×10^{-5} .

Increases in magnetic field strengths increase the polarization of nuclear spins, and, over the last ~60 years, operating frequencies and polarizations have increased by almost two orders of magnitude. Moreover, as frequencies increase the NMR signals in the spectra show improved signal-to-noise ratio (S/N). In addition, there have been other improvements in instrumentation such as indirect detection of low- γ nuclei³¹, which is widely used in liquid state NMR, and in the last few years cryogenic probes that show sensitivity gains of 2-4 times have become commercially available. Third, it has become very common to perform isotopic enrichment of rare nuclear spins, such as ^{13}C , ^{15}N and ^{17}O which are biologically relevant and NMR active. In the solid state, indirect detection

of low- γ nuclei ³² is less effective since the larger dipolar interactions associated with the high- γ nuclei such as ¹H dominate the spectra.. Nevertheless, transferring polarization from a high- γ nucleus to low- γ nuclei in solids is used routinely and is well known as 'cross-polarization' (CP). Benefits of low- γ NMR from the CP-MAS methodology include narrower NMR peaks with larger intensities and a faster rate of acquisition that is defined by the more rapid spin-lattice relaxation of the high- γ nucleus.

In addition to the approaches to sensitivity enhancement mentioned above, the last few years has witnessed the development of several more *exotic* methods to enhanced polarization of the nuclear spins, including optical pumping, para-hydrogen induced hyper polarization, the Haupt effect and dynamic nuclear polarization. Optical pumping experiments transfer polarization from photons in circularly polarized light to electrons and then to nuclei ³³. Applications of these experiments have involved studies of semiconductors (e.g., GaAs quantum wells or layers ³⁴ and InP semiconductors ³⁵) and in productions of hyper-polarized noble gases (e.g. ³He ³⁶, ⁸³Kr ^{37, 38} and ¹²⁹Xe ³⁹ through optically pumped rubidium vapors). Several tens of percent (compared to typical tens of parts-per-millions) of nuclear polarization can be achieved with optical pumping. The polarized ¹²⁹Xe absorbents can further polarize surface nuclei through the SPINOE (spin polarization induced nuclear Overhauser effect) ⁴⁰ or the CP mechanisms. Recently, a biosensor containing hyperpolarized ¹²⁹Xe has been developed and some applications discussed ^{41, 42}. However, despite the success in producing highly polarized gases, it has proved difficult to transfer, in a generally applicable manner, the polarization of the gas to a solute or solvent that is of chemical or physical interest.

Polarization of proton spins is also possible with enriched para-hydrogen (*p*-H₂).

Recall that $p\text{-H}_2$ has a product spin-state that is asymmetric with respect to exchange and occupies the symmetric rotational states obeying the exchange symmetry of a fermion. Since the lowest rotational state is symmetric, the $p\text{-H}_2$ becomes its only occupant and thermodynamically favored at low temperatures (99.99% at 15 K) over the ortho-hydrogen ($o\text{-H}_2$), which has one of the three remaining symmetric exchange product spin-states. $o\text{-H}_2$ and the $p\text{-H}_2$ are populated in a 3:1 ratio at a room temperature, and conversion between them at a low temperature is catalyzed by a charcoal or a transition-metal complex⁴³. The $p\text{-H}_2$ has a long life time (years) at room temperature; and transfer of high polarization from hydrogen atoms to interesting molecules is feasible via catalyzed chemical reactions, leading to signal enhancements of related NMR spectra⁴⁴. Again, however, this approach has not found wide applicability to date since the number of chemical systems to which it is applicable is limited.

A significant gain of nuclear polarization can be obtained from the Haupt effect, in which the proton dipolar order is aligned via the relaxation between rotational states with different nuclear spin product states. The methyl-group rotor is ubiquitous in all demonstrations of such an effect, and the temperature jump between liquid helium temperature (4.2 K) and about 50 K is found to optimize the gain of nuclear polarization. Although the direction of temperature jump is arbitrary, a sudden temperature increase from 4.2 K to 50 K is empirically easier. In this field-independent process, an enhancement of ~ 50 has been measured at 50 K and 5 T⁴⁵⁻⁴⁷. The Haupt effect works best with a methyl group with a low barrier to rotation such as found in γ -picoline.

As we will see below, microwave driven dynamic nuclear polarization (DNP) is considerably more general in its applicability for normal sample compositions and

experimental conditions than the three approaches for producing enhanced nuclear polarization mentioned above. The following sections provide an in-depth description on a number of pathways leading to DNP with doped paramagnetic species as the source of electron polarization in normal diamagnetic samples. Moreover, the requirements for high-field DNP applications are discussed.

2.2. Dynamic Nuclear Polarization

DNP transfers the larger spin polarization from electrons to nuclei, leading to an enhancement of nuclear polarization, which is maximally γ_e/γ_n (e.g., ~ 660 for ^1H). This polarization transfer relies on an electron–nuclear mutual spin-flip which was first predicted by Overhauser⁴⁸ in 1953 as a result of cross relaxation due to time-dependent electron–nuclear scalar interactions of conducting electrons. Carver and Slichter experimentally verified the Overhauser effect in lithium metals demonstrating enhanced intensities of ^6Li NMR signals⁴⁹. Abragam introduced the time-dependent electron–nuclear dipolar interaction from molecular motions into the theory of the Overhauser effect, illustrating experimental enhancements of nuclear polarization with an inverted sign compared to the effect of scalar interactions. Furthermore, he proposed and proved another DNP mechanism operative with time-independent electron–nuclear interactions, the solid state effect⁵⁰. Since this early work in the 1950's, theories describing DNP in solids have evolved, and two other DNP mechanisms known as the cross effect⁵¹⁻⁵⁵ and thermal mixing⁵⁶ were discovered and confirmed experimentally.

Applications of DNP initially involved studies of nuclear magnetic ordering⁵⁰ and production of polarized targets⁵⁷ for particle scattering physics. These experiments

generated high nuclear polarizations (>90 %) through a long polarizing time (>1 hr) at a very low temperature (<1 K) and a low field (< 1 T). In the 1980's and early 90's the integration of DNP and contemporary high resolution solid state NMR experiments were explored by Wind and Yannoni; specifically, DNP was combined with MAS to obtain sensitivity enhanced high resolution spectra of polymers and carbonaceous materials⁵⁸.⁵⁹ Significant signal enhancements were observed in polymers doped with free radicals, and coals or diamonds containing endogenous unpaired electrons at a magnetic field near 1.4 T (40 GHz EPR and 60 MHz ¹H NMR). Schaefer *et al.* implemented similar DNP techniques to study the interface between two polymer layers^{60, 61}. However, all of these efforts were limited to ¹H NMR frequencies of < 60 MHz, and were therefore more of a curiosity than of real practical utility. In particular, NMR in the late 20th and 21st century was usually performed at ¹H frequencies >400 MHz. Higher-field DNP experiments required stable microwave sources operating in the 100-600 GHz frequency regime. Accordingly, in 1993 Griffin *et al.* published the initial DNP results using cyclotron electron resonance masers (gyrotrons) as microwave sources in experiments at a magnetic field of 5 T. Successful applications of DNP to SSNMR of biological systems have subsequently been demonstrated and now become routine at 5 and 9 T^{62, 63}. Development of the instrumentation for experiments at 460 GHz (700 MHz for ¹H NMR) and above is in progress.

2.2.1. DNP mechanisms

Table 2.2. Sources of electron polarization and corresponding DNP mechanisms (from reference ²).

Source of unpaired electrons	Life time	Spin polarization	Polarizing mechanism	Instrumental requirement
Conducting electron ⁴⁹ Metal ions ⁶⁴ Defects ⁶⁵ Paramagnetic impurity ⁶⁶	Permanent	Boltzmann	Overhauser effect ⁵⁸ Solid effect ⁵⁸ Cross effect ^{53, 67} Thermal mixing ⁵⁸ NOVEL ISE DSSE ⁶⁸	Microwaves
Radicals in reaction	Short	Non-boltzmann	Cross relaxation Triplet-singlet mixing CIDNP ^{69, 70}	none
Photo excited triplet	Short	Non-boltzmann	Cross relaxation Triplet-singlet mixing ^{71, 72} Three-spin mixing ⁷³	Laser
Photo excited triplet	Medium	Non-boltzmann	MI-ONP ⁷⁴⁻⁷⁶ ISE ⁷⁷⁻⁷⁹ NOVEL ^{80, 81}	Laser, Microwaves
Spin injection ^{82, 83}	Short	Non-boltzmann	Cross relaxation	none

Mechanisms for polarization transfers from electrons to nuclei can be first distinguished by the source of electron spin polarization and then by the mechanism operating to transfer electron polarization to nuclear spins. Specifically, the unpaired electrons that provide spin polarization for DNP can be transient or permanent (Table 2.2). Transient electron spins are generated from chemical reaction, optical excitation or spintronic injection, generating a non-Boltzmann distribution of spin states and thus potentially leading to a significant enhancement of nuclear polarization. DNP experiments relying on transient electron spins also requires electron-nucleus ‘cross relaxation’ due to molecular motion, relaxation of excited states, or ‘three-spin-mixing’ due to level crossing achieved through the generation of transient electron spins. Microwave irradiation is usually not part of DNP experiments with transient unpaired electrons, because the spin polarization is prepared at a non-thermal equilibrium.

Nonetheless, long-lived excited triplet states do allow for microwave irradiation to transfer spin polarization through effects such as MI-ONP (**M**icrowave **I**nduced **O**ptical **N**uclear **P**olarization), NOVEL (**N**uclear **O**rientation via **E**lectron spin-**L**ocking) and ISE (**I**ntegrated **S**olid **E**ffect). Applications of DNP using transient electron spins are limited by the special conditions of the spin polarization of precursors and by the potential damage to samples by highly excited molecules.

Permanent unpaired electrons are found in conductors and dielectrics with defects, metal ions or free radicals and their spin polarization is described by the thermal equilibrium Boltzmann distribution. To drive DNP with endogenous or exogenous unpaired electrons, microwave irradiation near the electron Larmor frequency is required for perturbing the thermal equilibrium spin polarization. Further, some stable radicals are compatible with biological systems, the associated polarizing mechanisms driven by microwave excitation are of our considerable interest and summarized in Table 2.3.

Table 2.3. DNP mechanisms characterized by reference frameworks (from reference ²).

Electronic Frame	Nuclear Frame	Polarizing mechanisms
Laboratory	Laboratory	Overhauser effect Solid effect Cross effect Thermal mixing
Laboratory	Rotating	Thermal mixing or solid effect to the nuclear rotating frame ⁸⁴
Rotating	Laboratory	Nuclear orientation via electron spin-lock (NOVEL) Integrated solid effect (ISE) Dressed state solid effect (DSSE)

2.2.1.1. Polarizing mechanisms in rotating frames

The polarization transfer may occur in either the laboratory frame or the rotating frame with respect to the participating electrons and nuclei (Table 2.3). For the DNP experiment in the electron rotating frame and the nuclear laboratory frame, the frequency matching condition analogous to the Hartmann-Hahn condition (for effective polarization exchange between high- and low- γ nuclei in SSNMR) ⁸⁵ is accomplished by

$$\gamma_e B_{1e} = \gamma_n B_0, \quad (2)$$

where B_0 is the external magnetic field, B_{1e} is the microwave field at the EPR frequency, and γ_e and γ_n are the electron and nuclear gyromagnetic ratios, respectively. When the effective frequencies, in each appropriate frame of reference, of the electron and nuclear spins are equal, the nonsecular terms of the dipolar coupling between the two spins induce energy-conserving electron–nuclear flip-flop transitions that lead to the polarization transfer. The standard experiment for this type of mechanism is known as NOVEL ⁸¹, which contains a $\pi/2$ microwaves pulse followed by a long spin-locking pulse with a 90° phase shift. Due to the narrow bandwidth of electron spin-locking, the optimal performance of NOVEL is restricted to crystalline systems where the EPR linewidth is narrow.

While Hartmann-Hahn polarization transfer in the nuclear laboratory frame was accomplished at low magnetic fields, its high-field applications would prove difficult since microwave field strengths are generally insufficient to match $\gamma_n B_0$ in Eq. 2. Specifically, NOVEL experiments at 5 T (212 MHz ¹H NMR, 140 GHz EPR) would require generation of microwave field strength of 212 MHz. With present technology it is

possible to produce fields of only ~ 10 MHz. As an alternative to NOVEL, the integrated solid effect (ISE) ⁷⁸ employs an adiabatic passage through the Hartmann-Hahn condition by rapidly sweeping either the external field strength or the microwave frequency. The effective electron frequency in the matching condition of ISE is a geometric average of the microwave field strength and the frequency offset. Thus, the ISE may be more feasible for applications at high magnetic fields.

Although the Hartmann-Hahn polarization transfer in both electron and nuclear rotating frames is in principle possible, there is to date no experimental demonstration of enhanced nuclear polarization with this method. One of the main obstacles to the implementation is the large mismatch between the electron and nuclear gyromagnetic ratios. Matching the Hartmann-Hahn condition (with the RF field strength B_{1n}),

$$\gamma_e B_{1e} = \gamma_n B_{1n},$$

requires an extremely weak microwave field strength to satisfy the matching condition even with the strongest RF field strength available. Such a weak microwave field compromises the spin-locking efficiency and introduces offset effects that attenuate the polarization transfer. Methods that induce a weak effective field for electron spin-lock using a strong microwave field have been suggested to circumvent this problem but await experimental verification.

Hartmann-Hahn methods rely on the first order electron–nucleus dipolar interaction, and thereby make the polarization transfer efficient in comparison to CW irradiation methods where the second order effect of spin-spin interaction is utilized. However, technical requirements have made Hartmann-Hahn methods difficult at high magnetic

fields (5 and 9 T in our laboratory). Moreover, the typical broad EPR linewidth and short dephasing time of electron spins impose limitations on the spin-locking, undermining the feasibility of pulsed DNP schemes.

In the absence of satisfying the Hartmann-Hahn condition, the frequency offset of the CW irradiation is exploited to achieve energy conservation for the polarization transfer. Although this class of DNP mechanisms is typically explained on the basis of the electron and nuclear Larmor frequencies, the high-frequency oscillating field can redefine the effective energy associated with the spin polarization in a rotating frame. Thus, to match the microwave field strength for the electrons with the radiofrequency (RF) offset for nuclei, the dressed state solid effect (DSSE)⁶⁸ experiment utilizes off-resonant RF irradiation around the NMR frequency during the electron spin-locking. In this experiment, the decay of electron transverse magnetization was demonstrated, but measurements of the enhanced nuclear polarization were not attempted. Similar idea has been implemented in the experiment – DNP in the nuclear rotating frame – which exchanges spin polarization between spin-locked nuclei by RF irradiation and irradiated electrons by microwaves⁸⁴.

It is important to mention the role of nuclear spin diffusion in DNP processes. As low concentrations of electrons are preferred in NMR samples, polarizing the bulk nuclei, which are of interest of the NMR experiment, cannot be completed without nuclear spin diffusion. The secular and nonsecular zero quantum terms of homonuclear dipolar interaction control nuclear spin diffusion in the rotating frame and the laboratory frame, respectively. Nuclear spin diffusion in rotating or laboratory frames competes with $T_{1\rho}$ or T_1 relaxation, respectively, when spreading the enhanced nuclear polarization throughout

bulk nuclei. Since $T_1 > T_{1p}$, homonuclear spin diffusion can carry the enhanced nuclear polarization to longer distances as opposed to the spin diffusion in rotating frames. Therefore, minimizing the electron concentration without attenuating the DNP enhancements is more feasible using polarizing mechanisms in nuclear laboratory frames than in nuclear rotating frames. In addition, the electron T_1 needs to be short in order to restore the equilibrium electron polarization for multiple polarization transfers from each paramagnetic center to many nuclei. The DNP experiments in this thesis are performed in the laboratory frame for both the electrons and the nuclei, relying on polarizing mechanisms that require only CW microwave irradiation.

2.2.1.2. Polarizing mechanisms in the laboratory frame

Polarizing mechanisms in the laboratory frame for both electrons and nuclei involve CW microwave irradiation and are explained on the basis of spin Hamiltonian truncated from Eq. 1 as

$$H = \sum_i^{N_e} \omega_e^i S_z^i + \omega_n \sum_i^{N_n} I_z^i + H_{ee} + H_{en} + H_{nn} \quad (3)$$

with

$$\omega_e^i = g_i \beta_e B_0 / \hbar \text{ and } \omega_n = -\gamma_n B_0,$$

which are defined in Table 2.1. In DNP processes, the electron-nuclear interactions H_{en} in Eq. 3 are essential, which contain ¹³

$$H_{en} = H_{en}^{iso} + H_{en}^{aniso},$$

with

$$H_{en}^{iso} \equiv \sum_{i,j} a_{ij} I_i \cdot S_j = \sum_{i,j} a_{ij} \left(\frac{1}{2} (I_i^+ S_i^- + I_i^- S_i^+) + I_z^i S_z^j \right), \quad (4)$$

$$H_{en}^{aniso} \equiv \sum_{i,j} \frac{\gamma_e \gamma_n \hbar}{r_{ij}^3} (A_{ij} + B_{ij} + C_{ij} + D_{ij} + E_{ij} + F_{ij}), \quad (5)$$

where

$$\begin{aligned} A_{ij} &= (1 - 3 \cos^2 \theta) I_z^i S_z^j, \\ B_{ij} &= -\frac{1}{4} (1 - 3 \cos^2 \theta_{ij}) (I_i^+ S_j^- + I_i^- S_j^+), \\ C_{ij} &= -\frac{3}{2} \sin \theta_{ij} \cos \theta_{ij} e^{-i\phi_{ij}} (I_z^i S_j^+ + I_i^+ S_z^j), \\ D_{ij} &= -\frac{3}{2} \sin \theta_{ij} \cos \theta_{ij} e^{i\phi_{ij}} (I_z^i S_j^- + I_i^- S_z^j), \\ E_{ij} &= -\frac{3}{4} \sin^2 \theta_{ij} e^{-2i\phi_{ij}} I_i^+ S_j^+, \\ F_{ij} &= -\frac{3}{4} \sin^2 \theta_{ij} e^{2i\phi_{ij}} I_i^- S_j^-. \end{aligned}$$

Depending on the time-dependence of H_{en} , polarizing mechanisms discussed in the literature include the Overhauser effect (OE), the solid effect (SE), the cross effect (CE) and thermal mixing (TM) as are summarized in the reviews by Wind *et al.*⁵⁸ and by Atsarkin⁶⁷. In the following we provide a general description of those mechanisms.

The Overhauser Effect

The OE originates from polarization transfers between one electron and one nucleus, when H_{en} is stochastic with a correlation time $\tau_c \leq 1/\omega_e$, where ω_e is the electron Larmor frequency. First, for simplicity, we consider only H_{en}^{iso} (Eq. 4) which according to relaxation theories leads to W_0 (Figure 2.1) as

$$W_0 = \frac{1}{2} \langle a_{ij}^2(t) \rangle J(\omega_e, \tau_c),$$

where $J(\omega, \tau)$ is the spectral density function for the resonance frequency ω and the correlation time τ .

The influence of W_0 tends to keep the coupled spin-states (i.e., $|1\rangle$ and $|4\rangle$ in Figure 2.1) at a thermal equilibrium, resulting in

$$\begin{aligned}\frac{d}{dt}N_1 &= -W_0(N_1 - N_1^0) + W_0(N_4 - N_4^0), \\ \frac{d}{dt}N_4 &= W_0(N_1 - N_1^0) - W_0(N_4 - N_4^0),\end{aligned}\tag{6}$$

where the N_i and N_i^0 are the populations of states at some time and at thermal equilibrium, respectively. Following the state-populations, the Zeeman polarization for the electron and the nucleus, p_e and p_n , can be defined as

$$\begin{aligned}p_e &\equiv \frac{N_1 + N_2 - N_3 - N_4}{N_1 + N_2 + N_3 + N_4}, \\ p_n &\equiv \frac{N_2 + N_4 - N_1 - N_3}{N_1 + N_2 + N_3 + N_4}.\end{aligned}\tag{7}$$

The time dependence of p_e and p_n due to W_0 is (note that the sum of state-populations is constant)

$$\begin{aligned}\frac{d}{dt}p_n &= \frac{\frac{d}{dt}(N_4 - N_1)}{N_1 + N_2 + N_3 + N_4} = \frac{2W_0(N_1 - N_1^0 - N_4 + N_4^0)}{N_1 + N_2 + N_3 + N_4}, \\ \frac{d}{dt}p_e &= \frac{\frac{d}{dt}(N_1 - N_4)}{N_1 + N_2 + N_3 + N_4} = \frac{2W_0(N_4 - N_4^0 - N_1 + N_1^0)}{N_1 + N_2 + N_3 + N_4}.\end{aligned}\tag{8}$$

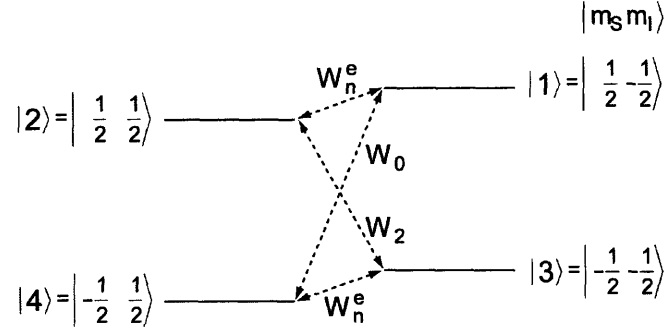


Figure 2.1. Illustration of an electron-nucleus two spin system, showing possible relaxation pathways due to time-dependent H_{en} .

Replacing the state-populations in Eq. 8 with spin polarization in Eq. 7, we obtain

$$\begin{aligned}\frac{d}{dt} p_n &= -W_0(p_n - p_e) + W_0(p_n^0 - p_e^0), \\ \frac{d}{dt} p_e &= W_0(p_n - p_e) - W_0(p_n^0 - p_e^0),\end{aligned}$$

which should be corrected for the condition that $N_n/N_e > 1$. Using the assumption that all nuclei can interact efficiently with at least one electron through molecular collisions, the correction for unequal numbers of electrons and nuclei yields

$$\begin{aligned}\frac{d}{dt} p_n &= -\frac{W_0}{C_n}(p_n - p_e) + \frac{W_0}{C_n}(p_n^0 - p_e^0), \\ \frac{d}{dt} p_e &= W_0(p_n - p_e) - W_0(p_n^0 - p_e^0),\end{aligned}\tag{9}$$

where $C_n = N_n/N_e$. With the definition of the intrinsic nuclear T_1 relaxation rate, $W_n^x = 1/T_{1n}^x$, the electron T_1 relaxation rate, $W_e = 1/T_{1e}$, and the microwave excited transition rate, $W = \pi \gamma_e^2 B_1^2 g(\omega - \omega_e)$, we extend the equation of motion in Eq. 9 to the

practical formula

$$\frac{d}{dt} p_n = -\frac{W_0}{C_n}(p_n - p_e) + \frac{W_0}{C_n}(p_n^0 - p_e^0) - W_n^x(p_n - p_n^0), \quad (10)$$

$$\frac{d}{dt} p_e = W_0(p_n - p_e) - W_0(p_n^0 - p_e^0) - W p_e - W_e(p_e - p_e^0). \quad (11)$$

The steady-state of electron polarization is attained rapidly and becomes ($dp_e/dt = 0$ in Eq. 11)

$$p_e^\infty \approx \frac{W_0(p_n - p_n^0) + p_e^0(W_0 + W_e)}{W_0 + W + W_e}. \quad (12)$$

Substituting p_e^∞ in Eq. 12 for p_e in Eq. 10, we obtain

$$\begin{aligned} \frac{d}{dt} p_n \approx & -\frac{W_0W + W_0W_e + W_n^xW_0C_n + W_n^xWC_n + W_n^xW_eC_n}{C_n(W_0 + W + W_e)}(p_n - p_n^0) \\ & - \frac{W_0W}{C_n(W_0 + W + W_e)} p_e^0. \end{aligned} \quad (13)$$

Here we define the enhancement factor as

$$\epsilon \equiv \frac{p_n - p_n^0}{p_n^0}, \quad (14)$$

and we find that Eq. 13 can be rewritten as

$$\frac{d}{dt} \epsilon \approx -\frac{W_0W + W_0W_e + W_n^xW_0C_n + W_n^xWC_n + W_n^xW_eC_n}{C_n(W_0 + W + W_e)} \epsilon - \frac{W_0W}{C_n(W_0 + W + W_e)} \frac{p_e^0}{p_n^0}.$$

As the enhanced nuclear polarization grows, the steady-state enhancement ϵ^∞ and the

growth time constant τ_{DNP} are

$$\varepsilon^\infty \approx -\frac{W_0 W}{W_0 W + W_0 W_e + W_n^x W_0 C_n + W_n^x W C_n + W_n^x W_e C_n} \frac{P_e^0}{P_n^0}, \quad (15)$$

and

$$\tau_{DNP} \approx \frac{C_n (W_0 + W + W_e)}{W_0 W + W_0 W_e + W_n^x W_0 C_n + W_n^x W C_n + W_n^x W_e C_n}. \quad (16)$$

Assuming $W_n^x W_0 C_n$ in Eq. 16 is much smaller than the remaining terms, we obtain (with the high-temperature approximation)

$$\varepsilon^\infty \approx -\frac{W}{W + W_e} \frac{W_0}{W_0 + W_n^x C_n} \frac{\gamma_e}{\gamma_n},$$

which is positive for $\gamma_e < 0$ and $\gamma_n > 0$. The saturation factor $W/(W+W_e)$ and the leakage factor $W_0/(W_0+W_n^x C_n)$ describe how microwave excitation and electron-nuclear cross-relaxation compete with electron and nuclear T_1 relaxation, respectively, in the DNP processes.

Full consideration of the OE should include the anisotropic hyperfine interaction term $H_{en}^{aniso}(t)$ (Eq. 6) which leads to several relaxation pathways which are denoted (after averaging the coefficients over the θ_{ij} and ϕ_{ij} in a solid angle) by¹³

$$W_0^D = \frac{1}{20} d_{ij}^2 J(\omega_e, \tau_c) \quad \text{for } |1\rangle \leftrightarrow |4\rangle, \quad (17)$$

$$W_2^D = \frac{6}{20} d_{ij}^2 J(\omega_e, \tau_c) \quad \text{for } |2\rangle \leftrightarrow |3\rangle, \quad (18)$$

$$W_n^e = \frac{3}{20} d_{ij}^2 J(\omega_n, \tau_c) \quad \text{for } |1\rangle \leftrightarrow |2\rangle \text{ and } |3\rangle \leftrightarrow |4\rangle. \quad (19)$$

Among the electron-nuclear cross-relaxation pathways (Figure 2.1) due to the stochastic electron-nuclear dipolar interaction, the influence of W_0^D is similar to W_0 . However, W_2^D acts differently as it connects $|2\rangle$ and $|3\rangle$ and leads to

$$\begin{aligned}\frac{d}{dt}N_2 &= -W_2^D(N_2 - N_2^0) + W_2^D(N_3 - N_3^0), \\ \frac{d}{dt}N_3 &= W_2^D(N_2 - N_2^0) - W_2^D(N_3 - N_3^0).\end{aligned}$$

According to the definitions of spin polarizations in Eq. 7, we find W_2^D affects p_e and p_n according to

$$\begin{aligned}\frac{d}{dt}p_n &= -\frac{W_2^D}{C_n}(p_n + p_e) + \frac{W_2^D}{C_n}(p_n^0 + p_e^0), \\ \frac{d}{dt}p_e &= -W_2^D(p_n + p_e) + W_2^D(p_n^0 + p_e^0),\end{aligned}\tag{20}$$

where $C_n = N_n/N_e$ for the correction due to the unequal numbers of electrons and nuclei. Moreover, the electron-nuclear dipolar interaction induces paramagnetic nuclear T_1 relaxation in a rate of W_n^e . The influence of W_n^e on state-populations appears

$$\begin{aligned}\frac{d}{dt}N_1 &= -\frac{1}{2}W_n^e(N_1 - N_1^0) + \frac{1}{2}W_n^e(N_2 - N_2^0), \\ \frac{d}{dt}N_2 &= \frac{1}{2}W_n^e(N_1 - N_1^0) - \frac{1}{2}W_n^e(N_2 - N_2^0), \\ \frac{d}{dt}N_3 &= -\frac{1}{2}W_n^e(N_3 - N_3^0) + \frac{1}{2}W_n^e(N_4 - N_4^0), \\ \frac{d}{dt}N_4 &= \frac{1}{2}W_n^e(N_3 - N_3^0) - \frac{1}{2}W_n^e(N_4 - N_4^0),\end{aligned}$$

which lead to the time-dependences of p_n and p_e due to W_n^e as

$$\frac{d}{dt} p_n = -\frac{W_n^e}{C_n} (p_n - p_n^0),$$

$$\frac{d}{dt} p_e = 0.$$

In consideration of electron and nuclear T_1 relaxation, scalar cross-relaxation and microwave excitation, the overall equations of motion for p_n and p_e are

$$\begin{aligned} \frac{d}{dt} p_n = & -\frac{W_0 + W_0^D}{C_n} (p_n - p_e) + \frac{W_0 + W_0^D}{C_n} (p_n^0 - p_e^0) \\ & - \frac{W_2^D}{C_n} (p_n + p_e) + \frac{W_2^D}{C_n} (p_n^0 + p_e^0) \end{aligned} \quad (21)$$

$$\begin{aligned} & - (W_n^x + \frac{W_n^e}{C_n}) (p_n - p_n^0), \\ \frac{d}{dt} p_e = & (W_0 + W_0^D) (p_n - p_e) - (W_0 + W_0^D) (p_n^0 - p_e^0) \\ & - W_2^D (p_n + p_e) + W_2^D (p_n^0 + p_e^0) \\ & - W p_e - W_e (p_e - p_e^0). \end{aligned} \quad (22)$$

Although we can solve Eqs. 21 and 23 without any assumption, the approximate solutions to p_n and p_e can be obtained by assuming that W and W_e dominate in Eq. 23 and letting p_e reach a steady state before a significant buildup of enhanced nuclear polarization. This leads to

$$p_e^\infty \approx \frac{W_e p_e^0}{W + W_e}, \quad (23)$$

which is used to replace p_e in Eq. 21 to yield

$$\begin{aligned} \frac{d}{dt} p_n \approx & -\left(\frac{W_0 + W_0^D + W_2^D + W_n^e}{C_n} + W_n^x\right)(p_n - p_n^0) \\ & - \frac{WW_0 + WW_0^D - WW_2^D}{C_n(W + W_e)} p_e^0. \end{aligned} \quad (24)$$

In Eq. 24, the microwave irradiation excites allowed EPR transitions and affects the quasi-equilibrium electron polarization as well as the steady-state nuclear polarization. However, the microwave excitation rate W does not affect the buildup rate of nuclear polarization, since the rate-determining step of polarization transfer is the electron-nuclear cross relaxation. As the enhancement factor is defined in Eq. 14, its time-dependence is obtained from Eq. 24 as

$$\frac{d}{dt} \varepsilon \approx -\frac{W_0 + W_0^D + W_2^D + W_n^e + C_n W_n^x}{C_n} \varepsilon - \frac{WW_0 + WW_0^D - WW_2^D}{C_n(W + W_e)} \frac{p_e^0}{p_n^0},$$

from which the steady-state enhancement ε^∞ (with the high-temperature approximation) and growth time constant τ_{DNP} are

$$\varepsilon^\infty \approx -\frac{W_0 + W_0^D - W_2^D}{W_0 + W_0^D + W_2^D + W_n^e + C_n W_n^x} \frac{W}{W + W_e} \frac{\gamma_e}{\gamma_n}, \quad (25)$$

and

$$\tau_{DNP} \approx \frac{C_n}{W_0 + W_0^D + W_2^D + W_n^e + C_n W_n^x}.$$

In the absence of the scalar hyperfine interaction ($W_0 = 0$), the assumption that W_n^x is much smaller than the remaining relaxation rates and that $W \gg W_e$ simplify Eq. 25 to

$$\varepsilon^\infty \approx -\frac{W_0^D - W_2^D}{W_0^D + W_2^D + W_n^e} \frac{\gamma_e}{\gamma_n}.$$

With motional narrowing ($\omega_e \tau_c \ll 1$), or $J(\omega_e, \tau_c) = 1$, we recall Eqs. 17, 18 and 20 and summarize that

$$\frac{W_0^D - W_2^D}{W_0^D + W_2^D + W_n^e} = -\frac{1}{2}.$$

Therefore, the steady-state nuclear enhancement becomes

$$\epsilon^\infty \approx \frac{1}{2} \frac{\gamma_e}{\gamma_n},$$

which is compared to $\epsilon^\infty = -\gamma_e/\gamma_n$ as a result of the pure scalar electron-nuclear interaction.

The Solid Effect

The SE occurs between one electron and one nucleus, when the electron-nuclear interaction H_{en} is time-independent. The semisecular terms of H_{en}^{aniso} ($S_z I^+$ and $S_z I^-$) lead to level-mixing which results in perturbed spin-states, $|1'\rangle = |1\rangle + q|2\rangle$, $|2'\rangle = |2\rangle - q|1\rangle$, $|3'\rangle = |3\rangle - q|4\rangle$ and $|4'\rangle = |4\rangle + q|3\rangle$ as are shown in Figure 2.2. The mixing factor q is a perturbation of the electron–nuclear interaction and is

$$q = -\frac{3}{4} \frac{\gamma_e \gamma_n \hbar}{\omega_n r_{ij}^3} \sin \theta_{ij} \cos \theta_{ij} e^{-i\phi_{ij}}. \quad (26)$$

The state-mixing allows microwave irradiation ($H_M = 2\omega_1 S_x$ in the rotating frame) to excite the forbidden transitions. In this circumstance, the transition moments are

$$\begin{aligned}\langle 1|H_M|4\rangle &= \langle (1+q|2\rangle)H_M(|4\rangle+q|3\rangle) = q(\langle 2|H_M|4\rangle + \langle 1|H_M|3\rangle) = 2q\omega_1, \\ \langle 2|H_M|3\rangle &= \langle (2-q|1\rangle)H_M(|3\rangle-q|4\rangle) = -q(\langle 2|H_M|4\rangle + \langle 1|H_M|3\rangle) = -2q\omega_1,\end{aligned}$$

which account for the probability of electron-nuclear flip-flop transitions.

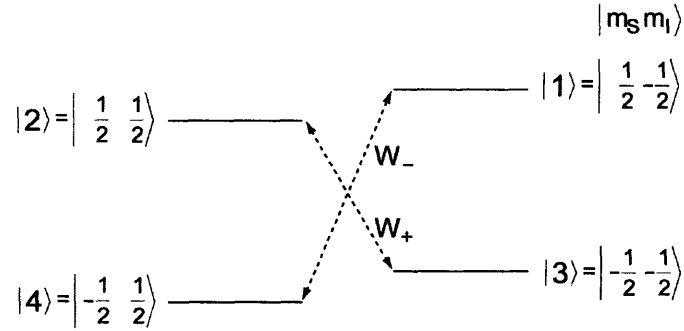


Figure 2.2. Illustration of an electron-nuclear two spin system showing forbidden transitions for the solid effect.

The transition rates W_{\pm} (Figure 2.2) are maximized at microwave frequencies $\omega_e \mp \omega_n$ and are expressed as

$$W_{\pm} = 2\pi |q|^2 \omega_1^2 g(\omega_e \pm \omega_n - \omega). \quad (27)$$

The influence of W_{\pm} on the populations of states is

$$\begin{aligned}\frac{d}{dt}N_2 &= -W_+N_2 + W_+N_3, \\ \frac{d}{dt}N_3 &= W_+N_2 - W_+N_3, \\ \frac{d}{dt}N_1 &= -W_-N_1 + W_-N_4, \\ \frac{d}{dt}N_4 &= W_-N_1 - W_-N_4.\end{aligned}$$

According to the definition of p_e and p_n in Eq. 7, we find the influence of W_{\pm} on the

electron and nuclear polarizations is (under a constant sum of state-populations)

$$\frac{d}{dt} p_n = \frac{\frac{d}{dt}(N_2 + N_4 - N_1 - N_3)}{N_1 + N_2 + N_3 + N_4} = \frac{-2W_+(N_2 - N_3) + 2W_-(N_1 - N_4)}{N_1 + N_2 + N_3 + N_4},$$

$$\frac{d}{dt} p_e = \frac{\frac{d}{dt}(N_1 + N_2 - N_3 - N_4)}{N_1 + N_2 + N_3 + N_4} = \frac{-2W_+(N_2 - N_3) - 2W_-(N_1 - N_4)}{N_1 + N_2 + N_3 + N_4},$$

which can be simplified to

$$\frac{d}{dt} p_n = -W_+(p_n + p_e) - W_-(p_n - p_e),$$

$$\frac{d}{dt} p_e = -W_+(p_n + p_e) + W_-(p_n - p_e),$$

and further be corrected for the condition of $N_n/N_e > 1$ as (with $C_n = N_n/N_e$)

$$\frac{d}{dt} p_n = -\frac{W_+}{C_n}(p_n + p_e) - \frac{W_-}{C_n}(p_n - p_e), \quad (28)$$

$$\frac{d}{dt} p_e = -W_+(p_n + p_e) + W_-(p_n - p_e). \quad (29)$$

In addition to the intrinsic nuclear T_1 relaxation (denoted by $W_n^x = 1/T_{1n}^x$), there exists paramagnetic nuclear relaxation (denoted by W_n^e) due to the electron-nuclear dipolar interaction, and when H_{en} is time-independent, the paramagnetic nuclear relaxation could be driven by electron spin-lattice relaxation T_{1e} as

$$W_n^e \approx 4|q|^2 \frac{\omega_n^2 T_{1e}}{1 + \omega_n^2 T_{1e}^2}.$$

Considering the intrinsic and paramagnetic nuclear T_1 -relaxation and the electron T_1 -relaxation (denoted by $W_e = 1/T_{1e}$), we rewrite Eqs. 28 and 29 to be

$$\frac{d}{dt} p_n = -\frac{W_+}{C_n}(p_n + p_e) - \frac{W_-}{C_n}(p_n - p_e) - (W_n^x + \frac{W_n^e}{C_n})(p_n - p_n^0), \quad (30)$$

$$\frac{d}{dt} p_e = -W_+(p_n + p_e) + W_-(p_n - p_e) - W_e(p_e - p_e^0). \quad (31)$$

In the SE, W_+ and W_- are usually much smaller than W_e . Thus, the W_e dominates the other terms and leads to a steady-state of electron polarization (see Eq. 31) as

$$p_e^\infty \approx p_e^0,$$

which is used to replace p_e in Eq. 30 to yield

$$\frac{d}{dt} p_n \approx -\left(\frac{W_+ + W_- + W_n^e}{C_n} + W_n^x\right)p_n + (W_n^x + \frac{W_n^e}{C_n})p_n^0 + \frac{W_- - W_+}{C_n}p_e^0.$$

With the definition of the enhancement factor in Eq. 14, we obtain

$$\frac{d}{dt} \epsilon \approx -\left(\frac{W_+ + W_- + W_n^e}{C_n} + W_n^x\right)\epsilon - \frac{W_+ + W_-}{C_n} + \frac{W_- - W_+}{C_n} \frac{p_e^0}{p_n^0}.$$

Subsequently, the steady-state nuclear enhancement ϵ^∞ (with the high-temperature approximation) and the growth time constant τ_{DNP} are

$$\epsilon^\infty \approx \frac{-W_+ - W_-}{W_+ + W_- + W_n^e + C_n W_n^x} + \frac{W_- - W_+}{W_+ + W_- + W_n^e + C_n W_n^x} \frac{\gamma_e}{\gamma_n},$$

and

$$\tau_{DNP} \approx \frac{C_n}{W_+ + W_- + W_n^e + C_n W_n^x}.$$

To clearly resolve the SE, it is required that the EPR linewidth be smaller than the

nuclear Larmor frequency ($\delta < \omega_n$). Under this condition, W_+ and W_- can be separately excited at different microwave frequencies. For example, the condition that $\omega = \omega_e + \omega_n$ drives W_- , and thereby, the steady-state enhancement is

$$\epsilon^\infty \approx \frac{-W_-}{W_- + W_n^e + C_n W_n^x} + \frac{W_-}{W_- + W_n^e + C_n W_n^x} \frac{\gamma_e}{\gamma_n},$$

which yields a negative nuclear enhancement as $\gamma_e < 0$ and $\gamma_n > 0$. In addition, the associated growth time constant is

$$\tau_{DNP} \approx \frac{C_n}{W_- + W_n^e + C_n W_n^x}.$$

The Cross Effect

The CE was first proposed by Kessenikh and Manenkov^{54,55}, involving two types of electron spins, S_1 and S_2 , the Larmor frequencies of which, ω_{e1} and ω_{e2} , satisfy the relation⁶⁷ (Figure 2.3)

$$\Delta_{12} = \omega_{e1} - \omega_{e2} \approx \pm \omega_n. \quad (32)$$

The cross effect occurs as a result of simultaneous operation of H_{ee} and H_{en} . The elementary event in this process is the simultaneous spin flip of all these spins, S_1 , S_2 and I , which tends to reach the equality of the polarization of each spin as (assuming $\Delta_{12} = \pm \omega_n$ and $\gamma_n > 0$)

$$p_n = \pm(p_{e1} - p_{e2}).$$

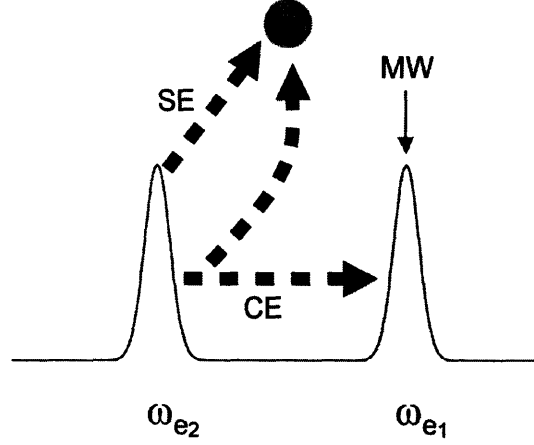


Figure 2.3. Illustration of the cross effect with two EPR lines at ω_{e1} and ω_{e2} . The polarization transfer is illustrated as the dash lines to the coupled nucleus (dot). Microwave irradiation at ω_{e1} drives not only the solid effect with respect to e_2 but the cross effect involving both e_1 and e_2 .

In an example that $\omega_{e1} - \omega_{e2} = \omega_n$, microwave irradiation at $\omega_M = \omega_{e1}$ leads to $p_{e1} = 0$ and lets p_n approach $-p_{e2}$. For details, when Eq. 32 is satisfied, the transition probability for the CE is

$$W_{\pm}(\Delta_{12}) \sim |q|^2 W_{CR}(\Delta_{12} \pm \omega_n),$$

where the state-mixing factor $|q|^2$ is on the same scale as was defined in Eq. 27 and

$$W_{CR}(\Delta_{12} \pm \omega_n) \propto T_{2e}^{-1} g(\Delta_{12} \pm \omega_n).$$

Using the previous example in which $\Delta_{12} = \omega_n$ and $\omega_M = \omega_{e1}$, we obtain

$$\begin{aligned}
\frac{d}{dt} p_{e1} &= -W_-(p_{e1} - p_{e2} + p_n) - W p_{e1} - W_e(p_{e1} - p_{e1}^0), \\
\frac{d}{dt} p_{e2} &= W_-(p_{e1} - p_{e2} + p_n) - W_e(p_{e2} - p_{e2}^0), \\
\frac{d}{dt} p_n &= -\frac{W_-}{C_n}(p_{e1} - p_{e2} + p_n) - (W_n^x + \frac{W_n^e}{C_n})(p_n - p_n^0).
\end{aligned} \tag{33}$$

To solve Eq. 33, p_{e1} and p_{e2} are assumed to reach a steady state rapidly and W_- is assumed to be much less than W and W_e . Thus, we obtain (defining $p_e^0 \equiv p_{e1}^0 = p_{e2}^0$)

$$\begin{aligned}
p_{e1}^\infty &\approx \frac{W_e}{W + W_e} p_e^0, \\
p_{e2}^\infty &\approx p_e^0.
\end{aligned} \tag{34}$$

Substituting p_{e1}^∞ and p_{e2}^∞ (Eq. 34) for p_{e1} and p_{e2} (Eq. 33), the equation of motion for the nuclear polarization becomes

$$\frac{d}{dt} p_n \approx -\left(\frac{W_- + W_n^e}{C_n} + W_n^x\right) p_n + (W_n^x + \frac{W_n^e}{C_n}) p_n^0 + \frac{W_-}{C_n} \frac{W}{W + W_e} p_e^0. \tag{35}$$

According to the definition of ε in Eq. 14, we obtain (from Eq. 35)

$$\frac{d}{dt} \varepsilon \approx -\left(\frac{W_- + W_n^e}{C_n} + W_n^x\right) \varepsilon - \frac{W_-}{C_n} + \frac{W_-}{C_n} \frac{W}{W + W_e} \frac{p_e^0}{p_n^0}.$$

Thus the steady-state DNP enhancement, ε^∞ , and growth time constant τ_{DNP} are

$$\varepsilon^\infty \approx \frac{-W_-}{W_- + W_n^e + C_n W_n^x} + \frac{W_-}{W_- + W_n^e + C_n W_n^x} \frac{W}{W + W_e} \frac{\gamma_e}{\gamma_n},$$

and

$$\tau_{DNP} \approx \frac{C_n}{W_- + W_n^e + C_n W_n^x}.$$

Thermal Mixing

When an EPR spectrum is homogeneously broadened, the electron spin system can be decomposed into two thermodynamic reservoirs: the electron Zeeman reservoir (EZ) and the spin-spin dipolar reservoir (SS), which are characterized by the spin temperatures T_{EZ} and T_{SS} (Figure 2.4), respectively⁵⁸. While the energy of the EZ reservoir defines the EPR frequency, the energy of SS accounts for the broadening of the associated EPR spectrum. At thermal equilibrium, T_{EZ} and T_{SS} are equal to T_L , the lattice temperature. The polarization of a thermodynamic system is understood to be proportional to the reciprocal of the spin temperature times the transition energy. For example, the polarization of EZ is

$$p_e = -\frac{1}{2} \frac{\omega_e \hbar}{kT_{EZ}}.$$

During microwave irradiation, the Provotorov's theory (summarized in the reference⁵⁶) describes the interaction between EZ and SS as:

$$\frac{d}{dt} p_e = -W(p_e - \frac{1}{2}\beta\Delta) - W_e(p_e - p_e^0), \quad (36)$$

$$\frac{d}{dt} \beta = W \frac{2\Delta}{\omega_L^2} (p_e - \frac{1}{2}\beta\Delta) - W_D(\beta - \beta^0), \quad (37)$$

where $W = \pi\gamma_e^2 B_1^2 g(\Delta)$, $\Delta = \omega_M - \omega_e$, $\beta = \hbar/(kT_{SS})$ corresponding to the polarization of SS, $\beta^0 = \hbar/(kT_L)$, $\omega_L^2 = Tr(H_i^2)/Tr(S_z^2)$, where H_i is part of spin Hamiltonian responsible for the broadening of the EPR line, W_e is electron spin-lattice relaxation rate for EZ, and W_D is the relaxation rate for SS.

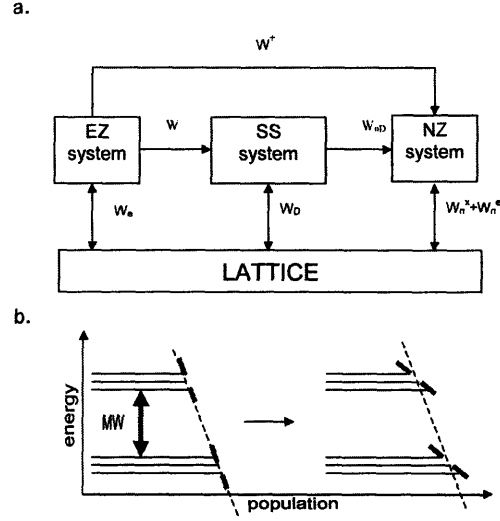


Figure 2.4. (a) An illustration of possible heat reservoirs in a spin system with electrons and nuclei. (b) The influence of microwave irradiation on EZ and SS. Spin temperatures are proportional to slopes of dash lines. Microwave irradiation at lower off-resonance frequencies cool the spin temperature of SS.

The steady-state solutions of p_e and β are (note that in Eq. 37, $p_e^0 = -\omega_e \beta^0 / 2$)

$$p_e^\infty = \frac{p_e^0 \left(W_e + W \left(\frac{\Delta^2}{a\omega_L^2} - \frac{\Delta}{\omega_e} \right) \right)}{W_e + W \left(\frac{\Delta^2}{a\omega_L^2} + 1 \right)}, \quad (38)$$

$$\beta^\infty = \frac{-\frac{2p_e^0}{\omega_e} \left(W_e - W \frac{\omega_e}{\Delta} \left(\frac{\Delta^2}{a\omega_L^2} - \frac{\Delta}{\omega_e} \right) \right)}{W_e + W \left(\frac{\Delta^2}{a\omega_L^2} + 1 \right)}, \quad (39)$$

where $a \equiv W_D / W_e$. Usually, we encounter the situation that $\frac{1}{\omega_e} \ll \frac{|\Delta|}{a\omega_L^2}$, unless Δ is close

to 0 on condition of on-resonance microwave irradiation. In addition, with strong microwave irradiation ($W \gg W_e$), we simplify Eq. 39 to be

$$\beta^\infty \approx \frac{2p_e^0 \frac{\Delta}{a\omega_L^2}}{\frac{\Delta^2}{a\omega_L^2} + 1} = \frac{-\omega_e \beta^0 \frac{\Delta}{a\omega_L^2}}{\frac{\Delta^2}{a\omega_L^2} + 1} \quad (40)$$

Eq. 40 indicates that microwave irradiation can enhance β (proportional to the polarization of SS), resulting in a positive enhancement, when $\Delta < 0$, and a negative enhancement, when $\Delta > 0$. The value of β^∞ becomes optimal, when $\Delta = \pm (a\omega_L^2)^{1/2}$, and is

$$\text{given by } \mp \frac{\beta^0 \omega_e}{2(a\omega_L^2)^{1/2}}.$$

The contact of the nuclear Zeeman system (NZ) with the EPR broadening system (SS) gives rise to enhancements of nuclear polarization. The polarization transfer involved is described as

$$\frac{d}{dt} p_n = -\frac{W_{nD}}{C_n} (p_n - \frac{1}{2} \beta \omega_n),$$

where $C_n = N_n/N_e$, and

$$W_{nD} = 4|q_{ij}|^2 \frac{1}{T_{2e}^{SS}} \frac{\int_{-\infty}^{\infty} g(\omega) g(\omega - \omega_n) d\omega}{g(0)}. \quad (41)$$

Eq. 41 implies that delocalized electron pairs are involved in TM, unlike a specific electron pair in the CE.

In fact, microwave-driven forbidden transitions are still possible under a broadened EPR lineshape. These forbidden transitions, analogous to those in the solid effect, involve

NZ, EZ and SS. For example, with microwave excitation at a frequency ω_M , an energy quantum of ω_e is absorbed by EZ, an energy quantum of ω_n is absorbed by NZ, and then the remaining $\omega_M - (\omega_e + \omega_n)$ is transferred to SS. This process refers to the forbidden transition W^+ in the following complete equation of motion for a buildup of nuclear polarization as

$$\begin{aligned} \frac{d}{dt} p_n = & -\frac{W_{nD}}{C_n} (p_n - \frac{1}{2}\beta\omega_n) \\ & + \frac{W^+}{C_n} (p_n - p_e - \frac{1}{2}\beta(\omega_n - \Delta)) - \frac{W^-}{C_n} (p_n + p_e - \frac{1}{2}\beta(\omega_n + \Delta)) \\ & - \left(\frac{W_n^e}{C_n} + W_n^X \right) (p_n - p_n^0). \end{aligned} \quad (42)$$

In Eq. 42, W^- depicts that an energy quantum of ω_e is absorbed by EZ, an energy quantum of ω_n is emitted by NZ, and the remaining $\omega_M - (\omega_e - \omega_n)$ is transferred to SS. Note a change of the sign of Δ in Eq. 42 reflects the overall absorption of ω_M by the EZ system.

Substituting p_e^∞ and β^∞ (Eqs. 38 and 39) for p_e and β (Eq. 42), we obtain (omitting Δ/ω_e and assuming $W_e \ll W\omega_e\Delta/(a\omega_L^2)$)

$$\begin{aligned} \frac{d}{dt} p_n \approx & - \left(\frac{-W^+ + W^- + W_{nD} + W_n^e}{C_n} + W_n^X \right) p_n + \left(\frac{W_n^e}{C_n} + W_n^X \right) p_n^0 \\ & + \left(\frac{W_{nD} - W^+ + W^-}{C_n} - \frac{W\omega_n\Delta}{a\omega_L^2} - \frac{W^- + W^+}{C_n} W_e \right) \frac{1}{W_e + W \left(\frac{\Delta^2}{a\omega_L^2} + 1 \right)} p_e^0. \end{aligned} \quad (43)$$

According to the definition of enhancement factor in Eq. 14, we transform Eq. 43 to

$$\frac{d}{dt}\epsilon \approx -\left(\frac{-W^+ + W^- + W_{nD} + W_n^e}{C_n} + W_n^X\right)\epsilon + \left(\frac{W^+ - W^- - W_{nD}}{C_n}\right) + \left(\frac{W_{nD} - W^+ + W^-}{C_n} - \frac{W\omega_n\Delta}{a\omega_L^2} - \frac{W^- + W^+}{C_n}W_e\right) \frac{1}{W_e + W\left(\frac{\Delta^2}{a\omega_L^2} + 1\right)} \frac{p_e^0}{p_n^0},$$

which implies the steady-state enhancement ϵ^∞ (with a high-temperature approximation)

and time constant τ_{DNP} as

$$\epsilon^\infty \approx \frac{W^+ - W^- - W_{nD}}{-W^+ + W^- + W_{nD} + W_n^e + C_n W_n^X} + \frac{(W^+ - W^-)W_e + (-W^+ + W^- + W_{nD})\frac{W\Delta\omega_n}{a\omega_L^2}}{(-W^+ + W^- + W_{nD} + W_n^e + C_n W_n^X) \left[W_e + W\left(\frac{\Delta^2}{a\omega_L^2} + 1\right) \right]} \frac{\gamma_e}{\gamma_n},$$

and

$$\tau_{DNP} \approx \frac{C_n}{-W^+ + W^- + W_{nD} + W_n^e + C_n W_n^X}.$$

2.2.2. Requirements for DNP at high magnetic fields

Successful DNP experiments at high fields rely on efficient polarizing mechanisms. High magnetic fields limit the utility of the OE, because it is difficult to satisfy the condition $\omega_e\tau_c \ll 1$, since τ_c is a characteristic of the sample and ω_e increases with increasing fields. Thus, polarizing mechanisms for high-field DNP are primarily the SE, the CE and TM, which are based on time-independent electron–nuclear interactions that are present in solid dielectrics. However, high magnetic fields still pose a challenge for

these polarizing mechanisms. For example, the SE relies on transitions due to a second order mixing of the electron–nuclear interactions, and therefore the SE enhancements scale as B_0^{-2} , where B_0 is the external magnetic field. In contrast the CE and TM rely on satisfying the frequency matching ($\omega_{e2}-\omega_{e1}=\omega_n$) and therefore the enhancement of these two polarizing mechanisms has a B_0^{-1} dependence. Therefore, the CE and TM are more efficient at high-field.

Performing DNP experiments at ever-increasing magnetic fields (5-20 T), which is appropriate for contemporary NMR spectroscopy, requires that the following four requirements be satisfied. First, a strong oscillating field at a high frequency (140-600 GHz) is necessary to drive the CW DNP transitions resulting from second order effects of electron–nuclear dipolar interactions. This also means that it is necessary to integrate microwave transmission lines into an NMR probe, which then efficiently deliver the microwave power to NMR samples. Second, the relaxation times and time-independent interactions of the spin system dictate that DNP experiments be optimally performed at low temperatures (usually ≤ 90 K), and, to obtain high resolution spectra of solids, magic-angle spinning (MAS) is incorporated into the experiment. Third, measuring NMR CP-signals in a cryogenic environment requires a transmission-line RF circuit with multiple channels (^1H , ^{13}C , ^{15}N , ^{17}O ...etc.). The fourth requirement is the presence of a suitable paramagnetic center that acts as the source of polarization. In addition, since current DNP experiments are performed with a constant microwave frequency, the ability to sweep the magnetic field is required for optimization of the DNP enhancement. Specifically, a superconductor sweep coil integrated with the main superconducting coil is necessary since the magnetic field usually has to be varied over a range of a few

hundred Gauss. Those requirements for high-field DNP are discussed in more detail in the following sections.

2.2.2.1. High power, high frequency microwave sources and transmission

Performing DNP at a high magnetic field (B_0) requires microwaves with not only a high frequency, but also high power so that a strong oscillating field is available to compensate for the low Q of the microwave circuit and inverse dependence of the DNP enhancements on the static magnetic field. A strong microwave field is achievable with microwave irradiation of several milliwatts in a high- Q , cylindrically resonant cavity that can have a $Q = 1000$ to $10,000$. The exciting field longitudinal (parallel to the cavity axis) magnetic field is given by $B_1 \propto \sqrt{PQ}$, where P is the incident power into the cavity. A high DNP enhancement at 5 T has been obtained by employing such a resonant cavity (Figure 2.5) with a Gunn diode (140 GHz)⁸⁶. However the diameter (< 3 mm) of a cavity resonator required for the high frequency microwaves limits the size of the NMR samples to ~ 0.30 μL . For typical SSNMR sample rotors with diameters of 2.5 to 4 mm the sample volume is 10-60 μL , and thus there is a decrease in the signal intensity of a factor of 33-200 from the smaller volume. Further, placing a spinning rotor with dimensions large compared to the wavelength in a cavity spoils the cavity characteristics. Thus, except in special circumstances, implementation of DNP with a resonant cavity seems impractical. Therefore, a high-frequency microwave source with high output power (several watts), such as a gyrotron, represents a solution to this problem.

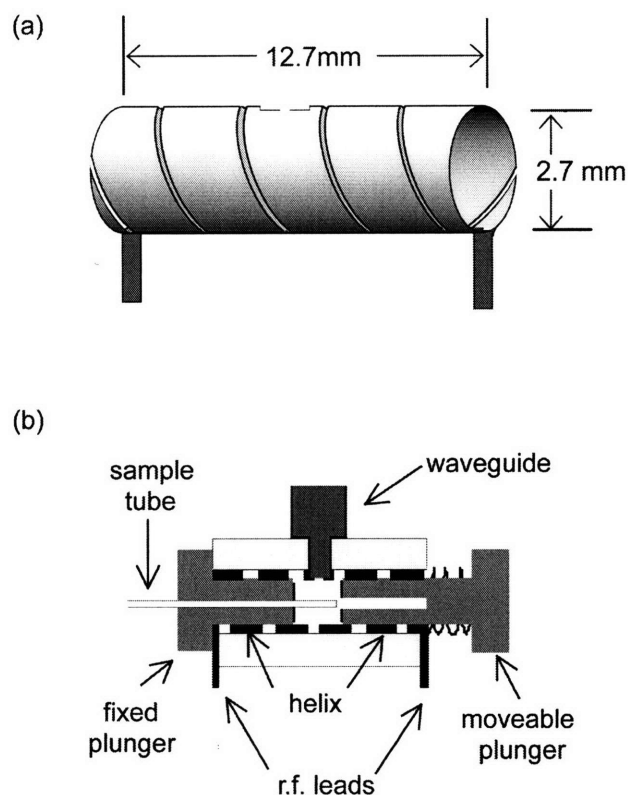


Figure 2.5. Illustration of a TE_{011} ENDOR resonator. (a) A drawing of the ribbon-cavity with outer conductor which serves as the NMR coil ; (b) the arrangement of components ¹.

Commercially available sources (Figure 2.6) include Gunn diodes, Impatt diodes, extended interaction oscillators (EIO) and backward wave oscillators (BWO); they either fail to provide sufficiently high power (the diodes) or cannot reliably provide the required frequency for high-field DNP (EIO, BWO). A slow-wave resonant structure involved in the latter devices constrains the resonant structure to a size comparable to the wavelength, and when the energy density increases at high microwave frequencies, the life time of the apparatus is reduced. The sources operative with laser excitation cover the higher frequency region of sub-tera hertz irradiation, but the available power from them is still limited.

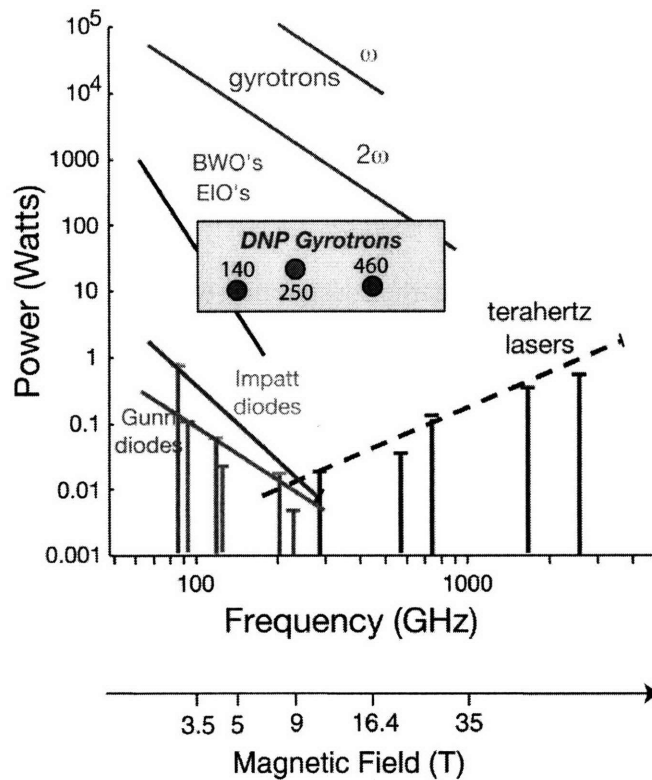


Figure 2.6. Summary of microwave sources ¹.

To circumvent the problems of generating high-frequencies and high-powers, plasma physicists developed gyrotron devices that generate microwaves by injecting free electron beams in high vacuum into a metal cavity aligned in a homogeneous magnetic field. Specifically, the electrons gyrate around the magnetic field lines at the electron cyclotron frequency in a helical motion as they traverse through the tube structure. Inside the resonator, a fast-wave interaction between the electron beam and millimeter wave takes place which converts some of the transverse kinetic energy (perpendicular to the field line) of the electron beam into millimeter wave energy in the form of TE_{mn} electromagnetic modes. The dimensions of the cylindrical resonator can be of the order of several wavelengths. This enables generation of high average power (10-100 W in CW,

kW-MW in pulse) at high frequencies (10 to 800 GHz) in gyrotrons due to lower thermal losses in the resonator walls.

The DNP experiments described in this thesis were performed exclusively with the 140 GHz gyrotron that was developed for DNP/NMR research at 5 T. This present gyrotron was modified⁸⁷ from an earlier design that was developed and used for plasma diagnostics⁸⁸. The basic components of this gyrotron include a superconducting magnet, a vacuum tube consist of a cathode (electron gun), a beam tunnel, a resonator, mode converters, beam collectors and a miter elbow with a mirror inside (Figure 2.7). Details about the design and construction of our three gyrotrons (140, 250 and 460 GHz) and their integrations into DNP spectrometers are discussed in other publications^{9, 62, 89}.

The distance between the gyrotron and the NMR magnet is long because of the strong magnetic field from the gyrotron can distort the field of the NMR magnet and vice versa. To transmit microwaves efficiently, the TE_{01} microwave output from the gyrotron is converted to the TE_{11} mode using a serpentine rippled wall mode converter⁹⁰. This mode converter was designed using coupled mode equations for a circular waveguide bent in a circular arc where one beat period is made up of two bent 6.53 cm long, 1.27 cm diameter copper sections with a bending radius of 1.21 m placed end to end. The structure consists of seven such periods yielding a design efficiency of over 94% at 140 GHz⁹¹ and was created by heating a copper pipe packed with sand and forcing it into a carved aluminum block to create the serpentine shape. Following this mode converter, the TE_{11} power is sent to the DNP probe by means of a smooth-wall copper waveguide. The losses in this waveguide total approximately 7 dB and the bulk of these losses appear in a downtaper section just before entry to the DNP probe^{1, 92}.

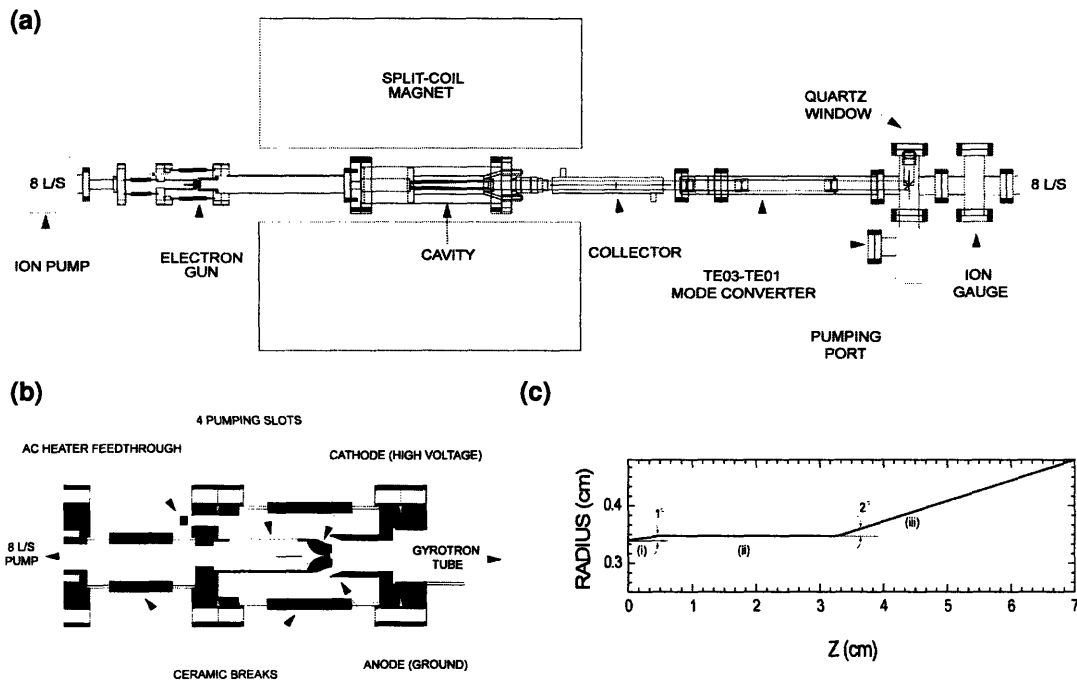


Figure 2.7. (a) 140 GHz gyrotron block diagram. “The vacuum base pressure is on the 10^{-9} torr scale and the operating pressure is kept well below 10^{-7} torr. “The cavity is water cooled to prevent it from being detuned due to thermal expansion. The heat lost by the finite conductivity of the copper is carried away by a water-cooled jacket brazed to the cavity. After the spent electron beam exits the cavity circuit, it is then collected by a water-cooled collector after the interaction cavity. The microwaves travel through the uptaper and collector sections and then propagates through a TE03 to TE02 axisymmetric rippled wall mode converter of $N = 5$ beat periods followed by a TE02 to TE01 mode converter that also uses $N = 5$ periods. A mirror and miter joint at the end of the second mode converter prevent stray electrons from striking the vacuum window and carry the TE01 mode out of the gyrotron via a 1.27 cm diameter overmoded copper waveguide. The fused quartz window is 2.73 cm in diameter and 3.43 mm thick and is designed to be transparent to microwaves at 140 GHz.” summarized from the reference ⁹. (b) A close look of the electron gun, which operates at a low voltage of -12.3 kV at up to 30 mA adjusted by an AC current through the heater filament. The electron gun can output pulses up to 60 seconds long at 50% duty cycle. For single-pulse operation, an emission period as long as 10 minutes is possible. (c) The axial profile of the interaction cavity. (i) Downtaper section allows the beam to pass through, but is cut off to the operating microwave field in the resonator so that no power leaks toward the electron gun. (ii) Straight section is a circular waveguide straight section approximately 15 wavelengths long with a radius of 3.480 mm. The theoretical diffractive Q of the cavity is almost 7000, restraining the purity of resonant frequency given stable cavity geometry. (iii) Uptaper section allows microwaves to diffract out of the cavity and is designed to prevent further interaction of the microwaves and electron beams.

While TE_{11} high-frequency microwave beams can be effectively transmitted in a smooth wall copper pipe with reflecting miter bends, improved transmission efficiency is obtainable in corrugated waveguides which are designed for transmission of microwaves in HE_{11} mode. The corrugations on the inner wall of the waveguide are $1/4$ wavelength (λ) in depth, $\lambda/10$ in width and $\lambda/4$ in span. Details of design and test of the corrugated transmission lines are discussed elsewhere⁹³. For MAS-NMR spectroscopy, microwaves for DNP experiments are directly coupled to the sample without resonance structure (Figure 2.8). As the wavelength is usually smaller than the coil diameter, the radiation can penetrate through the slit of a sinusoidal coil with a limited amount of diffraction.

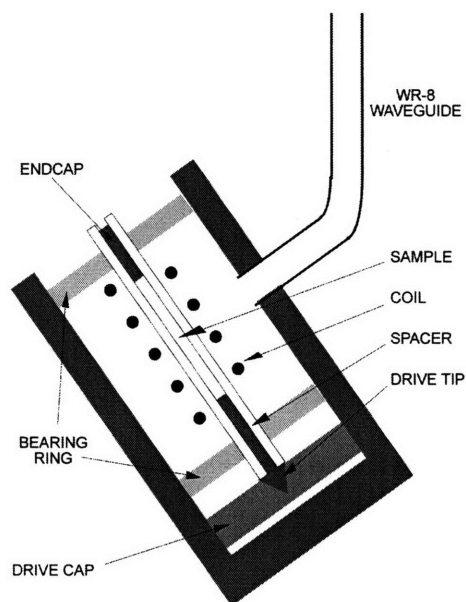


Figure 2.8. A schematic diagram of microwave irradiation on an NMR sample².

2.2.2.2. Cryogenic MAS devices

Magic-angle-spinning at cryogenic temperatures ($< 100\text{K}$) is achieved by blowing cooled N_2 gas at the bearing and driving that force the rotor to spin. Two N_2 gas lines from the high pressure tanks (CRYO-CYL) flow through the heat exchanger and vacuum jacked transfer lines which are routed to the MAS stator enclosed in a dewar inside the magnet (Figure 2.9). Cryogenic bayonet connections⁹⁴ are employed in junctions between the thermally isolated transfer lines of the NMR probe, the flexible section and the heat exchanger. The temperature of cool gas flow is controlled by the liquid N_2 level surrounding the heat exchange coils (copper) inside a can with variable N_2 pressures. To eliminate the impact of drastic temperature cycling, the spinning stator is made from the plastic Kel-F, which absorbs little RF power, and incorporates two ceramic bearing rings and a metal drive cap to contain a spinning rotor. Transfer lines for cold gases are typically made from stainless steels, but those inside the magnetic are fabricated from fiber glass (G10), brass and/or aluminum since stainless steels turn magnetic after several temperature-cycles. The magnetic materials should be kept at least 10 inches away from the sample to avoid problems with field inhomogeneity and shifts.

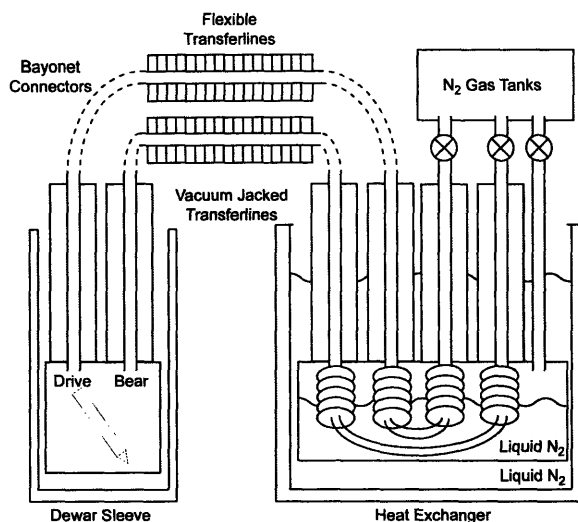


Figure 2.9. A schematic block diagram of the cryogenic MAS apparatus. The details are covered by the reference ⁶.

2.2.2.3. Cryogenic RF circuitry—transmission line probes

Transmission line RF circuitries ⁹⁵ are suitable for low temperature NMR operation since it provides good isolation between the sample coil (cold) and tuning capacitors (warm). Shown in Figure 2.10 is a schematic of a double-channel RF circuit using transmission lines. The main transmission line isolates the cold region containing the sample coil and the warm region outside the magnetic. Specifically, the impedance of a high frequency from the sample coil is transferred through the main transmission line, which runs from the center of the magnetic field to the outside of the magnet bore, reaching a node (zero reactant impedance) that can be a junction for the lower frequency. The reactant impedance of a low frequency can be zeroed at the same node by a balancing capacitor between the sample coil and the ground. Branch transmission lines after the node adjust the impedances to be tunable for the tuning/matching capacitors. For

a better isolation of high and low RF frequencies, band-stop networks (traps) are utilized. When a node for both the high and low frequencies is located, an intermediate frequency X' (as the third channel) can be connected to the node with good isolation by replacing the H- and X-traps with the X' -trap. Although a longer response time to RF pulses is present in transmission lines, it has not been important for typical SSNMR techniques. Only for the pulse sequence that requires fast modulations of amplitude, phase and/or carrier frequency would the transmission-line probe be problematic, and then a more delicate design of probe is required, e.g., a locally tuned circuit with good thermal isolation.

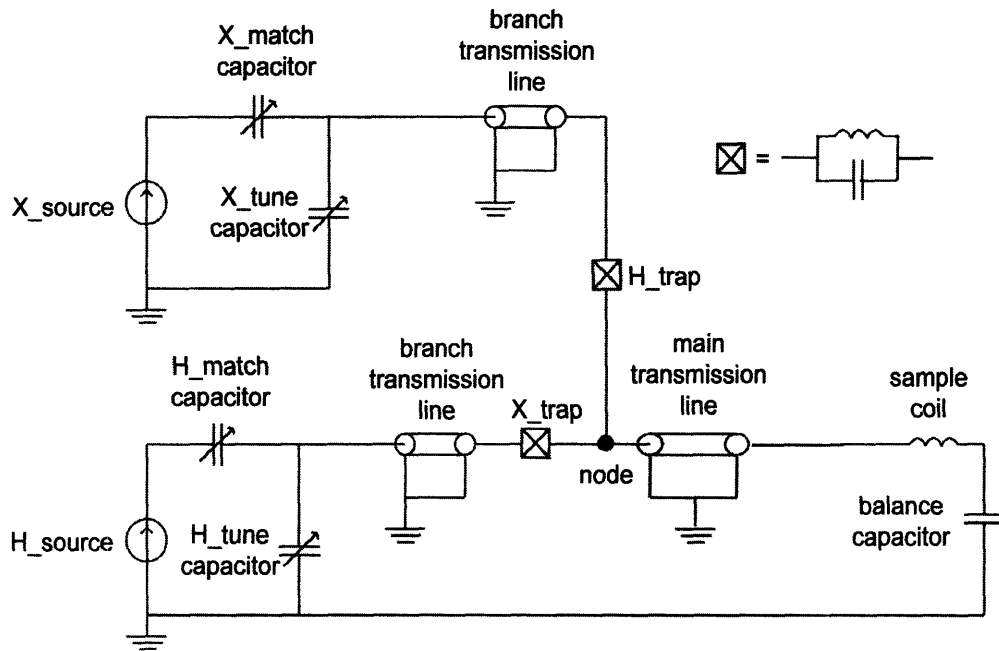


Figure 2.10. The RF circuit of a double resonance transmission-line probe.

2.2.2.4. Polarizing agents and cryoprotectants

The unpaired electrons in a diamagnetic system are introduced by doping the sample with paramagnetic species (polarizing agents). This paramagnetic center should: (a) be compatible with the polarization mechanism that yields the optimal signal enhancement, namely the three spin thermal mixing (TM) or cross effect (CE), (b) be useful in polarizing a large array of samples ranging from small molecules to proteins, (c) produce large signal enhancements at a reduced concentration of paramagnetic centers, and (d) be soluble in aqueous media for biological applications. The main goal of this thesis is to investigate how and why certain polarizing agents govern a desired polarizing mechanism. Through investigations in this thesis, methods to improve the DNP enhancement are developed theoretically and verified experimentally.

Commonly available paramagnetic species for DNP in aqueous media include radicals (trityl^{96,97}, TEMPO^{8,66,98,99}) and metal ions (Mn^{II}, Cr^V, Gd^{III}). These agents not only provide electron polarization but determine the underlying DNP mechanisms. For example, trityl radical induces the SE when used to dynamically polarize ¹H whereas TEMPO radical activates CE and/or TM in the polarization process. Nevertheless trityl can induce TM DNP when used to directly polarize ¹³C spins. The factor determining the polarizing mechanisms is the size of the EPR linewidth (δ) of the species compared with the nuclear Larmor frequency (ω_n). The CE and TM dominate a polarizing process when $\delta > \omega_n$ whereas the SE remains when $\delta < \omega_n$. In addition, BDPA was used in polystyrene¹⁰⁰ to generate proton enhancement through the SE; however, it is not soluble in water.

A glass-forming solution is employed to accommodate both the paramagnetic species and the interesting samples for: (a) even distribution of paramagnetic centers that

effectively contact the target nuclei, and (b) maintenance of macromolecule conformations (e.g., protein structures) at cryogenic temperatures which are required for high-field DNP ¹⁰¹. Various compositions of a solution form glasses when frozen (Table 2.4) ¹⁰². Some of them are compatible with aqueous media due to their high polarity, but others are non-polar and may be useful to suspend colloidal samples. In this thesis, we used DMSO/water and glycerol/water mixtures for less-polar and more-polar sample conditions, respectively. For example, DMSO/water is used in testing the biradical polarizing agents, and glycerol/water is required for protein or peptide samples. Other glass-forming compositions, e.g., PEG and MPD used as precipitating agents and cryoprotectors in X-ray diffraction experiments of biological solids, have found to provide effective conditions for DNP experiments on proteins and peptides ¹⁰³.

Table 2.4. Summary of glass-forming compositions. Data are from empirical tests at the liquid nitrogen temperature (77 K).

Bi-component mixture		Composition (w/w)
glycerol	water	60:40
Ethyleneglycol	water	50:50
dimethylsulfoxide (DMSO)	water	60:40
dimethylformamide (DMF)	water	70:30
methylpropanediol (MPD)	water	60:40
PEG200	water	40:60
glucose	water	70:30
dimethylsulfoxide (DMSO)	dichloromethane (DCM)	25:75
methanol	dichloromethane (DCM)	25:75
tetrahydrofurane (THF)	toluene	25:75

Chapter 3 Dynamic Nuclear Polarization Using Biradicals

Part of the works in this chapter is summarized in the publications:

Kan-Nian Hu, Hsiao-hua Yu, Timothy M. Swager and Robert G. Griffin, "Dynamic Nuclear Polarization with Biradicals," *J. Am. Chem. Soc.* **126**, 10844-10845 (2004).

Changsik Song, Kan-Nian Hu, Chan-Gyu Joo, Timothy M. Swager and Robert G. Griffin, "TOTAPOL—A Biradical Polarizing Agent for Dynamic Nuclear Polarization in Aqueous Media," *J. Am. Chem. Soc.* (2006), **in print**.

3.1. DNP with Biradicals Possessing a Polyethyleneglycol Tether

The last few years has witnessed a renaissance in the use of dynamic nuclear polarization (DNP) to enhance signal intensities in NMR spectra of solids and liquids. In a contemporary DNP experiment, a diamagnetic sample is doped with a paramagnet and the large polarization of the electron spins is transferred to the nuclei via microwave irradiation of the EPR spectrum⁵⁸. The development of gyrotron microwave sources (140 and 250 GHz)^{87, 104} has permitted these experiments to be performed at high fields (5 and 9 T) and signal enhancements ranging from 20 to 400 are observed depending on the details of the experiments – static magnetic field B_0 , microwave field strength ω_1 , temperature T , etc.^{62, 63, 86, 98, 100, 105}. The largest signal enhancements observed are in experiments where the thermal mixing (TM) or cross effect (CE) mechanisms^{51-53, 55, 106} are operative. Although multiple spins may be involved in both mechanisms, the underlying physics is essentially described by a three spin process that involves the coupling of two electrons whose frequencies, $\omega_{e1}/2\pi$ and $\omega_{e2}/2\pi$ in the EPR spectrum of

the polarizing agent, are spaced at the nuclear Larmor frequency, $\omega_n/2\pi$ (see Figure 3.1a). When these electrons are dipolar coupled, then irradiation at ω_{e1} produces a simultaneous spin flip of the second electron at ω_{e2} and the nucleus leading to the generation nuclear spin polarization (Figure 3.1b) through transitions such as $|\alpha_1\beta_2\beta_n\rangle \leftrightarrow |\alpha_1\alpha_2\alpha_n\rangle$ or $|\alpha_1\alpha_2\beta_n\rangle \leftrightarrow |\alpha_1\beta_2\alpha_n\rangle$. Since the introduction of the DNP technique 50 years ago^{48, 49}, all experiments have relied on monomeric paramagnetic centers such as a nitroxide or metal ion as a source of polarization. However, the electron-electron dipole coupling is clearly an important parameter governing the efficiency of the three spin TM and CE processes. Thus, it should be possible to optimize the enhancements in DNP experiments by constraining the distance between the two unpaired electrons. In this communication we demonstrate the validity of this concept with experiments that employ *biradical polarizing agents* consisting of two TEMPO (2,2,6,6-tetramethylpiperidinyl-1-oxyl) radicals tethered by a polyethylene glycol chain (Figure 3.1c). These biradical polarizing agents yield a factor of ~4 larger signal intensities over those obtained with monomeric TEMPO. Further, the larger enhancements are obtained at significantly lower concentrations, thereby reducing the paramagnetic broadening present in the NMR spectrum.

The biradicals illustrated in Figure 3.1c were prepared from 4-hydroxy-TEMPO and the di-, tri- or tetra-ethyleneglycol-di-tosylate using methods outlined by Gagnaire *et al.*¹⁰⁷ yielding a series of *bis*-TEMPO *n*-ethyleneglycol (BTnE) biradicals. Solution EPR spectra of BTnE (n=2, 3, or 4) (1 mM in methanol) showed the expected 5 lines indicating a strong exchange interaction (larger than ¹⁴N hyperfine interaction) between the electrons¹⁰⁸. Samples for the DNP experiments consisted of 5 mM biradical (10 mM

electrons) and 2 M ^{13}C -urea dispersed in a 60:40 $^2\text{H}_6$ -DMSO/ H_2O (90% $^2\text{H}_2\text{O}$) glass forming mixture. A control sample of 10 mM monomeric 4-hydroxy-TEMPO was also examined. The samples were contained in 4 mm sapphire rotors, and a series of DNP/CPMAS ^{13}C spectra were recorded as a function of the microwave irradiation time using a 140 GHz gyrotron source and a low temperature MAS probe operating at 90 K at $\omega_r/2\pi = 3.5 \text{ kHz}^{109}$.

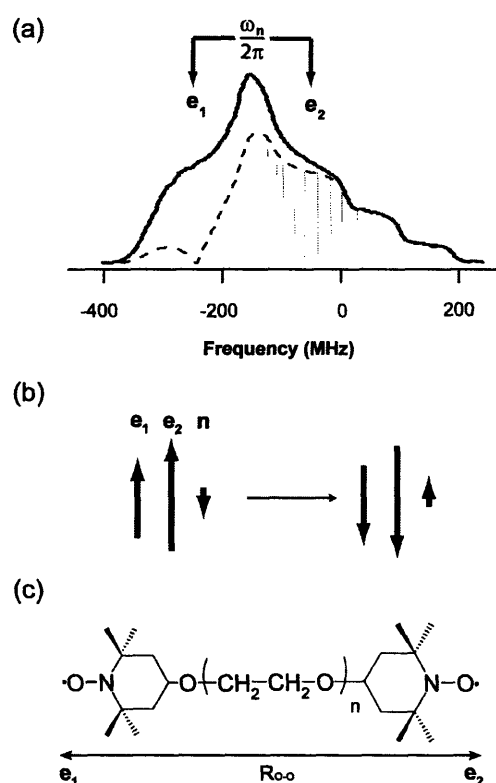


Figure 3.1. (a) An illustration of the EPR spectrum (solid line) of monomeric TEMPO nitroxide. Note that the breadth of the spectrum is ~ 600 MHz and is large compared to the ^1H Larmor frequency (212 MHz). The dashed line and the vertical sticks are the simulated inhomogeneous saturated EPR spectrum and the approximate frequency of the electron spins expected to participate in the DNP enhancement as a function of frequency, respectively. (b) An illustration of the microwave driven 3-spin process associated with TM or CE DNP where two coupled electrons undergo an energy conserving flip-flop process that leads to enhances nuclear spin polarization. (c) The molecular structure of the BTnE biradicals where n is the number of ethylene glycol units that tether two nitroxide radicals (TEMPO). The dots represent the two unpaired electrons whose displacement is approximated as the oxygen-oxygen distance, $R_{\text{O-O}}$.

Figure 3.2 illustrates a typical nuclear polarization build up curve obtained with a sample of BT2E. Note that the ^{13}C signal from urea is barely visible on the vertical used in the absence of microwave irradiation. However, with 3-15 seconds of microwave irradiation, the signal grows dramatically, reaching a plateau after ~ 15 seconds where we measure an enhancement of 175. Figure 3.3 illustrates the dependence of the enhancement on the length of the ethylene glycol linker and shows that as the linker is shortened from $n = 4, 3$ to 2 the enhancement increases from 80 to 110, and finally 175, respectively. The estimated error is ± 25 . For 10 mM TEMPO in this solvent system we observe an enhancement of 45. Thus, tethering the two TEMPO radicals yields a factor of 3.9 larger enhancement.

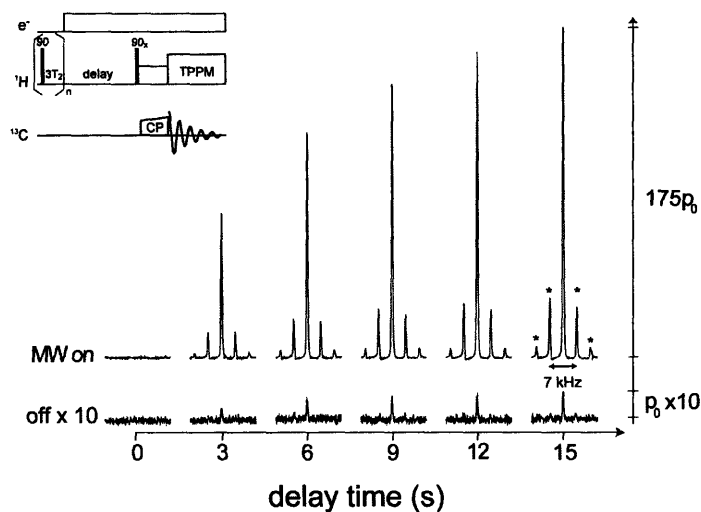


Figure 3.2. ^{13}C DNP-MAS spectra illustrating the growth of the ^{13}C -urea signal as the irradiation time is increased. The polarizing agent was BT2E at a concentration of 5 mM or 10 mM electrons. As indicated in the figure the maximum observed enhancement was 175 ± 25 . The inset shows the pulse sequence used to record the spectra. It utilizes a train of saturating pulses on the ^1H channel to insure that all of the polarization arises from the DNP effect. The spectra were recorded at 90 K, using a 4 mm sapphire rotor, $\omega_r/2\pi = 3.5$ kHz and the microwave power was 1.5 watts entering the probe.

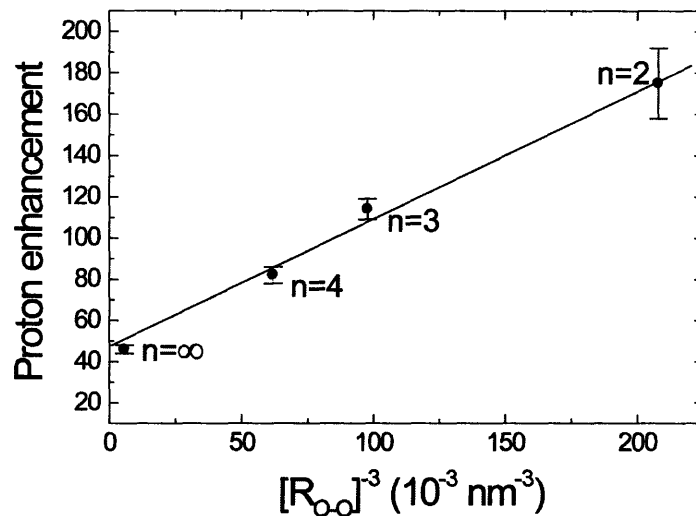


Figure 3.3. A plot of the ^1H enhancement measure indirectly through the ^{13}C spectrum as a function of the approximate electron-electron dipolar as measured by the distance, specifically $[R_{O-O}]^3$. The data points show the DNP enhancements obtained from molecules corresponding to the monomeric TEMPO ($n=\infty$) and the three biradicals that are tethered with 4,3, and 2 polyethylene glycol units. Notice that the shorter the linker the larger the enhancement. The electron concentration in all of the samples was 10 mM, corresponding to a concentration of 5 mM for the biradical molecules and 10 mM for monomeric TEMPO. The enhancements were recorded at 90 K at $\omega_r/2\pi = 3.5$ kHz.

As can be surmised from Figure 3.1, the efficiency of CE DNP process is affected by the polarizing agent through the size of the electron-electron dipole coupling and the relative orientations of the two radicals. At present we have not measured either of these quantities experimentally. However, an estimate of the electron-electron dipole coupling can be made using the intra-radical distance obtained from a simulated conformation assuming an all-trans polymer chain ¹¹⁰. The value of R_{O-O} from such specific conformations leads to approximate dipole couplings of 3.3, 5.2 and 11.0 MHz for the three BTnE ($n=4, 3$ and 2) compounds, respectively. Further, the simulations suggest that the TEMPOs at either end of the linker are oriented so that the planes of their rings are

approximately 90° with respect to one another. Thus, when the magnetic field is perpendicular to the ethylene glycol chain, the molecular orientation of the g-tensors¹¹¹,¹¹² leads to a frequency difference between the two TEMPO molecules approximately equal to $\omega_n/2\pi$ that would support the CE.

To achieve a larger DNP enhancement we could naively extrapolate the approximate linear dependence illustrated in Figure 3 to a $(R_{O-O})^{-3}$ value corresponding to a shorter linker. The shortest biradical in BTnE series is BT1E and with an estimated R_{O-O} of 1.43 nm ($\omega_d/2\pi=18.5$ MHz) which could yield a DNP enhancement of ~ 250 . Achieving this value may depend on the electron-electron dipole coupling (ω_d) remaining small compared to the frequency separation illustrated in Figure 3.1 and the CE mechanism dominating the DNP. In contrast when the dipole coupling is strong – i.e., when $|\omega_d| \sim |\omega_n|$ – the two coupled electrons form a ground state triplet^{108, 113}, and in this case the TM DNP mechanism may dominate to the polarization process. Thus, syntheses of biradicals with a variety of different rigid linkers, containing two TEMPO radicals and radicals that are different from TEMPO are discussed in the following chapters. These new polarizing agents together with studies of the high field EPR spectrum and the measurement of DNP enhancements will help us to distinguish between situations where CE or TM is the dominant enhancement mechanism. Those topics are discussed in Chapter 4.

3.2. TOTAPOL – A Biradical Polarizing Agent for Dynamic Nuclear Polarization Experiments in Aqueous Media

3.2.1. Introduction

Continuing from Section 3.1 which describes the use of biradicals as polarizing agents, we here present an alternative binitroxide radical – TOTAPOL – which acts as source of polarization to (a) be compatible with the polarization mechanism that yields the optimal signal enhancement, namely the three-spin thermal mixing (TM)^{56, 58} or cross effect (CE)^{51-55, 106, 67}, (b) be useful in polarizing a large array of samples ranging from small molecules to proteins, (c) produce large signal enhancements at a reduced concentration of paramagnetic species, and (d) be soluble in aqueous media. We have described the use of biradicals that satisfy the first three of these criteria and yield improved DNP enhancements¹¹⁴. In particular, we reported that bis-TEMPO-2-ethyleneglycol (BT2E), where TEMPO is 2,2,6,6-tetramethylpiperidin-1-oxyl and $n=2$ indicates a tether of two ethylene glycol units, produced DNP enhancements of ~175 at 90 K and 5 T. Further, this was accomplished at a reduced radical concentration (~5 mM biradicals or 10 mM electron spins, as opposed to ~40 mM monomeric TEMPO), thus reducing the electron nuclear dipolar broadening. The design, synthesis, and characterization of an improved polarizing agent, 1-(TEMPO-4-oxy)-3-(TEMPO-4-amino)propan-2-ol (TOTAPOL), satisfying the first three as well as the fourth requirement, is the topic of this section. Specifically, we have prepared a biradical

consisting of two TEMPO molecules tethered with a three carbon chain that increases the average electron-electron dipole coupling constant from about 0.5 MHz, in the typical 40 mM solution of TEMPO that we use for DNP experiments, to ~30 MHz in the biradical. At 140 GHz this yields a maximum enhancement of ~290 and again the electron concentration is reduced by a factor of six from the typical level of 40 mM to 6 mM. Very importantly, TOTAPOL has hydroxyl and secondary amine moieties on the tether and these functional groups increase the solubility of the biradical in aqueous media so that it is compatible with a variety of biological systems where DNP experiments are currently performed.

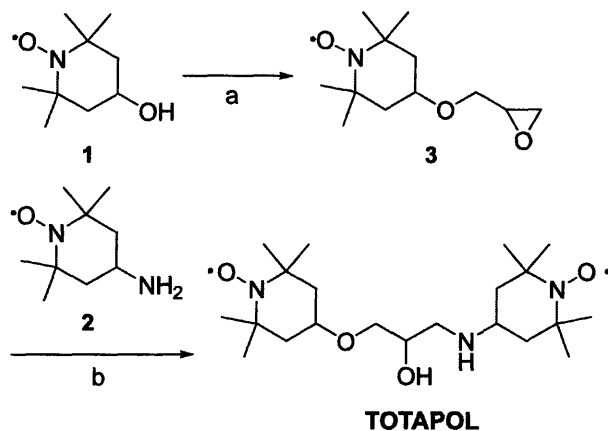
In this sub-chapter we describe the synthesis of TOTAPOL, and several EPR and DNP enhanced NMR experiments that characterize the molecule and illustrate its utility as an effective polarizing agent. These include a comparison of the enhancements obtained with TEMPO and several other biradicals, as well as its compatibility with low temperature MAS experiments in glycerol/water mixtures.

3.2.2. Experimental Section

3.2.2.1. Synthesis of TOTAPOL

1-(TEMPO-4-oxy)-3-(TEMPO-4-amino)-propan-2-ol (TOTAPOL) was prepared according to the two-step reaction illustrated in Scheme 3.1. Note that the molecule is an asymmetric biradical with an ether and a secondary amino linkage in contrast to the symmetrical bis-TEMPO-ethylene oxide biradicals that we described previously¹¹⁴.

Scheme 3.1. Synthesis of TOTAPOL^a



^a Conditions: (a) epichlorohydrin, tetrabutylammonium hydrogensulfate, 50% w/w NaOH_(aq), room temperature. (b) LiClO₄, CH₃CN, room temperature.

General Experimental Conditions. 4-hydroxy-TEMPO (1) and 4-amino-TEMPO (2), containing ≥ 97.0 % free radical, were purchased from Sigma-Aldrich (St. Louis, MO) and used without further purification. Anhydrous CH₃CN was purchased from the same company as a Sure-Seal bottle. All other chemicals were of reagent grade and used as received. For NMR analysis, TEMPO radicals were reduced to *N*-hydroxy compounds by ascorbic acid in methanol. NMR spectra were recorded on a Bruker Advance-400 or Varian Mercury-300 spectrometer, and chemical shift were referenced to residual solvent peaks. IR spectra were obtained on a Nicolet 8700 FT-IR spectrometer, in which sample was drop-casted on a KBr disc. High-resolution mass spectra were obtained on a Bruker Daltonics APEX II 3T FT-ICR-MS.

4-(2,3-epoxy-propoxy)-2,2,6,6-tetramethyl-1-piperidin-1-oxyl [4-(2,3-epoxy-propoxy)-TEMPO] (3). In a 100 mL round-bottom flask equipped with a stirring bar

were combined tetrabutylammonium hydrogensulfate (0.136 g, 4 mol%), 50 % w/w aqueous NaOH (10 mL), and epichlorohydrin (3.91 mL, 50 mmol). To the mixture was added 4-hydroxy-TEMPO (1.73 g, 10 mmol) in portions and the mixture was stirred overnight at room temperature. It was then poured into water and extracted with ethyl acetate. The organic layer was washed with brine, dried over MgSO₄, and evaporated under reduced pressure. The resulting crude product was purified by column chromatography (dichloromethane, methanol), providing a quantitative yield of red, viscous oil. IR (KBr disc, cm⁻¹): 2975, 2937, 1636, 1464, 1384, 1363, 1244, 1179, 1095. ¹H-NMR (300 MHz, DMSO-*d*₆) δ: 7.12 (bs, 1H), 3.69 (dd, 1H, *J* = 11, 2.7 Hz), 3.60 (m, 1H), 3.24 (dd, 1H, *J* = 11, 6.6 Hz), 3.04 (m, 1H), 2.70 (*pseudo-t*, 1H, *J* = 5.1 Hz), 2.52 (dd, 1H, *J* = 5.1, 2.7 Hz), 1.86 (dd, 2H, *J* = 12, 3.6 Hz), 1.24 (*pseudo-t*, 2H, *J* = 11 Hz), 1.05 (d, 12H, *J* = 11 Hz).

1-(2,2,6,6-tetramethyl-1-oxy-4-piperidinyl)oxy-3-(2,2,6,6-tetramethyl-1-oxy-4-piperidinyl)amino-propan-2-ol [1-(TEMPO-4-oxy)-3-(TEMPO-4-amino)-propan-2-ol] (**TOTAPOL**). In a 100 mL round-bottom flask equipped with a stirring bar were combined 4-(2,3-epoxy-propoxy)-TEMPO (**3**) (1.62 g, 7 mmol), LiClO₄ (0.745 mg, 7 mmol), and 10 mL of anhydrous CH₃CN under Ar. To the mixture was added a CH₃CN (3 mL) solution of 4-amino-TEMPO (1.20 g, 7 mmol) and the mixture was stirred overnight at room temperature. Most of the solvent was evaporated under reduced pressure, and the crude product was purified by column chromatography (dichloromethane, methanol). Yield: 1.98 g of orange-red solid. IR (KBr disc, cm⁻¹): 3446, 2977, 2938, 1635, 1465, 1364, 1244, 1178, 1098. ¹H-NMR (400 MHz, DMSO-*d*₆) δ: 7.31 (bs, 1H), 7.15 (bs, 1H), 4.57 (bs, 1H), 3.93 (m, 1H), 3.69 (m, 1H), 3.57 (m, 1H),

3.41 (m, 2H), 3.34 (m, 1H), 3.01 (pseudo-d, 1H, J = 11 Hz), 2.80 (m, 1H), 1.96 (m, 2H), 1.86 (m, 2H), 1.52 (m, 2H), 1.23 (pseudo-t, 2H, J = 11 Hz), 1.04 (dd, 24H, J = 17, 3.9 Hz). HR-MS (ESI): calcd for $C_{21}H_{41}N_3O_4^- [M + H]^+$, 400.3170; found, 400.3161.

3.2.2.2. EPR experiments

For 9 GHz solution EPR experiments, the samples consisted of a capillary containing ~10 μ L's of 0.5 mM TOTAPOL in absolute ethanol. In order to increase the resolution of powder EPR spectra from frozen solutions, TOTAPOL was synthesized with ^{15}N , 2H -labeled TEMPO's (CDN Isotope, Quebec, Canada). Samples for the X-band experiments were typically 60 μ L of 0.5 mM ^{15}N , 2H -TOTAPOL in the glass forming solvent 2H_6 -DMSO/ 2H_2O (6:4 w/w) in a 4 mm O.D. quartz tube. 9 GHz CW EPR spectra were recorded with a Bruker EMX spectrometer with the sample immersed in liquid nitrogen (77 K) in a finger dewar (Wilmad WG-819-B-Q). Samples for 140 GHz experiments consisted of 0.4 μ L of TOTAPOL in the same deuterated glass forming solution contained in a quartz capillary immersed in a helium cryostat (Oxford Instruments). 140 GHz spectra were recorded with echo detected experiments using a custom designed spectrometer ⁸⁷. The rigid-limit for EPR spectra of TOTAPOL is reached below 100 K in the glass forming mixture; thus, the 20 K and 77 K temperatures chosen for the above EPR experiments are sufficient for observing rigid limit EPR spectra.

3.2.2.3. DNP enhanced NMR experiments with TOTAPOL

Solutions for the DNP/NMR experiments – 2 M ^{13}C -urea or 0.2 M U- ^{13}C - ^{15}N -proline – were prepared in 2H_6 -DMSO/ 2H_2O / H_2O (60:34:6 w/w/w) or 2H_8 -

glycerol/²H₂O/H₂O (60:25:15 w/w/w), and doped with 3-5 mM TOTAPOL (6-10 mM electron spins). The reduced ¹H concentration was required to optimize the signal enhancements and chosen to maintain effective proton homonuclear spin diffusion. DNP experiments using TOTAPOL as a polarizing agent were performed on a custom designed DNP/NMR spectrometer and triple-resonance (e⁻, ¹H and ¹³C/¹⁵N) cryogenic (90 K) MAS probe (with a 4 or 2.5 mm rotor stator)^{63, 115} operating at 5 T (140 GHz EPR and 211 MHz ¹H NMR). The enhanced ¹H polarization developed by the microwave irradiation was detected indirectly via observation of the cross-polarized (CP) ¹³C signals. The 140 GHz microwaves were generated by a gyrotron, a vacuum electron device capable of producing high power (>10 W) millimeter waves⁹. Sapphire, rather than zirconia, rotors are preferred for the DNP experiments since they transmit microwaves with ~30% less attenuation and we have used rotors of two diameters, 2.5 mm and 4 mm, in the experiments reported here. As will be seen below, we find larger enhancements in the smaller diameter system probably because the microwave penetration is more complete. Finally, the 5 T magnet has a superconducting sweep coil used to vary the field by ±750 G for EPR and DNP experiments, and that facilitates locating the maximum and minimum in the DNP enhancement curve from its field dependence.

3.2.3. Results and discussion

The design of TOTAPOL was dictated by two considerations. First, following our successful experiments on the BTnE series of biradicals whose structures are illustrated in Figure 3.4 (top row), we wanted to prepare a radical with as short a linker as possible, and second it was supposed to be soluble in aqueous media. Initially we attempted to

prepare a polarizing agent with a two carbon linkage, such as TEMPO–O–CH₂–CH₂–O–TEMPO which would be BT1E, but despite exploration of several approaches, we were not successful. Subsequently, we did synthesize a biradical with a three carbon linker with asymmetric bridging atoms – N and O rather than two O's. In addition we added an –OH moiety to the central carbon in order to increase the solubility of the molecule – TEMPO–O–CH₂–CHOH–CH₂–NH–TEMPO. The fact that we obtained an enhancement factor of ~165 (in 4 mm rotors) is probably due to the short electron-electron distance and the fortuitously correct orientation of the two TEMPO g-tensors. In the next chapter we describe radicals such as BTurea (two TEMPOs tethered by –NH–CO–NH–) that have a shorter linker but yield enhancements of only about 100 (again in 4 mm rotors). We believe the lower enhancement is due to a suboptimal orientation of the g-tensors of the two TEMPO moieties. In 2.5 mm rotors we observe larger enhancements from all of the biradicals (up to ~290 from TOTAPOL) and we believe that this effect is due to more efficient microwave penetration of the sample as discussed further below.

The EPR spectra of flexible biradicals such as BTnE, two TEMPO's tethered by n ethylene glycol units ¹¹⁴, usually have two additional peaks yielding a quintet spectrum with the lines spaced at about half the ¹⁴N hyperfine splitting normally observed in TEMPO, 16.7 G. This five-line solution EPR spectrum is a result of proximity of the two TEMPO radicals and arises when the average J-coupling (exchange integral) is ≥10 times stronger than the hyperfine coupling ¹⁰⁸. This phenomenon is illustrated in Figure 3.4a,b which shows the solution EPR spectra of 4-hydroxy-TEMPO and the biradical BT2E. There are three lines present in the TEMPO spectrum, but in the BT2E spectrum there are two additional lines arising from the strong J-coupling between the electrons. In contrast,

the spectrum of TOTAPOL (Figure 3.4c) shows that the two additional biradical lines are broadened into the baseline due to the short tether ($-\text{O}-\text{CH}_2-\text{CHOH}-\text{CH}_2-\text{NH}-$) that restricts the proximity of two TEMPO moieties.

Moreover, the EPR spectrum of 0.5 mM TOTAPOL in $^2\text{H}_6\text{-DMSO}/^2\text{H}_2\text{O}$ (6:4 w/w) glass-forming solution at 77 K (Figure 3.4f) reveals a significantly broadened lineshape with a resolved dipolar splitting at 3360 G. Note for comparison that neither the broadening nor the splitting are present in the spectrum of frozen monomeric TEMPO at 1 mM (Figure 3.4d). For TOTAPOL, the ~ 8 Gauss (Figure 3.4f,i) splitting at g_{zz}^{111} result from an intramolecular electron-electron interaction, which is mainly attributed to a dipolar coupling. As a comparison, the powder EPR spectra of BT2E reveal broadened features (Figure 3.4e,h). Analyses of the powder EPR lineshapes yielded similar electron-electron distances ($\sim 12.8 \text{ \AA}$) for both BT2E and TOTAPOL, even though the involved molecular tethers are composed of different numbers of atoms. Since an electron-electron dipolar splitting can be observed in the powder EPR spectra (Figure 3.4f,i), we surmise that the conformational flexibility of the tether in TOTAPOL may be decreased by its short length. In contrast, the longer and conformationally more flexible tether in BT2E probably permits a distribution of orientations of the g-tensors of the two TEMPO moieties and thereby transforms the dipolar splitting visible at 3360 G to a broad peak (Figure 3.4e). A similar dipolar splitting and broadening are present in the 140 GHz biradical spectra (Figure 3.4h,i), where inhomogeneous broadening due to the larger g-anisotropy dominates the lineshape. Both the solution and solid-state EPR spectra of TOTAPOL provide information on the distance between the two TEMPO moieties and a detailed analysis of these lineshapes will be the subject of the next chapter.

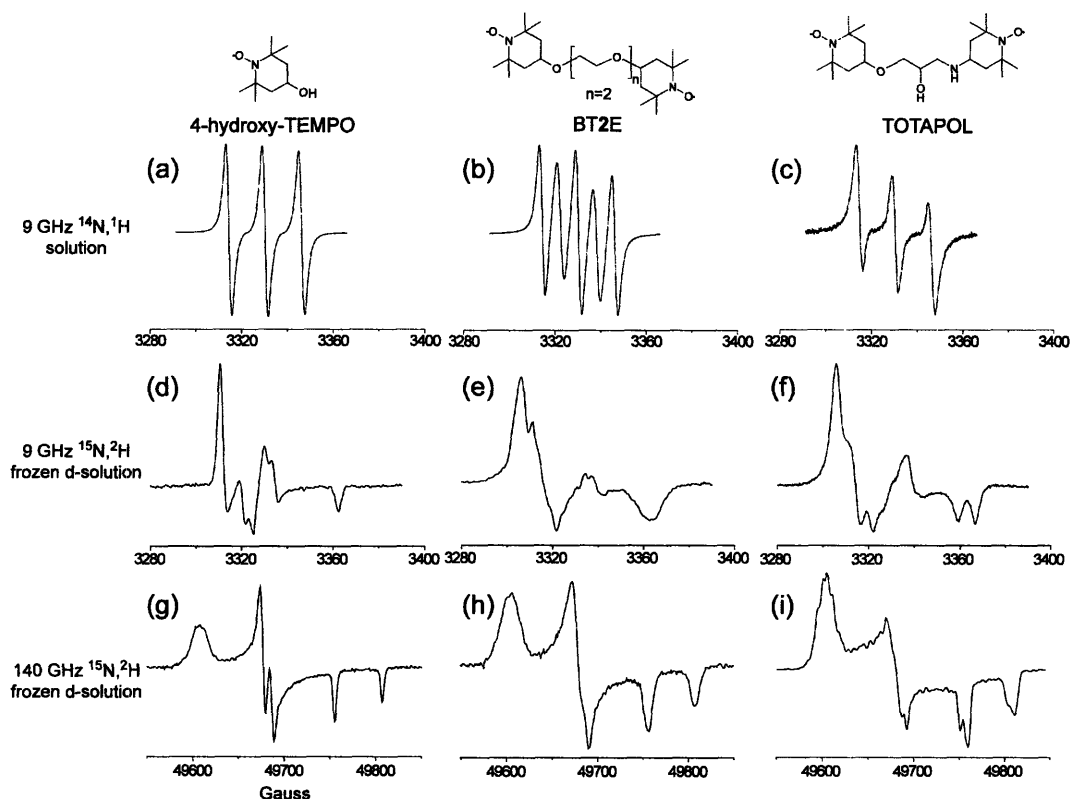


Figure 3.4. The 9 and 140 GHz EPR spectra of TEMPO, BT2E and TOTAPOL with the molecular structures shown in the top line. (a)-(c) are 9 GHz solution spectra illustrating the extra two lines in the spectrum from the transient proximity of two TEMPO moieties with a strong electron-electron J-coupling [compare (a) with (b)]. These lines in TOTAPOL are severely broadened in (c) by shorter life time of the transient proximity due to rigidity of the tether, which cannot bend the biradical easily. (d)-(f) illustrate the 9 GHz spectra obtained from frozen solutions at 77 K, and (g)-(i) illustrate the 140 GHz spectra from the same solutions frozen at 20 K.

The pulse sequence for DNP enhanced ^{13}C -CPMAS NMR experiments is shown in the inset of Figure 3.5. The ^1H polarization is initially saturated by a series of 90° pulses followed by a delay of $3 T_2$. Next, the microwave irradiation is applied to dynamically polarize the ^1H 's, or, in the absence of microwaves, the thermal equilibrium polarization develops. Finally, the ^1H polarization is transferred to ^{13}C via cross polarization and observed in the presence of TPPM decoupling¹¹⁶. The Fourier transforms of the FIDs are

shown (Figure 3.5) as a series of spectra with various microwave irradiation periods, leading to an enhancement factor for ^1H polarization $\epsilon=290\pm 30$ determined by comparing the saturated NMR signals after 40 s delay with and without microwaves. Sample rotation using a 2.5 mm sapphire rotor attributed to the rotational side bands spaced at $\omega_r/2\pi=7$ kHz. The enhanced signals developed during the microwave irradiation period with a time constant of ~ 9 s which was similar to the proton T_1 . Note that the error for the enhancement factor was determined primarily by the uncertainty in measuring the intensity of the un-enhanced NMR signal.

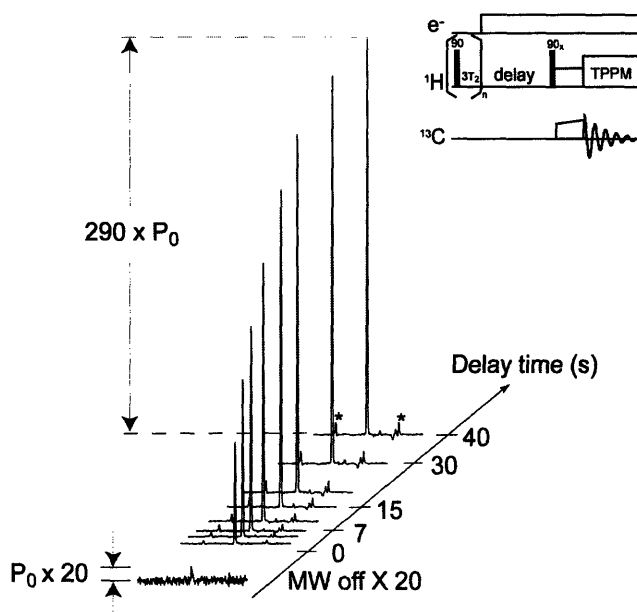


Figure 3.5. Illustration of the growth of the nuclear polarization as a result of microwave irradiation. Integration of the spectral intensities with and without irradiation yields a ^1H enhancement of ~ 290 measured indirectly through ^{13}C CP signal using the pulse sequence shown in the inset. The measurements were performed on a sample of 3 mM TOTAPOL and 2 M ^{13}C -urea in $^2\text{H}_6$ -DMSO/ $^2\text{H}_2\text{O}/\text{H}_2\text{O}$ (60:34:6 w/w/w) at 90 K, 5 T and $\omega_r/2\pi = 7$ kHz MAS (spinning side bands marked by asterisks). The time constant associated with the growth is ~ 9 s, approximately the nuclear T_1 of the sample.

In the top half of Figure 3.6 we show the EPR absorption of TOTAPOL recorded at 140 GHz/5 T. This inhomogeneous lineshape supports the cross effect mechanism in which two dipole-coupled electrons, separated by $\omega_n/2\pi$ in the EPR spectrum, execute a three-spin electron–electron–nucleus process involving the mutual flip of an electron and a second electron separated by $\omega_n/2\pi$ and a nuclear spin. The energy difference matches the nuclear Larmor frequency and results in nuclear spin flips that generate the enhanced nuclear polarization. The correct frequency separation of the two electrons is provided by the fact that the two TEMPO moieties have relative g-tensor orientations that satisfy the correct matching condition $\omega_{2e}-\omega_{1e}=\omega_n$. The field dependence of the DNP enhancement with TOTAPOL is shown in the bottom half of Figure 3.6, together with the enhancement curve of BT2E. To facilitate observation of NMR signals in the absence of microwave irradiation, the field-dependent DNP experiments were performed using a 4 mm sapphire rotor. The DNP enhancement ($\epsilon\sim 165$) in 4 mm rotors (25 μL) yielded by TOTAPOL was smaller than that observed ($\epsilon\sim 290$) in 2.5 mm rotors (9 μL), presumably because of limited microwave penetration by the larger sample volume. However, the shape of the curve in Figure 3.6 and the optimal external magnetic field for the maximum DNP enhancement showed no dependence within experimental error on the average microwave power at the sample ⁹⁸. In particular, TEMPO-based biradicals exhibit a universal DNP enhancement profile since the electron–electron dipolar splittings are relatively small compared to the inhomogeneous broadening of EPR lineshapes.

As is illustrated in Figure 3.6, the DNP enhancement profile is universal with respect to TEMPO-based biradicals as the electron-electron dipolar splittings involved are relatively smaller than the inhomogeneous broadenings of EPR lineshapes. The

enhancement profile curves generally resemble the first derivative of the EPR absorptive lineshapes, having the maxima and minima around 165 and -140 separated by 107 G (~300 MHz). The enhancement curves can be compared with the EPR lineshape in the top half of Figure 3.6. Although the TOTAPOL chain is shorter than in BT2E and probably less flexible, we nevertheless observe essentially the same shape for the enhancement curve for each case. The shape and amplitude of the two curves depend on the average electron–electron distance and relative orientations of the two g-tensors which must be very nearly the same in the two molecules.

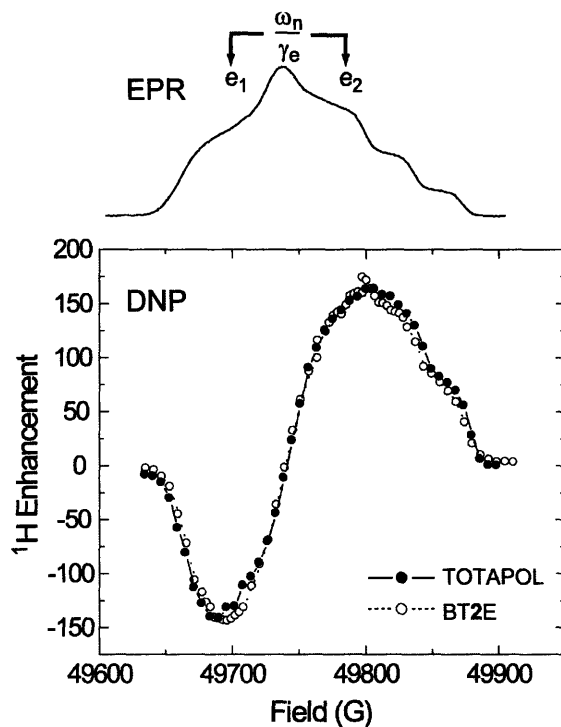


Figure 3.6. (top) EPR absorption of TOTAPOL measured on a 140 GHz spectrometer. The linewidth is much greater than the ^1H Larmor frequency ($\omega_n/2\pi$) and therefore can encompass two coupled electron spins with the correct EPR frequency separation, ω_n , required for the cross effect. (bottom) Solid circles show the field dependence of the ^1H enhancement (in a 4 mm rotor) in a DNP experiment using the biradical polarizing agent TOTAPOL. The field dependence from BT2E, shown as open circles, is essentially identical to TOTAPOL. The lines connecting the data points are for guidance of the eyes.

Figure 3.7 compares the enhancement obtained with TOTAPOL with those from the BTnE (n=2, 3, 4) series. The comparison was made using both 4 and 2.5 mm rotors in order to demonstrate the effect of microwave penetration into samples. Reducing the number of atoms separating the two TEMPO moieties increases the electron-electron dipolar interaction and the observed enhancement. Since the DNP enhancement strongly depends on the electron-electron dipolar interaction, it appears to be optimized for BT2E and TOTALPOL at $\epsilon \sim 165$ in a 4 mm rotor. In a 2.5 mm rotor, where the microwave penetration is more complete, the maximum enhancement from TOTAPOL grows to $\epsilon \sim 290$. Note that the increase in ϵ in going from 4 to 2.5 mm rotors is ~ 1.75 for TOTAPOL whereas for BT2E it is ~ 1.36 . The underlying reason for this difference is not clear at present. It could be related to differences in the electronic relaxation times of the two biradicals. For systems which are sample limited the smaller rotor offers advantages in sensitivity. However, when this is not the case then the 4 mm system could yield improved signal-to-noise.

It is surmised that although a short biradical such as TOTAPOL should induce efficient three-spin polarization transfers, it also facilitates electron spin-lattice relaxation which limits the essential microwave saturation. Clearly, limitation to microwave saturation is alleviated with stronger microwave irradiation in the smaller rotor. Thus, the improvement of DNP by a shorter electron-electron distance is pronounced. Moreover, different enhancements due to different tethers in TOTAPOL and BTnE may be explained in terms of the linkage flexibility that determines the constraints of distance and relative g-tensor orientation between two electrons. For example, a more rigid constraint of electron-electron distance in TOTAPOL than in BT2E provides a larger average dipole

coupling constant for the three-spin process. In the next chapter, we will thoroughly discuss this point on the basis of measurements of the above two geometrical parameters in biradicals using EPR spectroscopy.

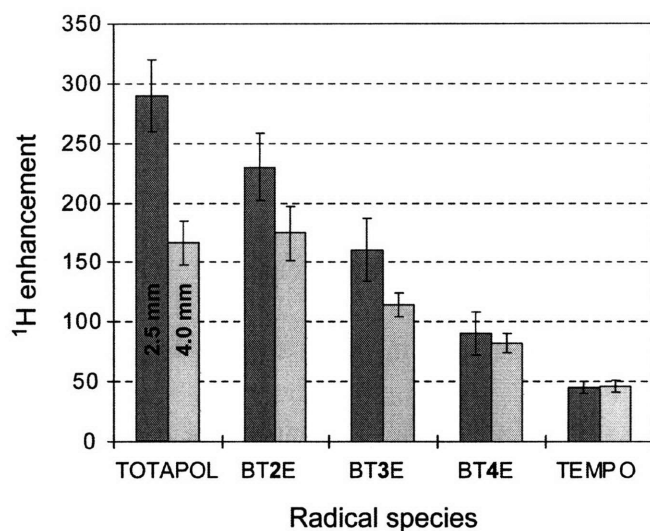


Figure 3.7. A histogram of DNP enhancements (with error bars) in 4 and 2.5 mm rotors with the TOTAPOL and a series of BTnE biradicals. A general trend shows that TOTAPOL yielded the largest enhancement, especially when more microwave power reaches the samples in 2.5 mm rotors.

A very important feature of TOTAPOL is its solubility in water due to the -OH group on the central carbon of the tethering chain and the -NH- linkage of the TEMPO moiety. Further, TOTAPOL is soluble in 200 mM salt, solvent conditions that are common in preparation of protein samples, and it is stable in glycerol/water (6:4 w/w) at -10 °C for months. In contrast, BT2E is insoluble in all of these media. To illustrate the utility of TOTAPOL in these circumstances we show in Figure 3.8 a DNP-enhanced high-resolution ^{13}C -NMR spectrum of 200 mM proline in $^2\text{H}_8$ -glycerol/ $^2\text{H}_2\text{O}/\text{H}_2\text{O}$ (60:25:15 w/w/w) which exhibits an enhancement of 240 ± 40 using 5 mM TOTAPOL at 90 K and 5 T. Note the enhancement with proline is slightly smaller than the 290 observed with ^{13}C -

urea. In addition, we have used TOTAPOL to polarize samples of membrane proteins such as bacteriorhodopsin^{117, 118}, amyloid peptide (e.g., GNNQQNY) nanocrystals^{4, 119}, and microcrystals of soluble proteins¹²⁰⁻¹²² so it appears to be compatible with a wide variety of different systems.

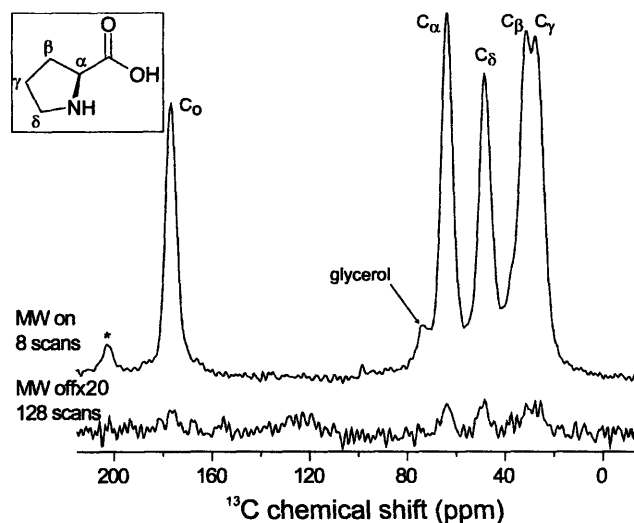


Figure 3.8. DNP enhanced spectrum of a 9 μ L sample of 200 mM proline solution doped with 5 mM TOTAPOL. An enhancement of 240 was observed in the experiment with 20 s microwave irradiation. The sample was prepared in $^2\text{H}_8$ -glycerol/ $^2\text{H}_2\text{O}/\text{H}_2\text{O}$ (60:25:15 w/w/w) and the spectra were recorded with $\omega_r/2\pi=7.4$ kHz MAS (2.5 mm rotor) at 90 K and 5 T. The spectrum is assigned according to the structure of proline shown in the inset. The rotational sideband is marked by an asterisk.

3.2.4. Conclusions

To summarize, we have synthesized a new TEMPO based biradical, TOTAPOL, which produces larger enhancements than those observed with BT2E and, very importantly, is soluble in aqueous media containing salt and glycerol at concentrations typically found in protein solutions. These properties should make this molecule widely applicable to DNP investigations involving biological systems. The sizes of the

enhancements presently observed reach 290 in a 2.5 mm rotor or 190 in a 4 mm rotor at 90 K and 5 T. As mentioned above, we have already used TOTAPOL in a number of other systems – in particular it has yielded interesting results in solid-state NMR studies of bR, GNNQQNY and soluble proteins – and observed larger enhancements than obtained with monomeric TEMPO. Thus it would appear that TOTAPOL will find wide applicability in DNP enhanced NMR spectroscopy of biological systems.

Chapter 4 Improvement of High-Frequency Dynamic Nuclear Polarization Using Biradicals: A Multifrequency EPR Lineshape Analysis

4.1. Introduction

Dynamic nuclear polarization (DNP) can be used in conjunction with cross-polarization (CP) and magic-angle-spinning (MAS) to enhance NMR signal-to-noise ratios by two to three orders of magnitude^{58, 59, 123}. The increased NMR signals arise from the enhanced nuclear polarization due to microwave-driven transfer of electron-spin polarization of endogenous⁶⁵ or exogenous⁶⁶ unpaired electrons. However, with the use of ever-increasing magnetic fields in modern NMR spectroscopy, the application of DNP is inhibited because of limitations to the polarizing processes imposed by the high magnetic fields. In particular, severe constraints arise in high-field DNP due to inefficient polarizing mechanisms and the unavailability of high-frequency (100–600 GHz) high-power (>10 W) microwave sources. Despite attempts to remedy the latter situation through the use of gyrotron devices^{9, 62, 63, 89, 109, 117, 118} in high magnetic fields (>5 T), a discrepancy persists between measurable DNP enhancement factors and the theoretical maximum, which is defined by γ_e/γ_n (e.g., ~660 for ¹H polarization), where γ_e and γ_n are electron and nuclear gyromagnetic ratios, respectively. Consequently, improving DNP enhancements is urgent, which has been attempted by designing specific polarizing agents that can promote efficient polarizing mechanisms at high magnetic fields.

Polarizing mechanisms involved during continuous microwave irradiation at or near the electron Larmor frequency ω_e include the Overhauser effect (OE), solid effect (SE),

cross effect (CE), and thermal mixing (TM)^{58, 67}. The OE arises from electron–nuclear cross-relaxation as a result of stochastic electron–nuclear interactions with correlation time τ_c . However, high magnetic fields restrict OE because the increased ω_e fails to satisfy the requirement $\omega_e\tau_c < 1$. Except in special cases of liquid-state DNP experiments based on scalar interactions involving transient molecular contacts¹²⁴, the successful polarization of nuclei in a liquid state would rely on polarization in the solid followed by a rapid melting as is elaborated in Chapter 7.

DNP in solid dielectrics occurs through SE, CE, or TM mechanisms and depends on the relationship between the nuclear Larmor frequency ω_n and linewidth δ of the electron paramagnetic resonance (EPR) of the paramagnetic species involved. In powder systems with randomly orientated paramagnetic species, SE dominates in DNP with $\delta < \omega_n$, whereas CE and TM are induced for the condition $\delta > \omega_n$. DNP enhancements arising from SE scale as B_0^{-2} , where B_0 is the static magnetic field; enhancements through CE and TM scale as B_0^{-1} . Therefore, CE and TM are favored for high-field DNP; both are induced by the TEMPO (2,2,6,6-tetramethyl-piperidine-1-oxyl) radical, which yields an inhomogeneous EPR lineshape with $\delta > \omega_n$ that results from anisotropies of g-values and ¹⁴N-hyperfine interactions^{125,98}. Both CE and TM rely on an electron–electron–nucleus mutual flipping process which requires the correct EPR frequency separation, $|\omega_{e1} - \omega_{e2}| = \omega_n$, and an appropriate electron–electron dipolar interaction. These two requirements for the three-spin process suggest new approaches that might be used to improve high-field (i.e., 5 T) DNP efficiency.

The use of radical mixtures to provide an EPR spectral density favoring the required EPR frequency separation has been shown to yield improved DNP enhancement relative

to that found using identical amounts of individual radical species ¹²⁶. Furthermore, the tethering of two TEMPOs as biradical polarizing agents has proven effective in improving DNP under high-field cryogenic conditions and has yielded a larger enhancement at lower radical concentrations ¹¹⁴. The improvements in DNP efficiency from using biradicals arise principally from an increased electron–electron dipole coupling constant and is a consequence of the fixed distance between two TEMPOs. The modifications of two-TEMPO biradicals that allow for solubility in aqueous biological media ¹²⁷ and associated applications ^{115, 117-119} have established a new era of DNP-based high-field NMR spectroscopy.

When designing new biradical polarizing agents, it is important to characterize the distance and relative g-tensor orientation between two tether radicals. While the contribution of the distance constraint to a biradical in improving its DNP efficiency is obvious, it is uncertain whether the molecular linkage between two TEMPOs also places a constraint on the relative g-tensor orientation that promotes the optimum EPR frequency separation. Although the distance between two electrons and their relative orientation may be determined by pulsed EPR techniques involving single ¹²⁸⁻¹³⁰ or double ¹³¹⁻¹³⁵ microwave frequencies, those methods are usually ineffective at close distances and large g-anisotropies such as those required for inducing CE or TM. The appropriate geometry of biradicals suitable for DNP can be determined using continuous-wave (CW) EPR lineshape analyses ^{12, 136, 137}, given that the electron–electron distance of concern is mainly $<25 \text{ \AA}$ for the required electron–electron interaction by either CE or TM.

This chapter describes a series of DNP and EPR experiments with several model

biradicals — the BTnE series that were reported in our previous communication ¹¹⁴, BTurea, BTOxA, and TOTAPOL (*vide infra*). DNP enhancements during microwave irradiation were investigated in terms of their dependence on the external magnetic field, irradiation times, radical concentrations, and microwave power. The corresponding DNP efficiency was analyzed in terms of structural data obtained from EPR characterization employing both solution and powder methods. In particular, the constraints of distance and relative g-tensor orientation between the two radicals were determined by solid-state EPR spectra at 9 and 140 GHz, and provided insights into the spectral parameters governing the polarization efficiency. We describe a simulation program for powder EPR spectra of biradicals, and the parameters that yield the best-fit simulation of the experimental results were refined using a simulated annealing protocol. Thus, the principles for improving DNP enhancements by using biradicals evolve naturally from electron–electron interactions and the EPR frequency separations.

4.2. Theoretical Background

4.2.1. DNP mechanisms in solid dielectrics

The enhancement, ϵ , in nuclear polarization in a DNP experiment is generally defined as

$$\epsilon = \frac{p}{p_0} - 1, \quad (1)$$

where p and p_0 are the nuclear polarization following microwave irradiation and at thermal equilibrium, respectively. Summarized from the background chapter, CW

microwave-based polarizing mechanisms, which depend on time-independent hyperfine interactions, include SE, CE, and TM involving single, double, and multiple electrons, respectively, as the source of electron polarization for polarization transfers to nuclei during microwave irradiation near the electron Larmor frequency ω_e . The mechanism that best explains DNP enhancements is determined by the EPR linewidth δ of the involved unpaired electrons, compared to the nuclear Larmor frequency ω_n . When $\delta < \omega_n$, only the SE mechanism is involved due to the microwave-driven, electron–nuclear transitions that simultaneously flip the electron spin and the coupled nuclear spin⁵⁸. These transitions arise from second-order effects of the semicircular electron–nuclear dipolar interaction¹³. Consequently, their intensities, as well as the consequent enhancements of nuclear polarization, scale as B_0^{-2} , where B_0 is the external magnetic field. For nuclei with $\gamma_n > 0$, where γ_n is the nuclear gyromagnetic ratio, a microwave irradiation at $\omega_e - \omega_n$ excites an electron–nuclear transition that results in the maximum positive enhancement, while the transition at $\omega_e + \omega_n$ leads to the greatest negative enhancement. The condition $\delta < \omega_n$ allows for apparent separation between the microwave frequencies that generate positive and negative enhancements, and hence avoid cancellation of enhancements from the differing signs. A narrower δ will further optimize SE due to effective microwave excitation of those electron–nuclear transitions.

The condition $\delta > \omega_n$ induces TM and CE, which are distinguished by the homogenous and inhomogeneous properties of the radical’s EPR spectra. Within the TM mechanism, the electron–electron dipolar reservoir in a homogeneous EPR lineshape is perturbed by excitation of an off-center EPR transition⁵⁰, and its nonequilibrium status can enhance nuclear polarization in a collection of three-spin processes. Two electrons

and one nucleus are mutually flipped in these three-spin processes, the probability of which is optimized by $\delta \sim \omega_n$ ⁵⁶. The electron–electron dipolar reservoir is perturbed mainly at the microwave frequencies of $\omega_e - \delta$ and $\omega_e + \delta$, which result, respectively, in the maximum positive or negative enhancement for $\gamma_n > 0$.

In comparison, CE requires two electrons with EPR frequencies, ω_{e1} and ω_{e2} , in an inhomogeneous lineshape and separated by ω_n ^{51-55, 67, 106}. The polarization difference of these two electrons that results from on-resonance microwave excitation can be used to enhance the nuclear polarization, again by way of a three-spin process. Assuming $\omega_{e1} < \omega_{e2}$ and $\gamma_n > 0$, microwave irradiation at ω_{e1} or ω_{e2} leads to the maximum positive or negative enhancement, respectively. For both TM and CE the essentials for the three-spin process are electron–electron interactions, electron–nuclear interactions, and the correct EPR frequency separation between the two electrons. Specifically, the correct frequency separation, i.e., $|\omega_{e1} - \omega_{e2}| = \omega_n$, will yield degenerate spin states involving mutual flips of the spin quantum numbers of the three spins, and the subsequent mixing of the degenerate spin states could induce a transition for the desired polarization transfer. The probability of obtaining the correct frequency separation decreases linearly with an increasing EPR linewidth which is almost entirely due to g-anisotropy in a higher magnetic field. Consequently, enhancement of nuclear polarization from TM and CE scales as B_0^{-1} in high magnetic fields.

While TM is deduced directly from the EPR lineshape of paramagnetic species¹²⁵, CE can be determined from microscopic conformations of radical pairs reflected by the lineshape. Furthermore, for both CE and TM, the distance and relative g-tensor orientation between two electrons affect the essential electron–electron interactions and

the EPR frequency separation. Both can be determined by multifrequency EPR lineshape analyses of the biradical, given that only a short electron–electron distance is involved.

4.2.2. Powder EPR lineshape of a biradical

For a biradical with an electron–electron distance $< 25 \text{ \AA}$, an analysis of the CW–EPR spectra can be used to determine the distance and relative orientation of the g -tensors of the two unpaired electrons¹². Specifically, the multifrequency EPR lineshape-fitting used here employs the known principal values of the g - and hyperfine-tensors of the monomeric TEMPO-based radical species that comprise the biradical of interest. Further, these principal values are assumed independent of the details of the molecular structures attached to the TEMPO ring, such as a hydroxy (or amino) functional group and the various molecular tethers. Simulation of the powder EPR spectrum of a biradical then involves varying the parameters that describe the angles defining the relative orientations of the g -tensors ($\mathbf{g}_1, \mathbf{g}_2$) and hyperfine-tensors ($\mathbf{A}_1, \mathbf{A}_2$), and the interelectron distance (\mathbf{R}). This is illustrated in Figure 4.1 which shows a schematic model of the BT2E biradical (*vide infra*). Specifically, the Cartesian coordinates are transformed from the principal axis system (PAS) of the \mathbf{g}_1 tensor to the PAS of the \mathbf{g}_2 tensor by a rotation matrix, $\mathbf{R}_{21}(\alpha, \beta, \gamma)$, from the PAS of the \mathbf{g}_1 tensor to the axis frame with its z -axis parallel to \mathbf{R} by $\mathbf{R}_{1D}(\eta, \xi, 0)$ and from the PAS of the \mathbf{g}_1 tensor to the laboratory frame with its z -axis along the external magnetic field \mathbf{B}_0 by $\mathbf{R}_{1L}(\phi, \theta, 0)$. The zero angle for the third rotation in the above coordinate transformations is a consequence of the axial symmetry of both \mathbf{R} and \mathbf{B}_0 . Note that for TEMPO-based biradicals, the principal axis systems of the g - and hyperfine-tensors are coaxial¹³⁸.

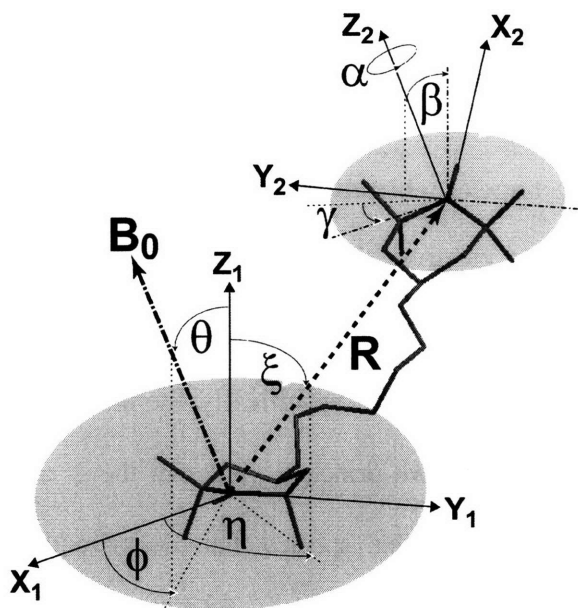


Figure 4.1. An illustration of the relative orientations between the principal axes systems of two tethered TEMPOs ($X_1Y_1Z_1$ and $X_2Y_2Z_2$) of the BT2E biradical (in the skeleton of heavy atoms), the interelectron vector (\mathbf{R}) and the external magnetic field (\mathbf{B}_0). The Euler angles (α, β, γ) transform $X_2Y_2Z_2$ into $X_1Y_1Z_1$; ($\eta, \xi, 0$) and ($\phi, \theta, 0$) orient \mathbf{R} and \mathbf{B}_0 , respectively, with respect to $X_1Y_1Z_1$. The Euler angles are listed in the order to rotate the axes along Z, Y' and Z' (the convention used by Rose⁵ and Edmonds⁷). The x-axis is along the N-O bond and z-axis is perpendicular to the C(NO)C plane and in the π orbital plane¹².

Subsequently, the spin Hamiltonian describing a nitroxide radical system is

$$H_0 = (\beta_e \mathbf{B}_0 \mathbf{g}_1 \mathbf{S}_1 - \gamma_n \mathbf{B}_0 \mathbf{I}_1 + \mathbf{S}_1 \mathbf{A}_1 \mathbf{I}_1) + (\beta_e \mathbf{B}_0 \mathbf{g}_2 \mathbf{S}_2 - \gamma_n \mathbf{B}_0 \mathbf{I}_2 + \mathbf{S}_2 \mathbf{A}_2 \mathbf{I}_2) + D(3S_{1z}S_{2z} - \mathbf{S}_1 \mathbf{S}_2) - 2J\mathbf{S}_1 \mathbf{S}_2, \quad (2)$$

where β_e is the Bohr magneton for the electrons ($\mathbf{S}_1, \mathbf{S}_2$), γ_n is the gyromagnetic ratio for the coupled nitrogen nuclei ($\mathbf{I}_1, \mathbf{I}_2$), D is the dipolar interaction between two electrons, and J is the exchange integral from the electron–electron Coulomb interaction¹³⁹. The orientation dependences of $\mathbf{g}_1, \mathbf{g}_2, \mathbf{A}_1$, and \mathbf{A}_2 are calculated from

$$\begin{aligned}
\mathbf{g}_1 &= \mathbf{R}_{1L} \mathbf{g}_1^{\text{PAS}} \mathbf{R}_{1L}^{-1}, \\
\mathbf{A}_1 &= \mathbf{R}_{1L} \mathbf{A}_1^{\text{PAS}} \mathbf{R}_{1L}^{-1}, \\
\mathbf{g}_2 &= \mathbf{R}_{1L} \mathbf{R}_{21} \mathbf{g}_2^{\text{PAS}} \mathbf{R}_{21}^{-1} \mathbf{R}_{1L}^{-1}, \\
\mathbf{A}_2 &= \mathbf{R}_{1L} \mathbf{R}_{21} \mathbf{A}_2^{\text{PAS}} \mathbf{R}_{21}^{-1} \mathbf{R}_{1L}^{-1},
\end{aligned}$$

where the rotation matrices are constructed in the usual manner^{5, 7, 140} with $\mathbf{R}_{21}(\alpha, \beta, \gamma)$

being

$$\mathbf{R}_{21} = \begin{pmatrix} \cos \alpha \cos \beta \cos \gamma - \sin \alpha \sin \gamma & \sin \alpha \cos \beta \cos \gamma + \cos \alpha \sin \gamma & -\sin \beta \cos \gamma \\ -\cos \alpha \cos \beta \sin \gamma - \sin \alpha \cos \gamma & -\sin \alpha \cos \beta \sin \gamma + \cos \alpha \cos \gamma & \sin \beta \sin \gamma \\ \cos \alpha \sin \beta & \sin \alpha \sin \beta & \cos \beta \end{pmatrix}$$

The g -anisotropy of TEMPO is much less than the associated isotropic g -value. Thus in Eq. 2 only g_{1zz} and g_{2zz} are considered, and hence the angular momenta of the electron spins are quantized along \mathbf{B}_0 . Omitting the nuclear Zeeman terms (see Appendix A), the Hamiltonian in Eq. 2 is simplified to

$$\begin{aligned}
H &= (\beta_e B_0 g_{1zz} S_{1z} + \tilde{A}_{1zz} S_{1z} I'_{1z}) + (\beta_e B_0 g_{2zz} S_{2z} + \tilde{A}_{2zz} S_{2z} I'_{2z}) \\
&\quad + D(2S_{1z} S_{2z} - S_{1x} S_{2x} - S_{1y} S_{2y}) - 2J(S_{1z} S_{2z} + S_{1x} S_{2x} + S_{1y} S_{2y}), \quad (3)
\end{aligned}$$

where the primed nuclear spin operators denote that the angular momenta of nuclei that are quantized along their own hyperfine fields that depend on the spin quantum states of the hyperfine-coupled electrons. In the new quantization frames the coefficients for the hyperfine terms in Eq. 3 are

$$\begin{aligned}\tilde{A}_{1zz} &= \sqrt{\mathbf{n} \cdot \mathbf{A}_1 \mathbf{A}_1 \mathbf{n}} = \sqrt{\mathbf{n} \cdot \mathbf{R}_{1L} (\mathbf{A}_1^{\text{PAS}})^2 \mathbf{R}_{1L}^{-1} \mathbf{n}}, \\ \tilde{A}_{2zz} &= \sqrt{\mathbf{n} \cdot \mathbf{A}_2 \mathbf{A}_2 \mathbf{n}} = \sqrt{\mathbf{n} \cdot \mathbf{R}_{1L} \mathbf{R}_{21} (\mathbf{A}_2^{\text{PAS}})^2 \mathbf{R}_{21}^{-1} \mathbf{R}_{1L}^{-1} \mathbf{n}},\end{aligned}$$

with

$$\mathbf{n} = \begin{pmatrix} 0 \\ 0 \\ 1 \end{pmatrix}.$$

Moreover, the interelectron dipolar interaction D is expanded as

$$D = \frac{\omega_d}{2} (1 - 3 \cos^2 \mu),$$

where μ is the angle between the directions of \mathbf{R} and \mathbf{B}_0 , and ω_d is a dipolar-coupling constant defined, with $\bar{g}_1 = \frac{1}{3}(g_{1xx} + g_{1yy} + g_{1zz})$ and $\bar{g}_2 = \frac{1}{3}(g_{2xx} + g_{2yy} + g_{2zz})$, as

$$\omega_d \approx \frac{\bar{g}_1 \bar{g}_2 \beta_e^2}{|R|^3}.$$

In the reference PAS of the g_1 -tensor, $\cos(\mu)$ can be evaluated as

$$\cos \mu = \mathbf{n} \cdot \mathbf{R}_{1L} \mathbf{R}_{1D}^{-1} \mathbf{n}.$$

The matrix representation of Eq. 3 is block-diagonal with $(2I_1 + 1)(2I_2 + 1)$ pseudo-two-spin (4×4) blocks labeled by the nuclear spin quanta, (m_{I_1}, m_{I_2}) . Subsequently, the hyperfine interactions are treated as effective electron Zeeman interactions, which appear in the (m_{I_1}, m_{I_2}) labeled sub-matrices H^k as

$$\begin{aligned}
H^k &= \langle m_{I1} m_{I2} | H | m_{I1} m_{I2} \rangle \\
&= (\beta_e B_0 g_{1zz} + m_{I1} \tilde{A}_{1zz}) S_{1z} + (\beta_e B_0 g_{2zz} + m_{I2} \tilde{A}_{2zz}) S_{2z} \\
&\quad + D(2S_{1z} S_{2z} - S_{1x} S_{2x} - S_{1y} S_{2y}) \\
&\quad - 2J(S_{1z} S_{2z} + S_{1x} S_{2x} + S_{1y} S_{2y}).
\end{aligned} \tag{4}$$

An EPR stick-spectrum is calculated from the eigenvalues (λ_i^k) and eigenvectors (Ψ_i^k) of the sub-matrices in Eq. 4 (see Appendix B). Among the four eigenstates in each sub-matrix, four allowed EPR transitions are identified as two transitions from the antiparallel electron spin states (Ψ_2^k, Ψ_3^k) to the highest Zeeman energy parallel spin state (Ψ_1^k) and two transitions from the lowest Zeeman energy parallel electron spin state (Ψ_4^k) to the antiparallel spin states. At a fixed microwave frequency ω_M , the resonance magnetic field for an EPR transition can be calculated from the relationship

$$\frac{\omega_M}{2\pi} = |\lambda_i^k - \lambda_j^k|.$$

For example, based on the result of Appendix B, the resonance magnetic field for the transition $\Psi_2^k \rightarrow \Psi_1^k$ satisfies the self-consistent equation

$$B_{res}^{L=1,k} = \frac{\frac{\omega_M}{2\pi} - c^k - D + J + \sqrt{(qB_{res}^{L=1,k} + f^k)^2 + (\frac{1}{2}D + J)^2}}{p}. \tag{5}$$

where p , q , c^k and f^k are functions of g_{1zz} , g_{2zz} , \tilde{A}_{1zz} and \tilde{A}_{2zz} , and are defined in the Appendix B. In practice, $B_{res}^{L=1,k}$ rapidly converges to an accurate value in the iteration (Eq. 5) starting from the central field of the EPR spectrum¹². To account for the

temperature dependence of the EPR frequency (ω_e), transitions probabilities are given by

$$\begin{aligned}
 P^{L=1,k} &\propto \left| \langle \Psi_2^k | S_1^+ + S_2^+ | \Psi_1^k \rangle \right|^2 = (a^k - b^k)^2, \\
 P^{L=2,k} &\propto \left| \langle \Psi_3^k | S_1^+ + S_2^+ | \Psi_1^k \rangle \right|^2 = (a^k + b^k)^2, \\
 P^{L=3,k} &\propto \left| \langle \Psi_4^k | S_1^+ + S_2^+ | \Psi_2^k \rangle \right|^2 \times \exp(-\hbar\omega_e / k_B T) = (a^k - b^k)^2 \times \exp(-\hbar\omega_e / k_B T), \\
 P^{L=4,k} &\propto \left| \langle \Psi_4^k | S_1^+ + S_2^+ | \Psi_3^k \rangle \right|^2 \times \exp(-\hbar\omega_e / k_B T) = (a^k + b^k)^2 \times \exp(-\hbar\omega_e / k_B T),
 \end{aligned}$$

where $S_1^+ = S_{1x} + iS_{1y}$, $S_2^+ = S_{2x} + iS_{2y}$, and a^k and b^k are given in Appendix B. When the electron–electron interactions (D and J) shift the energy of antiparallel electron spin states and lead to splittings in the EPR spectrum, the low temperature effect selects one branch of the splittings since the parallel electron spin state with the lowest Zeeman energy becomes significantly more populated by the Boltzmann factor $\exp(-\hbar\omega_e / k_B T)$ than the antiparallel spin state¹⁴¹. For single or weakly coupled TEMPO radicals, the altered transition probabilities modify the overall intensity of the signal but do not change the normalized lineshape. However, the lineshape of a biradical with strong electron–electron interactions can change significantly at low temperature. Specifically, the Boltzmann factor leads to significant temperature effects when $\kappa \equiv \hbar\omega_e / k_B T$ is no longer much less than 1. In discussing 140 GHz EPR spectra at 20 K, this temperature effect is not negligible since $\kappa \sim 0.34$.

Clearly, $B_{res}^{L=1,k}$ is a function of α , β , γ , η , ξ , R , J , θ , and ϕ . If the biradical molecule is rigid and has only one molecular conformation, α , β , γ , η , ξ , and R are fixed and can be determined from EPR lineshape analyses. However, θ and ϕ are randomly distributed and

depend on the orientation of the entire biradical in a powder system. The simulated derivative EPR spectrum $S(B_0)$ is then obtained from the double integral, which we approximate as a double sum over the angles θ and ϕ as

$$S(B_0) = \sum_{L=1}^4 \sum_k \sum_{n=1}^{N_\theta} \sum_{m=1}^{N_\phi} \frac{\sin \theta_n}{N_\theta N_\phi} \times \frac{-P^{L,k} \cdot [B_0 - B_{res}^{L,k}(\theta_n, \phi_m)]}{\{\frac{1}{4}\Gamma^2 + [B_0 - B_{res}^{L,k}(\theta_n, \phi_m)]^2\}^2}, \quad (6)$$

where $\theta = \pi(n - 1/2)/N_\theta$, $\phi = 2\pi(m - 1)/N_\phi$ and Γ is the linewidth for a Lorentzian lineshape¹⁴². In practice, the exchange integral J is usually small when it involves two electrons with a through space $R > 10 \text{ \AA}$, or when the number of covalent σ -bonds > 10 ¹⁰⁸. Consequently, J is usually excluded from the fitting parameters for biradicals with longer molecular linkages except for the case of the BTurea (*vide infra*) biradical where J is implicated by the biradical structure and manifests itself in the associative solution EPR spectrum.

4.3. Materials and Methods

4.3.1. Model biradicals

The structures of biradicals investigated in this chapter are illustrated in Figure 4.2. All reagents used in their preparation were of the highest grades and purchased from Sigma–Aldrich (St. Louis, MO). The biradicals BTnE, *bis* TEMPO tethered by n ethylene glycol monomers, where $n = 2, 3$ or 4 , were synthesized by reacting *di*-, *tri*- or *tetra*-ethylene glycol (0.1 mmol) with 4-hydroxy-TEMPO (2,2,6,6-tetramethylpiperidine-1-oxyl-4-ol, 97% free radical, 0.3 mmol) activated by NaH (0.4 mmol) in THF (3 mL) under a N_2 atmosphere at 60°C ¹⁰⁷. The biradical BTOXA, *bis*-TEMPO tethered by oxalyl

amide, was obtained by reacting oxalyl chloride (0.2 mmol) with 4-amino-TEMPO (4-amino-2,2,6,6-tetramethylpiperidine-1-oxyl, 97% free radical, 0.4 mmol) in the presence of triethylamine (1.0 mmol) in toluene (1 mL) at 0°C. The biradical BTurea, *bis*-TEMPO tethered by the urea structure, was made by reacting diimidazole carbonate (0.9 mmol) with 4-amino-TEMPO (1.8 mmol). The biradical TOTAPOL, 1-(TEMPO-4-oxy)-3-(TEMPO-4-amino)-propan-2-ol, was synthesized in two steps¹²⁷. In the first step, 4-hydroxy-TEMPO (60 mmol) was reacted with epichlorohydrin (3.91 mL, 50 mmol) in basic solution (50% w/w NaOH, 10 mL with 0.136 g tetrabutylammonium hydrogensulfate as a phase-transfer catalyst) to obtain 4-(2,3-epoxy-propoxy)-2,2,6,6-tetramethyl-1-piperidinyloxy [4-(2,3-epoxy-propoxy)-TEMPO]. A 1.62-g, 7-mmol aliquot of this product was reacted with 4-amino-TEMPO (1.20 g, 7 mmol) in anhydrous CH₃CN (13 mL) with LiClO₄ (0.745 g, 7 mmol) under argon atmosphere overnight at room temperature to obtain TOTAPOL. To provide narrower linewidths in the EPR powder spectra, the TEMPO moieties were ¹⁵N,²H-labeled. The isotope labeled 4-hydroxy-TEMPO and 4-amino-TEMPO for the above reactions were purchased from CDN Isotope (Quebec, Canada).

4.3.2. DNP experiments

Each DNP sample contained 5 mM biradicals (10 mM electrons) and 2 M ¹³C-urea in a ²H₆-DMSO/²H₂O/H₂O (60:34:6 w/w/w) mixture that forms a glass at 90 K where the DNP experiments were conducted. The high concentration of ¹³C-urea ensured a more accurate measurement of the NMR signal in the absence of microwaves, and the partial protonation of the solvent was adjusted to maximize the DNP enhancement and the ¹H-¹H

spin diffusion process. A sapphire rotor (4 mm OD from Revolution NMR) was center-packed with 25- μ L sample solution and maintained at \sim 90 K for cryogenic MAS-DNP experiments. Each cap stem was grooved and attached to the rotor with cryogenic epoxy (Hysol; Dexter Corporation, Olean, NY) to prevent the drive and sealing caps of the rotor from becoming loose while spinning at low temperature.

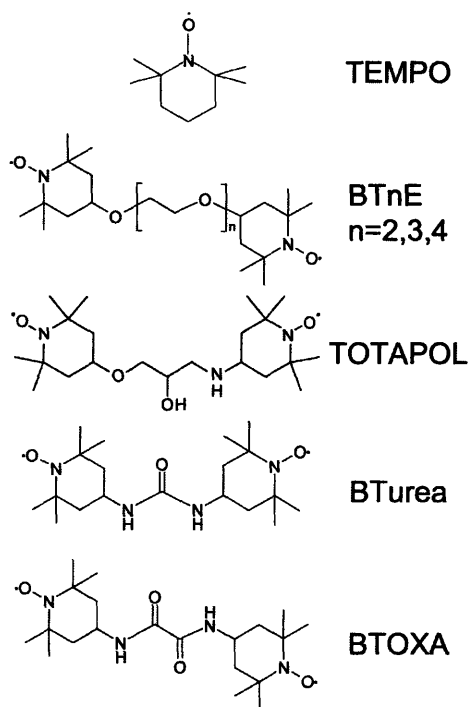


Figure 4.2. The structures of TEMPO and selected biradicals. While the TEMPO moiety usually contains natural abundant isotopes in DNP experiments, they are ^{15}N and ^2H labeled for better resolution of powder EPR spectra.

DNP-CPMAS experiments were performed on a custom designed, 5-Tesla (140-GHz EPR/211 MHz NMR) system equipped with a superconducting sweep coil (\pm 750 G), a 139.66 GHz/10 W gyrotron microwave source ⁹, and a triple channel (e^- , ^1H , and ^{13}C) probe capable of performing MAS experiments at \sim 90 K. The pulse sequence used

to acquire the DNP enhanced spectra is illustrated in Figure 4.3a. Initially, ^1H polarization was saturated by a series of 90° pulses, followed by the application of microwave irradiation generating a buildup of enhanced proton polarization, which was then detected through a standard CPMAS sequence in the presence of TPPM decoupling ($\omega_1/2\pi = 70$ kHz for ^1H)¹¹⁶.

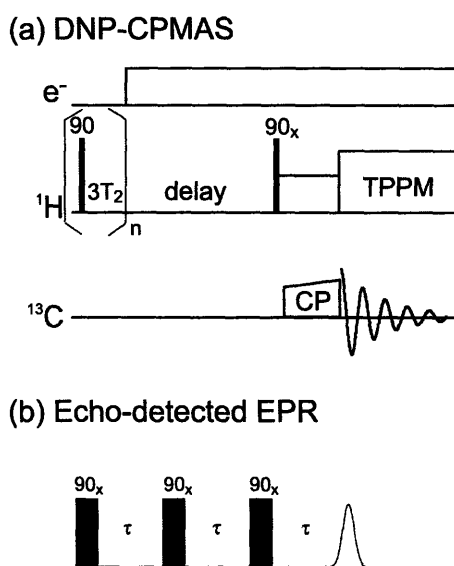


Figure 4.3. Pulse sequences for detection of (a) the enhancement of ^1H polarization and (b) 140 GHz EPR spectra.

4.3.3. Powder EPR spectra at 9 and 140 GHz

Each EPR sample contained 0.5 mM of biradicals (1 mM electrons) in a $^2\text{H}_6$ -DMSO/ $^2\text{H}_2\text{O}$ (60:40 w/w) mixture since the removal of environmental ^1H spins reduced the EPR linewidth by a factor of about two. A Bruker EMX spectrometer was used to record 9 GHz CW-EPR spectra at 77 K using a 4-mm quartz tube with a ~ 60 - μL sample immersed in a finger Dewar (WG-819-B-Q; Wilmad LabGlass, Buena, NJ). The spectra

measured from progressively diluted biradicals indicated that the residual linewidth was related to the glassy matrix that introduced a distribution of molecular conformations. High-field EPR spectra were recorded with 139.95 GHz microwaves in a 5 T superconducting magnet with a superconducting sweep coil capable of varying the stationary magnetic field by ± 4000 G. About a 0.4- μ L sample was introduced into a capillary (0.40 ID, 0.55 OD) and placed into a cavity resonator⁸⁶, which was then cooled to 20 K in a cryostat (Oxford Instruments, Oxford, UK). A stimulated-echo pulse sequence, $(\pi/2)_x-\tau-(\pi/2)_x-\tau-(\pi/2)_x-\tau$ -echo with $(\pi/2)_x = 100$ ns and $\tau = 200$ ns (Figure 4.3b), was used to detect EPR absorption signals as the magnetic field was swept. The first derivative of the pulsed-echo-detected absorption spectrum approximates the lineshape of the 140-GHz CW-EPR spectrum with a resolution of 1 G.

4.3.4. Multifrequency EPR lineshape fitting

The goal of lineshape fitting is to minimize the difference between the simulated EPR powder spectra (S^{sim} , from Eq. 6) of the biradical and the measured spectra (S^{exp}) at 9 and 140 GHz. Both of the simulated and experimental spectra are normalized and digitized as N data points. The mean square deviation χ^2 is given by

$$\chi^2(\alpha, \beta, \gamma, \eta, \xi, R, J, \Gamma) = \sum_{j=1}^N [S_j^{sim}(\alpha, \beta, \gamma, \eta, \xi, R, J, \Gamma) - S_j^{exp}]^2.$$

This fitting problem is complex and nonlinear and therefore standard methods that allow a change in the value of the fitting parameters only when the calculated χ^2 is reduced do not necessarily yield a global minimum for χ^2 . Therefore, we employed a simulated

annealing approach¹⁴³⁻¹⁴⁵ that circumvents the problem for the search for a minimum of χ^2 confined near the local minimum. In this manner, the fitting parameters are varied one by one in a sequence and the varied parameters are accepted as the new reference according to Metropolis criteria¹⁴⁶. The variation is made randomly within a 'reasonable' range that is proportional to the 'annealing temperature' T_A . When a proposed set of parameters generates a smaller χ^2 , it is accepted as the reference for the next trial. However, when the proposed parameter set fails to yield a smaller χ^2 , it is not automatically discarded as is done in standard methods, but is accepted within a Boltzmann-like probability defined by the annealing temperature. Specifically, a random number is generated, uniformly distributed between 0 and 1. If it proves to be smaller than $\exp(-\Delta\chi^2 / k_B T_A)$, the proposed set of parameters yielding $\Delta\chi^2 > 0$ is then accepted as the new reference set.

The 'reasonable' range for varying a fitting parameter is selected such that about one-half of the proposed trial parameters are accepted, and thus become actively adjusted within the annealing process. The parameter T_A , which emulates the temperature in the annealing process, is slowly reduced after χ^2 has been calculated for many sets of fitting parameters; these parameters statistically cover the desired range of fitting parameters (the whole range, when T_A is extremely high, and a focused range, when T_A is extremely low). The annealing process can be terminated after an absolute minimum χ^2 is found and the calculated trial χ^2 converges to this minimum. After a simulated annealing process, a further minimization of χ^2 may be achieved using a standard method, e.g., the Nelder-Mead simplex algorithm¹⁴⁴.

The best-fit parameters for the simulated annealing procedure were determined by

incorporating the simulated powder EPR spectra at 9 and 140 GHz via a MATLAB (MathWorks Inc., Natick, MA) environment running on a G4-PowerPC. The range for each set of fitting parameters was varied as described above, i.e., after 20 cycles of sequential changes in these parameters¹⁴⁷. T_A was then reduced to the 80% level after the range of the varying parameters had been adjusted 10 times. In each case, the initial T_A was chosen to keep the associated range of variation reasonable. For the eight variables in the present simulated EPR spectrum, it took about 1 day to explore 20,000 possible sets of fitting parameters. Although the initial set of fitting parameters should be randomly chosen, it can be roughly ascertained from fitting the 140-GHz EPR spectrum for J , R , η , and ξ , given that the splittings that arise from interelectron interactions are better resolved in the 140 GHz spectra. The errors for the refined fitting parameters were estimated according to F -statistics by calculating the minimized χ^2 with respect to the remaining parameters as function of the displacement from the optimal value. A conventional bow-shaped curve was fitted by a normal distribution whose standard deviation depicts the fitting error within a canonical level of statistical confidence. For example, two standard deviations represent the accuracy of fitting with 95% confidence.

4.4. Results

4.4.1. Solution EPR at 9 GHz

Figure 4.4 shows the 9 GHz EPR solution spectra of BT2E, BTurea, and BTOXA used to characterize the newly synthesized biradicals. The spectrum of BT2E has two extra lines (2 and 4) in addition to three lines (1, 3, and 5) whose positions coincide with spectral lines of monomeric TEMPO which arise from hyperfine coupling with the ^{14}N (I

= 1), $A_N \sim 15.9$ G. Similar five-peak spectra were observed for BT3E, BT4E, and TOTAPOL, which can be regarded as possessing an average exchange integral (J) much larger than A_N . A time-independent $J \gg A_N$ should result in five-line splitting with a peak intensity ratio $q_2/q_1 = 2$, where q_1 and q_2 are the intensities of peaks 1 and 2, respectively. However, the transient proximity of the two TEMPOs in BTnE yielded $q_2/q_1 < 2$ due to a flexible tether¹⁴⁸. The molecular dynamics involved can be described approximately with a two-state model in which the near proximity of TEMPO moieties leads to a strong J-coupling constant, while a distant separation results in a negligible J . The temporal fractions of these two states follow the relationships¹⁴⁹:

$$f_n + f_d = 1,$$

$$f_n / f_d = 3(q_2 / q_1) / [2 - (q_2 / q_1)],$$

where f_n and f_d are the fractions for the near and distant states of a biradical, respectively. The values of f_n/f_d of BT4E, BT3E, BT2E, and TOTAPOL in ethanol are 6.2, 5.5, 5.3, and 0.9, respectively. The absolute lifetimes of these two states cannot be determined by the above analysis but the timescale describing the two-state exchange should be less than A_N^{-1} (i.e., ~ 20 ns) in order to display an averaged effect of J-couplings. As we will see from the simulation below, the flexibility in the tether results in a distribution of molecular conformations of the BTnE series and TOTAPOL when these biradicals are frozen in a glass matrix.

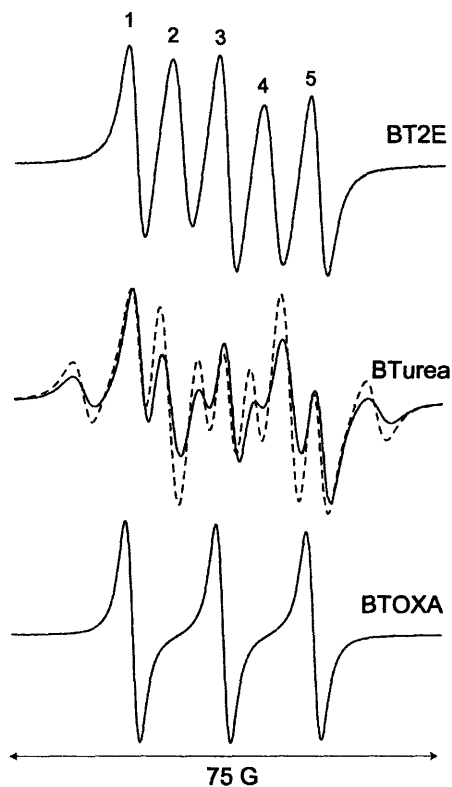


Figure 4.4. 9-GHz EPR solution (in ethanol) spectra of biradicals: BT2E, BTurea and BTOXA. The lineshape of BTurea is approximated by a simulation (dash line) with a time-independent exchange integral $J = \pm 7.7$ G.

In contrast, the rigidity of BTurea and BTOXA biradicals leads to different features of EPR solution spectra. Figure 4.4 shows that BTurea exhibits a complex spectrum arising largely from a J-coupling comparable to the ^{14}N -hyperfine coupling constant. A simulated EPR lineshape with a time-independent $J = \pm 7.7$ G reflects a good approximation relative to the solution EPR spectrum of BTurea. This time-independent J-coupling, known as either a through-bond or a through-space exchange integral, indicates a short and rigid tether consistent with the computed molecular models. Any discrepancy between the simulation and the experiment may arise from molecular

dynamics that perturb the J-coupling of BTurea. Figure 4.4 also shows that the spectrum of BTOXA features an insignificant J-coupling due to the rigid tether involved. Although the three-peak EPR solution spectrum apparently failed to show the presence of a biradical, the associated line broadening (~3 G) suggested the proximity of the other paramagnetic moiety in the BTOXA molecule. Despite the smaller number of atoms comprising the BTOXA tether, when compared to the BTnE series, the rigidity of BTOXA's tether keeps the two TEMPOs at a distance and the intensity of the exchange integral becomes negligible. The rigidity of the tethers in both BTurea and BTOXA could constrain the conformation of the biradical in a frozen solution and hence define the relative orientation of g-tensors between the two electrons.

4.4.2. Powder EPR spectra at 9 and 140 GHz

Multifrequency powder EPR spectra are useful in constraining both the distance and relative g-tensor orientations between two electrons, especially when the distance between the paramagnetic centers is short as is the case for the biradicals that are potential DNP polarizing agents. These constraints allow the electron–electron dipolar couplings and the EPR frequency separations to be evaluated in order to optimize both the CE and TM polarizing mechanisms. The EPR powder spectra of the TEMPO-based biradicals were recorded in frozen glassy solutions at <100 K. For $^{15}\text{N}, ^2\text{H}$ -labeled TEMPO ¹⁵⁰, the well-known principal values of the g-tensor (i.e., $g_{xx} = 2.0090$, $g_{yy} = 2.0061$, $g_{zz} = 2.0021$) and hyperfine-tensor (i.e., $A_{xx} = 9.30$ G, $A_{yy} = 9.46$ G, $A_{zz} = 51.39$ G) were verified with 9-GHz CW–EPR spectra of 4-hydroxy-TEMPO and 4-amino-TEMPO. These principal values also fit the pulsed-echo-detected 140-GHz EPR spectra, but the agreement with the 140-GHz experimental spectra and simulations is not as good

as with the 9 GHz spectra. The reason for this is the more rapid anisotropic relaxation which results in a distortion of the lineshapes in the downfield part of the echo-detected spectra.

Figure 4.5 illustrates the EPR spectra of the $^{15}\text{N}, ^2\text{H}$ -labeled biradicals at 9 and 140 GHz with the experimental and simulated spectra depicted as solid and dashed lines, respectively. A qualitative comparison of the 9- and 140-GHz EPR spectra of the flexible BTnE and TOTAPOL biradicals shows that the line broadening is approximately inversely proportional to the number of atoms contained in the tether. The quality of fitting is generally better with the flexible biradical due to the smaller number of splittings, consistent with the larger line broadening parameter Γ used. This broadening effect can be attributed to the multiple conformations of a flexible biradical. In contrast, the visual quality of the fit for both the BTOXA and BTurea spectra deteriorated as these spectra became rich in splittings as a result of electron–electron interactions and a reduction in the distribution of biradical conformations. The specific molecular conformations are consistent with both tethers being in rigid, well-defined conformations. As a result, the value of Γ was smaller than that for the flexible biradicals. However, despite the less satisfying visual agreement between the simulations and experimental lineshapes, the fitting parameters in fact regressed to smaller errors. That is, the simulated EPR lineshapes for BTurea or BTOXA can be derived from a unique set of parameters, whereas the EPR spectra of the BTnE series and TOTAPOL can be simultaneously simulated by distribution of sets of parameters.

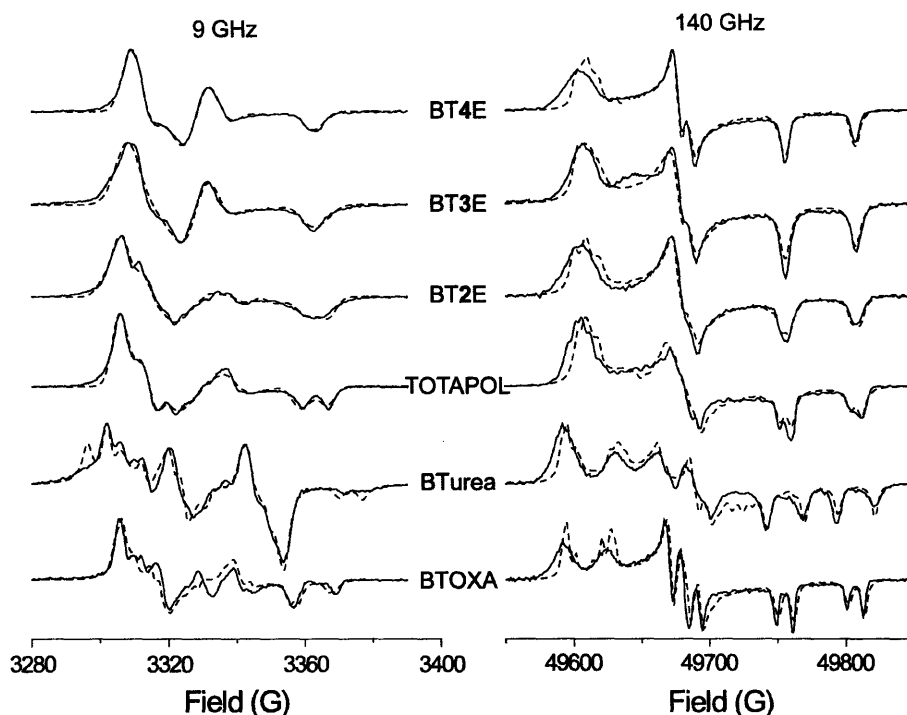


Figure 4.5. Powder 9 and 140 GHz EPR spectra (experiments: solid lines, simulations: dash lines) of six biradicals with ^{15}N and ^2H labeling. Note that the fitting parameters for BTurea and BTOXA are unique while the EPR lineshapes of the BTnE series and TOTAPOL can be simulated by distribution of fitting parameters.

Figure 4.6 displays the values of χ^2 as a function of the variation in the interelectron distance R and five Euler angles relating the orientation of the two g -tensors for BTurea and BTOXA (also a J -coupling constant for BTurea, whose error plot is not shown). Minima in the χ^2 plots strongly constrain the values of the fitting parameters, which provide support for the suggestion that the biradicals exist in a well defined conformation. Note that in the case of BTOXA the γ -angle is not well defined, which is due to the small value of β ($\pm 25^\circ$) which conflates the effect of α and γ on the EPR powder lineshape into that of α . Note that according to the reference ¹², the angles ξ , η , and β are related by a rotation through 90° , and the angles α and γ are related by a

reflection through 0° (or 180°). These symmetric properties of the angle parameters can be verified when the angles lie close to 0° , 90° , and 180° , as, for example, the ξ and η angles of BTurea and the α , β , γ , ξ , and η angles of BTOXA. In addition, the exact J of ~ -7.3 G simulated for BTurea is consistent with the absolute value from fitting the EPR solution spectrum. That both BTurea and BTOXA have $\xi \sim 90^\circ$ and $\eta \sim 180^\circ$ implies that approximately planar tethers exist in both of these biradicals. Moreover, the planar tether in BTOXA imposes a center symmetry between the g -tensors of tethered TEMPOs, as implied by the angle parameters of $\alpha \sim 180^\circ$, $\beta \sim 0^\circ$, and $\gamma \sim 0^\circ$.

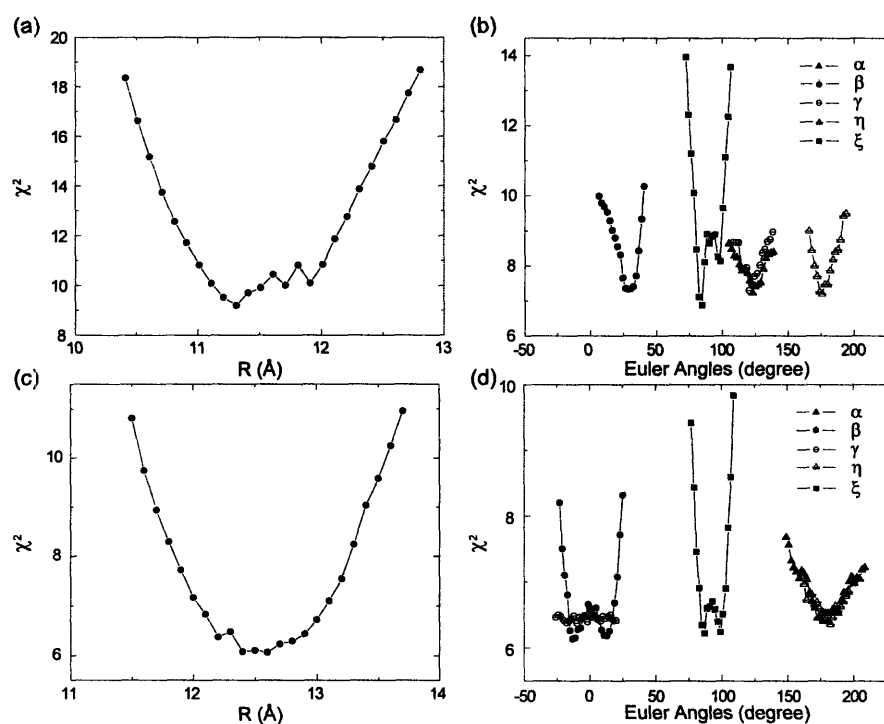


Figure 4.6. Fitting errors for the distance (R) and Euler angles (α , β , γ , η , ξ) in BTurea (a,b) and BTOXA (c,d).

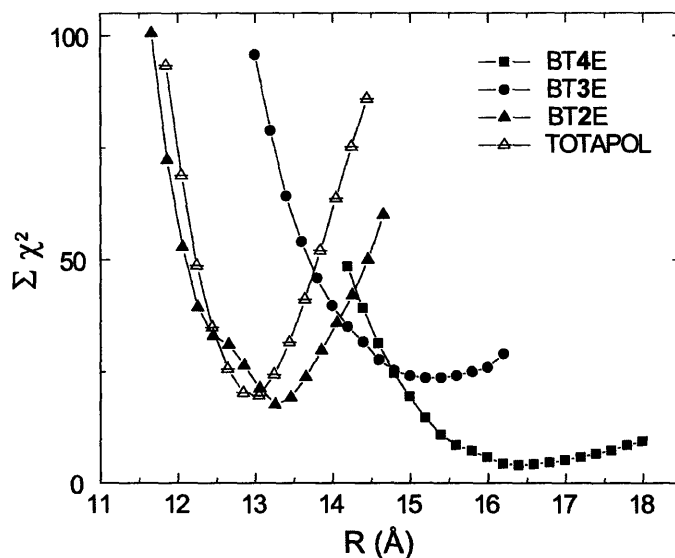


Figure 4.7. Fitting errors for the distances in the BTnE series and TOTAPOL.

Among the multiple sets of fitting parameters in powder EPR simulations of flexible biradicals such as BTnE and TOTAPOL, the orientation angles are distributed in a broad range and are consistent with the flexibility of the molecular structure. Nevertheless, the distribution of the distance parameter R is relatively narrow and can be treated as an uncertainty corresponding to an averaged distance between the two electrons. Figure 4.7 shows a slightly different parameter $\Sigma \chi^2$ plotted as a function of the variance of R for each member of the BTnE series and TOTAPOL. To obtain $\Sigma \chi^2$, the fitted χ^2 versus the variation of R is summed over 15 equally well-fitting parameter sets, so that the average electron–electron distance and the associated error are evaluated. Note that distances associated with indistinguishable orientations mentioned previously were only counted once. In general, the average R is close to the optimal value for the minimum $\Sigma \chi^2$. In addition, mapping a Gaussian function onto the $\Sigma \chi^2$ function yields the estimated errors for the derived R . From lineshape simulations, fitting parameters, Γ , α , β , γ , ξ , η , R , and

specifically for BTurea, J , that best fit the measured EPR spectra are summarized in Table 4.1.

Table 4.1. Summarized results of fitting parameters for 9 and 140 GHz EPR spectra.

Biradical	$e^- - e^-$ distance	Relative orientation of g- and A-tensors ^a			$e^- - e^-$ dipole orientation ^a		Exchange integral	broadening parameter
	R (Å)	α (degree)	β	γ	ξ	η	J (G)	Γ^b (G)
BTurea	11.4±0.2	128	29	120	85	175	-7.3±0.5	2.5
BTOXA	12.6±0.4	182	10	0	88	177	-	2.5
TOTAPOL	13.1±0.6	107	108	124	94	127	-	4
BT2E	13.3±0.8	81	47	16	30	104	-	4
BT3E	15.0±0.8	23	121	297	67	108	-	4
BT4E	16.5±0.9	27	50	211	132	321	-	3

^a The error associated with the angles is about 10°. Note that the angle parameters for TOTAPOL and BTnE series belong to the best-fit one among the multiple conformations.

^b Γ is the full width at half height of a Lorentzian lineshape.

With the knowledge of 4-hydroxy-TEMPO crystal structure¹⁵¹ and the relationship between the g-tensor principal axes and the geometry of nitroxide radical¹⁵², the distance and relative g-tensor orientation between two electrons can be converted into atom-atom distances among the atoms of two $\begin{matrix} C \\ \diagdown \\ C \end{matrix} \text{NO}^\bullet$ moieties and then input into the structural refinement software – crystallography NMR system (CNS)¹⁵³ to produce the refined structures as is shown in Error! Reference source not found.. The molecular structure databases of the biradicals for CNS were generated by XPLO2D¹⁵⁴. Clearly, the EPR constraints render a better defined structure such as in BTurea when the number of atoms in the tether decreases. Thus the relative orientation of two TEMPOs in BTnE biradicals is generally not constrained due long molecular linkages involved. Nevertheless, the

associated interelectron distance can be described by an average value from a distribution of a more restricted range. In contrast, the structures of BTurea and BTOXA are relatively well defined by the EPR characterization. Interestingly, although the refined structure of TOTAPOL illustrates a degree of flexibility, the TEMPO rings are constrained perpendicular to each other, so that the EPR frequency separation, in addition to the short distance, between the two electrons is favored by the cross effect polarizing mechanism.

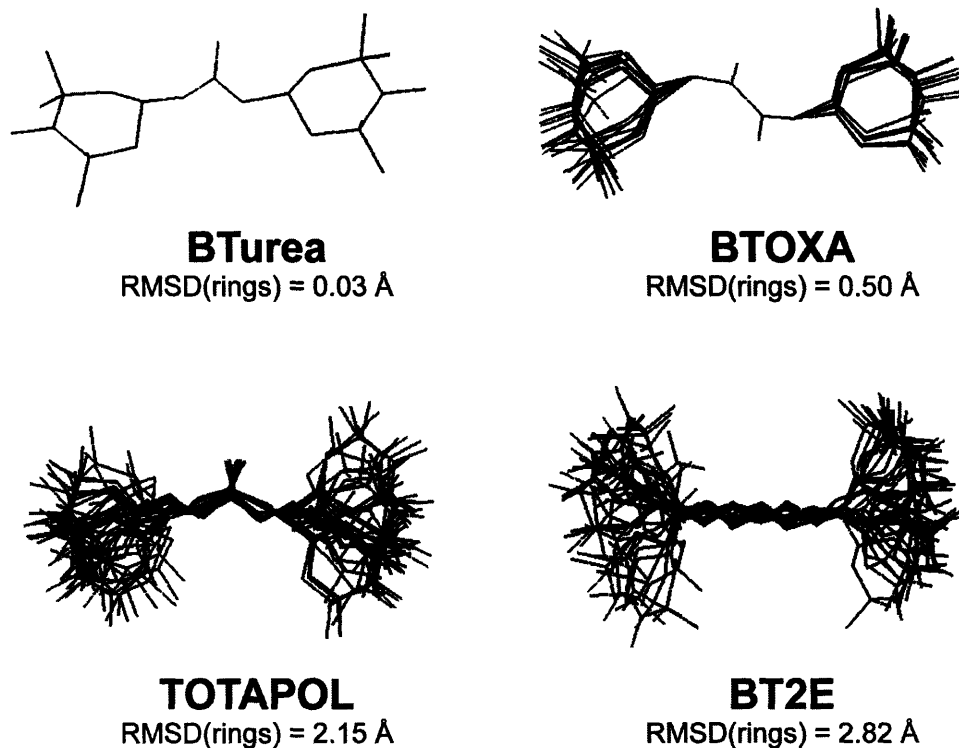


Figure 4.8. The structures of BTurea, BTOXA, TOTAPOL and BT2E were refined using geometrical constraints from the multifrequency EPR lineshape fitting. The root-mean-square-distances (RMSD) with respect to the atoms on TEMPO rings were also calculated.

4.4.3. Magnetic field dependence of DNP

DNP occurs when microwave radiation of the appropriate frequency excites the desired EPR transitions embedded in the spectral profile of a radical polarizing agent. Since the gyrotron microwave frequency is presently not tunable, the optimization of the excitation is performed by sweeping the external magnetic field. At the top of Figure 4.9 we illustrate 140-GHz EPR spectrum of TEMPO in frozen solution and the field-dependent profiles of DNP enhancement yielded by TEMPO and BT2E. These profiles depend on the probability of the correct EPR frequency separation from a randomly oriented TEMPO pair. The EPR spectrum of TEMPO (Figure 4.9, top), containing g - and ^{14}N -hyperfine-anisotropy, is an excellent approximation of the EPR spectral density displayed by the BTnE series as well as other biradicals investigated in this report, since the dipolar couplings due to the constrained interelectron distance are small relative to other spectral parameters such as g - and hyperfine-anisotropies and have small effects on EPR absorption lineshape. Note that the 140-GHz EPR spectrum of TEMPO is shifted along the field axis by 58 G in order to synchronize the resonance positions arising from the Gunn diode microwave source of the EPR spectrometer (139.95 GHz) with the microwave frequency provided by the gyrotron (139.66 GHz). The optimal magnetic field for DNP is indicated by an arrow at 49798 G in Figure 4.9, which is closely related to the central frequency of the EPR lineshape.

The field-dependent profile of ^1H enhancement obtained with 40 mM TEMPO achieves a maximum of about 55 at 49798 G and a minimum of about -55 at 49783 G. A zero value was obtained at 49735 G corresponding to maximum of EPR absorption. In contrast, the profile by 5 mM BT2E (10 mM electrons) exhibits a similar shape but different intensity from the profile of TEMPO, and shows a maximum of ~175 at 49798

G and a minimum of about -144 at 49696 G. The larger ^1H enhancement available from BT2E and changes in the relative intensity and position of the maximum in the negative enhancement could result from possible conformations of the polyethylene glycol tether. Note that the concentrations of TEMPO and BT2E are optimized for the largest DNP enhancement with reduced impact of paramagnetic relaxation. The similarity in shape of enhancement profiles of 40 mM TEMPO and 5 mM BT2E indicates the key role of electron–electron–nuclear processes involved in both the TM and CE polarizing mechanisms dominating at high and low radical concentrations, respectively.

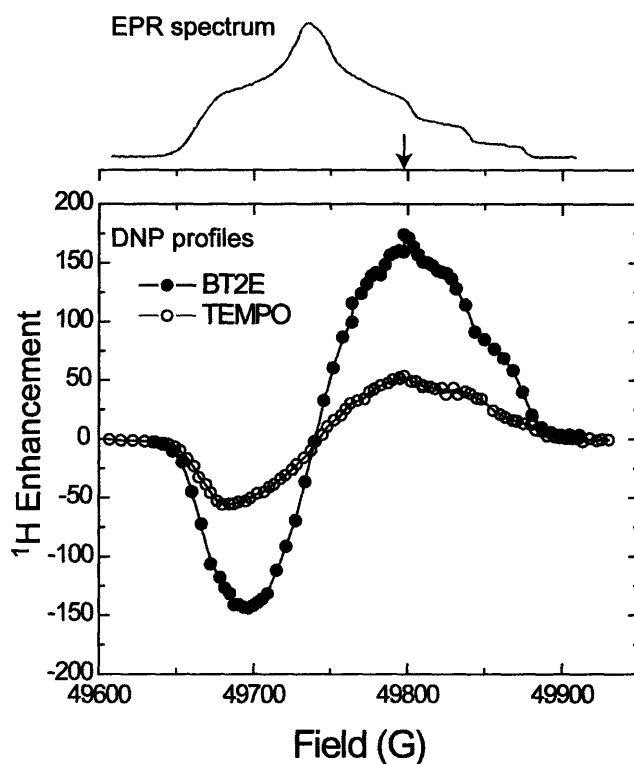


Figure 4.9. (Top) The 140 GHz EPR spectrum of TEMPO. (Bottom) Field-dependent ^1H DNP enhancement profiles using 5 mM BT2E and 40 mM TEMPO under MAS ($\omega_r/2\pi=3.5$ kHz) at 90 K and 5 T. The smooth lines are for eye-guidance.

4.4.4. DNP buildup during microwave irradiation

Enhancements in ^1H polarization were determined indirectly by ^{13}C -CPMAS NMR spectra because of higher spectral resolution and lower background signal intensities. Figure 4.10a illustrates intensive CP-signals of ^{13}C -urea after a period of microwave irradiation at the optimal magnetic field position. In contrast, signals without microwave irradiation were much smaller and required long periods of data accumulation in order to be clearly detected. Comparison of DNP enhanced signals with those at thermal equilibrium reflects an enhancement of 171 ± 20 when employing 5 mM BT2E. The enhanced signals grow as the microwave irradiation period increases and follows an exponential saturation-recovery defined by

$$\varepsilon(t) = \varepsilon_0[1 - \exp(-t/T_1)],$$

where ε is an enhancement factor, t is a delay for microwave irradiation, ε_0 is the equilibrium enhancement, and T_1 is the buildup time constant which is also the nuclear spin–lattice relaxation time. Figure 4.10b illustrates the growth in signal intensities following saturation of the proton polarization with and without microwave irradiation and implies that both the growth of the equilibrium-DNP enhancement and the saturation-recovery of the ^1H Boltzmann polarization are governed by the same time constant. Empirically, for a given polarizing agent, ε_0 depends on the magnetic field position, radical concentration, and microwave power, while T_1 apparently has only concentration dependence. The aim in designing polarizing agents is to provide a larger ^1H ε_0 and a lower T_1 for the optimal field position, a low radical concentration, and the available microwave power.

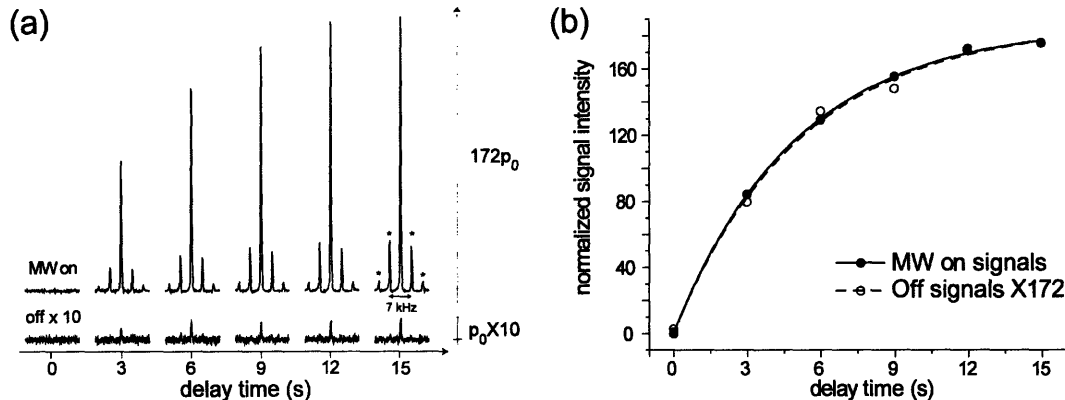


Figure 4.10. (a) Buildup of ^{13}C -CP signals of ^{13}C -urea from the enhanced ^1H polarization during a delay of microwave irradiation at the optimal magnetic field position. The ^1H enhancement is ~ 171 by comparing the signals with and without microwaves. (b) The buildup time constant is ~ 5 s, coincide with the ^1H spin-lattice relaxation time obtained without microwave irradiation. The numbers of acquisitions for enhanced and unenhanced signals are 4 and 32, respectively. The sample, containing 5 mM BT2E biradical, was rotated at a MAS frequency of 3.5 kHz indicated by spinning sidebands (asterisks).

4.4.5. Radical concentration dependence of DNP

A reduction in radical concentration, as long as DNP is still operative, is desirable since it attenuates electron–nuclear broadening that compromises resolution in the NMR spectra. Figure 4.11a shows that the BT2E biradical yields DNP enhancements that are relatively independent of electron concentrations while enhancements by the monomeric TEMPO radical are strongly influenced by electron concentrations. BT2E yielded $^1\text{H} \epsilon_0 \sim 175$ at an electron concentration from 10 to 50 mM (multiplied by 0.5 for the biradical concentration), while the $^1\text{H} \epsilon_0$ using TEMPO maximized at ~ 60 and decreased significantly when the corresponding electron concentration decreased below 40 mM. DNP measurements at higher radical concentration were discounted as the overall enhanced signals decayed due to a reduction in observable nuclear spins at high radical

concentration. The reduction in observable nuclei also led to weaker unenhanced NMR signals that contributed to larger error bars in measurements of DNP enhancement. Figure 4.11b indicates that the nuclear T_1 has a strong dependence on electron concentrations in the case of both BT2E and TEMPO. The reduction in T_1 by increased electron concentrations was more significant in the case of the TEMPO radical than with the BT2E biradical. At higher electron concentrations, this dependence of T_1 tended to converge regardless of whether TEMPO or BT2E was employed. The larger errors associated with lower T_1 values arose from instability in the microwave source within the first 0.3 s following triggering of the gyrotron.

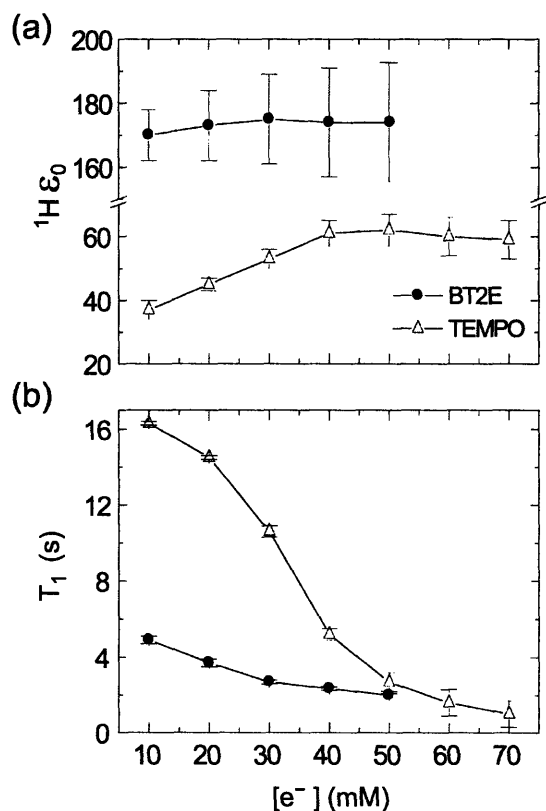


Figure 4.11. Radical concentration dependence of (a) DNP enhancement ϵ_0 and (b) buildup time constant T_1 using BT2E and TEMPO.

4.4.6. Microwave power dependence of DNP

A strong microwave field is required to produce efficient DNP, especially when the polarization efficiency decreases in increasing external magnetic fields. When designing polarizing agents, comparisons of DNP efficiency among biradical candidates must be made at a controlled level of microwave field strength, which depends on microwave power and the efficiency of transmission to the sample. However, variations exist in the efficiency with which microwave power is coupled to a sample, and DNP measurements may need to be obtained at different microwave field strengths. To circumvent this issue, one should always investigate the theoretical enhancement at infinite microwave power. This value can be obtained from the microwave power dependence of DNP enhancement described by

$$\frac{1}{\epsilon_0} = \frac{1}{\epsilon_{\max}} \left(1 + \frac{1}{aP} \right),$$

where ϵ_0 is the irradiation time-saturated enhancement, P is the microwave power, ϵ_{\max} is the enhancement at infinite microwave power, and a is the saturation parameter, which depends on the microwave transmission efficiency and EPR relaxation properties. Different instrumental conditions affect only a and ϵ_0 rather than ϵ_{\max} .

Figure 4.12 illustrates the relationship between $1/\epsilon_0$ and $1/P$ for various biradicals and is depicted in two panels for clarity. The regressive linear relationships provide parameters, ϵ_{\max} and a , which are summarized in Table 4.2. In addition, DNP enhancements under 1.5 W of microwave power that is proved stable in long-term experiments are also given, along with the associated T_1 values that were found to be independent of P , since any microwave heating of the sample was alleviated by cryogenic

MAS. The electron–electron distances R from the EPR analyses are listed as are the corresponding electron–electron dipole coupling constants.

With 10 mM electrons (5 mM biradicals), the trend in the DNP enhancement ϵ_0 was consistent with the theoretical power-saturated DNP enhancement ϵ_{\max} , while the proton relaxation time T_1 remained at about 5 to 6 s. The value of ϵ_{\max} reached a maximum with TOTAPOL but decreased with increasing electron–electron distances in going from BT2E, to BT3E and BT4E. The shorter electron–electron distances in BTurea and BTOXA failed to optimize ϵ_{\max} , with BTOXA yielding insignificant improvement of DNP enhancements ($\epsilon_0 \sim 50$) notwithstanding its short distance. Despite larger errors associated with the results for the microwave saturation parameter a , a trend clearly shows that the close proximity of two electrons leads to difficulties in obtaining the microwave saturation required for DNP. Exceptions to this trend occurred with both BTOXA and TEMPO and may be attributable to the unique molecular tether in BTOXA and the possible aggregation of TEMPO.

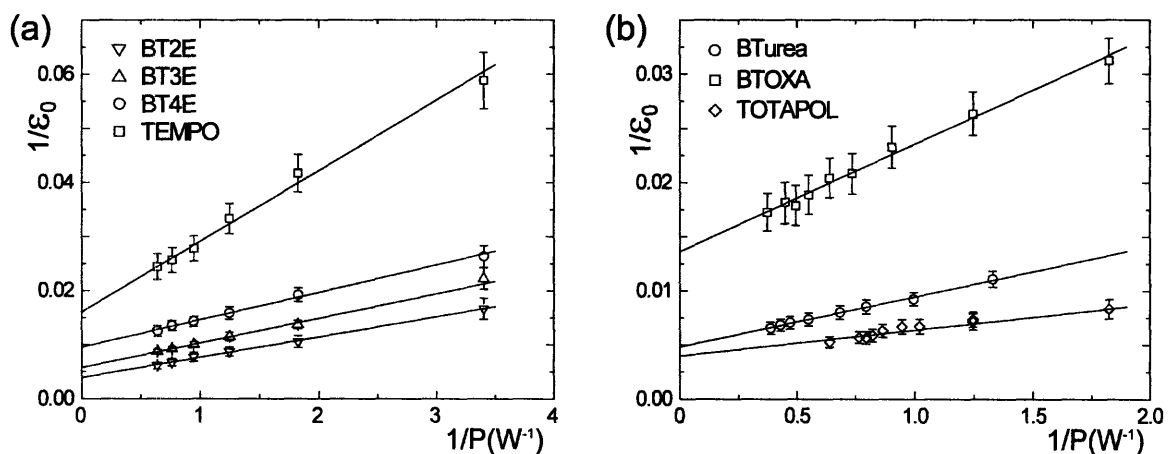


Figure 4.12. Microwave power dependence of DNP experiments using (a) the 5 mM BTnE with $n=2, 3$ and 4, and 10 mM monomeric TEMPO, and (b) BTurea, BTOXA and TOTAPOL, all of which have fewer atoms in their molecular linkers than BT2E does.

Table 4.2. Summary of ^1H DNP measurements from employment of various polarizing agents.

Biradical [e ⁻]=10 mM	Enhancement at 1.5 W ^a ϵ_0	Buildup time constant T_1 (s)	Enhancement at ∞ power ϵ_{max}	Saturation factor a (W ⁻¹)	e ⁻ - e ⁻ distance R (Å)	DCC ^b ω_d (MHz)
TOTAPOL	190±20	5.5±0.2	335±65	0.83±0.30	13.1±0.6	23.2±3.2
BT2E	175±20	4.9±0.2	260±55	1.03±0.40	13.3±0.8	22.2±4.0
BT3E	115±10	5.9±0.2	175±30	1.25±0.35	15.0±0.8	15.5±2.5
BT4E	80±10	6.3±0.2	105±20	1.87±0.35	16.5±0.9	11.6±1.9
BTurea	125±10	5.1±0.2	205±40	1.03±0.40	11.4±0.2	35.2±1.9
BTOXA	50±5	11.3±0.5	70±10	1.37±0.45	12.6±0.4	26.1±2.5
TEMPO	40±5	16.5±0.5	60±15	1.23±0.50	56 ^c	0.3

^a A stable microwave power for long experimental time

^b Dipole coupling constant: $\omega_d = 52160/R^3$ (MHz) for a TEMPO pair

^c The inter-electron distance for the monomeric TEMPO approximates the average intermolecular distance determined by the radical concentration. At the electron concentration of 10 mM, $\langle R \rangle$ is ~56 Å.

4.5. Discussion

DNP experiments using TEMPO-based polarizing agents rely on CE or TM polarizing mechanisms that dominate at low or high concentrations of the paramagnetic species, respectively. Electron–electron–nucleus three-spin processes involved in both CE and TM are characterized by an essential electron–electron interaction and an exact EPR frequency separation that provide the foundation for designing better polarizing agents and optimizing polarization conditions in DNP experiments. Information on the important spectral parameters involved in DNP mechanisms can be ascertained using solution- and solid-state EPR spectroscopy.

4.5.1. Designs of better polarizing agents

The essential electron–electron interaction constrained by the electron–electron distance in a biradical depends on the electron concentration in the monomeric radicals used. In general, biradicals yield larger DNP enhancements ($\epsilon_0 \sim 190$) over shorter

polarizing times ($T_1 \sim 5.5$ s) and at lower concentrations ($[e^-] \sim 10$ mM). These improvements, when compared to the results of TEMPO, show dramatic increases in the potential for DNP applications. The BTnE biradicals demonstrate a trend of increasing DNP enhancement with a decrease in intramolecular electron–electron distance. However, this trend is not shown in the DNP results of TOTAPOL, BTurea, and BTOXA, and in fact the largest DNP enhancement to date was obtained from TOTAPOL, which has a similar R to that of the BT2Es. The corresponding ϵ_{\max} given at theoretical infinite microwave power further emphasizes the superior DNP performance of TOTAPOL over BT2E; this superiority may be attributable to the constraint of the fixed distance between two electrons in TOTAPOL, which is implied by the relevant solution- and solid-state EPR spectra that reveal the smallest ratio of ‘near’ state to ‘distant’ state in solution spectra and show clear features of dipolar splitting in the solid.

Moreover, BTurea and BTOXA both have a smaller R value but failed to yield a better ϵ_0 . The theoretical ϵ_{\max} of BTurea ranks between that of BT2E and BT3E, indicating that the involved electron–electron dipole coupling constant is too strong to be optimal because possible increases of electron spin–lattice and spin–spin relaxation rates can suppress the microwave saturation, which provides the driving force for both CE and TM mechanisms. BTOXA, which has a smaller R than BT2E, displayed little improvement in DNP efficiency when compared to TEMPO. This result may reflect not only the high level of electron–electron interaction but also the other important parameter in the three-spin process: EPR frequency separation.

EPR frequency separations in powder biradical samples are controlled by the constraint of the relative g -tensor orientation. The complexity of powder distributions and

the multiple conformations of a biradical imply that the correct EPR frequency separation may not differ too greatly from that yielded by two independently orientated TEMPOs. Even with a rigid tether, the rotations along the bonds between a TEMPO moiety and its tether and the flipping of the TEMPO ring can still result in a distribution of molecular conformations with line broadenings in EPR spectra. Nevertheless, the features of dipole splittings that can be clearly observed in the EPR spectra of BTurea and BTOXA serve as standards to compare EPR lineshape fitting methodologies. While the unique constraint of g -tensor orientation in BTurea does not appear to affect DNP efficiency, the constraint in BTOXA does show a significant influence in DNP enhancement. The EPR powder spectra at 9 and 140 GHz revealed that the relative g -tensor orientation in BTOXA is constrained about a center symmetry that produces few EPR frequency separations, regardless of how the biradical is orientated within the powder distribution. Therefore, the three-spin-process is suppressed and the required condition $|\omega_{e1} - \omega_{e2}| = \omega_n$ is not satisfied.

To summarize, the DNP efficiency is optimized by varying the electron–electron distance in the flexible BTnE series and TOTAPOL. In addition, the failure to improve DNP using rigid BTOXA verifies the importance of the CE mechanism at low electron concentrations and explains the lack of EPR frequency separation in the center-symmetric g -tensor orientations.

4.5.2. Optimization of DNP experimental conditions

With a better designed biradical, DNP efficiency can be optimized for various experimental conditions, including magnetic field position, irradiation time, biradical concentration, and microwave power. At a constant microwave frequency, a correct

magnetic field position allows for EPR saturation that induces the strongest CE enhancement. The net DNP enhancement results from two counteracting CE processes that arise from EPR spectral densities at resonance offsets from the microwave frequency of $\pm\omega_n$, if the associated EPR absorption line is inhomogeneous and broader than ω_n . Given that the electron–electron interactions involved in the selected biradicals are smaller than ω_n (212 MHz for ^1H), the various EPR spectral densities yield similar magnetic field-dependent enhancement profiles.

Buildup of enhanced nuclear polarization occurs during the microwave irradiation period that succeeds a saturation-recovery process and is characterized by nuclear spin–lattice relaxation time T_1 . Although the designed biradical polarizing agents allow for efficient polarization transfer from electrons to coupled nuclei, complete polarization of bulk nuclei using diluted paramagnetic species also relies on homo-nuclear spin diffusion. The rate of nuclear spin diffusion is determined by the average homonuclear dipolar interaction, which can be described by the population density and is potentially affected by the MAS frequency. In order to observe larger DNP enhancements, the glass matrices were deuterated to the extent in which the ^1H – ^1H spin diffusion remained effective in DNP–CPMAS experiments.

A low radical concentration is desirable in DNP applications, since the side effect of electron–nuclear relaxation increases NMR linewidths and reduces the number of detectable nuclei close to the radicals. With constrained electron–electron distances, biradicals can yield a DNP enhancement that is independent of electron concentration C , unlike the case with TEMPO when a higher C is required to allow contacts between two electrons. Note that at $C < 10$ mM, T_1 becomes impractically long for applications, and

that ϵ_0 for the biradicals eventually decreases with a reduction in C . At higher electron concentrations ($C \geq 10$ mM) than those typically used in EPR spectroscopy, analysis of $1/\epsilon_0$ versus $1/C$ becomes no longer applicable because of unavoidable electron–electron interactions between the two molecules. Instead, the influence of concentration on DNP is determined through the inter-radical distance, density of polarizing centers, and the radical-induced nuclear relaxation. Since a biradical already has the required electron–electron distance, the influences of polarization density and paramagnetic relaxation counteract and lead to an insignificant concentration dependence of DNP with the biradical. The concentration-saturated enhancement also depends on the population density of nuclear spins. The natural abundance of protons in typical samples will empirically reduce the DNP enhancement factor by at least twofold, when compared to the protonation level in deuterated samples.

Microwave irradiation in CE and TM mechanisms is used to saturate the on-resonance EPR transitions and then to generate polarization differences between the on- and off-resonance electrons. As mentioned previously, the polarization difference is simultaneously transferred to the coupled nuclei via three-spin processes. The independence of T_1 from the applied microwave power reflects the fact that the nuclear polarization is regulated by the three-spin processes under a quasi-equilibrium resulting from microwave saturation. Successful saturation of EPR transitions requires a strong microwave field and long EPR relaxation times. However, microwave saturation can be impeded by a short electron spin–lattice relaxation time, which is required for multiple polarization transfers at diluted electron concentrations and is a consequence of efficient three-spin processes with strong electron–electron interactions. Therefore, strong

microwave power is a usual requirement to provide efficient polarization transfers, with any heating arising from microwave irradiation being compensated by the purging gas used for MAS.

Although infinite microwave irradiation power is impractical, the theoretical ϵ_{\max} can be derived from the relationship between $1/\epsilon_0$ and $1/P$, and the saturation parameter obtained, dependent on microwave coupling, relaxation times, and electron concentration. A reasonable comparison of DNP efficiencies among various biradicals can be performed on the basis of ϵ_0 and a . To date, TOTAPOL yields the largest DNP enhancement of ~ 190 at 1.5 W in a 4-mm rotor. Its theoretical enhancement $\epsilon_{\max} \sim 335$ is also the largest and is consistent with a separate measurement made in a 2.5-mm rotor. Furthermore, the associated a has the smallest value, reflecting a more efficient three-spin process.

4.6. Conclusions

A variety of designer biradicals having different tethers were analyzed with the goal of improving CE-DNP. Each biradical could be characterized by its EPR lineshape, which serves to characterize the intramolecular electron–electron distance and the relative g -tensor orientation between electrons. Good agreement between ^1H enhancements in DNP experiments and the parameters used to fit EPR spectra provide insights into the underlying electron–electron–nucleus processes involving the cross effect and thermal mixing. Powder EPR lineshape simulations can be modified to estimate the probability of a correct EPR frequency separation by a randomly orientated biradical. The nuclear enhancement obtained from the spectral parameters of DNP, i.e., the EPR, NMR, and

microwave frequencies, electron–electron and electron–nuclear interactions, electron and nuclear relaxation, and microwave field strength can be calculated theoretically, which allow for plausible quantitative explanations of the DNP results and of the EPR characterization by combining the theoretical model of CE with a simulation program developed for biradical powder EPR spectra.

While it is possible to establish the optimal distance constraint for CE between two electrons, finding the similar constraint involved in relative g-tensor orientation in a biradical composed of two TEMPOs is not straightforward. It is possible, however, to tether two different radicals in such a way as to optimize the required EPR frequency separation for CE.

Appendix A: Absence of the ^{15}N Zeeman interaction in 140-GHz EPR spectra

The nuclear (^{15}N) Zeeman interaction in Eq. 2 can be ignored since it is usually much smaller than the associated hyperfine interaction. Although this argument may not be true at a higher magnetic field like 5 T, there are only a small portion of TEMPO orientations that yield a hyperfine interaction smaller than the nuclear Larmor frequency. For example, small hyperfine interactions occur only when \mathbf{B}_0 lies close to the xy -plane of the PAS of one TEMPO. Despite the small hyperfine interaction, the resulting forbidden transitions ($\Delta m_S = \pm 1$, $\Delta m_I = \pm 1$) are not easily resolved due to various homogeneous and inhomogeneous broadenings in the EPR spectrum. Thus, ^{15}N Zeeman interactions are ignored in simulations of both 9- and 140-GHz EPR powder spectra.

Appendix B: Diagonalization of a two-pseudo-spin-1/2 4x4 matrix

The sub-matrix described by Eq. 4 is

$$H^k = \begin{pmatrix} pB_0 + c^k + \frac{1}{2}(D-J) & 0 & 0 & 0 \\ 0 & qB_0 + f^k - \frac{1}{2}(D-J) & -\frac{1}{2}D-J & 0 \\ 0 & -\frac{1}{2}D-J & -qB_0 - f^k - \frac{1}{2}(D-J) & 0 \\ 0 & 0 & 0 & -pB_0 - c^k + \frac{1}{2}(D-J) \end{pmatrix},$$

where the basis states are given by

$$\begin{aligned} \psi_1^k &= |m_{s1} = +\frac{1}{2}, m_{s2} = +\frac{1}{2}, m_{I1}, m_{I2} \rangle, \\ \psi_2^k &= |m_{s1} = +\frac{1}{2}, m_{s2} = -\frac{1}{2}, m_{I1}, m_{I2} \rangle, \\ \psi_3^k &= |m_{s1} = -\frac{1}{2}, m_{s2} = +\frac{1}{2}, m_{I1}, m_{I2} \rangle, \\ \psi_4^k &= |m_{s1} = -\frac{1}{2}, m_{s2} = -\frac{1}{2}, m_{I1}, m_{I2} \rangle, \end{aligned}$$

and

$$\begin{aligned} p &= \frac{1}{2}\beta_e(g_{1zz} + g_{2zz}), \\ q &= \frac{1}{2}\beta_e(g_{1zz} - g_{2zz}), \\ c^k &= \frac{1}{2}\gamma_e(\tilde{A}_{1zz}m_{I1} + \tilde{A}_{2zz}m_{I2}), \\ f^k &= \frac{1}{2}\gamma_e(\tilde{A}_{1zz}m_{I1} - \tilde{A}_{2zz}m_{I2}). \end{aligned}$$

The eigenvalues are

$$\begin{aligned} \lambda_1^k &= pB_0 + c^k + \frac{1}{2}(D-J), \\ \lambda_2^k &= \sqrt{(\frac{1}{2}D+J)^2 + (qB_0 + f^k)^2} - \frac{1}{2}(D-J), \\ \lambda_3^k &= -\sqrt{(\frac{1}{2}D+J)^2 + (qB_0 + f^k)^2} - \frac{1}{2}(D-J), \\ \lambda_4^k &= -pB_0 - c^k + \frac{1}{2}(D-J), \end{aligned}$$

And the eigenvectors are

$$\begin{aligned}\Psi_1^k &= \psi_1^k, \\ \Psi_2^k &= a^k \psi_2^k - b^k \psi_3^k, \\ \Psi_3^k &= b^k \psi_2^k + a^k \psi_3^k, \\ \Psi_4^k &= \psi_4^k,\end{aligned}$$

with

$$\begin{aligned}a^k &= \cos \varphi^k, \\ b^k &= \sin \varphi^k, \\ \tan \varphi^k &= \frac{\frac{1}{2}D + J}{qB_0 + f^k + \sqrt{\left(\frac{1}{2}D + J\right)^2 + (qB_0 + f^k)^2}}.\end{aligned}$$

Chapter 5 High-Frequency Dynamic Nuclear Polarization Using Mixtures of TEMPO and Trityl Radicals

5.1. Introduction

In recent years dynamic nuclear polarization (DNP)^{50, 58, 59, 61, 123} has been used to address this sensitivity problem through experiments where the large spin polarization present in the electron spin reservoir is transferred to the nuclei. Most DNP experiments involve microwave irradiation of the sample at a frequency close to the electron Larmor frequency (ω_e) of endogenous¹⁵⁵ or exogenous⁵⁸ unpaired electrons coupled to nuclei which are polarized. This approach was first proposed by Overhauser⁴⁸ and implemented by Carver and Slichter^{49, 156}, and has been applied to both liquid and solid systems, usually in low magnetic fields, typically <1.4 T^{58, 67}.

In the 1980's and early 90's DNP was integrated into MAS experiments at ~1.4 T (60 MHz for ¹H and 40 GHz for e⁻) and demonstrated the advantages of enhanced sensitivity in high-resolution SSNMR^{62, 63, 109}. However, the klystron microwave technology employed in those experiments cannot be readily extended to higher frequencies, a fact that motivated us to introduce millimeter wave gyrotrons as microwave sources for high field DNP^{98, 100}. These devices are robust and provide high power (>10 W) at the high frequencies (140–460 GHz) required for contemporary NMR experiments in magnetic fields >5 T^{9, 62, 87, 89}. Since that time several high-field DNP experiments have demonstrated the utility of gyrotron microwave sources in providing enhanced NMR signals in MAS spectra. Nevertheless, further improvements in DNP

efficiency are desirable in order for the method to become widely applicable. In this chapter we discuss another approach to this goal that involves the design of polarizing agents that promote the efficiency of DNP experiments in high magnetic fields. In particular we focus on polarizing agents that optimize the cross effect polarization mechanism by satisfying the matching condition $|\omega_{2e} - \omega_{1e}| = \omega_n$ where ω_n is the nuclear Larmor frequency and $|\omega_{2e} - \omega_{1e}|$ is the frequency separation of two electrons in the EPR spectrum.

Of the four commonly discussed DNP mechanisms – the Overhauser effect (OE), the solid effect (SE), the cross effect (CE), and thermal mixing (TM)^{58, 67} – the OE is usually not important for high field experiments because the sample must contain mobile electrons and the electron–nuclear cross relaxation is inefficient since $\omega_e \tau_c > 1$, where ω_e is the electron Larmor frequency and τ_c is the correlation time for time-dependent electron–nuclear interactions. Thus, DNP in solid dielectrics usually occurs via the SE, CE, and/or TM mechanisms, which involve single, paired, and multiple electron spins during the polarization transfer from electrons to nuclei through time-independent dipolar interactions. These three mechanisms are distinguished empirically by comparing the EPR line width, δ , to the size of the nuclear Larmor frequency, ω_n . In particular, the SE dominates when $\delta < \omega_n$, whereas the CE and TM are important when $\delta > \omega_n$. The CE and TM are further differentiated by whether or not the width of the EPR spectrum is governed by inhomogeneous broadening from the g-anisotropy and electronic cross relaxation or by homogeneous broadening from the electron–electron dipolar coupling, respectively.

Early experiments that utilized DNP to enhance signals in MAS spectra relied on the

solid effect and samples containing the radical *bis*-diphenylene-phenylallyl (BDPA) which has $\delta \sim 20$ MHz^{58, 59, 61, 87, 100, 123, 157}. This approach was motivated by the view that a narrow line spectrum could be easily saturated with microwaves and therefore should facilitate optimal polarization transfer to the nuclei. However, because the SE relies on mixing of states to render the electron-nuclear transitions allowed, the enhancements scale as ω_n^{-2} . In contrast the enhancement involving the CE and TM scales as ω_n^{-1} .^{98, 100} Thus, it was established experimentally that paramagnetic species with $\delta > \omega_n$, such as the nitroxide TEMPO (2,2,6,6-tetramethylpiperidin-1-oxyl) support the TM and CE and yield substantially larger enhancements at high magnetic fields⁹⁸.

Both the CE and TM mechanisms rely on a three-spin electron–electron–nucleus process. Briefly, the microwave radiation flips an electron at ω_{1e} in the EPR spectrum that is coupled to a second electron at ω_{2e} . If the frequency separation satisfies the condition $|\omega_{2e} - \omega_{1e}| = \omega_n$ then a nuclear spin flip occurs concurrently, and the polarization of the nuclear spin reservoir is enhanced. Not surprisingly, the primary parameters that facilitate this three-spin process are the magnitude of the electron–electron dipolar coupling and the population of the electrons in the sample that satisfy the constraint $|\omega_{2e} - \omega_{1e}| = \omega_n$. To satisfy the first requirement we recently introduced biradical polarizing agents^{114, 127} in which we tethered two TEMPO molecules with a chain of carbon atoms increasing the electron-electron dipolar coupling from ~ 1 MHz to 25 MHz¹¹⁴. In order to satisfy the frequency matching condition, we rely on the fraction of molecules in the sample that have correct relative orientation of the two TEMPO moieties that fortuitously leads to the correct *g*-tensor orientations. These biradicals exhibit improved DNP efficiency, the enhancement factors are a factor of 3-4 larger than observed with TEMPO

(165 as opposed to 45), and they yield this enhancement at an electron concentration (~10 mM) that is a factor of four lower than commonly used for TEMPO (40 mM).

In this chapter we explore another approach to satisfying the frequency matching condition mentioned above. It follows from the discussion above that the ideal polarizing agent for CE DNP experiments consists of two radicals with isotropic g -values separated by $|\omega_{e1} - \omega_{e2}| = \omega_n$. At the moment we are not aware of two radicals that rigorously satisfy this condition, but using a narrow line radical such as trityl or BDPA together with TEMPO is a reasonable approximation. In the case discussed in this chapter, the pseudo-isotropic line from trityl (Figure 5.1) is separated by 225 MHz (~80 Gauss) from the g_{yy} component of the TEMPO powder pattern that contains the maximal spectral intensity. This closely matches the ^1H Larmor frequency of 211 MHz and therefore the mixture serves as an excellent polarizing agent. Note that this separation will scale with ω_n and thus will also function at higher magnetic fields. Thus we are also suggesting a new avenue for designing better polarizing agents for high-field DNP.

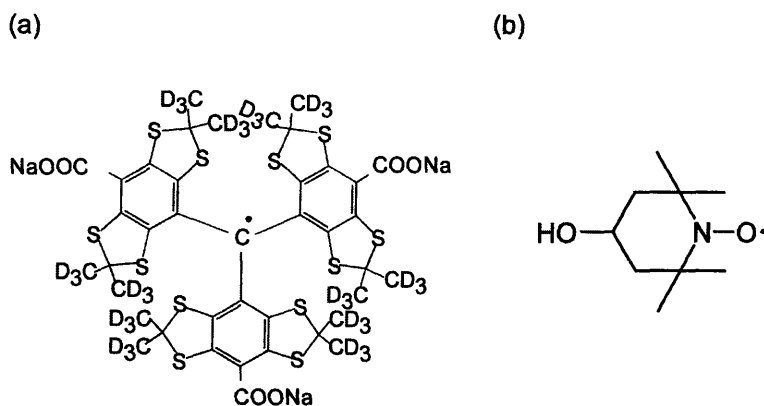


Figure 5.1. Molecular structures of (a) the trityl radical (molecular weight = 1080), which has principal g -values of $g_{xx} = 2.0034$, $g_{yy} = 2.0031$, and $g_{zz} = 2.0027$ ³, and (b) the 4-hydroxy-TEMPO radical (molecular weight = 172), which has principal g -values of $g_{xx} = 2.0090$, $g_{yy} = 2.0061$, and $g_{zz} = 2.0021$, and principal hyperfine A -values (^{14}N) of $A_{xx} = 6.63$ G, $A_{yy} = 6.75$ G, and $A_{zz} = 36.63$ G⁸.

5.2. Experimental Section

The symmetric trityl radical was a gift of K. Golman and J. Ardenkjær-Larsen of Nycomed Innovation AB (now GE Healthcare, Malmö, Sweden); a synthesis of one version of the molecule was recently described in the literature⁹⁶. 4-hydroxy-TEMPO (97% free radical) was purchased from Sigma–Aldrich (St. Louis, MO). EPR samples (~0.4 μL) with 1 mM radicals were prepared in a $^2\text{H}_6$ -DMSO/ $^2\text{H}_2\text{O}$ 60:40 w/w solution and loaded into a synthetic quartz (Suprasil) capillary with 0.40 I.D. and 0.55 O.D. (Wilmad) for cryogenic EPR spectroscopy.

DNP samples with 10 to 40 mM TEMPO or trityl or a mixture of the two (50/50 mole ratio) were prepared in a frozen $^2\text{H}_6$ -DMSO/ $^2\text{H}_2\text{O}$ / H_2O 60:34:6 w/w solution with 2 M ^{13}C -urea. The high concentration of ^{13}C -urea ensures accurate measurements of the NMR signals in the absence of a DNP enhancement. Partial deuteration increases the

bulk DNP enhancement by reducing the ^1H spin concentration, but not to the point where ^1H - ^1H spin diffusion is attenuated. The samples ($\sim 25\ \mu\text{L}$) used for the DNP experiments were center-packed into a 4 mm O.D. sapphire rotor. To prevent mechanical instability associated with thermal contraction of the vespel drive tip at 90 K, a small groove was machined into the drive tip, and it was bonded to the sapphire rotor using a low-temperature epoxy (Hysol, Dexter, CA). Details of DNP-CPMAS experiments had been described in the previous chapter.

5.3. Results

The upper traces of Figure 5.2 show the echo-detected EPR spectra (normalized) of 1 mM trityl, 1 mM TEMPO and a mixture of 0.5 mM trityl and 0.5 mM TEMPO in frozen $^2\text{H}_6\text{-DMSO}/^2\text{H}_2\text{O}$ 60:40 w/w solutions. The EPR spectra corresponding to the frequency of the gyrotron (139.66 GHz) was obtained from shifting the recorded spectra (at 139.50 GHz) along the field axis by 57 G (160 MHz). The EPR spectrum of trityl had a peak at 49815 G and a line width (δ) of 15 G (42 MHz), reflecting the small axial asymmetry of the g -anisotropy at the radical center. Note the fact that the spectrum is not axially symmetric indicates that there is less than threefold symmetry at the central carbon. In contrast, TEMPO yielded a broad EPR line shape resulting from both g -anisotropy and anisotropic hyperfine interaction with the ^{14}N ($I = 1$) nucleus. The EPR spectrum, corresponding to 139.66 GHz irradiation, has a maximum at 49735 G, spanning 220 G (or 616 MHz) and featured three hyperfine steps on the high-field edge.

The lower panels of Figure 5.2 show the field-dependent ^1H enhancement profiles with 40 mM trityl radical, 40 mM TEMPO radical, and a 40 mM mixture of 50:50

trityl/TEMPO, respectively. Trityl, with δ (27 MHz) $<$ ω_n (211 MHz for ^1H), leads to a SE polarization mechanism and well-resolved maxima and minima in the ^{13}C detected ^1H enhancements at 49891 and 49740 G, respectively. These field positions were ± 75 G (or ± 212 MHz, the ^1H Larmor frequency) from the EPR peak. The maximum ^1H enhancement from trityl was ~ 15 , which is relatively small and consistent with the ω_n^{-2} dependence of the SE enhancement. In contrast TEMPO has $\delta > \omega_n$ and this leads to the TM mechanism dominating the polarization process with maximum positive and negative ^1H enhancements at 49798 and 49683 G, or ± 161 MHz rather than $\omega_e \pm \omega_n$. As can be seen from the figure the maximum ^1H enhancement from TEMPO was ~ 55 , almost fourfold higher than that with trityl.

As expected, the ^1H enhancement profile changed drastically when half of the 40 mM TEMPO radicals were replaced by trityl. This sample yielded an even larger enhancement of ~ 162 , which is a threefold higher than with pure TEMPO. The positive enhancement peak was located at 49815 G, corresponding to the EPR peak of trityl. A smaller negative enhancement peak was found at 49740 G, corresponding to the EPR peak of TEMPO. The displacement of 76 G between the positive and negative enhancement peaks matched the ^1H Larmor frequency and is consistent with the CE mechanism. The field-dependent enhancement profiles for the SE and TM were simulated based on published theory^{58, 125, 158}, and details of the calculations of the CE enhancements are discussed below.

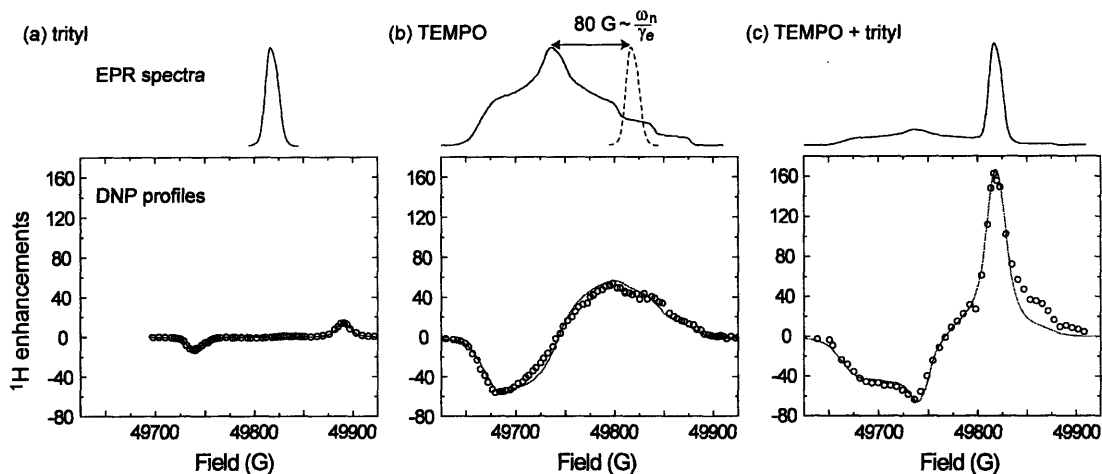


Figure 5.2. The pulse-echo-detected EPR spectra (upper traces) and proton DNP enhancement profiles (lower panels) at 139.66 GHz measured from (a) trityl (b) TEMPO and (c) TEMPO and trityl mixture (50:50). The EPR spectra represented a total radical concentration of 1 mM in frozen $^2\text{H}_6$ -DMSO/ $^2\text{H}_2\text{O}$ 60:40 w/w solutions at 20 K, whereas the DNP profiles were obtained from a total radical concentration of 40 mM in frozen $^2\text{H}_6$ -DMSO/ $^2\text{H}_2\text{O}/\text{H}_2\text{O}$ 60:34:6 w/w/w solutions at 90 K. The enhancement profiles are characteristic of the SE, TM, and CE mechanisms with paramagnetic species of trityl, TEMPO, and the mixture, respectively. The red line is a simulation of the experimental data.

Figure 5.3 illustrates the growth of the ^{13}C detected enhanced ^1H polarization during microwave irradiation at the optimal magnetic field (49815 G). The NMR signal intensity grows exponentially with a time constant, $\tau_{\text{DNP}} \sim 5 \text{ s}$ and a steady-state ^1H signal enhancement, $\epsilon = 162 \pm 20$. The random error arises from the low sensitivity of measurements conducted without DNP, which are required to calculate the DNP enhancement.

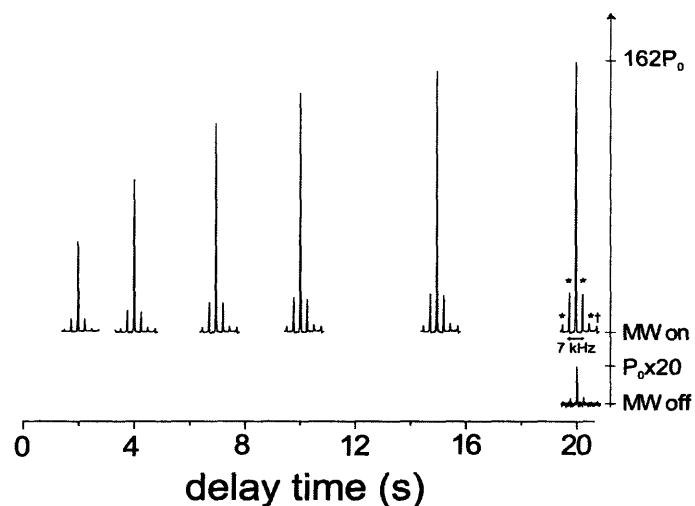


Figure 5.3. Buildup of the DNP-CPMAS ^{13}C -NMR signals of ^{13}C -urea with 40 mM 50:50 TEMPO/trityl mixtures after various delays of microwave irradiation (139.66 GHz, ~ 1.5 W) at 49815 G. The asterisks indicate the spinning sidebands and the dagger marks the solvent peak. The growth of nuclear polarization features a time constant of ~ 5 s and indicates the ^1H enhancement of 162 ± 20 .

Figure 5.4 illustrates the influence of the total electron concentration ($[\text{TEMPO}] + [\text{trityl}]$) on the DNP enhancement with 50:50 TEMPO/trityl mixtures at the magnetic field corresponding to the maximum enhancement. Not unexpectedly, the size of ϵ increases with the radical concentration, while the value of τ_{DNP} decreases. Beyond ~ 40 mM of radicals, the resulting paramagnetic broadening begins to eliminate a substantial number of the nuclei from observation, as evidenced by the attenuation of unenhanced NMR signals.

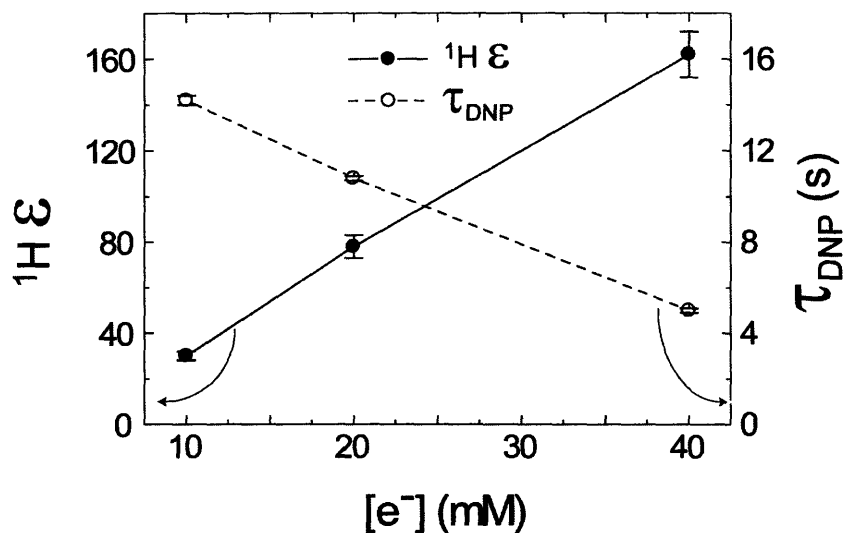


Figure 5.4. Radical concentration dependence of the measured proton enhancement ($^1\text{H } \epsilon$) and buildup time constant (τ_{DNP}) from the 50:50 TEMPO/trityl mixture at 49815 G and 90 K.

5.4. Discussion

The polarization mechanisms that dominate DNP processes in insulating solids—the SE, TM, or the CE—depends on the EPR line width of the paramagnetic species relative to the Larmor frequency of the nuclei being polarized. This behavior is well established in many previous experiments^{58, 67, 98} and is illustrated again in Figure 5.2. In general, the SE dominates when $\delta < \omega_n$ (e.g., with trityl) and in samples where the EPR spectral width $\delta > \omega_n$ (TEMPO, biradicals and TEMPO/trityl mixtures) the TM and CE provide the polarization mechanism. The TM and CE mechanisms are further distinguished by whether the EPR spectrum is broadened by homogeneous or inhomogeneous interactions, respectively. The polarizing mechanism with TEMPO is thought to be TM or the CE depending on the radical concentration used. Although TEMPO presents an

inhomogeneously broadened EPR spectrum at high fields, the electron dipolar bath for TM can be established via electron–electron cross-relaxation at high radical concentrations used in DNP experiments¹²⁵. In contrast, low TEMPO concentrations should limit the polarizing mechanism to the CE. For both the CE and TM, the required EPR frequency separation $|\omega_{2e} - \omega_{1e}| = \omega_n$ is satisfied when the g-tensor orientations of two dipolar coupled molecules in the sample randomly have the correct mutual orientations.

Our^{62, 98, 100} and other⁵⁸ experiments have demonstrated that in high magnetic fields (>5T) the TM and CE mechanisms are more efficient than the SE and that the two class of mechanisms scale approximately as ω_0^{-1} and ω_0^{-2} , respectively. They also depend on the available microwave power and the electronic and nuclear relaxation times; consequently, high field DNP experiments employ high microwave powers available from gyrotron sources and are conducted at cryogenic temperatures, where the relaxation times are longer. In principle, EPR frequency separations can be manipulated by controlling the orientations and principal values of the g-tensors of the dipolar coupled electrons. While the control of orientations is straightforward in single crystal systems, it is impossible to control orientation in powder samples where the relative orientation of g-tensors is a function of crystallite orientation. However, using mixtures of two radicals with maxima in their EPR spectra that correspond to the correct frequency separation is another approach to satisfying the CE matching condition. Thus, mixtures of TEMPO and trityl yield large improvements in the DNP ϵ since the desired g-value difference is achieved by the fact that one radical species with a small g-anisotropy and therefore a sharp EPR line is separated from the g_{yy} maxima in the TEMPO powder spectrum by the

proper frequency.

The increase in ϵ with increasing concentration of TEMPO/trityl mixtures shown in Figure 5.4 illustrates the other requirement for an efficient three-spin process; in particular, the average electron–electron dipole interaction needs to be strong for efficient DNP and it is reduced by the larger inter-radical distance that accompanies dilution. In the contrasting regime – at a higher radical concentration – the electron–nuclear paramagnetic broadening will not only reduce the resolution of NMR spectra, but will also diminish the number of observable nuclear spins, and therefore decrease the overall signal intensity. The electron–electron interactions at a low radical concentration could be optimized by chemically linking TEMPO and trityl radicals. The use of molecular linkers has proven successful for increasing the CE enhancement with two tethered TEMPO moieties from ~50 to ~165-290 depending on the experimental circumstances^{114, 127}. Therefore, additional improvement of the DNP enhancement beyond the current maximum value of 162 observed with trityl/TEMPO mixtures is expected when these two species are successfully coupled.

The simulation of field-dependent CE enhancements (Figure 5.2c) was performed on the basis of microscopic interactions of the dipolar coupled electron and nuclear spins. The spin Hamiltonian includes spin-lattice interactions and spin interactions involving g -, hyperfine- and dipolar-tensors, which are functions of molecular orientations with respect to the external magnetic field and yield DNP through microwave-driven spin dynamics that will be discussed in Chapter 6. Prior to the CE simulation, the separation of the enhancements arising from TEMPO/trityl (20 mM/20 mM) pairs from the background enhancements due to coexisting TEMPO pairs (20 mM) reveals asymmetric intensities of

positive and negative enhancements, which are separated by the ^1H Larmor frequency and characterize the CE mechanism. Different sizes of the DNP enhancements generated by the EPR excitations of the radical-pair components can be explained by the non-uniform T_{1e} associated with the coupled radicals. This T_{1e} effect on DNP profiles is illustrated by the spin dynamics in an isolated electron–electron–nucleus system. Further, although treatments of the SE and TM mechanisms with microscopic details are feasible, these mechanisms are generally understood with classical DNP theories^{58, 125} that consider macroscopic thermodynamic properties of ensemble spins.

The ideal polarizing agent for the CE consists of two dipolar coupled electrons with narrow EPR spectra separated by ω_n . The CE from a broad inhomogeneous EPR spectrum may be attenuated by cancellation between electron pairs with EPR frequency separations of ω_n and $-\omega_n$, similar to the attenuation that occurs in the differential solid effect⁷⁸. This differential effect limits the average DNP enhancement produced by participating electrons. In addition, because the microwave irradiation occurs at a fixed frequency and has a finite bandwidth, only a portion of the electrons under the broad EPR line shape participate in the CE process; the remainder contribute to paramagnetic nuclear relaxation and broadening. Combining TEMPO and trityl as the polarizing agent partially resolves the problems with differential CE enhancements and with non-participating radicals. Despite the broad EPR spectrum of TEMPO, the trityl resonance in the upfield part of the EPR spectrum of TEMPO caused the electron pairs to yield positive CE enhancements. Moreover, the narrow EPR line width of trityl increases the effectiveness of the microwave excitation at the trityl EPR transitions.

The choice of radical pairs that provide the desired EPR frequency separation for the

CE is not limited to TEMPO and trityl, especially when a nuclear Larmor frequency different from ^1H is involved. For example, a hyperfine splitting (^{13}C , ^{15}N , ^{14}N , etc) could result in two narrow lines and the external magnetic field could be adjusted to match a nuclear Larmor frequency to this separation. However, hyperfine splittings are field independent so polarizing agents designed in this manner would be specific to a particular field and nucleus. In contrast, matching the nuclear Larmor frequency through g-value differences is independent of the external magnetic field and presents the possibility of an efficient, universal polarizing agent.

5.5. Conclusion

In Chapter 3 and 4 we have shown that tethering two nitroxides increases the dipolar coupling between two electron spins and leads to a more efficient polarizing agent for DNP experiments. This chapter has demonstrated a second important approach to the design of an efficient polarizing agent. In particular we have shown that the frequency separation between the pseudo isotropic g-value of trityl and the g_{yy} component of the TEMPO powder pattern matches the nuclear Larmor frequency and provides a significant improvement in the efficiency of DNP at high-field. This approach to optimizing the EPR frequency separation is easier to achieve than constraining the relative g-tensor orientations of the two electrons. Ultimately the optimal DNP polarizing agent will utilize both of these approaches to achieve both a correct EPR frequency separation and a strong electron–electron dipolar interaction. Synthetic efforts to tether different radical moieties with an EPR frequency separation that matches the nuclear Larmor frequency will be the topic of a future discussion.

Chapter 6 Quantum Mechanical Theory of Dynamic Nuclear Polarization in Solid Dielectrics

6.1. An Analytical Approach

6.1.1. Introduction

DNP experiments involve high power microwaves^{9, 62, 89} excitation near the electron Larmor frequency ω_e and low experimental temperatures to increase the relaxation times. In addition, an efficient polarizing mechanism is essential for successful high-field DNP experiments. Recently we demonstrated that biradicals – in particular two TEMPO molecules tethered by a short linker – are efficient polarizing agents. The short tether increases the electron–electron dipolar coupling from ~1 MHz in a 40 mM solution of TEMPO to about 25 MHz, and therefore is a new approach that facilitates the cross effect polarization mechanism at high magnetic fields^{114, 127}. Thus, the purpose of this sub-chapter is to present a formalism that will enable understanding and improvement of the above DNP experiments at high magnetic fields.

In the existing literature DNP processes are usually treated using equations of motion that relate macroscopic quantities which are averaged over an ensemble of spins^{50, 56, 58, 67}. These quantities are either measurable parameters or parameters that can be fitted and describe thermodynamic baths, including the electron and nuclear Zeeman and the electron spin-spin bath which is assumed to be homogeneously coupled via the electron–electron dipolar interaction. However, at high magnetic fields and low radical concentrations, the g-anisotropy is large and the electron-electron dipole coupling is

small; thus the electron spin reservoir is inhomogeneously broadened. Therefore, classical descriptions of polarizing mechanisms are less appropriate in high-field DNP experiments with dilute radical concentrations. In this situation, a microscopic description of polarization transfer between the paramagnetic polarizing species and a coupled nucleus potentially provides more insight into the mechanism whereby a chosen biradical improves the observed DNP enhancement factors as discussed in Chapters 3-5. Such a microscopic picture can be derived from the quantum dynamics calculations presented here.

Polarizing mechanisms for DNP in solid dielectrics include the solid effect (SE)⁵⁰, the cross effect (CE)^{51-55, 106}, and thermal mixing (TM)^{58, 67}. From an experimental perspective, they are distinguished first by comparing the EPR linewidth, δ , of the paramagnetic polarizing species with the nuclear Larmor frequency, ω_n . When $\delta < \omega_n$ then the SE dominates the polarization process and the enhancement maximum and minimum are observed with the microwave irradiation frequencies at $\omega_e \pm \omega_n$. In the opposite limit, when the EPR spectrum is broad compared to the nuclear Larmor frequency, $\delta > \omega_n$, the larger linewidth enable the CE or TM to emerge as the dominant mechanisms. These two mechanisms are further distinguished by whether the EPR spectrum is inhomogeneously or homogeneously broadened, respectively. With respect to the microscopic physics, the number of electrons involved in a polarizing mechanism – one, two, or multiple electrons – characterizes the SE, the CE or TM. For example, the two unpaired electrons associated with the two radical moieties of a biradical¹¹⁴ correspond to the two electrons required for the CE. Thus, the spin dynamics of an electron–electron–nucleus system can be used to understand the functions of a biradical

in DNP. Further, in the limit that the two electron transitions are degenerate and the spectrum is narrow, then the three-spin system reduces to the SE which requires only a single electron-nucleus spin interaction. Finally, TM depends on the presence of a strongly coupled multiple electron spin system that can be viewed as an extension of the three-spin system. However, to simplify the framework of our description of DNP, we focus in the following sections on the SE and the CE, which together provide an interesting comparison of the difference in the efficiency between single- and double-electron polarizing agents.

Elegant quantum mechanical descriptions of an electron–nucleus system ¹⁵⁹ and an electron–electron–nucleus system ¹⁶⁰ have appeared previously in connection with a description of spin correlated radical pairs and CIDNP experiments. However, that discussion was concerned primarily with effects at low magnetic fields, and the effect of larger nuclear Zeeman interactions on DNP was not emphasized. In that case treatment of a two-spin Hamiltonian was used to understand microwave-excited electron-nuclear transitions that lead to enhancements of nuclear polarization via the SE. Further, calculations with a three-spin Hamiltonian provided not only an understanding of the generation of nuclear coherences with spin-correlated radical pairs, but also illustrated how DNP was possible from the transient electron polarization ⁷³. However, the microwave-driven DNP in the three-spin model was derived only through intricate transformations of basis-sets. Thus, in this sub-chapter we examine an alternative and systematic approach that focuses on DNP phenomena occurring with microwave irradiation at high magnetic fields and low radical concentrations.

Our theoretical work is aimed at clarifying the frequency matching conditions for

the SE and the CE, and at evaluating the time-dependent growth of the nuclear polarization during microwave irradiation. In practice, the polarizing mechanisms in DNP experiments involve an ensemble of electron and nuclear spins. However, a simplified spin system for discussion of polarization transfers is feasible. In Section 6.1.2.1, we first rationalize a localized spin system that is isolated from the bulk nuclear spin system with dilute electron concentrations and containing one or two electron spins and one nuclear spin. In Section 6.1.2.2 and Section 6.1.2.3, we calculate the evolution of the density matrix in a diagonalized frame for an electron–nucleus two-spin system and an electron–electron–nucleus three-spin system. The DNP phenomenon is in fact an evolution of electron Zeeman order to nuclear Zeeman order. Thus, we describe the systematic analytical diagonalization of multispin Hamiltonians and the following extraction of the effective microwave operators that transfer the electron Zeeman operators to the nuclear Zeeman operator. In Section 6.1.3 we summarize and compare the influences of microwave fields and external magnetic fields on the SE and the CE.

6.1.2. Theory

6.1.2.1. Polarization transfer in a spin system

DNP involves polarization transfer between the electron and nuclear spin-systems which are in contact with a lattice. The physics of DNP is governed by the following Hamiltonian:

$$H = H_S + H_{SS} + H_I + H_{SI} + H_{II} + H_M + H_{SL} + H_{IL} + H_L, \quad (1)$$

where H_S and H_I are the Zeeman Hamiltonians of the electron spins S and nuclear spins I ,

H_{SS} , H_{SI} and H_{II} describe the isotropic and anisotropic electron-electron and the electron-nuclear couplings, H_M accounts for the microwave excitation, H_{SL} and H_{IL} are the spin-lattice interactions, and H_L is a generalized lattice interaction. The important terms in the Hamiltonian for DNP are H_S , H_I , H_{IS} , and in some cases, H_{SS} . Further, in practical conditions of diluted electron concentration, H_{II} mediates the propagation of enhanced nuclear polarization throughout the bulk nuclei. Concurrently, the coupling of the electron and nuclear relaxation due to H_{SL} , H_{IL} and H_L , regulate the efficiency of polarization transfer in DNP.

Figure 6.1 is a schematic representation of polarization transfer in a DNP experiment. The electron spin polarization is initially transferred to a strongly coupled nucleus residing outside a diffusion barrier (Region B). It subsequently propagates throughout the bulk nuclei (Region A) via homonuclear spin diffusion. Note that nuclear spins inside the diffusion barrier, which typically covers a region within $\sim 3 \text{ \AA}^{161}$ from an unpaired electron, are effectively isolated from the bulk nuclear spin diffusion by the strong electron-nuclear coupling. In particular, the electron-nuclear couplings shift the resonances of the near neighbor nuclei ¹⁶¹, ¹⁶² so that they do not interact with the bulk nuclear spins. Thus, the DNP process involves electron spins and a nuclear spin immediately outside Region B. To simplify the quantum mechanical calculations we limit the size of spin system, and discuss the approximations required for focusing on polarization transfers involving the terms H_S , H_{SS} , H_I and H_{IS} which are combined into H_0 is the following derivations.

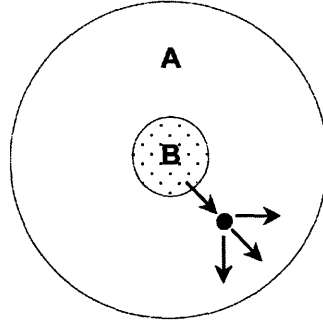


Figure 6.1. A model of polarization transfers in DNP. Region A represents the observable bulk nuclei. Region B represents the paramagnetic center and nuclei within the diffusion barrier. The electron polarization is transferred to a nuclear spin with the strongest hyperfine interaction outside region B and then propagated throughout the bulk nuclei via homonuclear spin diffusion.

Projection of the macroscopic DNP onto a microscopic polarization transfer

Efficient nuclear spin diffusion is assumed to uniformly distribute the enhanced polarization among the bulk nuclei, so that the nuclear polarization in a localized spin system can represent the polarization of bulk nuclei during a reduced time scale t' :

$$t' \equiv \frac{N_e}{N_n} t, \quad (2)$$

where N_e and N_n are the numbers of polarizing paramagnetic centers and observable nuclei (usually $N_n \gg N_e$), respectively. For spin diffusion on a reduced time scale, the effective nuclear longitudinal relaxation time, T'_{1n} , is much less than the intrinsic nuclear spin-lattice relaxation time T_{1n}^x . Under spin-lattice relaxation, the enhanced bulk nuclear polarization develops exponentially to a steady-state enhancement ϵ_{ss} with the time constant τ'_{DNP} which depends on microwave excited transition probability for DNP. The

growth of enhanced polarization of bulk can be described by

$$\frac{dP(t)}{dt} = \frac{1}{\tau'_{DNP} \cdot \frac{N_n}{N_e}} [(\epsilon_{ss} + 1)P_0 - P(t)] - \frac{1}{T_{1n}^x} (P(t) - P_0), \quad (3)$$

where $P(t)$ and P_0 are the bulk nuclear polarization at time t and at thermal equilibrium, respectively, ϵ_{ss} and τ'_{DNP} are the steady-state enhancement and buildup time constant on the reduced time scale, and T_{1n}^x is the intrinsic nuclear spin-lattice relaxation time. In the steady-state, $dP(t)/dt = 0$, the enhancement of bulk nuclei E_{ss} becomes

$$E_{ss} \equiv \frac{P_{ss}}{P_0} - 1 = \frac{1}{1 + \frac{\tau'_{DNP}}{T_{1n}} \cdot \frac{N_n}{N_e}} \epsilon_{ss}. \quad (4)$$

The microscopic ϵ_{ss} results from the microwave-excited electron-nuclear transitions that can be discussed in the eigen basis-sets of the Hamiltonian H_0 of a spin system composed of electron spins with $S_i=1/2$ and a nuclear spin with $I=1/2$. Specifically, H_0 is

$$H_0 = \sum_i \omega_{ei} S_{iz} + \sum_{i,j>i} [d_{ij} (3S_{iz} S_{jz} - \mathbf{S}_i \cdot \mathbf{S}_j) - 2J_{ij} \mathbf{S}_i \cdot \mathbf{S}_j] - \omega_n I_z + \sum_i (A_i S_{iz} I_z + B_i S_{iz} I_x), \quad (5)$$

where ω_{ei} and ω_n are the Larmor frequencies of the electrons and nucleus, d_{ij} and J_{ij} are the dipolar interaction and exchange integral, respectively, between electron spin i and j , A_i and B_i are the coefficients of secular and semisecular terms of the hyperfine interactions, respectively. Note that both the electron–electron and electron–nuclear dipolar interactions are truncated by the high EPR frequency, and that J_{ij} is an isotropic

quantity whereas d_{ij} depends on the orientation of the dipolar vector as

$$d_{ij} = \frac{\omega_d^{ij}}{2}(1 - 3\cos^2 \mu_{ij}), \quad (6)$$

where ω_d^{ij} is the electron–electron dipolar coupling constant, and μ_{ij} is the angle between the dipolar vector and the external magnetic field. Note that $S_{iz}I_x$ are sufficient to describe the semisecular terms after a rotation of the spin operator along $S_{iz}I_z$. The orientation dependence of the hyperfine interaction is ignored, and instead A_i and B_i are treated as average quantities for a randomly oriented powder sample. In addition, the Hamiltonian of microwave field H_M for DNP is defined as

$$H_M \equiv 2\omega_1 \cos(\omega_M t) \sum_i S_{ix}, \quad (7)$$

where the ω_M and ω_1 are the frequency and strength of microwave irradiation, respectively.

The electron–nucleus transitions are determined by expressing H_M in the eigen basis-sets (EBS) of H_0 . They can be further selected as effective Hamiltonians by ω_M to interact with the density operator to generate enhanced nuclear polarization. The density operator evolves according to the Liouville-von Neumann equation ($\hbar = 1$) as

$$\frac{d}{dt} \tilde{\rho}^* = -i[\tilde{H}_M^{eff*}, \tilde{\rho}^*], \quad (8)$$

where $\tilde{\rho}^*$ and \tilde{H}_M^{eff*} are the density operator and the effective microwave Hamiltonian,

respectively, in the eigen basis-sets (tilde) and the interaction frame (asterisk) that is defined by ω_M . The time-independent \tilde{H}_M^{eff*} leads to time-evolution of $\tilde{\rho}^*$ in the usual manner

$$\tilde{\rho}^*(t) = \exp(-it\tilde{H}_M^{eff*})\tilde{\rho}_0^* \exp(it\tilde{H}_M^{eff*}). \quad (9)$$

DNP mechanisms in solid dielectrics are distinguished by the number of electrons involved in Eq. 5. The known SE, CE and TM polarizing mechanisms transfer polarization from single, pair and multiple electron spins, respectively, to the dipolar coupled nuclear spin as are illustrated in Figure 6.2 where the energy level diagrams appropriate for the $S_i=I=1/2$ basis functions $|\alpha_{S_i}\rangle, |\beta_{S_i}\rangle, |\alpha_I\rangle, |\beta_I\rangle$ are drawn. The SE arises from single electron–nuclear interaction, and the DNP and electron–nucleus double resonance (ENDOR) transitions excited by the microwave field (indicated as dashed arrows in Figure 6.2a) that become allowed are due to a mixing of the states $|1\rangle$ and $|3\rangle$ and a mixing of the states $|2\rangle$ and $|4\rangle$ by semiseccular hyperfine interactions. Double-quantum (flip-flip) and zero-quantum (flip-flop) transitions occur between states $|1\rangle$ and $|4\rangle$ and $|2\rangle$ and $|3\rangle$. The mixing factor that describes the probabilities of the above transitions is proportional to ω_n^{-2} as it arises from a second order perturbation with respect to spin interactions. Thus, the efficiency of the SE scales with B_0^{-2} , where B_0 is the external magnetic field.

In the case of the CE (Figure 6.2b) there are two participating electrons – S_1 and S_2 – and a single nuclear spin I , and there are now eight energy levels to consider. Microwave transitions occur between the levels connected with the dashed lines and occur due to

mixing of the states $|2\rangle$ and $|7\rangle$, or a mixing of the states $|3\rangle$ and $|6\rangle$ if $\gamma_n < 0$. The mixing results from electron–electron and electron–nucleus interactions and becomes important when the degeneracy is provided by the frequency matching condition $|\omega_{e1} - \omega_{e2}| \approx \omega_n$. The frequency matching mentioned here implies electron–electron interactions (~ 25 MHz) that are weaker than the EPR frequency separation due to inhomogeneous interactions such as g - and hyperfine-anisotropies (≥ 600 MHz). However, stronger electron–electron interactions are possible and lead to a different regime of frequency matching, in which the dipolar or hyperfine couplings approximate ω_n . We briefly discuss this strong electron–electron coupling regime for the CE in Appendix I as it is not of our primary interest.

TM shares many features with the CE but is due to the coupling of multiple, rather than two, electrons in the paramagnetic center. Weak couplings among those electrons produce manifolds of states illustrated in Figure 6.2c. Similar to the frequency matching condition in the CE, the energy overlap between manifolds is required for maximizing the probabilities of electron–nuclear transitions. Since the TM is related to the CE, our calculations are focused on the SE and the CE and are aimed at understanding the important parameters that can be controlled to improve DNP in high magnetic fields.

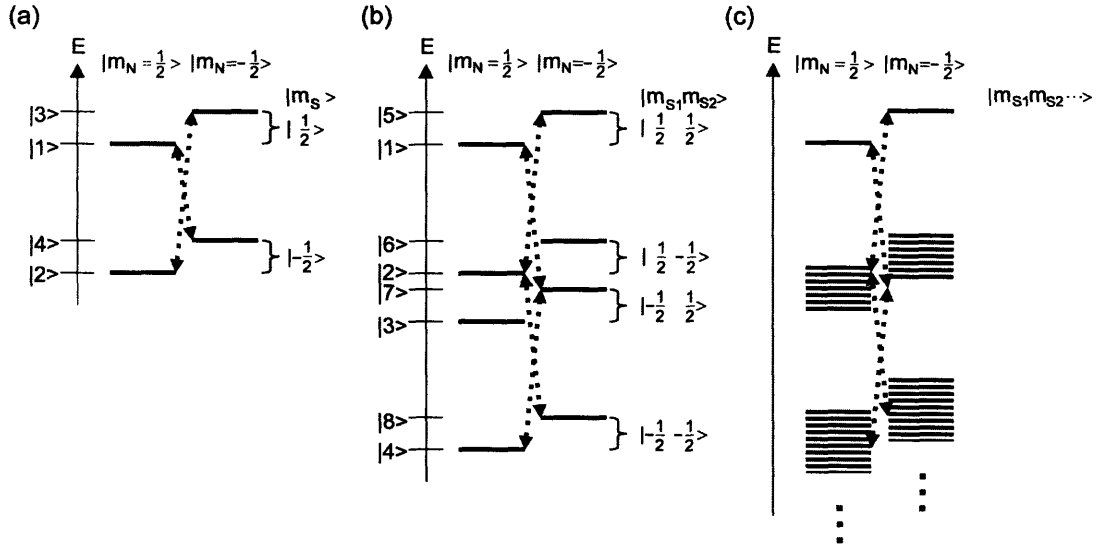


Figure 6.2. Quantum mechanical pictures of the electron-nuclear transitions (dash arrows) in (a) the SE, (b) the CE and (c) TM mechanisms, which involves single, pair and multiple electron spins, respectively. Note that the probabilities of electron-nuclear transitions are always small in the SE but could be large in the CE and TM with a degeneracy between the states with alternating nuclear spin quantum numbers.

6.1.2.2. The SE in an electron–nucleus spin system

The SE is based on polarization transfer between a single electron and nuclear spin described by the time-independent Hamiltonian (simplified from Eq. 5)

$$H_0^{en} = \omega_{e1} S_{1z} - \omega_n I_z + A_1 S_{1z} I_z + B_1 S_{1z} I_x, \quad (10)$$

that can be represented in the product spin bases (PSB) shown in Figure 6.3.

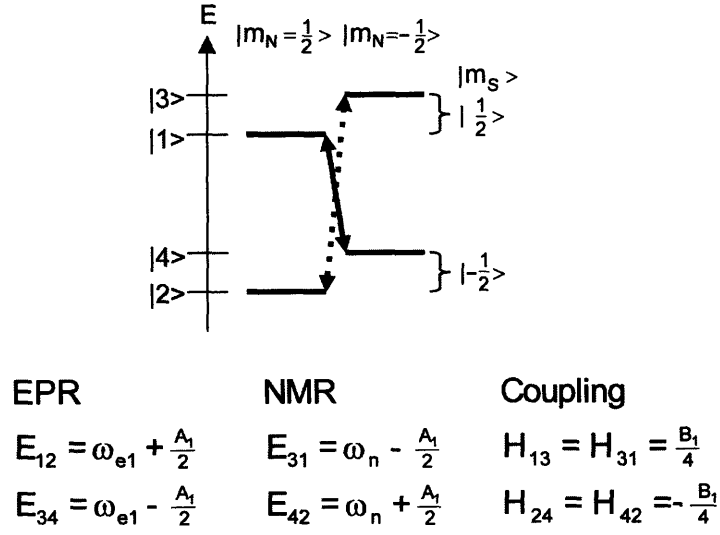


Figure 6.3. A level diagram of an electron-nucleus system. Transition energies of EPR/NMR and couplings between product spin states are calculated to the first order. The DNP transitions leading to positive and negative enhancements are indicated by the solid and dashed arrows, respectively. Note that $E_{ij} = E_i - E_j$ and $H_{ij} = \langle i | H | j \rangle$.

Diagonalization of a two-spin Hamiltonian

The H_0^{en} is diagonalized to \tilde{H}_0^{en} by a unitary transformation as

$$\tilde{H}_0^{en} = U_\eta H_0^{en} U_\eta^{-1}. \quad (11)$$

The propagator U_η is

$$U_\eta = \exp\left[i\left(\eta_\alpha S_1^\alpha I_y + \eta_\beta S_1^\beta I_y\right)\right], \quad (12)$$

where the scalar components ($-\pi/2 < \eta_\alpha$ and $\eta_\beta < \pi/2$) satisfy

$$\tan \eta_\alpha = \frac{B_1}{A_1 - 2\omega_n}, \quad \tan \eta_\beta = \frac{B_1}{A_1 + 2\omega_n}. \quad (13)$$

The operator components of U_η which correspond to two subspaces in the PSB (Figure 6.3) are defined as

$$\begin{aligned} S_1^\alpha &\equiv \frac{1}{2}E + S_{1z}, \text{ for the subspace } \{|1\rangle, |3\rangle\}, \\ S_1^\beta &\equiv \frac{1}{2}E - S_{1z}, \text{ for the subspace } \{|2\rangle, |4\rangle\}. \end{aligned} \quad (14)$$

Following Eqs. 11 and 13, the time-independent electron–nuclear Hamiltonian becomes

$$\begin{aligned} \tilde{H}_0^{en} &= \omega_{e1}S_{1z} + S_1^\alpha [(-\omega_n + \frac{1}{2}A_1)(I_z \cos \eta_\alpha - I_x \sin \eta_\alpha) \\ &\quad + \frac{1}{2}B_1(I_x \cos \eta_\alpha + I_z \sin \eta_\alpha)] \\ &\quad + S_1^\beta [(-\omega_n - \frac{1}{2}A_1)(I_z \cos \eta_\beta - I_x \sin \eta_\beta) - \frac{1}{2}B_1(I_x \cos \eta_\beta + I_z \sin \eta_\beta)], \end{aligned} \quad (15)$$

whose off-diagonal terms disappear due to the relationships in Eq. 13. After rearranging the diagonal terms in Eq. 15, the diagonalized electron-nucleus Hamiltonian in the eigen basis-sets (EBS) becomes

$$\tilde{H}_0^{en} = \omega_{e1}S_{1z} - \tilde{\omega}_n I_z + \tilde{A}_1 S_{1z} I_z, \quad (16)$$

where the coefficients are

$$\tilde{\omega}_n = \frac{1}{2}\omega_n(\cos \eta_\alpha + \cos \eta_\beta) - \frac{1}{4}A_1(\cos \eta_\alpha - \cos \eta_\beta) - \frac{1}{4}B_1(\sin \eta_\alpha - \sin \eta_\beta), \quad (17a)$$

$$\tilde{A}_1 = -\omega_n(\cos \eta_\alpha - \cos \eta_\beta) + \frac{1}{2}A_1(\cos \eta_\alpha + \cos \eta_\beta) + \frac{1}{2}B_1(\sin \eta_\alpha + \sin \eta_\beta). \quad (17b)$$

Representing the microwave Hamiltonian in the EBS

The microwave Hamiltonian in the PSB and the laboratory frame is

$$H_M = 2\omega_1 S_{1x} \cos(\omega_M t), \quad (18)$$

which is transformed from the PSB to the EBS by the same propagator U_η (Eq. 12) as

$$\tilde{H}_M = 2\omega_1 \cos(\omega_M t) U_\eta S_{1x} U_\eta^{-1}. \quad (19)$$

Subsequently,

$$\begin{aligned} \tilde{H}_M = \omega_1 \cos(\omega_M t) \{ & S_{1x} \cos \frac{\eta_\alpha - \eta_\beta}{2} \\ & - \frac{1}{2} (S_1^+ I^- + S_1^- I^+) \sin \frac{\eta_\alpha - \eta_\beta}{2} + \frac{1}{2} (S_1^+ I^+ + S_1^- I^-) \sin \frac{\eta_\alpha - \eta_\beta}{2} \}. \end{aligned} \quad (20)$$

To obtain Eq. 20 more easily, one can rewrite the propagator U_η (Eq. 12) as

$$U_\eta = \exp[i(\eta_\alpha - \eta_\beta) S_{1z} I_y + \frac{i}{2}(\eta_\alpha + \eta_\beta) I_y]. \quad (21)$$

Note that the second term in Eq. 21 does not affect S_{1x} in the microwave Hamiltonian.

In Eq. 20, either the zero quantum term, $S_1^+ I^- + S_1^- I^+$, or the double quantum term, $S_1^+ I^+ + S_1^- I^-$, of \tilde{H}_M mediates the DNP process. The selection of those terms is made by matching the microwave frequency ω_M with the oscillation frequency of each term of \tilde{H}_M in the interaction frame of \tilde{H}_0^{en} (see Eq. 16). For this purpose, the following transformations are useful:

$$e^{it\tilde{H}_0^{en}} \frac{1}{2}(S_1^+ I^- + S_1^- I^+) e^{-it\tilde{H}_0^{en}} = \frac{1}{2} S_1^+ I^- \exp[it(\omega_{e1} + \tilde{\omega}_n)] + \frac{1}{2} S_1^- I^+ c.c., \quad (22a)$$

$$e^{it\tilde{H}_0^{en}} \frac{1}{2}(S_1^+ I^+ + S_1^- I^-) e^{-it\tilde{H}_0^{en}} = \frac{1}{2} S_1^+ I^+ \exp[it(\omega_{e1} - \tilde{\omega}_n)] + \frac{1}{2} S_1^- I^- c.c., \quad (22b)$$

where c.c. is the complex conjugate of the Hermitian operators.

Polarization transfer during microwave excitation

As is indicated in Figure 6.3, a positive enhancement of the nuclear polarization is observed following the onset of microwave irradiation at $\omega_M \sim \omega_{e1} - \omega_n$. Specifically, according to Eq. 22b, the $S_1^+ I^+ + S_1^- I^-$ term in Eq. 20 is selected by $\omega_M = \omega_{e1} - \tilde{\omega}_n$, and drives the polarization transfer leading to enhanced nuclear polarization. In this case, the effective Hamiltonian in the interaction frame contains the double quantum terms and is

$$\tilde{H}_M^{eff*} = \omega_1 \sin \frac{\eta_\alpha - \eta_\beta}{2} \frac{1}{2} (S_1^+ I^+ + S_1^- I^-). \quad (23)$$

And, under the condition that $\omega_{te} \gg \omega_n$, the initial density operator is

$$\tilde{\rho}_0^* = \tilde{\rho}_0 \approx -\frac{1}{Z} \frac{\hbar}{k_B T} \omega_{e1} S_{1z}, \quad (24)$$

where T is the temperature and \hbar , k_B and Z are constants. Note that the exclusion of nuclear Zeeman order from $\tilde{\rho}_0$ means the attempted calculation of the gain of nuclear polarization due to DNP. As a consequence the enhancement factor is defined as

$$\varepsilon \equiv \frac{\langle P_n \rangle(t)}{\langle P_n \rangle_{eq}}, \quad (25)$$

where $\langle P_n \rangle_{eq}$ is the thermal equilibrate nuclear polarization

$$\langle P_n \rangle_{eq} = \text{tr}(I_z \cdot \frac{-\hbar}{Zk_B T} H_0^{en}) \approx \frac{\hbar \omega_n}{Zk_B T}, \quad (26)$$

and the nuclear polarization at any time t during DNP is

$$\langle P_n \rangle (t) = \text{tr}(\tilde{P}_n^* \tilde{\rho}^*). \quad (27)$$

Note that in Eq. 27 the nuclear polarization operator in the appropriate frame is

$$\begin{aligned} \tilde{P}_n^* &= e^{i\tilde{H}_0^{en}} U_\eta I_z U_\eta^{-1} e^{-i\tilde{H}_0^{en}} \\ &= \frac{\cos \eta_\alpha + \cos \eta_\beta}{2} I_z - \frac{\sin \eta_\alpha + \sin \eta_\beta}{4} \left\{ I^+ e^{i(-\tilde{\omega}_n + \tilde{A}_1 S_{1z})} + I^- c.c. \right\} \\ &\quad + (\cos \eta_\alpha - \cos \eta_\beta) S_{1z} I_z - (\sin \eta_\alpha - \sin \eta_\beta) S_{1z} \frac{1}{2} \left\{ I^+ e^{i(-\tilde{\omega}_n + \tilde{A}_1 S_{1z})} + I^- c.c. \right\} \end{aligned} \quad (28)$$

and following Eq. 9 the time-dependent density operator is

$$\begin{aligned} \tilde{\rho}^* (t) &= \exp(-it\tilde{H}_M^{eff*}) \tilde{\rho}_0^* \exp(it\tilde{H}_M^{eff*}) \\ &= \frac{\hbar}{Zk_B T} \frac{-\omega_{e1}}{2} [(S_{1z} - I_z) + (S_{1z} + I_z) \cos(2\sin(\frac{\eta_\alpha - \eta_\beta}{2})\omega_1 t) \\ &\quad + i(S_1^+ I^+ - S_1^- I^-) \sin(2\sin(\frac{\eta_\alpha - \eta_\beta}{2})\omega_1 t)]. \end{aligned} \quad (29)$$

Therefore, the gain of nuclear polarization due to DNP is (using Eq. 27)

$$\langle P_n \rangle (t) = \frac{\hbar}{Zk_B T} \frac{-\omega_{e1}}{2} \frac{\cos \eta_\alpha + \cos \eta_\beta}{2} [-1 + \cos(2\sin(\frac{\eta_\alpha - \eta_\beta}{2})\omega_1 t)]. \quad (30)$$

Note that $(\frac{\cos \eta_\alpha + \cos \eta_\beta}{2})$ is close to 1 when η_α and η_β are small. In addition, Eq. 30 is a

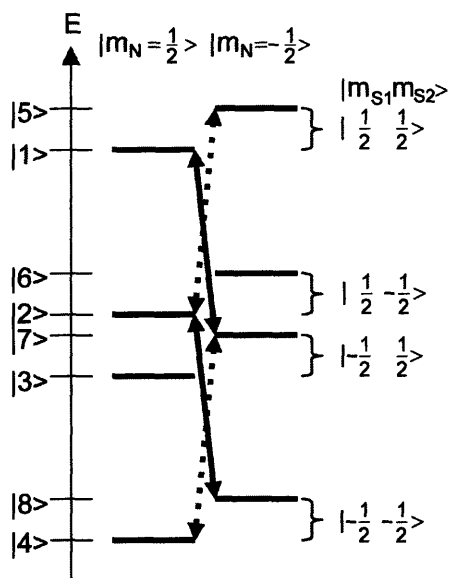
statement that the polarization of the electron can be transferred to the nucleus. Inserting the expressions for $\langle P_n \rangle(t)$ and $\langle P_n \rangle_{eq}$ from Eq. 30 and Eq. 26, respectively, into Eq. 25 yields an expression for the theoretical enhancement of the nuclear polarization that is $|\gamma_e/\gamma_n|$.

6.1.2.3. The CE in an electron–electron–nucleus spin system

The CE is a polarization transfer involving three spins—two coupled electrons and one nucleus. An electron–electron–nucleus spin-system is described by the time-independent Hamiltonian (simplified from Eq. 5)

$$H_0^{een} = \omega_{e1}S_{1z} + \omega_{e2}S_{2z} - \omega_n I_z + (A_1S_{1z} + A_2S_{2z})I_z + (B_1S_{1z} + B_2S_{2z})I_x + d(3S_{1z}S_{2z} - \vec{S}_1 \cdot \vec{S}_2) - 2J\vec{S}_1 \cdot \vec{S}_2, \quad (31)$$

which in the PSB is represented schematically in Figure 6.4.



EPR1

$$E_{13} = \omega_{e1} + \frac{A_1}{2} + \frac{D_d}{2}$$

$$E_{24} = \omega_{e1} + \frac{A_1}{2} - \frac{D_d}{2}$$

$$E_{57} = \omega_{e1} - \frac{A_1}{2} + \frac{D_d}{2}$$

$$E_{68} = \omega_{e1} - \frac{A_1}{2} - \frac{D_d}{2}$$

EPR2

$$E_{12} = \omega_{e2} + \frac{A_2}{2} + \frac{D_d}{2}$$

$$E_{34} = \omega_{e2} + \frac{A_2}{2} - \frac{D_d}{2}$$

$$E_{56} = \omega_{e2} - \frac{A_2}{2} + \frac{D_d}{2}$$

$$E_{78} = \omega_{e2} - \frac{A_2}{2} - \frac{D_d}{2}$$

NMR

$$E_{51} = \omega_n - \frac{A_1 + A_2}{2}$$

$$E_{62} = \omega_n - \frac{A_1 - A_2}{2}$$

$$E_{73} = \omega_n + \frac{A_1 - A_2}{2}$$

$$E_{84} = \omega_n + \frac{A_1 + A_2}{2}$$

e - n Coupling

$$H_{15} = H_{51} = \frac{B_1 + B_2}{4}$$

$$H_{26} = H_{62} = \frac{B_1 - B_2}{4}$$

$$H_{37} = H_{73} = \frac{-B_1 + B_2}{4}$$

$$H_{48} = H_{84} = \frac{-B_1 - B_2}{4}$$

e - e Coupling

$$H_{23} = H_{32} = \frac{D_o}{2}$$

$$H_{67} = H_{76} = \frac{D_o}{2}$$

Figure 6.4. A diagram of a three spin electron-electron-nucleus system showing the energy levels associated with the various spin states. The diagonal and off-diagonal Hamiltonian terms correspond to the EPR/NMR transitions and the couplings between states, respectively. DNP transitions leading to positive and negative enhancements are indicated by the solid and dashed arrows, respectively. Note that $D_d \equiv 2(d-J)$, and $D_o \equiv -d-2J$.

Diagonalization of a three-spin Hamiltonian

Due to the involved interactions, H_0^{een} is block diagonal with two 2×2 blocks (corresponding to $\{|1\rangle, |5\rangle\}$ and $\{|4\rangle, |8\rangle\}$) and one 4×4 block (corresponding to $\{|2\rangle, |3\rangle, |6\rangle, |7\rangle\}$). The interesting phenomena are related to mixing of states in the 4×4 block. Isolation of those subspaces becomes clear when H_0^{een} in Eq. 31 is written as

$$H_0^{een} = \omega_\Sigma S_{\Sigma z} + \omega_\Delta S_{\Delta z} - \omega_n I_z + (A_\Sigma S_{\Sigma z} + A_\Delta S_{\Delta z}) I_z + D_d S_{1z} S_{2z} + (B_\Sigma S_{\Sigma z} + B_\Delta S_{\Delta z}) I_x + D_o S_{\Delta x}, \quad (32)$$

where the new sum (S_Σ) and difference (S_Δ) operators in Eq. 32 are defined as

$$S_{\Sigma z} = \frac{1}{2}(S_{1z} + S_{2z}), \quad S_{\Sigma x} = \frac{1}{2}(S_1^+ S_2^+ + S_1^- S_2^-), \quad S_{\Sigma y} = \frac{1}{2i}(S_1^+ S_2^+ - S_1^- S_2^-), \\ E_{S\Sigma} = 4S_{\Sigma z}^2, \quad S_\Sigma^\alpha = \frac{1}{2} + S_{\Sigma z}, \quad S_\Sigma^\beta = \frac{1}{2} - S_{\Sigma z}, \quad (33a)$$

for the subspace $\{|1\rangle, |4\rangle, |5\rangle, |8\rangle\}$, and

$$S_{\Delta z} = \frac{1}{2}(S_{1z} - S_{2z}), \quad S_{\Delta x} = \frac{1}{2}(S_1^+ S_2^- + S_1^- S_2^+), \quad S_{\Delta y} = \frac{1}{2i}(S_1^+ S_2^- - S_1^- S_2^+), \\ E_{S\Delta} = 4S_{\Delta z}^2, \quad S_\Delta^\alpha = \frac{1}{2} + S_{\Delta z}, \quad S_\Delta^\beta = \frac{1}{2} - S_{\Delta z}, \quad (33b)$$

for the subspace $\{|2\rangle, |3\rangle, |6\rangle, |7\rangle\}$,

and the coefficients in Eq. 32 are

$$\omega_\Sigma = \omega_{e1} + \omega_{e2}, \quad \omega_\Delta = \omega_{e1} - \omega_{e2}, \quad (34) \\ A_\Sigma = A_1 + A_2, \quad A_\Delta = A_1 - A_2, \\ B_\Sigma = B_1 + B_2, \quad B_\Delta = B_1 - B_2, \\ D_d = 2(d - J), \quad D_o = -(d + 2J).$$

Note that the $S_{1z}S_{2z}$ term commutes with all operators in the $\{|1\rangle, |4\rangle, |5\rangle, |8\rangle\}$ and $\{|2\rangle, |3\rangle, |6\rangle, |7\rangle\}$ subspaces, since it is composed of the identity operators with respect to the

two subspaces

$$S_{1z}S_{2z} = \frac{1}{4}(E_{S\Sigma} - E_{S\Delta}). \quad (35)$$

For biradical polarizing agents, the electron–electron interactions (~25 MHz) are assumed to be larger than electron–nucleus dipolar interaction (< 1 MHz), so that

$$\frac{D_o}{\omega_\Delta} > \frac{B_\Sigma}{2\omega_n}, \frac{B_\Delta}{2\omega_n}. \quad (36)$$

The first unitary transformation applied to H_0^{een} is to eliminate the coefficient of the $D_oS_{\Delta x}$ term in Eq. 32 and is performed by the propagator

$$U_\zeta = \exp[i\zeta_\alpha S_{\Delta y} I^\alpha + i\zeta_\beta S_{\Delta y} I^\beta], \quad (37)$$

where the nuclear spin operators and the scalar coefficients ($-\pi/2 < \zeta_\alpha$ and $\zeta_\beta < \pi/2$) are

$$I^\alpha = \frac{1}{2} + I_z, I^\beta = \frac{1}{2} - I_z, \quad (38)$$

$$\tan \zeta_\alpha = \frac{D_o}{\frac{A_\Delta}{2} + \omega_\Delta}, \tan \zeta_\beta = \frac{D_o}{-\frac{A_\Delta}{2} + \omega_\Delta}. \quad (39)$$

We arrange the result of the first unitary transformation as

$$\tilde{H}_0^{een} \equiv U_\zeta H_0^{een} U_\zeta^{-1} = \tilde{H}_{00}^{een} + \tilde{H}_{01}^{een}, \quad (40)$$

where \tilde{H}_{00}^{een} is the sum of the diagonal terms, and \tilde{H}_{01}^{een} is the sum of the off-diagonal

terms. These two terms are further collected (but not completely simplified) as

$$\begin{aligned}\tilde{H}_{00}^{een} &= U_\zeta [\omega_\Sigma S_{\Sigma z} + \omega_\Delta S_{\Delta z} - \omega_n I_z \\ &\quad + (A_\Sigma S_{\Sigma z} + A_\Delta S_{\Delta z}) I_z + D_d S_{1z} S_{2z} + D_o S_{\Delta x}] U_\zeta^{-1},\end{aligned}\quad (41a)$$

$$\tilde{H}_{01}^{een} = U_\zeta (B_\Sigma S_{\Sigma z} I_x + B_\Delta S_{\Delta z} I_x) U_\zeta^{-1}.\quad (41b)$$

The unitary transformation in Eq. 41a is expanded as

$$\begin{aligned}\tilde{H}_{00}^{een} &= \omega_\Sigma S_{\Sigma z} - \omega_n I_z + A_\Sigma S_{\Sigma z} I_z + D_d S_{1z} S_{2z} \\ &\quad + I^\alpha [(\omega_\Delta + \frac{1}{2} A_\Delta)(S_{\Delta z} \cos \zeta_\alpha - S_{\Delta x} \sin \zeta_\alpha) + D_o (S_{\Delta x} \cos \zeta_\alpha + S_{\Delta z} \sin \zeta_\beta)] \\ &\quad + I^\beta [(\omega_\Delta - \frac{1}{2} A_\Delta)(S_{\Delta z} \cos \zeta_\beta - S_{\Delta x} \sin \zeta_\beta) + D_o (S_{\Delta x} \cos \zeta_\beta + S_{\Delta z} \sin \zeta_\beta)].\end{aligned}\quad (42)$$

Due to the relationships in Eq. 39, the off-diagonal terms in Eq. 42 disappear and the diagonal terms are rearranged to yield

$$\tilde{H}_{00}^{een} = \omega_\Sigma S_{\Sigma z} + \tilde{\omega}_\Delta S_{\Delta z} - \omega_n I_z + (A_\Sigma S_{\Sigma z} + \tilde{A}_\Delta S_{\Delta z}) I_z + D_d S_{1z} S_{2z},\quad (43)$$

where the coefficients are

$$\tilde{\omega}_\Delta = \frac{1}{2} \omega_\Delta (\cos \zeta_\alpha + \cos \zeta_\beta) + \frac{1}{2} D_o (\sin \zeta_\alpha + \sin \zeta_\beta) + \frac{1}{4} A_\Delta (\cos \zeta_\alpha - \cos \zeta_\beta),\quad (44a)$$

$$\tilde{A}_\Delta = \omega_\Delta (\cos \zeta_\alpha - \cos \zeta_\beta) + D_o (\sin \zeta_\alpha - \sin \zeta_\beta) + \frac{1}{2} A_\Delta (\cos \zeta_\alpha + \cos \zeta_\beta).\quad (44b)$$

For the process of simplifying Eq. 41b, the propagator in Eq. 37 needs to be rearranged as

$$U_\zeta = \exp[i \frac{\zeta_\alpha + \zeta_\beta}{2} S_{\Delta y} + i(\zeta_\alpha - \zeta_\beta) S_{\Delta y} I_z].\quad (45)$$

Since $S_{\Sigma z} S_{\Delta y} = S_{\Delta y} S_{\Sigma z} = 0$, we can treat the first term in the parenthesis of Eq. 41b and then simply it as

$$\begin{aligned}
U_{\zeta} S_{\Sigma z} I_x U_{\zeta}^{-1} &= S_{\Sigma z} \{ I_x \cos[(\zeta_{\alpha} - \zeta_{\beta}) S_{\Delta y}] - I_y \sin[(\zeta_{\alpha} - \zeta_{\beta}) S_{\Delta y}] \} \\
&= S_{\Sigma z} (I_x \cos \frac{\zeta_{\alpha} - \zeta_{\beta}}{2} - 2I_y S_{\Delta y} \sin \frac{\zeta_{\alpha} - \zeta_{\beta}}{2}) \\
&= S_{\Sigma z} I_x \cos \frac{\zeta_{\alpha} - \zeta_{\beta}}{2}.
\end{aligned} \tag{46}$$

Moreover, because the commutator $[S_{\Delta y} I_z, S_{\Delta z} I_x] = 0$, it is apparent that the second term in the parenthesis of Eq. 41b becomes

$$U_{\zeta} S_{\Delta z} I_x U_{\zeta}^{-1} = S_{\Delta z} I_x \cos \frac{\zeta_{\alpha} + \zeta_{\beta}}{2} - S_{\Delta x} I_x \sin \frac{\zeta_{\alpha} + \zeta_{\beta}}{2}. \tag{47}$$

The combination of Eqs. 46 and 47 then leads to the simplified result of Eq. 41b as

$$\tilde{H}_{01}^{een} = (\tilde{B}_{\Sigma} S_{\Sigma z} + \tilde{B}_{\Delta} S_{\Delta z} + \tilde{K} S_{\Delta x}) I_x, \tag{48}$$

Where the coefficients are

$$\tilde{B}_{\Sigma} = B_{\Sigma} \cos \frac{\zeta_{\alpha} - \zeta_{\beta}}{2}, \quad \tilde{B}_{\Delta} = B_{\Delta} \cos \frac{\zeta_{\alpha} + \zeta_{\beta}}{2}, \quad \tilde{K} = -B_{\Delta} \sin \frac{\zeta_{\alpha} + \zeta_{\beta}}{2}. \tag{49}$$

The first two terms in the parenthesis of Eq. 48 contribute to SE DNP processes. Thus, for the moment they are not interesting since our goal is to derive expressions for the more efficient CE polarization mechanism, and this involves the last term. Note that the last term in Eq. 48 affects only the $\{| \tilde{6} \rangle, | \tilde{2} \rangle, | \tilde{7} \rangle, | \tilde{3} \rangle\}$ subspace illustrated in Figure 6.5, and provides an effective coupling for the CE mechanism. This coupling is not large due to small size of ζ_{α} and ζ_{β} , but potentially mixes degenerate states if the matching condition among the EPR and NMR frequencies is satisfied.

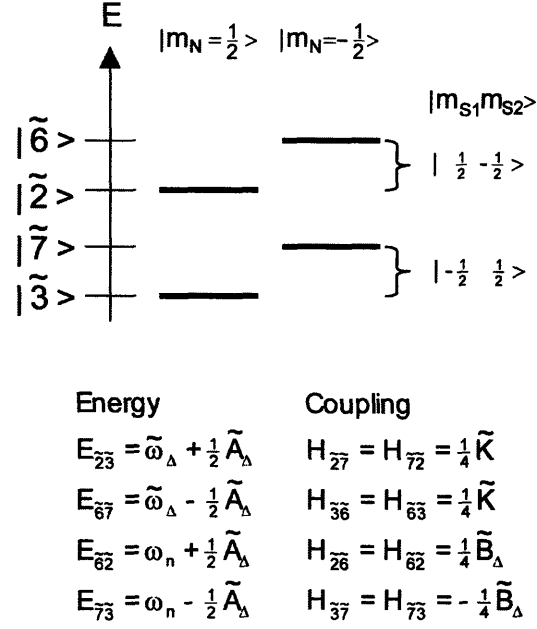


Figure 6.5. The subspace of the electron–electron–nucleus three-spin system. The tilde indicates the intermediate states that are different from the PSB.

A systematic discussion of the truncation of the terms in Eq. 48 involves the transformation of \tilde{H}_{01}^{een} into the interaction frame of \tilde{H}_{00}^{een} . The results of such a transformation for each term in \tilde{H}_{01}^{een} (Eq. 48) are as follows:

$$\begin{aligned}
& e^{it\tilde{H}_{00}^{een}} S_{\Sigma_z} I_x e^{-it\tilde{H}_{00}^{een}} \\
&= \frac{1}{2} S_{\Sigma_z} \{ I^+ e^{it(-\omega_n + A_\Sigma S_{\Sigma_z})} + I^- c.c. \} \\
&= \frac{1}{4} S_{\Sigma}^\alpha \{ I^+ e^{it(-\omega_n + \frac{1}{2}A_\Sigma)} + I^- c.c. \} - \frac{1}{4} S_{\Sigma}^\beta \{ I^+ e^{it(-\omega_n - \frac{1}{2}A_\Sigma)} + I^- c.c. \},
\end{aligned} \tag{50a}$$

$$\begin{aligned}
& e^{it\tilde{H}_{00}^{een}} S_{\Delta_z} I_x e^{-it\tilde{H}_{00}^{een}} \\
&= \frac{1}{2} S_{\Delta_z} \{ I^+ e^{it(-\omega_n + \tilde{A}_\Delta S_{\Delta_z})} + I^- c.c. \} \\
&= \frac{1}{4} S_{\Delta}^\alpha \{ I^+ e^{it(-\omega_n + \frac{1}{2}\tilde{A}_\Delta)} + I^- c.c. \} - \frac{1}{4} S_{\Delta}^\beta \{ I^+ e^{it(-\omega_n - \frac{1}{2}\tilde{A}_\Delta)} + I^- c.c. \},
\end{aligned} \tag{50b}$$

$$\begin{aligned}
& e^{it\tilde{H}_{00}^{een}} S_{\Delta x} I_x e^{-it\tilde{H}_{00}^{een}} \\
&= \frac{1}{4} \{ S_{\Delta}^+ e^{it(\tilde{\omega}_{\Delta} + \tilde{A}_{\Delta} I_z)} I^+ e^{it(-\omega_n + \tilde{A}_{\Delta} S_{\Delta z})} + S_{\Delta}^- e^{-it(\tilde{\omega}_{\Delta} + \tilde{A}_{\Delta} I_z)} I^- e^{-it(-\omega_n + \tilde{A}_{\Delta} S_{\Delta z})} \\
&\quad + S_{\Delta}^+ e^{it(\tilde{\omega}_{\Delta} + \tilde{A}_{\Delta} I_z)} I^- e^{-it(-\omega_n + \tilde{A}_{\Delta} S_{\Delta z})} + S_{\Delta}^- e^{-it(\tilde{\omega}_{\Delta} + \tilde{A}_{\Delta} I_z)} I^+ e^{it(-\omega_n + \tilde{A}_{\Delta} S_{\Delta z})} \} \\
&= \frac{1}{4} \{ S_{\Delta}^+ I^{\alpha} e^{it(\tilde{\omega}_{\Delta} + \frac{1}{2}\tilde{A}_{\Delta})} I^+ S_{\Delta}^{\beta} e^{it(-\omega_n - \frac{1}{2}\tilde{A}_{\Delta})} + S_{\Delta}^- I^{\beta} e^{-it(\tilde{\omega}_{\Delta} - \frac{1}{2}\tilde{A}_{\Delta})} I^- S_{\Delta}^{\alpha} e^{-it(-\omega_n + \frac{1}{2}\tilde{A}_{\Delta})} \\
&\quad + S_{\Delta}^+ I^{\beta} e^{it(\tilde{\omega}_{\Delta} - \frac{1}{2}\tilde{A}_{\Delta})} I^- S_{\Delta}^{\beta} e^{-it(-\omega_n - \frac{1}{2}\tilde{A}_{\Delta})} + S_{\Delta}^- I^{\alpha} e^{-it(\tilde{\omega}_{\Delta} + \frac{1}{2}\tilde{A}_{\Delta})} I^+ S_{\Delta}^{\alpha} e^{it(-\omega_n + \frac{1}{2}\tilde{A}_{\Delta})} \} \\
&= \frac{1}{4} \{ S_{\Delta}^+ I^+ e^{it(\tilde{\omega}_{\Delta} - \omega_n)} + S_{\Delta}^- I^- e^{-it(\tilde{\omega}_{\Delta} - \omega_n)} + S_{\Delta}^+ I^- e^{it(\tilde{\omega}_{\Delta} + \omega_n)} + S_{\Delta}^- I^+ e^{-it(\tilde{\omega}_{\Delta} - \omega_n)} \}.
\end{aligned} \tag{50c}$$

Note that the raising and lowering operators for each spin follow the definitions in Eq.

33b. Using the results in Eqs. 50a-c, we express \tilde{H}_{01}^{een} in the interaction frame of \tilde{H}_{00}^{een} as

$$\begin{aligned}
e^{it\tilde{H}_{00}^{een}} \tilde{H}_{01}^{een} e^{-it\tilde{H}_{00}^{een}} &= \frac{1}{4} \tilde{B}_{\Sigma} \{ S_{\Sigma}^{\alpha} (I^+ e^{it(-\omega_n + \frac{1}{2}A_{\Sigma})} + I^- c.c.) - S_{\Sigma}^{\beta} (I^+ e^{it(-\omega_n - \frac{1}{2}A_{\Sigma})} + I^- c.c.) \} \\
&\quad + \frac{1}{4} \tilde{B}_{\Delta} \{ S_{\Delta}^{\alpha} (I^+ e^{it(-\omega_n + \frac{1}{2}\tilde{A}_{\Delta})} + I^- c.c.) - S_{\Delta}^{\beta} (I^+ e^{it(-\omega_n - \frac{1}{2}\tilde{A}_{\Delta})} + I^- c.c.) \} \\
&\quad + \frac{1}{4} \tilde{K} [S_{\Delta}^+ I^+ e^{it(\tilde{\omega}_{\Delta} - \omega_n)} + S_{\Delta}^- I^- c.c.] \\
&\quad + \frac{1}{4} \tilde{K} [S_{\Delta}^+ I^- e^{it(\tilde{\omega}_{\Delta} + \omega_n)} + S_{\Delta}^- I^+ c.c.].
\end{aligned} \tag{51}$$

The first and second terms in Eq. 51 oscillate at ω_n , which is much larger than the electron–nuclear dipolar interactions at high magnetic fields, and these terms average to zero. However, frequency matching can arise from the third or the fourth term in Eq. 51 when

$$\tilde{\omega}_{\Delta} = \pm \omega_n, \tag{52}$$

and the exponential vanishes, leaving a form of \tilde{H}_{01}^{een} consisting of non-oscillating terms.

For example, the condition $\tilde{\omega}_{\Delta} \approx -\omega_n$ yields the $\frac{1}{4} \tilde{K} (S_{\Delta}^+ I^- + S_{\Delta}^- I^+)$ term in Eq. 48, so

that the truncated \tilde{H}_0^{een} in Eq. 40 approximates (from Eqs. 43 and 48 which is then truncated)

$$\begin{aligned}
& \tilde{H}_{0, truncated}^{een} \\
&= \omega_{\Sigma} S_{\Sigma z} - \omega_n E_{S\Sigma} I_z + (\tilde{\omega}_{\Delta} - \omega_n) M_{\Sigma z} + (\tilde{\omega}_{\Delta} + \omega_n) M_{\Delta z} \\
&+ (A_{\Sigma} S_{\Sigma z} + \tilde{A}_{\Delta} S_{\Delta z}) I_z + D_d S_{1z} S_{2z} \\
&+ \frac{1}{2} \tilde{K} M_{\Delta x},
\end{aligned} \tag{53}$$

where the new spin operators are defined as

$$\begin{aligned}
M_{\Sigma z} &= \frac{1}{2}(S_{\Delta z} + E_{S\Delta} I_z), \quad M_{\Sigma x} = \frac{1}{2}(S_{\Delta}^+ I^+ + S_{\Delta}^- I^-), \quad M_{\Sigma y} = \frac{-i}{2}(S_{\Delta}^+ I^+ - S_{\Delta}^- I^-), \\
E_{M\Sigma} &= 4M_{\Sigma z}^2, \quad M_{\Sigma}^{\alpha} = \frac{1}{2} E_{M\Sigma} + M_{\Sigma z}, \quad M_{\Sigma}^{\beta} = \frac{1}{2} E_{M\Sigma} - M_{\Sigma z},
\end{aligned} \tag{54a}$$

for the subspace $\{|\tilde{2}\rangle, |\tilde{7}\rangle\}$ (see Figure 6.5), and

$$\begin{aligned}
M_{\Delta z} &= \frac{1}{2}(S_{\Delta z} - E_{S\Delta} I_z), \quad M_{\Delta x} = \frac{1}{2}(S_{\Delta}^+ I^- + S_{\Delta}^- I^+), \quad M_{\Delta y} = \frac{-i}{2}(S_{\Delta}^+ I^- - S_{\Delta}^- I^+), \\
E_{M\Delta} &= 4M_{\Delta z}^2, \quad M_{\Delta}^{\alpha} = \frac{1}{2} E_{M\Delta} + M_{\Delta z}, \quad M_{\Delta}^{\beta} = \frac{1}{2} E_{M\Delta} - M_{\Delta z},
\end{aligned} \tag{54b}$$

for the subspace $\{|\tilde{3}\rangle, |\tilde{6}\rangle\}$ (see Figure 6.5).

Note that $M_{\Delta x}$ in Eq. 53 commutes with $S_{\Delta z} I_z$ and $S_{1z} S_{2z}$ since

$$S_{\Delta z} I_z = \frac{1}{4}(E_{M\Sigma} - E_{M\Delta}), \tag{55a}$$

$$S_{1z} S_{2z} = \frac{1}{4}(E_{S\Sigma} - E_{M\Sigma} - E_{M\Delta}). \tag{55b}$$

Moreover, $M_{\Delta x}$ commutes with $S_{\Sigma z}$, $E_{S\Sigma} I_z$, $M_{\Sigma z}$ and $S_{\Sigma z} I_z$ as shown by the following:

- (1) From the definitions in Eq. 33b,

$$S_{\Delta}^{\pm} S_{\Sigma z} = S_1^{\pm} S_2^{\mp} \cdot \frac{1}{2} (S_{1z} + S_{2z}) = 0 \quad (56)$$

and we have (see Eq. 54b)

$$M_{\Delta x} S_{\Sigma z} = \frac{1}{2} (S_{\Delta}^+ I^- + S_{\Delta}^- I^+) S_{\Sigma z} = 0 \quad (57)$$

(2) The results of Eq. 57 are,

$$[M_{\Delta x}, S_{\Sigma z} I_z] = M_{\Delta x} S_{\Sigma z} I_z - S_{\Sigma z} I_z M_{\Delta x} = 0 \quad (58)$$

and (see Eq. 54b)

$$[M_{\Delta x}, E_{S\Sigma} I_z] = M_{\Delta x} E_{S\Sigma} I_z - E_{S\Sigma} I_z M_{\Delta x} = 4(M_{\Delta x} S_{\Sigma z}^2 I_z - S_{\Sigma z}^2 I_z M_{\Delta x}) = 0 \quad (59)$$

(3) From the definitions in Eqs. 54a, b,

$$\begin{aligned} [M_{\Delta x}, M_{\Sigma z}] &= \frac{1}{4} [S_{\Delta}^+ I^- + S_{\Delta}^- I^+, S_{\Delta z} + E_{S\Delta} I_z] \\ &= \frac{1}{4} (-S_{\Delta}^+ I^- + S_{\Delta}^- I^+ + S_{\Delta}^+ I^- - S_{\Delta}^- I^+) \\ &= 0. \end{aligned} \quad (60)$$

With the above commutation relations, a second unitary transformation

$\tilde{\tilde{H}}_0^{een} = U_{\xi} \tilde{H}_{0, truncated}^{een} U_{\xi}^{-1}$ with respect to $M_{\Delta x}$ in Eq. 53 is performed with the propagator

$$U_{\xi} = \exp[i\xi M_{\Delta y}], \quad (61)$$

where the scalar coefficient $(-\pi/2 < \xi < \pi/2)$ satisfies

$$\tan \xi = \frac{\tilde{K}}{2(\tilde{\omega}_\Delta + \omega_n)}. \quad (62)$$

It is then apparent that

$$\begin{aligned} \tilde{H}_0^{een} = & \omega_\Sigma S_{\Sigma z} - \omega_n E_{S\Sigma} I_z + (\tilde{\omega}_\Delta - \omega_n) M_{\Sigma z} + (A_\Sigma S_{\Sigma z} + \tilde{A}_\Delta S_{\Delta z}) I_z + D_d S_{1z} S_{2z} \\ & + \tilde{\Omega} M_{\Delta z}, \end{aligned} \quad (63)$$

with the new coefficient

$$\tilde{\Omega} = (\tilde{\omega}_\Delta + \omega_n) \cos \xi + \frac{1}{2} \tilde{K} \sin \xi. \quad (64)$$

Using Eqs. 33a, 33b, 54a and 54b, the diagonalized electron–electron–nucleus Hamiltonian (Eq. 63) can be described by the conventional spin operators as

$$\tilde{H}_0^{een} = \tilde{\omega}_{1e} S_{1z} + \tilde{\omega}_{2e} S_{2z} - \tilde{\omega}_n I_z + D_d S_{1z} S_{2z} + \tilde{A}_1 S_{1z} I_z + \tilde{A}_2 S_{2z} I_z + \tilde{V} S_{1z} S_{2z} I_z, \quad (65)$$

where the new coefficients are

$$\tilde{\omega}_{1e} = \frac{1}{2} \omega_\Sigma + \frac{1}{4} (\tilde{\omega}_\Delta - \omega_n) + \frac{1}{4} \tilde{\Omega}, \quad (66a)$$

$$\tilde{\omega}_{2e} = \frac{1}{2} \omega_\Sigma - \frac{1}{4} (\tilde{\omega}_\Delta - \omega_n) - \frac{1}{4} \tilde{\Omega}, \quad (66b)$$

$$\tilde{\omega}_n = \frac{1}{2} \omega_n - \frac{1}{4} (\tilde{\omega}_\Delta - \omega_n) + \frac{1}{4} \tilde{\Omega}, \quad (66c)$$

$$\tilde{A}_1 = \frac{1}{2} (A_\Sigma + \tilde{A}_\Delta), \quad (66d)$$

$$\tilde{A}_2 = \frac{1}{2} (A_\Sigma - \tilde{A}_\Delta), \quad (66e)$$

$$\tilde{V} = -(\omega_n + \tilde{\omega}_\Delta) + \tilde{\Omega}. \quad (66f)$$

The microwave Hamiltonian in the EBS

To obtain the effective microwave excitations for DNP, the microwave Hamiltonian $H_M=2\omega_1(S_{1x}+S_{2x}) \cos(\omega_M t)$ for the two electrons needs to be transformed from the PSB to the EBS as the following:

$$\tilde{\tilde{H}}_M = 2\omega_1 \cos(\omega_M t) \cdot U_\xi U_\zeta (S_{1x} + S_{2x}) U_\zeta^{-1} U_\xi^{-1} \quad (67)$$

The operators in $\tilde{\tilde{H}}_M$ can be collected in six groups such as

$$\tilde{\tilde{H}}_M = 2\omega_1 \cos(\omega_M t) \cdot (\tilde{\tilde{H}}_M^1 + \tilde{\tilde{H}}_M^2 + \tilde{\tilde{H}}_M^3 + \tilde{\tilde{H}}_M^4 + \tilde{\tilde{H}}_M^5 + \tilde{\tilde{H}}_M^6) \quad (68)$$

To evaluate the terms on the right-hand-side in Eq. 68, we need to utilize the unitary transformations in Eq. 67 as follows:

(1) Letting $U_\phi = e^{i\phi S_{\Delta y}} = \exp[\frac{1}{2}\phi(S_1^+ S_2^- - S_1^- S_2^+)]$, where ϕ represents ζ_α or ζ_β in Eq.

37, we find

$$\begin{aligned} U_\phi S_{1z} U_\phi^{-1} &= U_\phi (S_{\Sigma z} + S_{\Delta z}) U_\phi^{-1} \\ &= S_{\Sigma z} + S_{\Delta z} \cos \phi - S_{\Delta x} \sin \phi \\ &= \frac{1}{2}(S_{1z} + S_{2z}) + \frac{1}{2}(S_{1z} - S_{2z}) \cos \phi - \frac{1}{2}(S_1^+ S_2^- + S_1^- S_2^+) \sin \phi, \end{aligned} \quad (69a)$$

$$\begin{aligned} U_\phi S_1^+ U_\phi^{-1} &= S_1^+ + \frac{\phi}{2}(2S_{1z} S_2^+) + \left(\frac{\phi}{2}\right)^2 \frac{1}{2!} (-S_1^+) + \left(\frac{\phi}{2}\right)^3 \frac{1}{3!} (-2S_{1z} S_2^+) + \dots \\ &= S_1^+ \cos \frac{\phi}{2} + 2S_{1z} S_2^+ \sin \frac{\phi}{2}, \end{aligned} \quad (69b)$$

$$\begin{aligned}
U_\phi S_1^- U_\phi^{-1} &= S_1^- + \frac{\phi}{2}(2S_{1z}S_2^-) + \left(\frac{\phi}{2}\right)^2 \frac{1}{2!}(-S_1^-) + \left(\frac{\phi}{2}\right)^3 \frac{1}{3!}(-2S_{1z}S_2^-) + \dots \\
&= S_1^- \cos \frac{\phi}{2} + 2S_{1z}S_2^- \sin \frac{\phi}{2}.
\end{aligned} \tag{69c}$$

Similarly

$$\begin{aligned}
U_\phi S_{2z} U_\phi^{-1} &= U_\phi (S_{\Sigma z} - S_{\Delta z}) U_\phi^{-1} \\
&= S_{\Sigma z} - S_{\Delta z} \cos \phi + S_{\Delta x} \sin \phi \\
&= \frac{1}{2}(S_{1z} + S_{2z}) - \frac{1}{2}(S_{1z} - S_{2z}) \cos \phi + \frac{1}{2}(S_1^+ S_2^- + S_1^- S_2^+) \sin \phi,
\end{aligned} \tag{70a}$$

$$\begin{aligned}
U_\phi S_2^+ U_\phi^{-1} &= S_2^+ + \frac{\phi}{2}(-2S_1^+ S_{2z}) + \left(\frac{\phi}{2}\right)^2 \frac{1}{2!}(-S_2^+) + \left(\frac{\phi}{2}\right)^3 \frac{1}{3!}(2S_1^+ S_{2z}) + \dots \\
&= S_2^+ \cos \frac{\phi}{2} - 2S_1^+ S_{2z} \sin \frac{\phi}{2},
\end{aligned} \tag{70b}$$

$$\begin{aligned}
U_\phi S_2^- U_\phi^{-1} &= S_2^- + \frac{\phi}{2}(-2S_1^- S_{2z}) + \left(\frac{\phi}{2}\right)^2 \frac{1}{2!}(-S_2^-) + \left(\frac{\phi}{2}\right)^3 \frac{1}{3!}(2S_1^- S_{2z}) + \dots \\
&= S_2^- \cos \frac{\phi}{2} - 2S_1^- S_{2z} \sin \frac{\phi}{2},
\end{aligned} \tag{70c}$$

(2) Letting $U_\chi = e^{i\chi M_{\Delta y}} = \exp[\frac{1}{2}\chi(S_1^+ S_2^- I^- - S_1^- S_2^+ I^+)]$, where χ represents ξ in Eq.

61, we also derive

$$\begin{aligned}
U_\chi I_z U_\chi^{-1} &= U_\chi (E_{S\Sigma} I_z + E_{S\Delta} I_z) U_\chi^{-1} = U_\chi (E_{S\Sigma} I_z + M_{\Sigma z} - M_{\Delta z}) U_\chi^{-1} \\
&= E_{S\Sigma} I_z + M_{\Sigma z} - M_{\Delta z} \cos \chi + M_{\Delta x} \sin \chi \\
&= \frac{1}{4} S_{1z} - \frac{1}{4} S_{2z} + \frac{3}{4} I_z + S_{1z} S_{2z} I_z \\
&\quad - \left(\frac{1}{4} S_{1z} - \frac{1}{4} S_{2z} - \frac{1}{4} S_{2z} + S_{1z} S_{2z} I_z\right) \cos \chi \\
&\quad + \frac{1}{2}(S_1^+ S_2^- I^- + S_1^- S_2^+ I^+) \sin \chi,
\end{aligned} \tag{71a}$$

$$\begin{aligned}
U_\chi I^+ U_\chi^{-1} &= I^+ + \frac{\chi}{2}(-2S_1^+ S_2^- I_z) + \left(\frac{\chi}{2}\right)^2 \frac{1}{2!} \left(\frac{-1}{2} I^+ + 2S_{1z} S_{2z} I^+\right) \\
&\quad + \left(\frac{\chi}{2}\right)^3 \frac{1}{3!} (2S_1^+ S_2^- I_z) + \left(\frac{\chi}{2}\right)^4 \frac{1}{4!} \left(\frac{1}{2} I^+ - 2S_{1z} S_{2z} I^+\right) + \dots \\
&= \frac{1}{2} I^+ + 2S_{1z} S_{2z} I^+ \\
&\quad + \left(\frac{1}{2} I^+ - 2S_{1z} S_{2z} I^+\right) \cos \frac{\chi}{2} - 2S_1^+ S_2^- I_z \sin \frac{\chi}{2},
\end{aligned} \tag{71b}$$

$$\begin{aligned}
U_\chi I^- U_\chi^{-1} &= I^- + \frac{\chi}{2}(-2S_1^- S_2^+ I_z) + \left(\frac{\chi}{2}\right)^2 \frac{1}{2!} \left(\frac{-1}{2} I^- + 2S_{1z} S_{2z} I^-\right) \\
&\quad + \left(\frac{\chi}{2}\right)^3 \frac{1}{3!} (2S_1^- S_2^+ I_z) + \left(\frac{\chi}{2}\right)^4 \frac{1}{4!} \left(\frac{1}{2} I^- - 2S_{1z} S_{2z} I^-\right) + \dots \\
&= \frac{1}{2} I^- + 2S_{1z} S_{2z} I^- \\
&\quad + \left(\frac{1}{2} I^- - 2S_{1z} S_{2z} I^-\right) \cos \frac{\chi}{2} - 2S_1^- S_2^+ I_z \sin \frac{\chi}{2}.
\end{aligned} \tag{71c}$$

Further,

$$\begin{aligned}
U_\chi S_{1z} U_\chi^{-1} &= U_\chi (S_{\Sigma z} + M_{\Sigma z} + M_{\Delta z}) U_\chi^{-1} \\
&= S_{\Sigma z} + M_{\Sigma z} + M_{\Delta z} \cos \chi - M_{\Delta x} \sin \chi \\
&= \frac{3}{4} S_{1z} + \frac{1}{4} S_{2z} + \frac{1}{4} I_z - S_{1z} S_{2z} I_z \\
&\quad + \left(\frac{1}{4} S_{1z} - \frac{1}{4} S_{2z} - \frac{1}{4} S_{2z} + S_{1z} S_{2z} I_z\right) \cos \chi \\
&\quad - \frac{1}{2} (S_1^+ S_2^- I^- + S_1^- S_2^+ I^+) \sin \chi,
\end{aligned} \tag{72a}$$

$$\begin{aligned}
U_\chi S_1^+ U_\chi^{-1} &= S_1^+ + \frac{\chi}{2} (2S_{1z} S_2^+ I^+) + \left(\frac{\chi}{2}\right)^2 \frac{1}{2!} \left(\frac{-1}{2} S_1^+ - 2S_1^+ S_{2z} I_z\right) \\
&\quad + \left(\frac{\chi}{2}\right)^3 \frac{1}{3!} (-2S_{1z} S_2^+ I^+) + \left(\frac{\chi}{2}\right)^4 \frac{1}{4!} \left(\frac{1}{2} S_1^+ + 2S_1^+ S_{2z} I_z\right) + \dots \\
&= \frac{1}{2} S_1^+ - 2S_1^+ S_{2z} I_z \\
&\quad + \left(\frac{1}{2} S_1^+ + 2S_1^+ S_{2z} I_z\right) \cos \frac{\chi}{2} + 2S_{1z} S_2^+ I^+ \sin \frac{\chi}{2},
\end{aligned} \tag{72b}$$

$$\begin{aligned}
U_\chi S_1^- U_\chi^{-1} &= S_1^- + \frac{\chi}{2} (2S_{1z} S_2^- I^-) + \left(\frac{\chi}{2}\right)^2 \frac{1}{2!} \left(\frac{-1}{2} S_1^- - 2S_1^- S_{2z} I_z\right) \\
&\quad + \left(\frac{\chi}{2}\right)^3 \frac{1}{3!} (-2S_{1z} S_2^- I^-) + \left(\frac{\chi}{2}\right)^4 \frac{1}{4!} \left(\frac{1}{2} S_1^- + 2S_1^- S_{2z} I_z\right) + \dots \\
&= \frac{1}{2} S_1^- - 2S_1^- S_{2z} I_z \\
&\quad + \left(\frac{1}{2} S_1^- + 2S_1^- S_{2z} I_z\right) \cos \frac{\chi}{2} + 2S_{1z} S_2^- I^- \sin \frac{\chi}{2}.
\end{aligned} \tag{72c}$$

And finally,

$$\begin{aligned}
U_\chi S_{2z} U_\chi^{-1} &= U_\chi (S_{\Sigma z} - M_{\Sigma z} - M_{\Delta z}) U_\chi^{-1} \\
&= S_{\Sigma z} - M_{\Sigma z} - M_{\Delta z} \cos \chi + M_{\Delta x} \sin \chi \\
&= \frac{1}{4} S_{1z} + \frac{3}{4} S_{2z} - \frac{1}{4} I_z + S_{1z} S_{2z} I_z \\
&\quad - \left(\frac{1}{4} S_{1z} - \frac{1}{4} S_{2z} - \frac{1}{4} S_{2z} + S_{1z} S_{2z} I_z \right) \cos \chi \\
&\quad + \frac{1}{2} (S_1^+ S_2^- I^- + S_1^- S_2^+ I^+) \sin \chi.
\end{aligned} \tag{73a}$$

$$\begin{aligned}
U_\chi S_2^+ U_\chi^{-1} &= S_2^+ + \frac{\chi}{2} (-2S_1^+ S_{2z} I^-) + \left(\frac{\chi}{2}\right)^2 \frac{1}{2!} \left(\frac{-1}{2} S_2^+ + 2S_{1z} S_2^+ I_z\right) \\
&\quad + \left(\frac{\chi}{2}\right)^3 \frac{1}{3!} (2S_1^+ S_{2z} I^-) + \left(\frac{\chi}{2}\right)^4 \frac{1}{4!} \left(\frac{1}{2} S_2^+ - 2S_{1z} S_2^+ I_z\right) + \dots \\
&= \frac{1}{2} S_2^+ + 2S_{1z} S_2^+ I_z \\
&\quad + \left(\frac{1}{2} S_2^+ - 2S_{1z} S_2^+ I_z\right) \cos \frac{\chi}{2} - 2S_1^+ S_{2z} I^- \sin \frac{\chi}{2},
\end{aligned} \tag{73b}$$

$$\begin{aligned}
U_\chi S_2^- U_\chi^{-1} &= S_2^- + \frac{\chi}{2} (-2S_1^- S_{2z} I^+) + \left(\frac{\chi}{2}\right)^2 \frac{1}{2!} \left(\frac{-1}{2} S_2^- + 2S_{1z} S_2^- I_z\right) \\
&\quad + \left(\frac{\chi}{2}\right)^3 \frac{1}{3!} (2S_1^- S_{2z} I^+) + \left(\frac{\chi}{2}\right)^4 \frac{1}{4!} \left(\frac{1}{2} S_2^- - 2S_{1z} S_2^- I_z\right) + \dots \\
&= \frac{1}{2} S_2^- + 2S_{1z} S_2^- I_z \\
&\quad + \left(\frac{1}{2} S_2^- - 2S_{1z} S_2^- I_z\right) \cos \frac{\chi}{2} - 2S_1^- S_{2z} I^+ \sin \frac{\chi}{2}.
\end{aligned} \tag{73c}$$

(3) Recalling $U_\zeta = \exp(i\zeta_\alpha S_{\Delta y} I^\alpha + i\zeta_\beta S_{\Delta y} I^\beta)$ (see Eq. 37) and referring to Eqs. 69a-

c and 70a-c, we find for the first unitary transformation in Eq. 68 the following

$$\begin{aligned}
\tilde{H}_M &= U_\zeta (S_{1x} + S_{2x}) U_\zeta^{-1} \\
&= S_{1x} (I^\alpha \cos \frac{\zeta_\alpha}{2} + I^\beta \cos \frac{\zeta_\beta}{2}) + 2S_{1z} S_{2x} (I^\alpha \sin \frac{\zeta_\alpha}{2} + I^\beta \sin \frac{\zeta_\beta}{2}) \\
&\quad + S_{2x} (I^\alpha \cos \frac{\zeta_\alpha}{2} + I^\beta \cos \frac{\zeta_\beta}{2}) - 2S_{1x} S_{2z} (I^\alpha \sin \frac{\zeta_\alpha}{2} + I^\beta \sin \frac{\zeta_\beta}{2}) \\
&= \frac{1}{2} (S_{1x} + S_{2x}) (c_\alpha + c_\beta) + (S_{1x} + S_{2x}) I_z (c_\alpha - c_\beta) \\
&\quad + (S_{1z} S_{2x} - S_{1x} S_{2z}) (s_\alpha + s_\beta) + 2(S_{1z} S_{2x} - S_{1x} S_{2z}) I_z (s_\alpha - s_\beta),
\end{aligned} \tag{74}$$

with the coefficients defined as

$$c_\alpha = \cos \frac{\zeta_\alpha}{2}, c_\beta = \cos \frac{\zeta_\beta}{2}, s_\alpha = \sin \frac{\zeta_\alpha}{2}, s_\beta = \sin \frac{\zeta_\beta}{2}. \tag{75}$$

(4) The second unitary transformation in Eq. 68 involves Eqs. 71a-c, 72a-c and 73a-c

and is further simplified by the following derivations:

$$\begin{aligned} [M_{\Delta y}, S_{1z}I_z] &= [M_{\Delta y}, S_{1z}S_{2z}] = [M_{\Delta y}, S_{2z}I_z] = 0, \\ S_{1x} &= -2iS_{1y}S_{1z}, \quad S_{2x} = -2iS_{2y}S_{2z}. \end{aligned} \quad (76)$$

On the basis of Eq. 76, we can rewrite Eq. 74 as

$$\begin{aligned} \tilde{H}_M &= \frac{1}{2}(c_\alpha + c_\beta)(S_{1x} + S_{2x}) - 2i(c_\alpha - c_\beta)(S_{1y}S_{1z}I_z + S_{2y}S_{2z}I_z) \\ &\quad + 2i(s_\alpha + s_\beta)(S_{1y} - S_{2y})S_{1z}S_{2z} - 2(s_\alpha - s_\beta)(S_{1x}S_{2z}I_z - S_{2x}S_{1z}I_z). \end{aligned} \quad (77)$$

To obtain \tilde{H}_M in Eq. 68, we use results from Eqs. 72a-c and 73a-c and continue to calculate

$$\begin{aligned} U_\xi \tilde{H}_M U_\xi^{-1} &= (c_\alpha + c_\beta) \left\{ \frac{1}{4}(S_{1x} + S_{2x}) - (S_{1x}S_{2z} - S_{1z}S_{2x})I_z \right. \\ &\quad \left. + \left[\frac{1}{4}(S_{1x} + S_{2x}) + (S_{1x}S_{2z} - S_{1z}S_{2x})I_z \right] \cos \frac{\xi}{2} \right. \\ &\quad \left. + \frac{1}{2}[S_{1z}(S_2^+I^+ + S_2^-I^-) - (S_1^+I^- + S_1^-I^+)S_{2z}] \sin \frac{\xi}{2} \right\} \\ &\quad + \frac{1}{2}(c_\alpha - c_\beta) \left\{ (S_{1x} + S_{2x})I_z - (S_{1x}S_{2z} - S_{1z}S_{2x}) \right. \\ &\quad \left. + [(S_{1x} + S_{2x})I_z + (S_{1x}S_{2z} - S_{1z}S_{2x})] \cos \frac{\xi}{2} \right. \\ &\quad \left. + \frac{1}{2}(S_2^+I^+ + S_2^-I^- + S_1^+I^- + S_1^-I^+) \sin \frac{\xi}{2} \right\} \\ &\quad + \frac{1}{2}(s_\alpha + s_\beta) \left\{ (S_{1x} + S_{2x})I_z - (S_{1x}S_{2z} - S_{1z}S_{2x}) \right. \\ &\quad \left. - [(S_{1x} + S_{2x})I_z + (S_{1x}S_{2z} - S_{1z}S_{2x})] \cos \frac{\xi}{2} \right. \\ &\quad \left. - \frac{1}{2}(S_2^+I^+ + S_2^-I^- + S_1^+I^- + S_1^-I^+) \sin \frac{\xi}{2} \right\} \\ &\quad + (s_\alpha - s_\beta) \left\{ \frac{1}{4}(S_{1x} + S_{2x}) - (S_{1x}S_{2z} - S_{1z}S_{2x})I_z \right. \\ &\quad \left. - \left[\frac{1}{4}(S_{1x} + S_{2x}) + (S_{1x}S_{2z} - S_{1z}S_{2x})I_z \right] \cos \frac{\xi}{2} \right. \\ &\quad \left. - \frac{1}{2}[S_{1z}(S_2^+I^+ + S_2^-I^-) - (S_1^+I^- + S_1^-I^+)S_{2z}] \sin \frac{\xi}{2} \right\}. \end{aligned} \quad (78)$$

Collecting the terms in Eq. 78, we obtain the six terms on the right-hand-side of Eq. 68 as

$$\tilde{H}_M^1 = \tilde{h}_1(S_{1x} + S_{2x}), \quad \tilde{h}_1 = \frac{1}{4}[(c_\alpha + c_\beta + s_\alpha - s_\beta) + (c_\alpha + c_\beta - s_\alpha + s_\beta)\cos\frac{\xi}{2}] \quad (79a)$$

$$\tilde{H}_M^2 = \tilde{h}_2(S_{1x} + S_{2x})I_z, \quad \tilde{h}_2 = \frac{1}{2}[(c_\alpha - c_\beta + s_\alpha + s_\beta) + (c_\alpha - c_\beta - s_\alpha - s_\beta)\cos\frac{\xi}{2}] \quad (79b)$$

$$\tilde{H}_M^3 = \tilde{h}_3(S_{1x}S_{2z} - S_{1z}S_{2x}), \quad \tilde{h}_3 = \frac{1}{2}[(-c_\alpha + c_\beta - s_\alpha - s_\beta) + (c_\alpha - c_\beta - s_\alpha - s_\beta)\cos\frac{\xi}{2}] \quad (79c)$$

$$\tilde{H}_M^4 = \tilde{h}_4(S_{1x}S_{2z} - S_{1z}S_{2x})I_z, \quad \tilde{h}_4 = [(-c_\alpha - c_\beta - s_\alpha + s_\beta) + (c_\alpha + c_\beta - s_\alpha + s_\beta)\cos\frac{\xi}{2}] \quad (79d)$$

$$\tilde{H}_M^5 = \tilde{h}_5(S_2^+I^+ + S_2^-I^- + S_1^+I^- + S_1^-I^+), \quad \tilde{h}_5 = \frac{1}{4}(c_\alpha - c_\beta - s_\alpha - s_\beta)\sin\frac{\xi}{2} \quad (79e)$$

$$\tilde{H}_M^6 = \tilde{h}_6[(S_2^+I^+ + S_2^-I^-)S_{1z} - (S_1^+I^- + S_1^-I^+)S_{2z}], \quad \tilde{h}_6 = \frac{1}{2}(c_\alpha + c_\beta - s_\alpha + s_\beta)\sin\frac{\xi}{2} \quad (79f)$$

Some terms of \tilde{H}_M (see Eqs. 79a-f) which are selected by a certain microwave frequency can lead to polarization transfer for DNP. Note that DNP is established through the terms that have coefficients involving ξ ; the remaining terms are associated with EPR transitions. We can now delineate the selection rules for microwave excitation, which can be identified within the interaction frame with respect to the Hamiltonian \tilde{H}_0^{een} .

Specifically, we recall from Eqs. 79a-f that it is necessary to calculate

$$\tilde{H}_M^{n*} = e^{it\tilde{H}_0^{een}} \tilde{H}_M^n e^{-it\tilde{H}_0^{een}} \quad (80)$$

For example, setting $n=1$ in Eq. 80 which corresponds to Eq. 79a, we use the analogous procedure for calculation of Eqs. 50a-c to obtain

$$\begin{aligned} \tilde{H}_M^{1*} &= \tilde{h}_1 e^{it\tilde{H}_0^{een}} (S_{1x} + S_{2x}) e^{-it\tilde{H}_0^{een}} \\ &= \frac{1}{2} \tilde{h}_1 [S_1^+ e^{it(\tilde{\omega}_{1e} + D_d S_{2z} + \tilde{A}_1 I_z + \tilde{V} S_{2z} I_z)} + S_1^- c.c. + S_2^+ e^{it(\tilde{\omega}_{2e} + D_d S_{1z} + \tilde{A}_2 I_z + \tilde{V} S_{1z} I_z)} + S_2^- c.c.], \end{aligned} \quad (81)$$

which is further expanded to

$$\begin{aligned} \tilde{H}_M^{5*} = & \tilde{h}_5 \{ S_2^+ I^+ S_1^\alpha e^{it(\tilde{\omega}_{2e} + \frac{D_d - \tilde{\omega}_n + \tilde{A}_1}{2})} + S_2^- I^- S_1^\alpha c.c. + S_1^+ I^- S_2^\alpha e^{it(\tilde{\omega}_{1e} + \frac{D_d + \tilde{\omega}_n - \tilde{A}_2}{2})} + S_1^- I^+ S_2^\alpha c.c. \\ & + S_2^+ I^+ S_1^\beta e^{it(\tilde{\omega}_{2e} - \frac{D_d - \tilde{\omega}_n - \tilde{A}_1}{2})} + S_2^- I^- S_1^\beta c.c. + S_1^+ I^- S_2^\beta e^{it(\tilde{\omega}_{1e} - \frac{D_d + \tilde{\omega}_n + \tilde{A}_2}{2})} + S_1^- I^+ S_2^\beta c.c. \} \end{aligned} \quad (82e)$$

$$\begin{aligned} \tilde{H}_M^{6*} = & \frac{1}{2} \tilde{h}_6 \{ S_2^+ I^+ S_1^\alpha e^{it(\tilde{\omega}_{2e} + \frac{D_d - \tilde{\omega}_n + \tilde{A}_1}{2})} + S_2^- I^- S_1^\alpha c.c. - S_1^+ I^- S_2^\alpha e^{it(\tilde{\omega}_{1e} + \frac{D_d + \tilde{\omega}_n - \tilde{A}_2}{2})} - S_1^- I^+ S_2^\alpha c.c. \\ & - S_2^+ I^+ S_1^\beta e^{it(\tilde{\omega}_{2e} - \frac{D_d - \tilde{\omega}_n - \tilde{A}_1}{2})} - S_2^- I^- S_1^\beta c.c. + S_1^+ I^- S_2^\beta e^{it(\tilde{\omega}_{1e} - \frac{D_d + \tilde{\omega}_n + \tilde{A}_2}{2})} + S_1^- I^+ S_2^\beta c.c. \} \end{aligned} \quad (82f)$$

yielding

$$\tilde{H}_M^* = 2\omega_1 \cos(\omega_M t) \cdot (\tilde{H}_M^{1*} + \tilde{H}_M^{2*} + \tilde{H}_M^{3*} + \tilde{H}_M^{4*} + \tilde{H}_M^{5*} + \tilde{H}_M^{6*}), \quad (83)$$

from which, after combining Eqs. 82a-d, we obtain the first part of \tilde{H}_M^* as

$$\begin{aligned} & \tilde{H}_M^{1*} + \tilde{H}_M^{2*} + \tilde{H}_M^{3*} + \tilde{H}_M^{4*} \\ = & \frac{1}{2} (c_\alpha - s_\alpha) \cos \frac{\xi}{2} [S_1^+ S_2^\alpha I^\alpha e^{it(\tilde{\omega}_{e1} + \frac{D_d + \tilde{A}_1 + \tilde{V}}{2 + 2 + 4})} + S_1^- S_2^\alpha I^\alpha c.c.] \\ & + \frac{1}{2} (c_\beta - s_\beta) [S_1^+ S_2^\alpha I^\beta e^{it(\tilde{\omega}_{e1} + \frac{D_d - \tilde{A}_1 - \tilde{V}}{2 + 2 + 4})} + S_1^- S_2^\alpha I^\beta c.c.] \\ & + \frac{1}{2} (c_\alpha + s_\alpha) [S_1^+ S_2^\beta I^\alpha e^{it(\tilde{\omega}_{e1} - \frac{D_d + \tilde{A}_1 + \tilde{V}}{2 + 2 + 4})} + S_1^- S_2^\beta I^\alpha c.c.] \\ & + \frac{1}{2} (c_\beta + s_\beta) \cos \frac{\xi}{2} [S_1^+ S_2^\beta I^\beta e^{it(\tilde{\omega}_{e1} - \frac{D_d - \tilde{A}_1 - \tilde{V}}{2 + 2 + 4})} + S_1^- S_2^\beta I^\beta c.c.] \\ & + \frac{1}{2} (c_\alpha + s_\alpha) [S_2^+ S_1^\alpha I^\alpha e^{it(\tilde{\omega}_{e2} + \frac{D_d + \tilde{A}_2 + \tilde{V}}{2 + 2 + 4})} + S_2^- S_1^\alpha I^\alpha c.c.] \\ & + \frac{1}{2} (c_\beta + s_\beta) \cos \frac{\xi}{2} [S_2^+ S_1^\alpha I^\beta e^{it(\tilde{\omega}_{e2} + \frac{D_d - \tilde{A}_2 - \tilde{V}}{2 + 2 + 4})} + S_2^- S_1^\alpha I^\beta c.c.] \\ & + \frac{1}{2} (c_\alpha - s_\alpha) \cos \frac{\xi}{2} [S_2^+ S_1^\beta I^\alpha e^{it(\tilde{\omega}_{e2} - \frac{D_d + \tilde{A}_2 + \tilde{V}}{2 + 2 + 4})} + S_2^- S_1^\beta I^\alpha c.c.] \\ & + \frac{1}{2} (c_\beta - s_\beta) [S_2^+ S_1^\beta I^\beta e^{it(\tilde{\omega}_{e2} - \frac{D_d - \tilde{A}_2 - \tilde{V}}{2 + 2 + 4})} + S_2^- S_1^\beta I^\beta c.c.] \end{aligned} \quad (84a)$$

And combining Eqs. 82e and 82f, we obtain the remaining part of \tilde{H}_M^* as

$$\begin{aligned}
& \tilde{H}_M^{5*} + \tilde{H}_M^{6*} \\
&= \frac{1}{2}(c_\alpha - s_\alpha) \sin \frac{\xi}{2} [S_2^+ I^+ S_1^\alpha e^{it(\tilde{\omega}_{e2} + \frac{D_d}{2} - \tilde{\omega}_n + \frac{\tilde{A}_1}{2})} + S_2^- I^- S_1^\alpha c.c.] \\
& - \frac{1}{2}(c_\beta + s_\beta) \sin \frac{\xi}{2} [S_2^+ I^+ S_1^\beta e^{it(\tilde{\omega}_{e2} - \frac{D_d}{2} - \tilde{\omega}_n - \frac{\tilde{A}_1}{2})} + S_2^- I^- S_1^\beta c.c.] \\
& - \frac{1}{2}(c_\beta + s_\beta) \sin \frac{\xi}{2} [S_1^+ I^- S_2^\alpha e^{it(\tilde{\omega}_{e1} + \frac{D_d}{2} + \tilde{\omega}_n - \frac{\tilde{A}_2}{2})} + S_1^- I^+ S_2^\alpha c.c.] \\
& + \frac{1}{2}(c_\alpha - s_\alpha) \sin \frac{\xi}{2} [S_1^+ I^- S_2^\beta e^{it(\tilde{\omega}_{e1} - \frac{D_d}{2} + \tilde{\omega}_n + \frac{\tilde{A}_2}{2})} + S_1^- I^+ S_2^\beta c.c.]
\end{aligned} \tag{84b}$$

Polarization transfer by effective microwave excitation

The oscillation frequencies in Eqs. 84a and 84b can be canceled by a microwave frequency ω_M which selects the effective microwave operators that have coefficients proportional to the microwave field strength ω_1 . According to Eqs. 8 and 9, the effective microwave operator contained in \tilde{H}_M^* in the interaction frame of \tilde{H}_0^{een} interacts with the density operator with an initial value

$$\tilde{\rho}_0^* = \tilde{\rho}_0 = -\frac{\hbar}{Zk_B T} \tilde{H}_0^{een} \approx \frac{-\hbar}{Zk_B T} \frac{\omega_{e1} + \omega_{e2}}{2} (S_{1z} + S_{2z}). \tag{85}$$

The exclusion of the nuclear Zeeman order from $\tilde{\rho}_0$ is again aimed to calculate the gain of nuclear polarization due to DNP. Thus the resulting enhancement factor still follows Eq. 25 which is based on the thermal equilibrate nuclear polarization $\langle P_n \rangle_{eq}$ given by

$$\langle P_n \rangle_{eq} \equiv \text{tr}(I_z \cdot \frac{-\hbar}{Zk_B T} H_0^{een}) \sim \frac{2\hbar\omega_n}{Zk_B T}. \quad (86)$$

The nuclear polarization at any time t during DNP is calculated through

$$\langle P_n \rangle(t) = \text{tr}(\tilde{P}_n^* \tilde{\rho}^*), \quad (87)$$

which is analogous to Eq. 27. The nuclear polarization operator \tilde{P}_n^* is derived as (see Eqs. 71a-c, 72a-c and 73a-c and the analogous procedures used to calculate Eqs. 50a-c)

$$\begin{aligned} \tilde{P}_n^* &= e^{ii\tilde{H}_0^{en}} U_\xi U_\zeta I_z U_\zeta^{-1} U_\xi^{-1} e^{-ii\tilde{H}_0^{en}} \\ &= \frac{3}{4} I_z + \frac{1}{4} S_{1z} - \frac{1}{4} S_{2z} + S_{1z} S_{2z} I_z \\ &\quad - (\frac{1}{4} S_{1z} - \frac{1}{4} S_{2z} - \frac{1}{4} I_z + S_{1z} S_{2z} I_z) \cos \xi \\ &\quad + \frac{1}{2} (S_1^+ S_2^- I^- e^{i\tilde{\Omega}t} + S_1^- S_2^+ I^+ e^{-i\tilde{\Omega}t}) \sin \xi. \end{aligned} \quad (88)$$

Recall that any term of \tilde{H}_M^* (Eq. 84a and 84b) that has a coefficient dependent on ξ will enhance nuclear polarization. We will demonstrate the generation of positive DNP enhancements from combinations of four possible transitions when $\omega_M \sim \omega_{e1}$. Although those transitions — $S_{1x} S_2^\alpha I^\alpha$, $S_{1x} S_2^\beta I^\beta$, $\frac{1}{2} S_1^\alpha (S_2^+ I^+ + S_2^- I^-)$ and $-\frac{1}{2} S_1^\beta (S_2^+ I^+ + S_2^- I^-)$ — occur at different microwave frequencies near ω_{e1} , they can be simultaneously excited by a sufficiently intense ω_1 and a broad frequency distribution of ω_M . The following examples illustrate calculations of the enhanced nuclear polarization.

Example 1

When ω_M matches the oscillation frequency of the first term in Eq. 84a as

$$\omega_M = \tilde{\omega}_{1e} + \frac{1}{2}D_d + \frac{1}{2}\tilde{A}_1 + \frac{1}{4}\tilde{V}, \quad (89)$$

the effective microwave interaction (from Eq. 83 and the first line of Eq. 84a) is

$$\tilde{H}_M^{eff*} = \tilde{\omega}_1^* S_{1x} S_2^\alpha I^\alpha, \quad (90)$$

where $\tilde{\omega}_1^* = \omega_1(c_\alpha - s_\alpha) \cos \frac{\xi}{2}$ referring to Eqs. 75 and 62. Since the effective Hamiltonian only affects S_{1z} , the time-dependent density operator is readily calculated (through Eqs. 8 and 9) as

$$\begin{aligned} \tilde{\rho}^* = & \frac{-\hbar}{Zk_B T} \frac{\omega_{e1} + \omega_{e2}}{2} \{S_{2z} + S_{1z}(E - S_2^\alpha I^\alpha) \\ & + S_{1z} S_2^\alpha I^\alpha \cos \tilde{\omega}_1^* t - S_{1y} S_2^\alpha I^\alpha \sin \tilde{\omega}_1^* t\}. \end{aligned} \quad (91)$$

According to Eqs. 87 and 88, the time-dependent nuclear polarization is

$$\langle P_n \rangle (t) = \frac{-\hbar}{Zk_B T} \frac{\omega_{e1} + \omega_{e2}}{2} \frac{1}{4} (1 - \cos \xi) (\cos \tilde{\omega}_1^* t - 1), \quad (92)$$

which, when compared to the initial nuclear polarization in Eq. 86, suggests that the

maximal NMR enhancement is $\frac{1}{4} \left| \frac{\gamma_e}{\gamma_n} \right|$ if $\xi=90^\circ$ (see Eq. 62 for the exact frequency

matching). Note that when $\omega_M = \tilde{\omega}_{1e} - \frac{1}{2}D_d - \frac{1}{2}\tilde{A}_1 + \frac{1}{4}\tilde{V}$, the term selected is $S_{1x} S_2^\beta I^\beta$ (from Eq. 83 and the forth line of Eq. 84a,) and yields the same maximal DNP

enhancement in this example.

Example 2

As in Example 1, we let ω_M match the oscillation frequency of the first term in Eq. 84b as

$$\omega_M = \tilde{\omega}_{2e} - \tilde{\omega}_n + \frac{1}{2}D_d + \frac{1}{2}\tilde{A}_1, \quad (93)$$

the effective microwave interaction (from Eq. 83 and the first line of Eq. 84b) becomes

$$\tilde{H}_M^{eff*} = \tilde{\omega}_2^* \frac{1}{2} (S_2^+ I^+ + S_2^- I^-) S_1^\alpha, \quad (94)$$

where $\tilde{\omega}_2^* = \omega_1 (c_\alpha - s_\alpha) \sin \frac{\xi}{2}$ referring to Eqs. 75 and 62. The effective Hamiltonian interacts with the density operator according to the Liouville-von Neumann equation (Eqs. 8 and 9). To simplify the calculation of the evolution, we define

$$\begin{aligned} I_{2\Sigma z} &= \frac{1}{2}(S_{2z} + I_z), & E_{I2\Sigma} &= 4I_{2\Sigma z}^2, & I_{2\Sigma}^+ &= S_2^+ I^+, & I_{2\Sigma}^- &= S_2^- I^-, \\ I_{2\Delta z} &= \frac{1}{2}(S_{2z} - I_z), & E_{I2\Delta} &= 4I_{2\Delta z}^2, & I_{2\Delta}^+ &= S_2^+ I^-, & I_{2\Delta}^- &= S_2^- I^+. \end{aligned} \quad (95)$$

The spin part of the evolving density operator results from the following derivation (θ is an arbitrary angle)

$$\begin{aligned}
& e^{-i\theta\frac{1}{2}(S_2^+I^+ + S_2^-I^-)S_1^\alpha} (S_{1z} + S_{2z})c.c. \\
& = e^{-i\theta I_{2z} S_1^\alpha} (S_{1z} + I_{2\Sigma z} + I_{2\Delta z})c.c. \\
& = S_{1z} + I_{2\Delta z} + S_1^\beta I_{2\Sigma z} + S_1^\alpha (I_{2\Sigma z} \cos \theta - I_{2\Sigma y} \sin \theta) \\
& = S_{1z} + \frac{1}{2}(S_{2z} - I_z) + \frac{1}{2}S_1^\beta (S_{2z} + I_z) \\
& \quad + \frac{1}{2}S_1^\alpha [(S_{2z} + I_z) \cos \theta + i(S_2^+I^+ - S_2^-I^-) \sin \theta].
\end{aligned} \tag{96}$$

Thus, the time-dependent density operator is

$$\begin{aligned}
\tilde{\rho}^* & = \frac{-\hbar}{Zk_B T} \frac{\omega_{1e} + \omega_{2e}}{2} \{S_{1z} + \frac{1}{2}(S_{2z} - I_z) + \frac{1}{2}S_1^\beta (S_{2z} + I_z) \\
& \quad + \frac{1}{2}S_1^\alpha (S_{2z} + I_z) \cos \tilde{\omega}_2^* t + \frac{i}{2}S_1^\alpha (S_2^+I^+ - S_2^-I^-) \sin \tilde{\omega}_2^* t\}.
\end{aligned} \tag{97}$$

According to Eqs. 87 and 88, the time-dependent nuclear polarization during DNP is

$$\langle P_n \rangle (t) = \frac{-\hbar}{Zk_B T} \frac{\omega_{1e} + \omega_{2e}}{2} \frac{1}{4} (1 + \cos \xi) (\cos \tilde{\omega}_2^* t - 1), \tag{98}$$

which in comparison with Eq. 86 indicates the maximal NMR enhancement $\frac{1}{4} \left| \frac{\gamma_e}{\gamma_n} \right|$. This

is of course the same result as contained in Eq. 92 when $\xi=90^\circ$ (see Eq. 62 for the exact

frequency matching). Note that when $\omega_M = \tilde{\omega}_{2e} - \tilde{\omega}_n - \frac{1}{2}D_d - \frac{1}{2}\tilde{A}_1$, the selected

$\frac{1}{2}(S_2^+I^+ + S_2^-I^-)S_1^\beta$ term (from Eq. 83 and the second line of 84b) yields the same

maximal DNP enhancement in this example.

Example 3

In this example, we assume that the microwave field is stronger than the difference of the selective frequencies (Eqs. 93 and 89), such as

$$\tilde{\omega}_1^* \text{ or } \tilde{\omega}_2^* > \left| \tilde{\omega}_{1e} + \frac{1}{4}\tilde{V} - \tilde{\omega}_{2e} + \tilde{\omega}_n \right| = \tilde{\Omega}. \quad (99)$$

and both the $S_{1x}S_2^\alpha I^\alpha$ and $\frac{1}{2}(S_2^+ I^+ + S_2^- I^-)S_1^\alpha$ terms (Eqs. 84a and 84b) are excited. In fact, $\tilde{\Omega}$ is usually small because it originates from the second order effect of the dipolar interactions and therefore is small compared to ω_1 . Using the condition in **Eq. 99** and $\xi=90^\circ$ (exact frequency matching), the effective microwave Hamiltonian becomes

$$\tilde{H}_M^{eff*} = \tilde{\omega}_3^* [S_{1x}S_2^\alpha I^\alpha + \frac{1}{2}(S_2^+ I^+ + S_2^- I^-)S_1^\alpha], \quad (100)$$

where $\tilde{\omega}_3^* = \frac{1}{\sqrt{2}}\omega_1(c_\alpha - s_\alpha)$ referring to Eq. 75. To propagate the density operator (through Eqs. 8 and 9), one needs the following recursive commutations:

Letting

$$\tilde{H}_{M3}^{eff*} = S_{1x}S_2^\alpha I^\alpha + \frac{1}{2}S_1^\alpha(S_2^+ I^+ + S_2^- I^-) = S_{1x}I_{2\Sigma}^\alpha + S_1^\alpha I_{2\Sigma x}, \quad (101)$$

we obtain

$$\begin{aligned} & [\tilde{H}_{M3}^{eff*}, S_{1z} + S_{2z}] \\ &= -iS_{1y}S_2^\alpha I^\alpha - \frac{1}{2}S_1^\alpha(S_2^+ I^+ - S_2^- I^-), \end{aligned} \quad (102a)$$

$$\begin{aligned}
& [\tilde{H}_{M3}^{eff*}, [\tilde{H}_{M3}^{eff*}, S_{1z} + S_{2z}]] \\
&= [\tilde{H}_{M3}^{eff*}, iS_{1y}S_2^\alpha I^\alpha + \frac{1}{2}S_1^\alpha (S_2^+ I^+ - S_2^- I^-)] \\
&= [S_{1x}I_{2\Sigma}^\alpha + S_1^\alpha I_{2\Sigma x}, iS_{1y}I_{2\Sigma}^\alpha + iS_1^\alpha I_{2\Sigma y}] \\
&= i(S_{1x}I_{2\Sigma}^\alpha S_{1y}I_{2\Sigma}^\alpha + S_{1x}I_{2\Sigma}^\alpha S_1^\alpha I_{2\Sigma y} + S_1^\alpha I_{2\Sigma x} S_{1y}I_{2\Sigma}^\alpha + S_1^\alpha I_{2\Sigma x} S_1^\alpha I_{2\Sigma y} \\
&\quad - S_{1y}I_{2\Sigma}^\alpha S_{1x}I_{2\Sigma}^\alpha - S_{1y}I_{2\Sigma}^\alpha S_1^\alpha I_{2\Sigma x} - S_1^\alpha I_{2\Sigma y} S_{1x}I_{2\Sigma}^\alpha - S_1^\alpha I_{2\Sigma y} S_1^\alpha I_{2\Sigma x}) \quad (102b) \\
&= i(\frac{i}{2}S_{1z}I_{2\Sigma}^\alpha + \frac{1}{2}S_1^- \frac{1}{2i}I_{2\Sigma}^+ + \frac{1}{2i}S_1^+ \frac{1}{2}I_{2\Sigma}^- + S_1^\alpha \frac{i}{2}I_{2\Sigma z} \\
&\quad - \frac{-i}{2}S_{1z}I_{2\Sigma}^\alpha - \frac{-1}{2i}S_1^- \frac{1}{2}I_{2\Sigma}^+ - \frac{1}{2}S_1^+ \frac{-1}{2i}I_{2\Sigma}^- - S_1^\alpha \frac{-i}{2}I_{2\Sigma z}) \\
&= -S_{1z}I_{2\Sigma}^\alpha + \frac{1}{2}S_1^- I_{2\Sigma}^+ + \frac{1}{2}S_1^+ I_{2\Sigma}^- - S_1^\alpha I_{2\Sigma z} \\
&= -S_1^\alpha S_2^\alpha I^\alpha + \frac{1}{2}S_1^\beta S_2^\alpha I^\alpha + \frac{1}{2}S_1^\alpha S_2^\beta I^\beta + \frac{1}{2}(S_1^+ S_2^- I^- + S_1^- S_2^+ I^+),
\end{aligned}$$

$$\begin{aligned}
& [\tilde{H}_{M3}^{eff*}, [\tilde{H}_{M3}^{eff*}, [\tilde{H}_{M3}^{eff*}, S_{1z} + S_{2z}]]] \\
&= [\tilde{H}_{M3}^{eff*}, -S_1^\alpha S_2^\alpha I^\alpha + \frac{1}{2}S_1^\beta S_2^\alpha I^\alpha + \frac{1}{2}S_1^\alpha S_2^\beta I^\beta + \frac{1}{2}(S_1^+ S_2^- I^- + S_1^- S_2^+ I^+)] \\
&= [S_{1x}I_{2\Sigma}^\alpha + S_1^\alpha I_{2\Sigma x}, -S_{1z}I_{2\Sigma}^\alpha + \frac{1}{2}S_1^- I_{2\Sigma}^+ + \frac{1}{2}S_1^+ I_{2\Sigma}^- - S_1^\alpha I_{2\Sigma z}] \\
&= -S_{1x}I_{2\Sigma}^\alpha S_{1z}I_{2\Sigma}^\alpha + S_{1x}I_{2\Sigma}^\alpha \frac{1}{2}S_1^- I_{2\Sigma}^+ + S_{1x}I_{2\Sigma}^\alpha \frac{1}{2}S_1^+ I_{2\Sigma}^- - S_{1x}I_{2\Sigma}^\alpha S_1^\alpha I_{2\Sigma z} \\
&\quad - S_1^\alpha I_{2\Sigma x} S_{1z}I_{2\Sigma}^\alpha + S_1^\alpha I_{2\Sigma x} \frac{1}{2}S_1^- I_{2\Sigma}^+ + S_1^\alpha I_{2\Sigma x} \frac{1}{2}S_1^+ I_{2\Sigma}^- - S_1^\alpha I_{2\Sigma x} S_1^\alpha I_{2\Sigma z} \\
&\quad + S_{1z}I_{2\Sigma}^\alpha S_{1x}I_{2\Sigma}^\alpha - \frac{1}{2}S_1^- I_{2\Sigma}^+ S_{1x}I_{2\Sigma}^\alpha - \frac{1}{2}S_1^+ I_{2\Sigma}^- S_{1x}I_{2\Sigma}^\alpha + S_1^\alpha I_{2\Sigma z} S_{1x}I_{2\Sigma}^\alpha \\
&\quad + S_{1z}I_{2\Sigma}^\alpha S_1^\alpha I_{2\Sigma x} - \frac{1}{2}S_1^- I_{2\Sigma}^+ S_1^\alpha I_{2\Sigma x} - \frac{1}{2}S_1^+ I_{2\Sigma}^- S_1^\alpha I_{2\Sigma x} + S_1^\alpha I_{2\Sigma z} S_1^\alpha I_{2\Sigma x} \quad (102c) \\
&= \frac{i}{2}S_{1y}I_{2\Sigma}^\alpha + \frac{1}{4}S_1^\alpha I_{2\Sigma}^+ + 0 - \frac{1}{4}S_1^- I_{2\Sigma}^\alpha \\
&\quad - \frac{1}{4}S_1^\alpha I_{2\Sigma}^- + 0 + \frac{1}{4}S_1^+ I_{2\Sigma}^\alpha + \frac{i}{2}S_1^\alpha I_{2\Sigma y} \\
&\quad + \frac{i}{2}S_{1y}I_{2\Sigma}^\alpha + 0 - \frac{1}{4}S_1^\alpha I_{2\Sigma}^- + \frac{1}{4}S_1^+ I_{2\Sigma}^\alpha \\
&\quad + \frac{1}{4}S_1^\alpha I_{2\Sigma}^+ - \frac{1}{4}S_1^- I_{2\Sigma}^\alpha + 0 + \frac{i}{2}S_1^\alpha I_{2\Sigma y} \\
&= 2iS_{1y}I_{2\Sigma}^\alpha + 2iS_1^\alpha I_{2\Sigma y} \\
&= 2[iS_{1y}S_2^\alpha I^\alpha + \frac{1}{2}S_1^\alpha (S_2^+ I^+ - S_2^- I^-)].
\end{aligned}$$

Thus, the time-dependent density operator is obtained by summing Eqs. 102a-c as

$$\begin{aligned}
\tilde{\rho}^* &= \frac{-\hbar}{Zk_B T} \frac{\omega_{e1} + \omega_{e2}}{2} \{S_{1z} + S_{2z} \\
&+ [-\frac{1}{2}S_1^\alpha S_2^\alpha I^\alpha + \frac{1}{4}S_1^\beta S_2^\alpha I^\alpha + \frac{1}{4}S_1^\alpha S_2^\beta I^\beta + \frac{1}{4}(S_1^- S_2^+ I^+ + S_1^+ S_2^- I^-)] [1 - \cos\sqrt{2\tilde{\omega}_3^* t}] \\
&+ \frac{1}{\sqrt{2}} [S_{1y} S_2^\alpha I^\alpha + \frac{1}{2i} S_1^\alpha (S_2^+ I^+ - S_2^- I^-)] \sin\sqrt{2\tilde{\omega}_3^* t}\}.
\end{aligned} \quad (103)$$

Since $\xi=90^\circ$, the nuclear polarization operator is simplified to

$$\tilde{P}_n^* = \frac{3}{4}I_z + \frac{1}{4}S_{1z} - \frac{1}{4}S_{2z} + S_{1z}S_{2z}I_z + \frac{1}{2}(S_1^+ S_2^- I^- e^{i\tilde{\Omega}t} + S_1^- S_2^+ I^+ e^{-i\tilde{\Omega}t}). \quad (104)$$

Therefore following Eqs. 87 and 104, the time-dependent nuclear polarization is

$$\langle P_n \rangle (t) = \text{tr}(\tilde{P}_n^* \tilde{\rho}^*) = \frac{\hbar}{Zk_B T} \frac{\omega_{e1} + \omega_{e2}}{2} \sin^2(\frac{1}{2}\tilde{\Omega}t) \sin^2(\frac{\sqrt{2}}{2}\tilde{\omega}_3^* t) \quad (105)$$

Eq. 105 shows that the polarization transfer rate is determined by the smaller of $\frac{1}{2}\tilde{\Omega}$ and $\frac{\sqrt{2}}{2}\tilde{\omega}_3^*$. Comparing Eqs. 105 and 86, we find the maximal enhancement of

nuclear polarization is equal to $\frac{1}{2} \left| \frac{\gamma_e}{\gamma_n} \right|$.

Example 4

As in Example 3, we assume that the microwave irradiation is sufficiently broadband to cover two frequencies (differing by $D_d + \tilde{A}_1 + \tilde{\Omega}$ due to dipolar interactions):

$$\tilde{\omega}_{2e} + \frac{1}{2}D_d - \tilde{\omega}_n + \frac{1}{2}\tilde{A}_1 \quad \text{and} \quad \tilde{\omega}_{1e} - \frac{1}{2}D_d - \frac{1}{2}\tilde{A}_1 + \frac{1}{4}\tilde{V}, \quad (106)$$

which select $\frac{1}{2}(S_2^+ I^+ + S_2^- I^-)S_1^\alpha$ and $S_{1x}S_2^\beta I^\beta$ terms (in Eqs. 84a and 84b) to be the

effective excitation Hamiltonian. With additional assumptions that s_α is small (see Eq. 75) and $\xi = 90^\circ$ (exact frequency matching), the effective microwave Hamiltonian becomes

$$\tilde{H}_M^{eff*} = \tilde{\omega}_4^* [\frac{1}{2} S_1^\alpha (S_2^+ I^+ + S_2^- I^-) + S_{1x} S_2^\beta I^\beta], \quad (107)$$

where $\tilde{\omega}_4^* = \frac{1}{\sqrt{2}} \omega_1$. To calculate the time-dependent density operator (through Eqs. 8 and 9), one needs the following recursive commutation relationships:

Letting

$$\tilde{H}_{M4}^{eff*} = S_{1x} S_2^\beta I^\beta + \frac{1}{2} S_1^\alpha (S_2^+ I^+ + S_2^- I^-) = S_{1x} I_{2\Sigma}^\beta + S_1^\alpha I_{2\Sigma x}, \quad (108)$$

we obtain

$$\begin{aligned} & [\tilde{H}_{M4}^{eff*}, S_{1z} + S_{2z}] \\ &= -i S_{1y} S_2^\beta I^\beta - \frac{1}{2} S_1^\alpha (S_2^+ I^+ - S_2^- I^-), \end{aligned} \quad (109a)$$

$$\begin{aligned} & [\tilde{H}_{M4}^{eff*}, [\tilde{H}_{M4}^{eff*}, S_{1z} + S_{2z}]] \\ &= [\tilde{H}_{M4}^{eff*}, i S_{1y} S_2^\beta I^\beta + \frac{1}{2} S_1^\alpha (S_2^+ I^+ - S_2^- I^-)] \\ &= [S_{1x} I_{2\Sigma}^\beta + S_1^\alpha I_{2\Sigma x}, i S_{1y} I_{2\Sigma}^\beta + i S_1^\alpha I_{2\Sigma y}] \\ &= i(S_{1x} I_{2\Sigma}^\beta S_{1y} I_{2\Sigma}^\beta + S_{1x} I_{2\Sigma}^\beta S_1^\alpha I_{2\Sigma y} + S_1^\alpha I_{2\Sigma x} S_{1y} I_{2\Sigma}^\beta + S_1^\alpha I_{2\Sigma x} S_1^\alpha I_{2\Sigma y} \\ &\quad - S_{1y} I_{2\Sigma}^\beta S_{1x} I_{2\Sigma}^\beta - S_1^\alpha I_{2\Sigma y} S_{1x} I_{2\Sigma}^\beta - S_{1y} I_{2\Sigma}^\beta S_1^\alpha I_{2\Sigma x} - S_1^\alpha I_{2\Sigma y} S_1^\alpha I_{2\Sigma x}) \quad (109b) \\ &= i(\frac{i}{2} S_{1z} I_{2\Sigma}^\beta - \frac{1}{4i} S_1^- I_{2\Sigma}^- + \frac{1}{4i} S_1^+ I_{2\Sigma}^+ + \frac{i}{2} S_1^\alpha I_{2\Sigma z} \\ &\quad + \frac{i}{2} S_{1z} I_{2\Sigma}^\beta - \frac{1}{4i} S_1^+ I_{2\Sigma}^+ + \frac{1}{4i} S_1^- I_{2\Sigma}^- + \frac{i}{2} S_1^\alpha I_{2\Sigma z}) \\ &= -S_{1z} I_{2\Sigma}^\beta - S_1^\alpha I_{2\Sigma z} \\ &= -S_{1z} S_2^\beta I^\beta - \frac{1}{2} S_1^\alpha (S_2^+ I^+ - S_2^- I^-), \end{aligned}$$

$$\begin{aligned}
& [\tilde{H}_{M4}^{eff*}, [\tilde{H}_{M4}^{eff*}, [\tilde{H}_{M4}^{eff*}, S_{1z} + S_{2z}]]] \\
&= [\tilde{H}_{M4}^{eff*}, S_{1z} S_2^\beta I^\beta + \frac{1}{2} S_1^\alpha (S_2^\alpha I^\alpha - S_2^\beta I^\beta)] \\
&= [S_{1x} I_{2\Sigma}^\beta + S_1^\alpha I_{2\Sigma x}, S_{1z} I_{2\Sigma}^\beta + S_1^\alpha I_{2\Sigma z}] \\
&= S_{1x} I_{2\Sigma}^\beta S_{1z} I_{2\Sigma}^\beta + S_{1x} I_{2\Sigma}^\beta S_1^\alpha I_{2\Sigma z} + S_1^\alpha I_{2\Sigma x} S_{1z} I_{2\Sigma}^\beta + S_1^\alpha I_{2\Sigma x} S_1^\alpha I_{2\Sigma z} \\
&\quad - S_{1z} I_{2\Sigma}^\beta S_{1x} I_{2\Sigma}^\beta - S_1^\alpha I_{2\Sigma z} S_{1x} I_{2\Sigma}^\beta - S_{1z} I_{2\Sigma}^\beta S_1^\alpha I_{2\Sigma x} - S_1^\alpha I_{2\Sigma z} S_1^\alpha I_{2\Sigma x} \\
&= \frac{-i}{2} S_{1y} I_{2\Sigma}^\beta - \frac{1}{4} S_1^- I_{2\Sigma}^\beta + \frac{1}{4} S_1^+ I_{2\Sigma}^+ - \frac{i}{2} S_1^\alpha I_{2\Sigma y} \\
&\quad - \frac{i}{2} S_{1y} I_{2\Sigma}^\beta + \frac{1}{4} S_1^+ I_{2\Sigma}^\beta - \frac{1}{4} S_1^\alpha I_{2\Sigma}^- - \frac{i}{2} S_1^\alpha I_{2\Sigma y} \\
&= -\frac{i}{2} S_{1y} I_{2\Sigma}^\beta - \frac{i}{2} S_1^\alpha I_{2\Sigma y} \\
&= -\frac{i}{2} S_{1y} S_2^\beta I^\beta - \frac{1}{4} S_1^\alpha (S_2^+ I^+ - S_2^- I^-).
\end{aligned} \tag{109c}$$

Thus, the time-dependent density operator is obtained from summarizing Eqs. 109a-c as

$$\begin{aligned}
\tilde{\rho}^* &= \frac{-\hbar}{Zk_B T} \frac{\omega_{e1} + \omega_{e2}}{2} \{ (S_{1z} + S_{2z}) \\
&\quad - 2[S_{1z} S_2^\beta I^\beta + \frac{1}{2} S_1^\alpha (S_2^\alpha I^\alpha - S_2^\beta I^\beta)] [1 - \cos(\frac{1}{\sqrt{2}} \tilde{\omega}_4^* t)] \\
&\quad - \sqrt{2} [S_{1y} S_2^\beta I^\beta + \frac{1}{2i} S_1^\alpha (S_2^+ I^+ - S_2^- I^-)] \sin(\frac{1}{\sqrt{2}} \tilde{\omega}_4^* t) \}.
\end{aligned} \tag{110}$$

And the time-dependent nuclear polarization is calculated from Eqs. 87 and 88 as

$$\langle P_n \rangle (t) = \frac{-\hbar}{Zk_B T} \frac{\omega_{e1} + \omega_{e2}}{2} [-1 + \cos(\frac{1}{\sqrt{2}} \tilde{\omega}_4^* t)], \tag{111}$$

which in comparison with the initial nuclear polarization (Eq. 86) implies a maximal DNP enhancement of $|\gamma_e/\gamma_n|$.

Example 5

In this example we assume that the microwave frequency is broadband and the irradiation amplitude is strong. We therefore excited the following four

transitions— $S_{1x}S_2^\alpha I^\alpha$, $S_{1x}S_2^\beta I^\beta$, $\frac{1}{2}S_1^\alpha(S_2^+I^+ + S_2^-I^-)$ and $-\frac{1}{2}S_1^\beta(S_2^+I^+ + S_2^-I^-)$ — near the microwave frequency of ω_{e1} . On the assumption that s_α and s_β are small (see Eq. 75) and $\xi = 90^\circ$ (exact frequency matching), the effective microwave Hamiltonian is the sum of the above four transitions. This effective Hamiltonian is further simplified as (using the definitions in Eq. 95)

$$\tilde{H}_M^{eff*} = \tilde{\omega}_5^*(S_{1x}E_{I2\Sigma} + 2S_{1z}I_{2\Sigma x}), \quad (112)$$

where $\tilde{\omega}_5^* = \frac{1}{\sqrt{2}}\omega_1$. To propagate the density operator according to Eqs. 8 and 9 in a easier way, one needs to rewrite the initial density operator (Eq. 85) as

$$\tilde{\rho}_0^* = \frac{-\hbar}{Zk_B T} \frac{\omega_{e1} + \omega_{e2}}{2} (S_{1z}E_{I2\Sigma} + S_{1z}E_{I2\Delta} + I_{2\Sigma z} + I_{2\Delta z}). \quad (113)$$

Following commutation relationships, the $S_{1x}E_{I2\Sigma}$ and $S_{1z}I_{2\Sigma x}$ terms of the effective microwave Hamiltonian in Eq. 112 affect the $S_{1z}E_{I2\Sigma}$ and $I_{2\Sigma z}$ terms in the density operator in Eq. 113, respectively. Therefore, the time-dependent density operator becomes

$$\begin{aligned} \tilde{\rho}^* &= \frac{-\hbar}{Zk_B T} \frac{\omega_{e1} + \omega_{e2}}{2} \{ (S_{1z} + S_{2z}) \\ &+ \frac{1}{2} (S_{1z}E_{I2\Sigma} - 2S_{1y}I_{2\Sigma y} - 2S_{1x}I_{2\Sigma x} + I_{2\Sigma z}) [\cos(\sqrt{2}\tilde{\omega}_5^*t) - 1] \\ &- \frac{1}{\sqrt{2}} (S_{1y}E_{I2\Sigma} + 2S_{1z}I_{2\Sigma y}) \sin(\sqrt{2}\tilde{\omega}_5^*t) \}. \end{aligned} \quad (114)$$

Thus, the time-dependent nuclear polarization becomes (from Eqs. 87 and 88)

$$\langle P_n \rangle (t) = \frac{-\hbar}{Zk_B T} \frac{\omega_{e1} + \omega_{e2}}{2} \left(-2 \sin^2 \frac{\tilde{\Omega} t}{2} \sin^2 \frac{\tilde{\omega}_5^* t}{\sqrt{2}} \right), \quad (115)$$

which in comparison with the initial nuclear polarization (Eq. 86) indicates a maximum DNP enhancement of $|\gamma_e/\gamma_n|$. The maximal DNP enhancements and time-dependence of nuclear polarization from the examples 1 to 5 for microwave irradiation frequency near ω_{e1} are summarized in Table 6.1.

Table 6.1. The effective excitation Hamiltonians and the corresponding microwave frequencies that produce positive DNP enhancements are listed. The selection of excitation depends on the microwave bandwidth and amplitude. The maximal enhancement and Rabi oscillation characterize the time dependence of the nuclear polarization. The results are based on small ζ_α and ζ_β (moderate electron-electron dipolar interaction) and $\xi = 90^\circ$ (full three-spin mixing).

Effective excitation \tilde{H}_M^{eff*}	Microwave frequency ω_M	Selected excitations by ω_M (Checked by crosses)			
$S_{1x} S_2^\alpha I^\alpha$	$\tilde{\omega}_{1e} + \frac{1}{2} D_d + \frac{1}{2} \tilde{A}_1 + \frac{1}{4} \tilde{V}$	X	X		X
$\frac{1}{2} S_1^\alpha (S_2^+ I^+ + S_2^- I^-)$	$\tilde{\omega}_{2e} + \frac{1}{2} D_d - \tilde{\omega}_n + \frac{1}{2} \tilde{A}_1$		X	X	X
$S_{1x} S_2^\beta I^\beta$	$\tilde{\omega}_{1e} - \frac{1}{2} D_d - \frac{1}{2} \tilde{A}_1 + \frac{1}{4} \tilde{V}$			X	X
$-\frac{1}{2} S_1^\beta (S_2^+ I^+ + S_2^- I^-)$	$\tilde{\omega}_{2e} - \frac{1}{2} D_d - \tilde{\omega}_n - \frac{1}{2} \tilde{A}_1$				X
Maximal enhancement of nuclear polarization		$\frac{1}{4} \left \frac{\gamma_e}{\gamma_n} \right $	$\frac{1}{2} \left \frac{\gamma_e}{\gamma_n} \right $	$\left \frac{\gamma_e}{\gamma_n} \right $	$\left \frac{\gamma_e}{\gamma_n} \right $
Oscillation between electron and nuclear polarizations		$\frac{1}{2} (1 - \cos \frac{\omega_1 t}{\sqrt{2}})$	$\sin^2 \frac{\tilde{\Omega} t}{2} \sin^2 \frac{\omega_1 t}{2}$	$\frac{1}{2} (1 - \cos \frac{\omega_1 t}{\sqrt{2}})$	$\sin^2 \frac{\tilde{\Omega} t}{2} \sin^2 \frac{\omega_1 t}{2}$

6.1.3. Discussion

We have shown systematic diagonalization of multiple spin Hamiltonian and derived the effective microwave irradiation Hamiltonian that leads to the evolution of

electron Zeeman order into nuclear Zeeman order and yields DNP. It is worthy of emphasizing the frequency matching conditions for polarization transfers in the SE and CE mechanisms, and comparing influences of microwave irradiation strength ω_1 and static magnetic field B_0 on those polarizing mechanisms to protrude the favorability of the CE at high magnetic fields.

6.1.3.1. Frequency matching conditions for DNP

The frequency matching requirements for both the SE and CE are mentioned in the literature^{50, 58, 67}. However, the exact EPR and microwave frequencies, depending on the specific electron–electron and electron–nuclear interactions are ignored due to the presence of relaxation in realistic spin systems. Nonetheless, those exact frequencies become interesting as we attempt to understand polarizing mechanisms using quantum dynamics of ideal spin systems. According to Eqs. 22a, 22b and 17a, the exact frequency matching for the SE is $\omega_M = \omega_{e1} \pm \tilde{\omega}_n$. Taylor expansions of the cosine and sine terms in Eq. 17a show

$$\tilde{\omega}_n \approx \omega_n + \frac{B_1^2}{4\omega_n}, \quad (116)$$

which is consistent with a second order perturbation of the semisecular hyperfine interaction B_1 . Since B_1 is usually small and thus $B_1^2 \ll \omega_n$, the microwave frequency generally matches $\omega_{e1} \pm \omega_n$. Without relaxation, the frequency matching allows the nuclear polarization to be enhanced through an oscillation of polarization between the electron and nuclear spin systems. The maximum enhancement in the oscillation is $|\gamma_e/\gamma_n|$.

Efficient microwave excitation for the CE relies on the full mixing of states which

according to Eqs. 52 and 44a exactly requires $\tilde{\omega}_\Delta = \pm\omega_n$. Taylor expansions of the cosine and sine terms in Eq. 44a yield

$$\tilde{\omega}_\Delta \approx \omega_\Delta + \frac{D_o^2}{\omega_\Delta}, \quad (117)$$

where $\omega_\Delta = \omega_{e1} - \omega_{e2}$ (see Eq. 34), and the result is consistent with a second order perturbation of the off-diagonal electron–electron interactions D_o . It is obvious that electron–electron interactions affect the matching condition for the EPR frequency separation. While the derivations of the CE in the above discussion are primarily based on moderate electron–electron interactions, the frequency matching for the CE in the region of extremely strong electron–electron interactions is discussed in Appendix I.

Furthermore, the microwave transitions for the CE are excited by microwave irradiation at $\omega_M \sim \omega_{e1}$ or $\omega_M \sim \omega_{e2}$. Those transitions are divided into two groups of four transitions at the exact microwave frequencies shown in Eqs. 84a and 84b. Without relaxation, the correct EPR and microwave frequencies allow the nuclear polarization to be enhanced through various oscillations depending on selected transitions:

(1) When microwave irradiation is narrowband and weak, thus choosing only one of the four transitions, the oscillation between the electron and nuclear polarizations contains one frequency $\sim \frac{\omega_1}{\sqrt{2}}$ and leads to a maximum nuclear polarization enhancement $|\gamma_e/\gamma_n|/4$.

(2) When microwave irradiation is narrowband and strong, thus choosing only two of the four transitions that are separated by $\tilde{\Omega}$ (usually small due to a second-order

effect of spin-spin interactions, see Eq. 64), the oscillation between the electron and nuclear polarizations contains two frequencies $\frac{\tilde{\Omega}}{2}$ and $\sim \frac{\omega_1}{2}$, and leads to a maximum nuclear polarization enhancement $|\gamma_e/\gamma_n|/2$.

(3) When microwave irradiation is broadband and weak, thus choosing only two of the four transitions that are separated by $D_d + \tilde{A}_1 + \tilde{\Omega}$ (usually large due to the first-order electron–electron interactions), the oscillation between the electron and nuclear polarizations contains one frequency $\sim \frac{\omega_1}{\sqrt{2}}$ and leads to a maximum nuclear polarization enhancement $|\gamma_e/\gamma_n|$.

(4) When microwave irradiation is broadband and strong, thus choosing all of the four transitions despite their separations in excitation frequency, the oscillation between the electron and nuclear polarizations contains two frequencies $\frac{\tilde{\Omega}}{2}$ and $\sim \frac{\omega_1}{2}$, and leads to a maximum nuclear polarization enhancement of $|\gamma_e/\gamma_n|$.

The frequency matching conditions derived in this sub-chapter appear to be independent of the microwave field strength ω_1 because we generally assume weak microwave field perturbations given that ω_1 leaves the eigenstates unaffected. However, in practical DNP experiments it is often the case that a strong microwave field strength is available; thus the matching condition would break down, the couplings between the mixed states would become less effective, and the polarization transfer would be attenuated. This ω_1 disturbance to the frequency matching is more serious in the CE where the effective couplings for state-mixing result from a second order effect of spin-spin interactions as opposed to a first order interaction in the SE. Nevertheless, in reality the frequency matching range for DNP can be broadened by relaxation and in the case of

CE is further increased by strong electron–electron interactions.

6.1.3.2. Influences of microwave field and external magnetic field strengths on DNP

Except for the perturbation of microwave irradiation to the eigenstates of a spin system, microwave field strength ω_1 affects the efficiency of DNP. According to Fermi's golden rule, the polarization rate approximates the initial slope of the involved oscillation between the electron and nuclear polarizations. In the SE, the polarization rate approximates the first term of the Taylor expansion of Eq. 30, which is $\sim(B_1\omega_1/\omega_n)^2$ under the assumption of $A_1 \ll \omega_n$; note that A_1 and B_1 represent secular and semiseccular hyperfine interactions. This result indicates that the efficiency of the SE is proportional to PB_0^{-2} , where P is the microwave power P as $P \propto \omega_1^2$, and B_0 is the external magnetic field.

In the CE, the time-dependent nuclear polarization oscillates in a more complicated manner. For the positive DNP enhancements, the strong microwave irradiation excites all of the four transitions mentioned previously, and the smaller of $\frac{\tilde{\Omega}}{2}$ and $\frac{\omega_1}{2}$ determines the oscillating envelope of the DNP enhancement and yields an initial slope which is either $(\frac{\tilde{\Omega}}{2})^2$ or $(\frac{\omega_1}{2})^2$. Thus, when $\omega_1 \ll \tilde{\Omega}$, the polarization rate is proportional to $(\omega_1)^2$ or P , and so is the DNP enhancement. When $\omega_1 \sim \tilde{\Omega}$, the DNP efficiency becomes independent of the microwave power, and a saturation of the DNP enhancement by the microwave power is reached.

The magnetic field effect on a single CE process is reflected by $\tilde{\Omega}$ which is a second-order effect with respect to electron–electron dipole, hyperfine and nuclear

Zeeman interactions. However, typical DNP enhancements result from many polarization processes with variations of the involved dipolar interactions that compensate for the difference of B_0 . Hence B_0 does not explicitly affect the CE through $\tilde{\Omega}$, especially when the oscillation of enhanced nuclear polarization is controlled by ω_1 . In fact, external magnetic fields affect the CE through frequency matching that requires the correct EPR frequency separation. When the desirable frequency separation is obtained from a broad EPR lineshape, the probability of frequency matching is linearly decreased by the linewidth. If the line broadening is primarily due to a g -anisotropy which scales with B_0 , then the overall DNP enhancement through the CE is proportional to B_0^{-1} . This magnetic field dependence is common for DNP using nitroxide radicals which exhibit relatively well resolved g -anisotropies at high magnetic fields.

6.1.4. Conclusions

The enhanced nuclear polarization in the CE polarizing mechanism is calculated in an electron–electron–nucleus system under the microwave irradiation. Our calculations verify the frequency matching which requires the correct EPR frequency separation and microwave frequency. Based on our theory, the influences of microwave field strength and external magnetic field on DNP are consistent with the conclusions of classical theories established on spin thermodynamics. Although stringent frequency matching conditions are inferred by our analytical approaches, they can be relaxed when relaxation effects are incorporated into the calculations. Simulations of DNP in electron–electron–nucleus systems with relaxation are discussed in section 6.2.

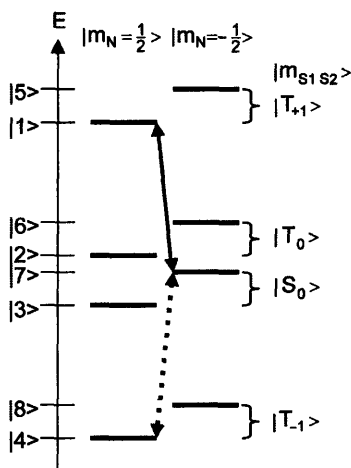
Appendix I: Strong electron–electron interactions in the three-spin system

Although the analytical approach to an electron–electron–nucleus system includes conditions of stronger electron–electron interactions, the overall discussion has implied that such interactions are much smaller than the nuclear Larmor frequency. Thus the required frequency separation in the EPR spectrum is mainly provided by the electron Zeeman interaction. However, the dipolar splittings can contribute to the EPR frequency separation. Specifically in the case with a small difference in g -values, the triplet-singlet basis-sets are more relevant than spin-pair bases in discussions of frequency matching for the CE. For example, if the electron–electron interaction terms d and J in Eq. 31 are larger than $|\omega_{e2}-\omega_{e1}|$, it is appropriate to represent the spin Hamiltonian in the electron triplet-singlet bases. The transformation from electron spin-pair bases to triplet-singlet bases involves

$$\begin{aligned} |T_1\rangle &= |\alpha\alpha\rangle, \quad |T_{-1}\rangle = |\beta\beta\rangle, \quad |T_0\rangle = \frac{1}{\sqrt{2}}(|\alpha\beta\rangle + |\beta\alpha\rangle), \\ |S_0\rangle &= \frac{1}{\sqrt{2}}(|\alpha\beta\rangle - |\beta\alpha\rangle). \end{aligned} \quad (118)$$

Therefore, we should redraw Figure 6.4 as Figure 6.6. If $|D_o| \sim |\omega_n|$, $|2\rangle$ and $|7\rangle$ come close to degeneracy, then these two states are fully mixed into $|2'\rangle$ and $|7'\rangle$ by H_{27} . According to the selection rules involving the triplet-singlet bases, the transitions, $|2'\rangle \leftrightarrow |1\rangle$ and $|7'\rangle \leftrightarrow |4\rangle$, are excited by microwave irradiation near E_{12} and E_{24} and lead to positive and negative DNP enhancements, respectively. Note that the two EPR peaks in this case are separated by $E_{12} - E_{24} = |D_d - D_o|$ since the EPR transitions are also near E_{12} and E_{24} . With negligible J , the definition in Eq. 34 suggests the two EPR peaks are

actually separated by $3\omega_n$ and the matching condition requires $d \sim \omega_n$.



EPR

$$E_{12} = \frac{\omega_{e1} + \omega_{e2}}{2} + \frac{D_d}{2} - \frac{D_o}{2} + \frac{A_1 + A_2}{4}$$

$$E_{24} = \frac{\omega_{e1} + \omega_{e2}}{2} - \frac{D_d}{2} + \frac{D_o}{2} + \frac{A_1 + A_2}{4}$$

$$E_{56} = \frac{\omega_{e1} + \omega_{e2}}{2} + \frac{D_d}{2} - \frac{D_o}{2} - \frac{A_1 + A_2}{4}$$

$$E_{68} = \frac{\omega_{e1} + \omega_{e2}}{2} - \frac{D_d}{2} + \frac{D_o}{2} - \frac{A_1 + A_2}{4}$$

forbidden EPR

$$E_{13} = \frac{\omega_{e1} + \omega_{e2}}{2} + \frac{D_d}{2} + \frac{D_o}{2} + \frac{A_1 + A_2}{4}$$

$$E_{34} = \frac{\omega_{e1} + \omega_{e2}}{2} - \frac{D_d}{2} - \frac{D_o}{2} + \frac{A_1 + A_2}{4}$$

$$E_{57} = \frac{\omega_{e1} + \omega_{e2}}{2} + \frac{D_d}{2} + \frac{D_o}{2} - \frac{A_1 + A_2}{4}$$

$$E_{78} = \frac{\omega_{e1} + \omega_{e2}}{2} - \frac{D_d}{2} - \frac{D_o}{2} - \frac{A_1 + A_2}{4}$$

NMR

$$E_{51} = \omega_n - \frac{A_1 + A_2}{2}$$

$$E_{62} = \omega_n$$

$$E_{73} = \omega_n$$

$$E_{84} = \omega_n + \frac{A_1 + A_2}{2}$$

e-n Coupling

$$H_{15} = H_{51} = \frac{B_1 + B_2}{4}$$

$$H_{27} = H_{72} = \frac{B_1 - B_2}{4}$$

$$H_{36} = H_{63} = \frac{B_1 - B_2}{4}$$

$$H_{48} = H_{84} = -\frac{B_1 + B_2}{4}$$

T_0 - S_0 Coupling

$$H_{23} = H_{32} = \frac{\omega_{e1} - \omega_{e2}}{2} + \frac{A_1 - A_2}{4}$$

$$H_{67} = H_{76} = \frac{\omega_{e1} - \omega_{e2}}{2} - \frac{A_1 - A_2}{4}$$

Figure 6.6. A level diagram for a triplet-singlet-nucleus system. The variables in the expression of transition and coupling energies are defined in Section 6.1.2.3. Because of the forbidden EPR transitions associated with the singlet state, only half of the DNP transitions are allowed. They are marked by the solid and dashed arrows for positive and negative DNP enhancements, respectively.

6.2. Simulation of Electron–Electron–Nucleus Spin Systems with Relaxation

6.2.1. Introduction

DNP in solid dielectrics relies on mechanisms such as the solid effect (SE)⁵⁰, cross effect (CE)^{2, 51-55, 106}, and thermal mixing (TM)^{58, 67}. In particular, the CE and TM provide the major pathways for DNP using biradicals consisting of two chemically tethered nitroxide radicals as Chapters 3, 4 discussed. While the SE universally involves a nuclear spin and an electron spin, the CE or TM occurs between a nucleus and two or multiple electrons, respectively. With contemporary computing power, we can numerically simulate the spin dynamics involving one nucleus and a number of electrons, and thus, the fundamentals of the SE, the CE and TM can be understood in greater detail. In this sub-chapter, we focus on a numerical study of the CE mechanism which provides the optimal polarizing efficiency in high magnetic fields and can be improved by using designer biradicals in which the tethered radicals correspond to the two electrons involving the CE mechanism. In addition, the SE emerges from the electron and nuclear spin system for the CE and is simulated to compare its polarizing efficiency.

Classical theories describing DNP are based largely on concepts emerging from spin temperature^{50, 56}, and do not explicitly describe DNP experiments using biradicals quantum mechanically. Specifically, in a biradical the intermolecular electron dipole interaction (~0.3 MHz in a 10 mM solution) is typically small compared to the intramolecular coupling (~23 MHz for a radical with a 13 Å interelectron distance). Thus, CE experiments involving biradicals are best described with a quantum mechanical

treatment of a three-spin system. Such an approach to an electron–electron–nucleus system was utilized by Jeschke to explain the generation of the nuclear coherence and polarization from transient electron polarization in CIDNP experiments^{73, 160}. Moreover, for the same three-spin system, we recently completed an analysis of the dynamics of spin interactions and successfully described the CE and SE in the presence of a strong external magnetic field and weakly perturbing microwave fields (see Section 6.1). From the calculations, based on a treatment of a localized electron–electron–nucleus spin system, emerges the exact frequency matching condition for frequency separation of the EPR lines and the microwave irradiation. However, relaxation effects were not considered despite their importance in maintaining frequency matching among the EPR frequencies in the randomly oriented powder sample of radical molecules.

Traditional relaxation theories, such as the Bloch equation and the Redfield theory, fail to describe incoherent processes in a quantum dynamic system with strong mixing of quantum states. Specifically, even though Bloch equations provide a simple way to introduce phenomenological relaxation parameters, the assignment of relaxation times to the Cartesian magnetization operators¹³ cannot be well defined because of the strong mixing of spin-states. Further, while Redfield theory is more rigorous in terms of its derivation from a time-dependent second order perturbation with respect to spin interactions, it does require definite spin eigenstates and correlation functions for evaluating the relaxation super operator¹³. Therefore with strong state-mixing it presents complexities and becomes nontrivial for a treatment of phenomenological relaxation.

Recently, a Stochastic Liouville equation (SLE) approach was developed that permits a phenomenological description of incoherent quantum dynamics¹⁶³. In this sub-

chapter, we employ the SLE approach to incorporate relaxation in an electron–electron–nucleus spin system for both the CE and SE. In Section 6.2.2, we discuss the modification and adaptation of SLE to the three-spin system. Because of the complexity of analytically solving the three-spin SLE, a numerical treatment of the quantum dynamics is implemented with empirical simulation parameters. The results of the simulations are illustrated in Section 6.2.3 and used to explain dependence of DNP enhancements on a number of spectral parameters, such as the microwave field strength, spin-spin interactions, relaxation and the external magnetic field strength. In addition to be consistent with conclusions of classical DNP theories, the numerical results of the three-spin simulations including relaxation provide insights into the improvement of DNP enhancements using designer biradicals.

6.2.2. Stochastic Liouville equations in a three-spin system

If we assume that nuclear spin diffusion efficiently distributes polarization throughout a bulk sample, then the DNP process in the bulk nuclear spin system can be understood by examining microscopic polarization transfers within a localized electron–electron–nucleus system. For the three-spin system, the time-independent Hamiltonian H_0 and microwave Hamiltonian H_M are given by

$$H_0 = \omega_{e1}S_{1z} + \omega_{e2}S_{2z} - \omega_n I_z + (A_1S_{1z} + A_2S_{2z})I_z + (B_1S_{1z} + B_2S_{2z})I_x + d(3S_{1z}S_{2z} - \mathbf{S}_1 \cdot \mathbf{S}_2) - 2JS_1 \cdot \mathbf{S}_2, \quad (119)$$

and

$$H_M = 2\omega_1 \cos(\omega_M t)(S_{1x} + S_{2x}), \quad (120)$$

where ω_{e1} , ω_{e2} and ω_n are the Larmor frequencies of the two electrons and the nucleus, respectively, d and J are the dipolar interaction and exchange integral between electrons, respectively, A_1 , A_2 and B_1 , B_2 are coefficients for secular and semisecular hyperfine terms, respectively, ω_M and ω_1 are the frequency and strength of the microwave fields. Both the electron–electron and electron–nuclear dipolar interactions are truncated by the high EPR frequency, and $S_{1z}I_x$ and $S_{2z}I_x$ represent the semisecular terms adequately after rotational transformations along $S_{1z}I_z$ and $S_{2z}I_z$, respectively. Moreover, the calculations mentioned here use isotropic values of EPR frequency and dipolar interaction, thus neglecting anisotropies of those spin interactions involved.

Spin relaxation plays a crucial role in the CE and is especially important in preserving frequency matching for state-mixing. This mixing relies on an effective coupling and degeneracy between the mixed product-spin-states (Figure 6.7). To achieve high CE enhancements in the absence of relaxation, the frequency degeneracy between $|\beta_1\alpha_1\alpha_n\rangle$ and $|\alpha_1\beta_1\beta_n\rangle$ has to be strictly maintained, because the effective coupling leading to state-mixing is small due to its origination in a second-order effect of dipolar interactions. In practical DNP experiments using paramagnetic species that are randomly oriented, the probability to obtain the exact frequency matching is small since the powder distribution randomizes the EPR frequencies involved. Therefore, spin relaxation, which broadens the frequency matching condition, is essential for the achieving CE enhancements.

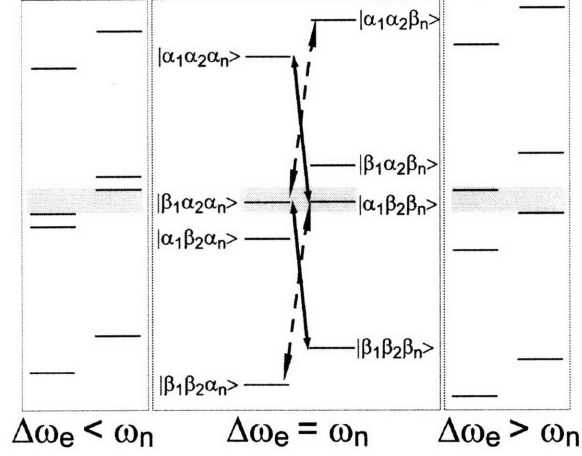


Figure 6.7. A representation of the zeroth order time-independent Hamiltonian for an electron-electron-nucleus spin system. The middle panel shows that microwave-excited transitions (arrows) for the CE result from mixing of spin states when $\omega_{e2} - \omega_{e1} = \omega_n$. The transition probabilities are optimized by the degeneracy between the product-spin-states marked by the shadow. The right and left panels illustrate breakdown of degeneracy when $\Delta\omega_e \neq \omega_n$.

Spin relaxation can be considered phenomenologically using a stochastic Liouville equation (SLE) of quantum dynamics¹⁶³. The SLE is derived by considering a quantum system with fluctuating Hamiltonian terms $h_\lambda(t)$ that model stochastic noises, such as fluctuating magnetic fields. To describe relaxation effects in a system of H_0 and H_M (Eqs. 119 and 120), we use the total Hamiltonian in the laboratory frame given by

$$H = H_0 + H_M + \sum_{\lambda} h_{\lambda}(t). \quad (121)$$

General stochastic noises are assumed to involve single-spin operators in the following:

$$h_{\lambda}(t) = \phi_{\lambda}(t)J_{\lambda},$$

where J_{λ} are spin operators $S_{1x}, S_{1y}, S_{1z}, S_{2x}, S_{2y}, S_{2z}, I_x, I_y$ and I_z , and $\phi_{\lambda}(t)$ are coefficients

which are assumed to follow a Markov process with zero mean and time dependence described by a auto-correlated δ -function. Subsequently, the following ensemble average, which is denoted by a bar, is obtained as

$$\overline{\Phi_\lambda(t_1)\Phi_\varepsilon(t_2)} = \frac{1}{T_\lambda} \delta_{\lambda\varepsilon} \delta(t_1 - t_2),$$

where $(1/T_\lambda)$ is proportional to the strength of coupling between the three-spin system and the random fields and corresponds to a measurable spin-lattice relaxation times T_1 and spin-spin relaxation times T_2 through the following relationships

$$\begin{aligned} T_{S1x} &= T_{S1y} = T_{S2x} = T_{S2y} = 2T_{1e}, \\ T_{S1z} &= T_{S2z} = T_{2e}, \\ T_{Ix} &= T_{Iy} = 2T_{1n}, \\ T_{Iz} &= T_{2n}. \end{aligned}$$

The complete Hamiltonian (Eq. 121) can be transformed into the rotating frame of the microwave frequency and its ensemble average can be calculated, so that the evolution of density operator follows the equation of motion

$$\frac{d}{dt} \overline{\sigma}_{mm'}^* = -i[(H_0^* + H_M^*), \overline{\sigma}^*]_{mm'} + \sum_{q,q'} \hat{\Gamma}_{mm',qq'} \overline{\sigma}_{qq'}^*, \quad (122)$$

where the asterisks denote the reference of the rotating frame, m, m', q and q' are matrix indices in the Liouville space, and $\overline{\sigma}^*$ is the density operator defined as

$$\overline{\sigma}^* \equiv \overline{\rho}^* - \overline{\rho}_{eq}^*.$$

The $\bar{\rho}_{eq}^*$ is the density matrix in a thermal equilibrium, and serves as the boundary condition at $t = 0$ and defined as

$$\bar{\rho}_{eq}^* \propto \text{tr} \left(\exp \left(-\frac{H_0}{k_B T} \right) \right),$$

where T is the temperature, k_B is the Boltzmann constant and H_0 is defined in Eq. 119.

The relaxation super operator $\hat{\Gamma}$ in Eq. 122 of the SLE is then expanded as

$$\hat{\Gamma}_{mm',qq'} = \frac{1}{2} \left[\frac{2}{T_\lambda} J_{mq}^\lambda J_{m'q'}^\lambda - \delta_{m'q'} \sum_r \frac{1}{T_\lambda} J_{rq}^\lambda J_{rm}^\lambda - \delta_{mq} \sum_r \frac{1}{T_\lambda} J_{rq'}^\lambda J_{rm'}^\lambda \right].$$

The parameters required for simulation of an electron–electron–nucleus spin system are listed in Table 6.2. Despite capabilities of measuring those parameters, reasonable values for them are adopted for the best fit of the simulated results with the experimental data of DNP and EPR. Specifically, the electron spin-lattice relaxation time T_{1e} is extrapolated from the known value at 10 K^{125, 136}, the electron spin-spin relaxation time T_{2e} corresponds to the broadening factor of the EPR spectrum, the nuclear spin-lattice relaxation time T_{1n} includes the effect of homonuclear spin diffusion, thus smaller than measured values, the electron–electron interaction is evaluated from the electron–electron distance determined by EPR measurements, and the electron–nuclear interaction is estimated from the radical employed in DNP experiments. The dependence of DNP on any parameter is investigated through variations of such a parameter, while the numerical enhancements are optimized with respect to the remaining parameters.

Table 6.2. Parameters for the simulation of an electron-electron-nucleus system.

Parameter Name	Symbol	Value	Note
Electron Larmor frequency	ω_{e1}, ω_{e2}	~140 GHz	to be optimized, corresponding to EPR at 5 T
Nuclear Larmor frequency	ω_n	211 MHz	proton NMR at 5 T
Microwave frequency	ω_M	~140 GHz	to be optimized, corresponding to EPR at 5 T
Microwave field strength	ω_1	~1 MHz	0.1 to 1 MHz from Gunn diode (10 mW) to gyrotron (800 mW) ^a with $Q=1$
Anisotropic hyperfine	A_1, B_1	0.7 MHz	methyl protons of TEMPO, $R_{H-e} = 2.7\text{--}3.9 \text{ \AA}$
Anisotropic hyperfine	A_2, B_2	0	a distant 2 nd electron from the nucleus
Electron-electron dipolar coupling	d	~12 MHz	variable from 1 to 50 MHz for $R_{e-e} > 10 \text{ \AA}$
Exchange integral	J	0	$R_{e-e} > 10 \text{ \AA}$
Electron spin-lattice relaxation	T_{1e}	2 μ s	extrapolated from 10 K to 90 K
Electron spin-spin relaxation	T_{2e}	0.1 μ s	considering local field broadening
Nuclear spin-lattice relaxation	T_{1n}	11.5 ms	considering ^1H - ^1H spin diffusion
Nuclear spin-spin relaxation	T_{2n}	$T_{1n}/3$	unimportant

^a For reference, ~10 mW microwaves coupled into a cavity with a Q-factor of 2000 generates $\omega_1/2\pi = 5$ MHz, and $\omega_1 \propto (PQ)^{1/2}$, where P is the microwave power.

6.2.3. Results and discussion

Enhancements of nuclear polarization during microwave irradiation are calculated from Eq. 122 as

$$\epsilon = \frac{\text{tr}(I_z \bar{\rho}^* - I_z \bar{\rho}_{eq}^*)}{\text{tr}(S_{1z} \bar{\rho}_{eq}^*)}. \quad (123)$$

In Eq. 123 $|\epsilon| \leq |\gamma_e/\gamma_n|$, and when $|\epsilon| = |\gamma_e/\gamma_n|$, the entire electron polarization is transferred to the nucleus.

6.2.3.1. Frequency matching in the SE and the CE

Figure 6.8 shows DNP enhancements as a function of the EPR frequency separation ($\omega_{e2} - \omega_{e1}$) and the microwave frequency offset ($\omega_M - \omega_{e1}$), calculated numerically

according to the SLE of an electron-electron-nucleus system. The peaks in these contour plots represent regions in which frequency matching condition is satisfied and the CE mechanism is feasible. Clearly, adding relaxation broadens the frequency matching region and leads to larger DNP enhancements. Simulations without relaxation reveal an extremely narrow frequency matching bandwidths (insets of Figure 6.8), ranging from 5 to 15 kHz, which is difficult to achieve within an EPR lineshape having a large inhomogeneity. Moreover, a comparison of the enhancement contour plots for different strengths of electron–electron interaction ($d/2\pi = 10$ MHz and 30 MHz) demonstrates that stronger electron–electron couplings also broaden the matching region, and that the matched EPR and microwave frequencies for the CE depend on the splitting due to the electron–electron interaction. Note that the full range of frequencies is not displayed in Figure 6.8. In the discussion below we will present other matching regions for both the CE and the SE mechanisms and show that the frequency matching bandwidth for the SE is also broadened by relaxation.

Figure 6.9 shows both the SE and the CE contributions to the DNP enhancements as a function of microwave frequency offset at several EPR frequency separations. Matching conditions for both the CE and the SE are calculated and referenced to the associated EPR stick-spectra. In addition, the pure SE enhancements are calculated by turning off electron-electron interactions in the simulation. We observe stronger CE enhancements at microwave irradiation near ω_{e1} and ω_{e2} , and the optimal microwave frequencies for the CE depend on the splittings due to electron-electron interactions.

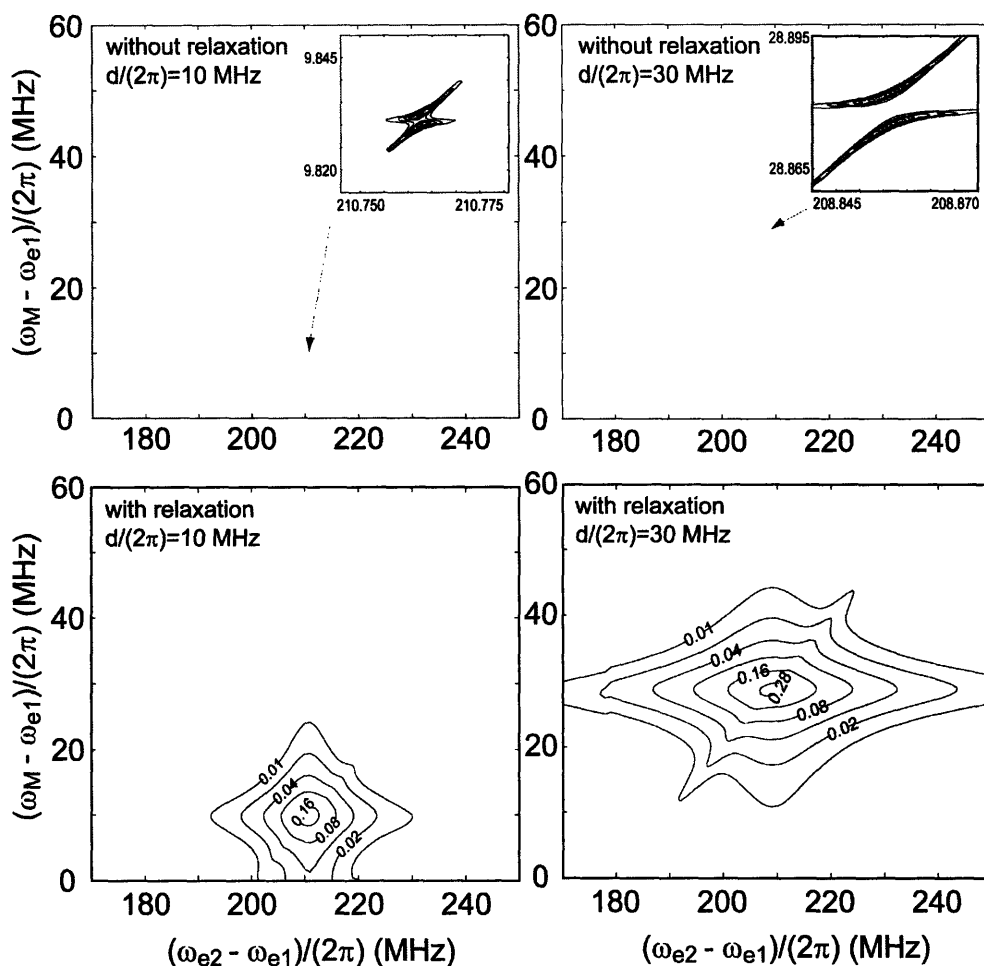


Figure 6.8. Contour plots of DNP enhancements, in units of $|\gamma_e/\gamma_n|$, as a function of microwave frequency offset ($\omega_M - \omega_{e1}$) and EPR frequency separation ($\omega_{e2} - \omega_{e1}$). $B_0 = 5T$ corresponding to $\omega_p/2\pi = 211$ MHz. Introducing relaxation into the simulation leads to a broadening of the regions of frequencies that yield DNP enhancements. The electron–electron interaction used for the simulation is 10 or 30 MHz, and all other parameters are listed in Table 6.2. The ranges of EPR and microwave frequencies are truncated to demonstrate the detail of enhancement peaks. The insets show the details when bandwidths of frequency matching become extremely small without relaxation.

Small frequency shifts of the microwave excitation, due to a second order effect regarding electron–electron interactions, become less important in the presence of relaxation, since the size of the shifts are small compared to the broadened matching

bandwidths. In addition, small enhancements are found at $\omega_M = \omega_{e1} \pm \omega_n$, especially when the EPR frequency separation fails to match ω_n . These small peaks are attributed to the SE, which become more intense when the CE is suppressed by an incorrect EPR frequency separation or by diminishing electron–electron interactions. Although the pure SE appears with the complete decoupling of one electron spin from the three-spin system, the DNP enhancements involved are still much smaller than those from the CE. Clearly, the CE generates superior DNP enhancements when the correct EPR frequency separation and appropriate electron–electron interactions are available.

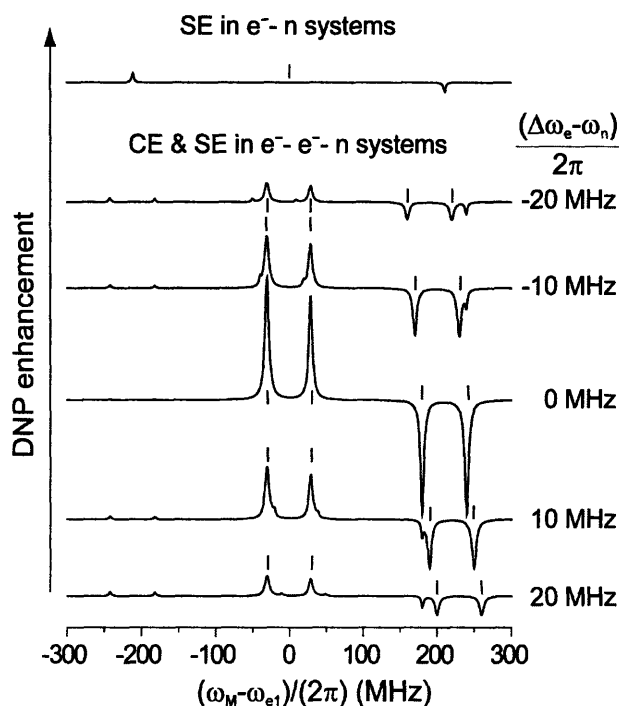


Figure 6.9. DNP enhancements as a function of microwave frequency offsets ($\omega_M - \omega_{e1}$). The frequency matching for microwave irradiation is shown for both the SE and the CE. Additional frequency matching of the EPR frequency separation ($\Delta\omega_e = \omega_{e2} - \omega_{e1}$) is required for the CE. In the CE simulation, $d/2\pi = 30$ MHz, and all other parameters are listed in Table 6.2. EPR absorptions are labeled by the sticks.

Calculations of spin systems without relaxation present extremely complicated patterns and narrow ranges of frequency matching for the optimal polarizing condition. Therefore, consideration of relaxation is essential in order to broaden the bandwidth of frequency matching for both the CE and SE. In fact, relaxation effects are indispensable in descriptions of experimental results, such as the buildup of enhanced polarization during microwave irradiation, microwave-power, the magnetic-field dependencies of the nuclear polarization, and the influence of temperature and/or radical concentration. The SLE approach in a three-spin system, which adequately describes the above observations, is illustrated in the following discussion in terms of DNP enhancements at the optimized EPR and microwave frequencies.

6.2.3.2. Polarization buildup during microwave irradiation

The microscopic nuclear polarization, which is enhanced in a three-spin system during microwave excitation, can represent the macroscopic nuclear polarization of the bulk spin system. Empirically, the growth of the enhanced macroscopic polarization of the bulk nuclei is described by the following master equation:

$$\frac{dP}{dt} = \frac{1}{\bar{\tau}} [(\bar{\epsilon} + 1) \cdot P_0 - P] - \frac{1}{T_{1n}^x} (P - P_0), \quad (124)$$

where P is the bulk nuclear polarization with a thermal equilibrium value P_0 , $1/\bar{\tau}$ is macroscopic polarizing rate, T_{1n}^x is the intrinsic nuclear spin-lattice relaxation time, and $\bar{\epsilon}$ is a theoretical enhancement of DNP. Accordingly, the microscopic polarization process in the electron–electron–nucleus spin system grows as an exponential function (Figure 6.10) that is characterized by a steady-state enhancement ϵ_{ss} and a microscopic

time constant τ'_{DNP} for the coupled nucleus. With efficient homonuclear spin diffusion that distributes the enhanced nuclear polarization throughout the bulk nuclei, we find that $\bar{\epsilon} = \epsilon_{ss}$ and $\bar{\tau} = \tau'_{DNP} \cdot N_n / N_e$, where N_n and N_e are the number of observable nuclei and the number of active paramagnetic centers, respectively (usually $N_n \gg N_e$ at diluted electron concentrations). Therefore, the steady-state enhancement of bulk nuclei E_{ss} is related to the microscopic parameters according to ($dP^\infty/dt = 0$ in Eq. 124)

$$E_{ss} = \frac{P^\infty}{P_0} - 1 = \frac{1}{1 + \frac{\tau'_{DNP}}{T_{1n}^x} \cdot \frac{N_n}{N_e}} \epsilon_{ss}, \quad (125)$$

and the time constant τ_{DNP} to reach a steady state of macroscopic nuclear polarization is

$$\tau_{DNP} = \frac{\tau'_{DNP} \cdot \frac{N_n}{N_e}}{1 + \frac{\tau'_{DNP}}{T_{1n}^x} \cdot \frac{N_n}{N_e}}. \quad (126)$$

According to Eqs. 125 and 126, an efficient polarizing process with very small τ'_{DNP} can satisfy $T_{1n}^x \gg \tau'_{DNP} \cdot N_n / N_e$, and lead to $E_{ss} \sim \epsilon_{ss}$ and $\tau_{DNP} \sim \tau'_{DNP} \cdot N_n / N_e$. Therefore, the results of calculating microscopic polarization transfer using ϵ_{ss} and τ'_{DNP} suffice to describe the macroscopic DNP phenomena in the bulk nuclei.

Using these expressions we simulated a three-spin system with optimized frequency matching conditions and calculated the microscopic polarization enhancement of a single nucleus. Figure 6.10 shows the growth of nuclear polarization as a function of time during microwave irradiation for both the SE and the CE. At the long time limits, the polarization curves approach their steady-state value ϵ_{ss} . Compared to the SE curve, the

CE curve show larger ϵ_{ss} and shorter τ'_{DNP} at constant microwave field strength ω_1 , indicating that, again, the CE is more efficient than the SE in transferring electron polarization to the nucleus. Specifically, at $\omega_1/2\pi = 1$ MHz, the polarizing rate $\epsilon_{ss}/\tau'_{DNP}$ of the CE is greater than the rate of the SE by a factor of ~ 100 . In addition, under the condition of current simulation parameters, an increase of ω_1 leads to a significant increase of ϵ_{ss} , but only a minor changes in τ'_{DNP} . Moreover, at a larger ω_1 , the ratio of increase in the SE enhancement is greater than that in the CE enhancement, despite larger amplitude of enhancement yielded by the CE. Therefore, microwave power is more demanded by the SE than by the CE.

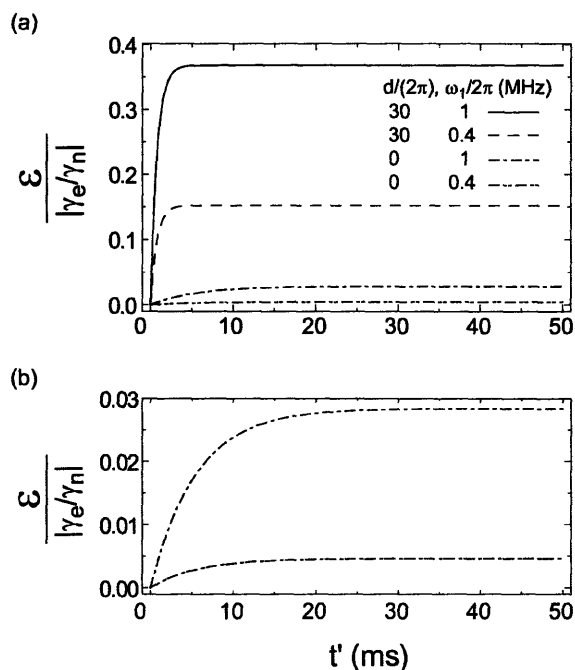


Figure 6.10. Simulated buildup curves of enhanced nuclear polarization in (a) the CE and (b) the SE under optimal frequency matching conditions. For the SE, $d/2\pi = 0$ MHz, $(\omega_M - \omega_{e1})/2\pi = -211$ MHz. For the CE, $d/2\pi = 30$ MHz, $(\omega_M - \omega_{e1})/2\pi = -30.798$ MHz and $(\omega_{e2} - \omega_{e1})/2\pi = 208.812$ MHz. For both mechanisms, $\omega_1/2\pi = 1$ and 0.4 MHz, and all other simulation parameters are in Table 6.2. The growth curves are fitted by exponential-recovery functions with growth time constants of 0.77, 0.75, 5.48 and 5.62 ms from top to down. (b) Expansion of the computed SE enhancement buildups. Note that the vertical axis in this figure is reduced by a factor of 10.

6.2.3.3. Essential microwave field and inter-electron interaction for DNP

Microwave irradiation is essential in both the CE and SE drive the polarization transfer from electron spins that are initially at a thermal equilibrium to the nuclear spins. In addition, electron–electron couplings are indispensable for the CE. Figure 6.11 shows the dependence of DNP enhancement, described by ϵ_{ss} and τ'_{DNP} , on the microwave field strength ω_1 for systems with different strengths of electron–electron dipole coupling $d/2\pi$. Both the CE and SE are simulated with $d/2\pi \neq 0$, whereas the SE simulation was performed with $d/2\pi = 0$. Note that the value of $\omega_1/2\pi$ is cut off at 2 MHz which corresponds to the limits of the microwave power (< 25 W) and the transmission efficiency from a realistic microwave source. The simulation parameters for CE enhancements ϵ_{ss} are chosen to best fit the experimental data from DNP and EPR measurements (Figure 6.11a). For the appropriate comparisons, the average strengths of electron–electron dipole coupling in the BT2E, BT3E, and BT4E biradicals are estimated from simulations of the biradical EPR spectra (see Chapter 4). Specifically, the average dipolar interaction is assessed on an assumption that the angle between the dipolar vector and the external magnetic field is 90° . With a reasonable range of relaxation times (Table 6.2), the theoretical curves of ϵ_{ss} shown in Figure 6.11 exhibit good agreement with experimental data. Such agreement indicates that our theoretical model is relevant to describing the DNP process.

According to simulations, significant enhancements of nuclear polarization can be achieved with a moderate ω_1 in the CE, and at high ω_1 , the enhancements tend to saturate (Figure 6.11a). In a classical picture of the CE, the microwave field generates a quasi steady-state of polarization difference between two electrons that is modulated by their

frequency difference in the EPR spectrum. The three-spin process then transfers the electron spin polarization difference to a coupled nucleus, leading to the enhancement of nuclear polarization. Therefore, as the microwave field strength increases, the amplitude of polarization difference induced by the microwave irradiation also increases, and hence the size of the DNP enhancement increases. However, at strong microwave fields, the electron spin polarization difference reaches its maximum value (the thermal equilibrium electron polarization), and hence saturation occurs. This tendency towards saturation indicates that the CE mechanism can be efficient in weak to moderate microwave fields. In contrast, the curve for the SE ($d/2\pi = 0$) saturates at a higher microwave field strength ω_1 . Because the SE is a second-order process involving electron–nucleus flip-flops, enhancing nuclear polarization directly, the growth of the SE DNP enhancement with initial increases of ω_1 is quadratic. In addition, due to its second-order nature, the same strength of ω_1 results in a smaller nuclear enhancement than observed for the CE.

In Figure 6.11b, we show the growth time constant τ'_{DNP} as a function of microwave field strength for systems with different electron–electron dipole couplings $d/2\pi$. The result shows that a larger $d/2\pi$ leads to a smaller τ'_{DNP} , i.e., a faster rate of DNP saturation, due to improved efficiency of the CE. Moreover, with a constant electron–electron interaction, a stronger ω_1 in the CE results in a longer τ'_{DNP} . This small increase of τ'_{DNP} is due to the substitution of the slower SE mechanism for the CE polarizing process. A strong microwave field not only excites the allowed transition belonging to the on-resonance electron, but it also excites the satellite transition, which leads to the SE, with respect to the off-resonance electron. In a pure SE process, a larger ω_1 reduces τ'_{DNP} because the efficiency of this direct polarization is improved.

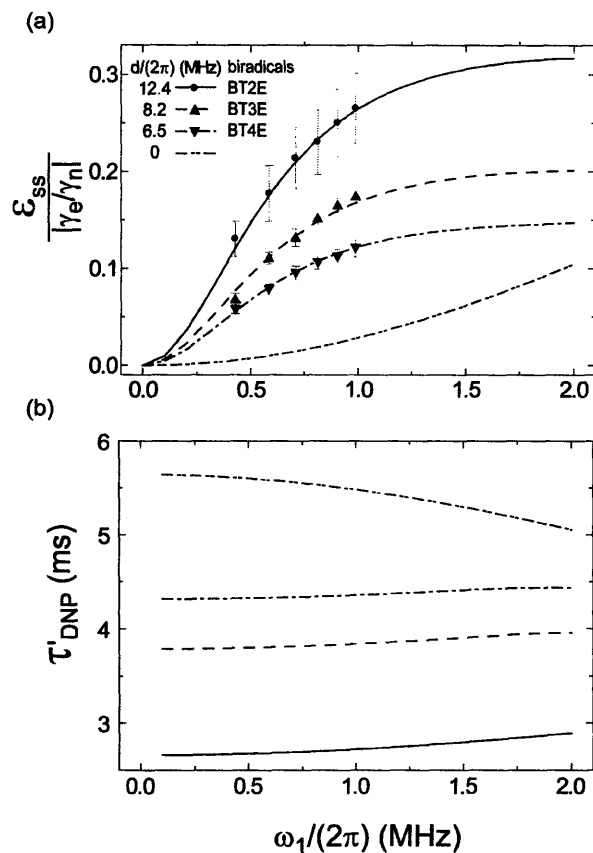


Figure 6.11. Simulations of (a) the steady-state enhancement ϵ_{ss} and (b) the growth time constant τ'_{DNP} , which are functions of the microwave field strength ω_1 . The pure SE is calculated with $d/2\pi = 0$, and the CE is simulated with $d/2\pi = 12.4, 8.2$ and 6.5 MHz, corresponding to the average electron–electron dipolar interaction in the BT2E, BT3E and BT4E biradicals, respectively. The theoretical curves are in good agreement with the experimental points from the DNP and EPR experiments.

We also studied the effect of varying electron–electron dipole coupling $d/2\pi$ on DNP enhancements from the CE. Figure 6.12 shows the CE enhancements as a function of $d/2\pi$ at different strengths of ω_1 . At a fixed ω_1 , the CE enhancement increases as $d/2\pi$ increases at small to intermediate $d/2\pi$. However, at strong electron–electron couplings, increasing $d/2\pi$ tends to decrease the CE enhancement, and there exists an optimal $d/2\pi$ that gives the maximal CE enhancement.

The experimental DNP results using the BTnE biradicals¹⁶⁴ verify the theoretical

curves of CE enhancements as a function of $d/2\pi$ at relatively small values ($< \sim 25$ MHz). However, the negative trend on DNP enhancements in the strong $d/2\pi$ regime has not been directly observed in experiments. We have studied a biradical that has a shorter electron–electron distance, hence stronger $d/2\pi$, than that of BT2E (Chapter 4), and the preliminary results indicating a smaller DNP enhancement in comparison to BT2Es in support the theoretical predictions. Note that a shorter distance between electrons generally induces larger electron–electron couplings. Consequently, the facilitated three-spin process efficiently transfers the polarization difference of two electrons to the coupled nucleus, but simultaneously suppresses this polarization difference generated by microwave excitation, because its function prevents the saturation of the polarization of the on-resonance electron. As a result, CE DNP enhancements appear decreasing at large $d/2\pi$. Novel biradicals and experimental techniques are required to verify the theoretical predictions at large $d/2\pi$, which will be the subject of our future work.

The influence of ω_1 and $d/2\pi$ on the CE appear independent, since a larger $d/2\pi$ improves the DNP enhancements in Figure 6.11a and it keeps the shape of ϵ_{ss} as a function of ω_1 unchanged. Similarly a larger ω_1 increases the intensity but keeps the shape of ϵ_{ss} function of $d/2\pi$ in Figure 6.12. Decoupling of ω_1 from $d/2\pi$ is a consequence of the assumption that $d/2\pi$ cannot affect the relaxation properties of electrons, which is not in practice correct. Thus, the experimental DNP results using biradicals reveal more complicated and coupled dependences on the parameters ω_1 and $d/2\pi$. Specifically, a larger $d/2\pi$ induces electron spin relaxation and attenuates microwave saturation for the CE enhancements. Therefore, when a shorter biradical is used, a larger steady-state enhancement actually occurs at an increased microwave power ($\propto \omega_1^2$).

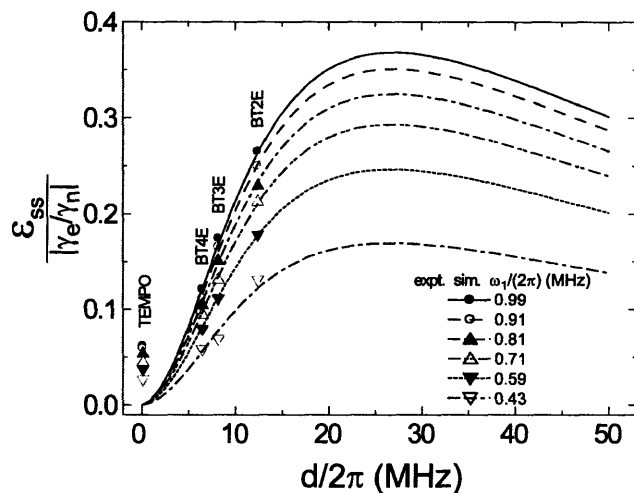


Figure 6.12. Simulation of the steady-state nuclear enhancement ϵ_{ss} as a function of electron-electron dipole interaction $d/2\pi$ in the CE under various microwave field strengths. The experimental points, grouped at $d/2\pi = 12.4$, 8.2 and 6.5 MHz, represent the DNP enhancements using BT2E, BT3E and BT4E, respectively.

6.2.3.4. Relaxation effects on DNP

Spin relaxation depends on temperature, radical concentration, and magnetic field and can have a significant influence on the dominant polarizing mechanism. In general, relaxation processes are characterized by phenomenological parameters including spin-lattice relaxation times (T_1) and spin-spin relaxation times (T_2) for the electrons (e_1 , e_2) and the nucleus (n). The dynamics of the spin system is then obtained from the stochastic Liouville equation (SLE) constructed from these relaxation parameters. In Section 6.2.3.1, we studied the effect of electron spin-spin relaxation (T_{2e}) that leads to a broader range of frequency matching. Phenomenological T_{2e} processes are assumed to result mainly from the homogeneous local field fluctuations due to electrons surrounding the paramagnetic center, so that it can be independent of temperatures. Moreover, since the

nuclear coherence does not contribute to DNP under continuous microwave irradiation, we expect that the influence of T_{2n} processes in our three-spin model is negligible. Therefore, the following discussion of relaxation in DNP experiments focus mainly on the effects of T_{1n} and T_{1e} with two caveats. First, the phenomenological relaxation times (T_{1n} and T_{1e}) employed are in separate functions of temperature, concentration and external magnetic field, since the SLE approach does not explicitly consider influences of those additional parameters. Second, the relaxation times should be verified by measurements in EPR and NMR experiments spins or by fitting data from DNP experiments.

Figure 6.13 shows the steady-state SE enhancement, ϵ_{ss} , and the buildup time constant, τ'_{DNP} , as functions of microwave field strength ω_1 in systems with different relaxation times (T_{1n} and T_{1e}) spanning three orders of magnitude. The simulations of the SE for ϵ_{ss} and τ'_{DNP} show a strong dependence only on the T_{1n} . Specifically, Figure 6.13a, b show that a longer T_{1n} increases both ϵ_{ss} and τ'_{DNP} at all levels of ω_1 in the simulations, and, for the longest T_{1n} the SE ϵ_{ss} approaches saturation as ω_1 is increased. The increase in τ'_{DNP} in systems with longer T_{1n} is more pronounced at weaker ω_1 , which reflects the slower completion of polarization transfers at weaker microwave field strengths. In contrast, Figure 6.13c, d demonstrate that the electron longitudinal relaxation T_{1e} has only minor effects on the SE ϵ_{ss} and τ'_{DNP} , because the electron–nucleus flip-flop transition is independent of the T_{1e} relaxation. Nonetheless, a short T_{1e} is required for multiple polarization transfers from one electron to many nuclei in DNP experiments using diluted concentrations of radicals.

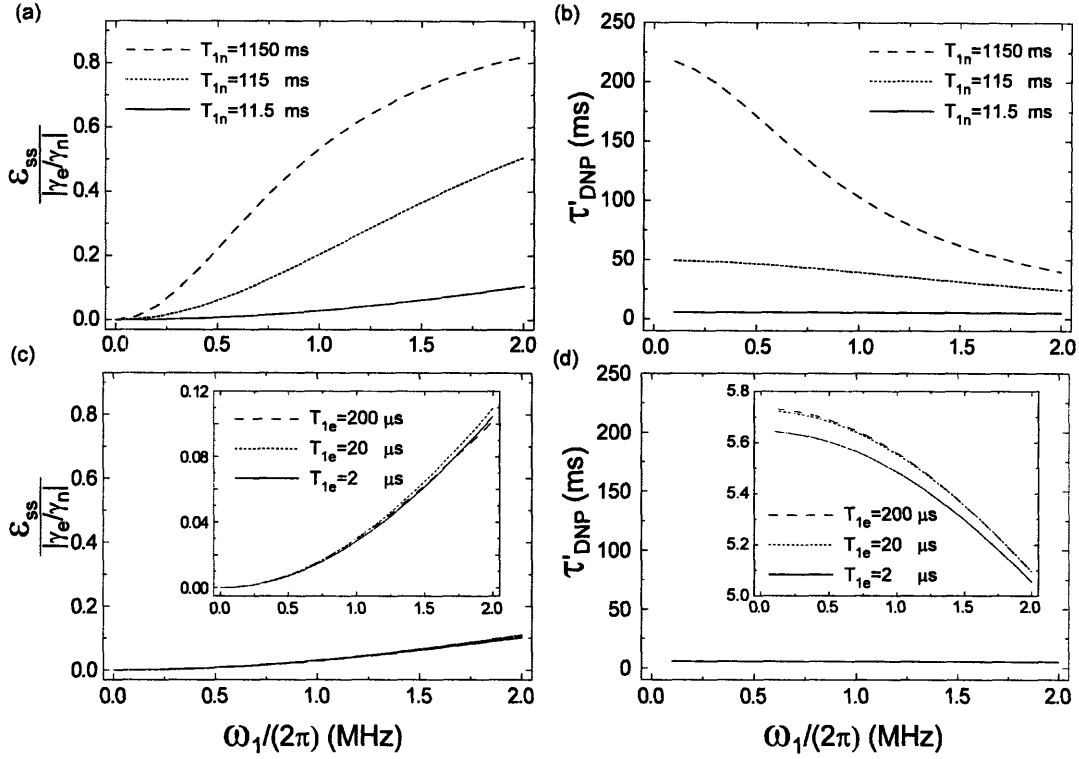


Figure 6.13. Plots illustrating SE enhancements and τ'_{DNP} as a function of T_{1n} and T_{1e} . The plots show simulated values of ϵ_{ss} and τ'_{DNP} as a function of $\omega_1/2\pi$. (a, b) T_{1n} assumes three values (11.5, 115 and 1150 ms) at constant $T_{1e} = 2 \mu\text{s}$. (c, d) T_{1e} assumes three values (2, 20 and 200 μs) at constant $T_{1n} = 11.5 \text{ ms}$. All other simulation parameters are listed in Table 6.2. Note that the relaxation times are selected to best fit the experimental data as shown in Figure 6.11 and Figure 6.12.

The CE, in contrast to the weak dependence on relaxation predicted for the SE, shows a pronounced influence of both T_{1n} and T_{1e} on the predicted values of ϵ_{ss} and τ'_{DNP} . Figure 6.14 shows the simulated CE ϵ_{ss} and τ'_{DNP} as a function of the electron–electron interaction, $d/2\pi$, for systems with different nuclear longitudinal relaxation times T_{1n} at two constant microwave fields ($\omega_1/2\pi = 1$ and 0.1 MHz). Note that using $d/2\pi$ to trace the CE results emphasizes its importance relative to ω_1 in the polarization transfer. At a constant T_{1n} , a stronger ω_1 increases the magnitude of the ϵ_{ss} function of $d/2\pi$ without

changing the shape of the dependence and it has negligible effects on τ'_{DNP} as a function of $d/2\pi$. This indicates, again, that microwave irradiation primarily affects the quasi steady-state polarization difference of the two electrons, rather than the subsequent three-spin process. Figure 6.14a, c, e clearly show that a longer T_{1n} increases ϵ_{ss} at the small to intermediate $d/2\pi$ regime, but leaves ϵ_{ss} almost unchanged at the strong $d/2\pi$ regime; as a result, a longer T_{1n} shifts the optimal $d/2\pi$ for maximal nuclear enhancement to a smaller value of $d/2\pi$. Although a slower three-spin process caused by a smaller $d/2\pi$ decreases the rate (long τ'_{DNP} in Figure 6.14b, d, f) of polarization transfer, it simultaneously increases the polarization difference between the two electrons at the same ω_1 excitation and raises the potential of achieving a larger DNP enhancement. Therefore, systems with a weak $d/2\pi$ can generate a large ϵ_{ss} via longer irradiation periods. These larger ϵ_{ss} 's are reflected in increased values of τ'_{DNP} (in the simultaneous presence of a long T_{1n}) shown in Figure 6.14b, d, f. In contrast for a large $d/2\pi$, the associated ϵ_{ss} and τ'_{DNP} (the insets of Figure 6.14b, d, f) are almost unchanged through a wide range of T_{1n} , since T_{1n} is relative long and does not limit the fast three-spin process.

Further, as shown in Figure 6.15, the CE enhancement ϵ_{ss} and buildup time constant τ'_{DNP} depend strongly on the values of T_{1e} . In contrast to the negligible effect of T_{1e} on the SE, a longer T_{1e} reduces the CE ϵ_{ss} , and again, the optimal $d/2\pi$ that maximizes ϵ_{ss} shifts to smaller values as T_{1e} increases (Figure 6.15a, c, e). However, the CE τ'_{DNP} has little dependence on T_{1e} as illustrated in Figure 6.15b, d, f. In addition, the differences between ϵ_{ss} at large (dash lines) and small (solid lines) ω_1 (Figure 6.15a, c, e) are largely reduced at long T_{1e} . In particular, as T_{1e} increases, the values of CE ϵ_{ss} at large ω_1

decrease while those at weak ω_1 increase. The longest T_{1e} of 200 μs in the simulations results in crossing of the ϵ_{ss} functions at $d/2\pi \sim 24$ MHz, beyond which a larger ω_1 leads to smaller ϵ_{ss} . As for the effect of T_{1e} on τ'_{DNP} , Figure 6.15b, d, f show that a longer T_{1e} slightly decreases τ'_{DNP} at the same ω_1 except for the abnormality at $T_{1e} = 200$ μs as shown in Figure 6.15f. In the same comparison, a larger ω_1 slightly increases τ'_{DNP} due to substitution of the lower SE for part of the CE. The abnormal response of τ'_{DNP} to ω_1 in Figure 6.15f is related to the transfer from the CE to the SE.

The CE simulations – that ϵ_{ss} depends strongly on T_{1e} at various values of $d/2\pi$ and ω_1 and that τ'_{DNP} is almost independent of T_{1e} – indicates that the primary influence of T_{1e} occurs in the step of generating a polarization difference between two electrons, rather than in the step of three-spin polarization transfer to the nuclear spin. A long T_{1e} facilitates saturation of the spin polarization by excitation of the on-resonance electron, but it also induces saturation of polarization of the off-resonance electron *via* three-spin processes. Since those three-spin processes are accelerated by larger $d/2\pi$, the overall reduction of polarization difference results in a turnover of the increasing ϵ_{ss} through increasing $d/2\pi$. Such a turnover occurs at smaller $d/2\pi$ with longer T_{1e} . In addition, a SE process can cause saturation of the polarization of the off-resonance electron. With a longer T_{1e} microwave irradiation more easily saturates the on-resonance electron, and the irradiation then excites the electron–nucleus flip-flop transition, leading to the SE with respect to the off-resonance electron. Without direct interactions between the off-resonance electron and the nucleus in the current simulations, the effective interaction for the SE arises from the three-spin-mixing. This electron–electron dipole mediated SE process, which might contribute to a decrease of ϵ_{ss} , occurs at relatively large ω_1 and

longer T_{1e} .

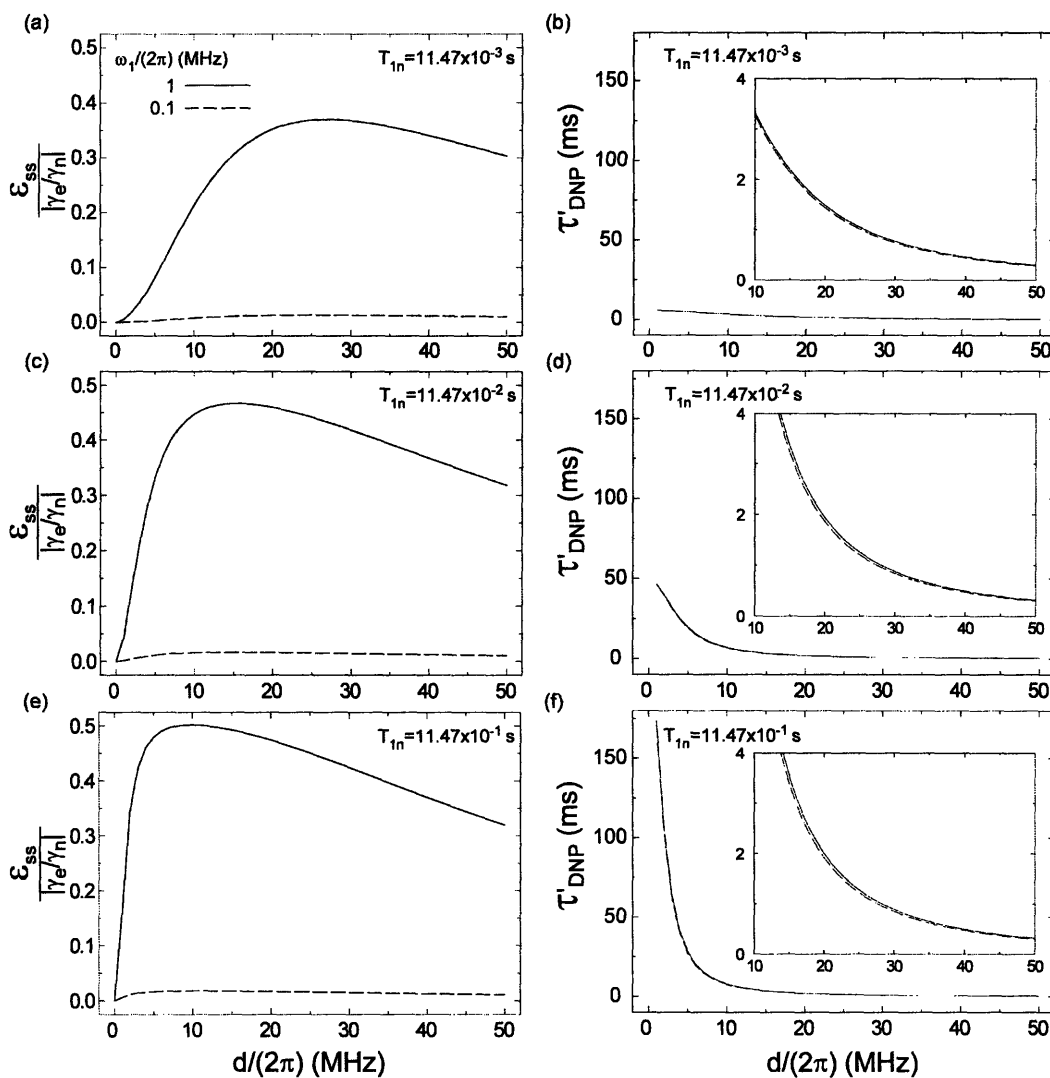


Figure 6.14. Influences of T_{1n} on simulated CE ε_{ss} and τ'_{DNP} functions of the electron-electron dipole interaction $d/2\pi$. The simulations used two microwave fields $\omega_1/2\pi = 1$ and 0.1 MHz. All other calculation parameters are listed in Table 6.2. Enlargements of the τ'_{DNP} functions are shown in the insets.

Varying the relaxation times according to experimental results or other relaxation models allows us to indirectly simulate the influence of temperature on the polarization mechanisms even though the SLE does not explicitly consider the temperature dependence. In general, lower temperatures elongate both T_{1e} and T_{1n} below a critical temperature. According to our simulations, the effects of long T_{1e} and long T_{1n} on the CE may present the optimal DNP enhancement at smaller $d/2\pi$. This conclusion is in good agreement with experimental results showing that longer average electron–electron distances optimize the CE DNP enhancement at 20 K. More specifically, in the DNP experiments with different TEMPO concentrations, the optimal concentration for the maximal DNP enhancement shifts to lower values at lower temperatures (Supporting Materials).

Radical concentration also has a significant influence on relaxation. A long T_{1n} , allowed by a low radical concentration, is desirable for polarizing nuclei that outnumber the number of polarizing agents that require polarization through multiple transfers and nuclear spin diffusion. Moreover, an appropriate T_{1e} is required for optimal CE enhancements of the bulk nuclei with a dilute electron concentration. In particular, the electron polarization at the off-resonance frequency (by ω_n) needs to be restored rapidly in order to polarize additional nuclei, whereas complete microwave saturation relies on intense ω_1 and long T_{1e} . Determination of the appropriate T_{1e} involves a proper choice of the electron–electron coupling. In fact for the optimal CE enhancements, the opposite regimes of T_{1e} favored by two electrons with different EPR frequencies can be provided with different hosts of unpaired electron as discussed in the following.

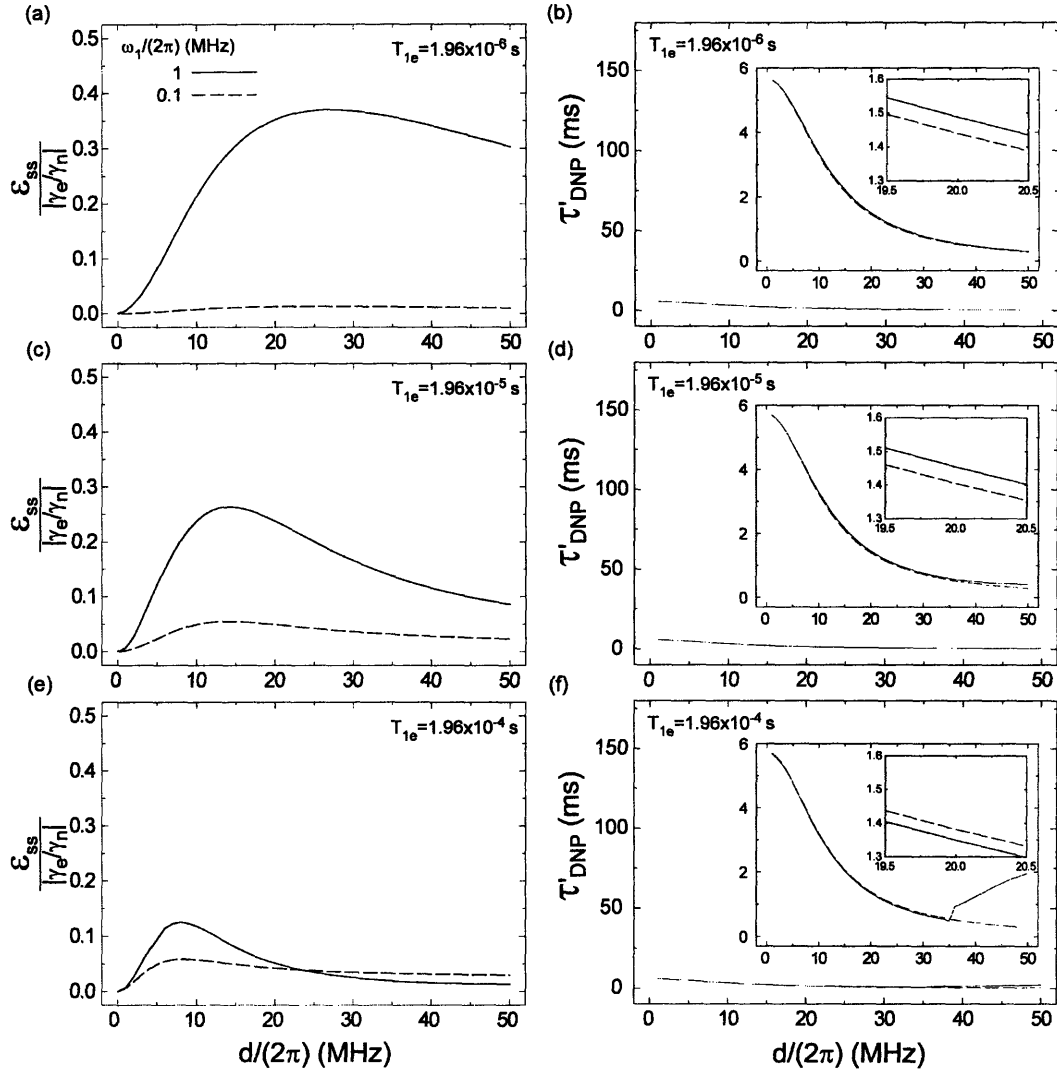


Figure 6.15. Influences of T_{1e} on simulated CE ϵ_{ss} and τ'_{DNP} in functions of the electron-electron dipole interaction $d/2\pi$. The simulations used two microwave fields $\omega_1/2\pi = 1$ and 0.1 MHz. All other calculation parameters are listed in Table 6.2. The τ'_{DNP} functions are gradually enlarged in the sequential insets.

The CE enhancement can be improved by coupling two different paramagnetic species having different T_{1e} 's. The long T_{1e} of the on-resonance electron improves microwave saturation, and the short T_{1e} of the off-resonance electron facilitates multiple

polarization transfers towards bulk nuclei. Figure 6.16 shows simulation results in a three-spin system with different T_{1e} 's of the two electrons that induce different intensities of the positive or negative DNP enhancement. Specifically, let one electron (at ω_{e1}) have a constant $T_{1e}(e_1)$ and the other (at $\omega_{e2} = \omega_{e1} + \omega_n$) have $T_{1e}(e_2)$ that varies, and the fact that $T_{1e}(e_2) = 10 \times T_{1e}(e_1)$ results in a larger intensity for positive enhancement at $\omega_M = \omega_{e2}$ than the intensity of negative enhancement at $\omega_M = \omega_{e1}$. A longer $T_{1e}(e_2)$, or $100 \times T_{1e}(e_1)$, yields an even larger increase in the maximum positive DNP enhancement while further decreasing the intensity of the negative enhancement at $\omega_M = \omega_{e1}$. From the simulation results, an increase of T_{1e} for the on-resonance electron ($\omega_M = \omega_{e2}$) leads to the improved CE because microwave saturation is facilitated, but the same increase of T_{1e} for the off-resonance electron ($\omega_M = \omega_{e1}$) results in suppression of the CE as the polarization difference of electrons is diminished by the slow restoration of e_2 which is now the off-resonance electron polarization. The result suggests a new strategy for designs of novel biradical polarizing agents that utilizes different values of T_{1e} to separately optimize microwave saturation and multiple polarization transfers. These occur in the trityl-TEMPO mixtures as a consequence of the difference in g -anisotropies of the two radicals.

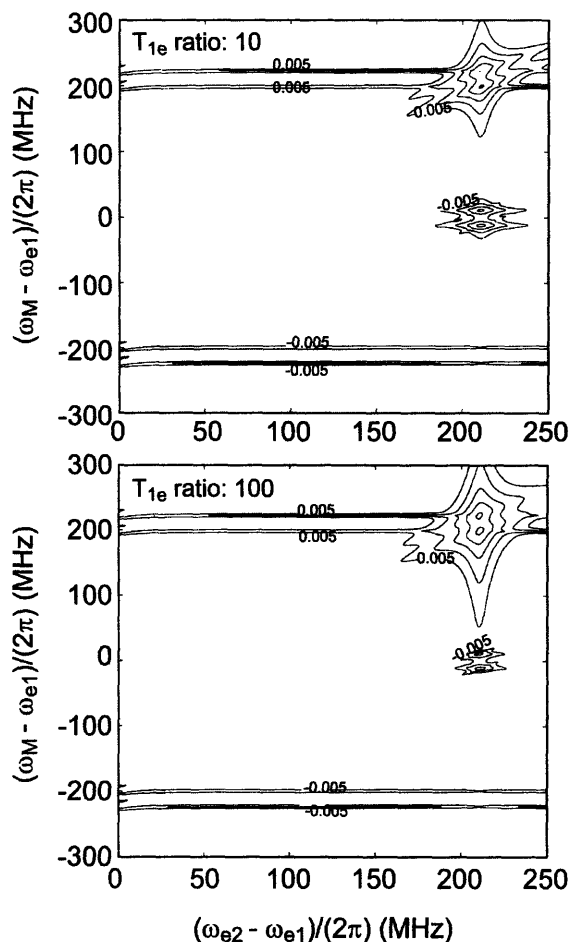


Figure 6.16. plots of DNP enhancements from the CE with different values of T_{1e} . Two T_{1e} ratios, $T_{1e}(e_2)/T_{1e}(e_1)$ with $T_{1e}(e_1)=2 \mu\text{s}$, were used. All other simulation parameters are in Table 6.2. The contour lines denote the steady-state enhancement ϵ_{ss} in the unit $|\gamma_e/\gamma_n|$. The proportionality between adjacent contour lines is 3. The SE enhancements are shown at $\omega_M = \omega_{e1} \pm \omega_n$.

6.2.3.5. Influence of external magnetic field on DNP

Thus far we have calculated DNP enhancements and buildup time constants as functions of the parameters associated with a 5-Tesla field, corresponding to 140 GHz EPR and 211 MHz ^1H NMR. In this sub-section we repeat our calculations for a higher magnetic field (9 T) to study the influence of B_0 on the DNP processes. The discussion is based on simulations of ϵ_{ss} and τ'_{DNP} as a function of ω_1/B_0 (for the SE and the CE) and

of d/B_0 (for the CE) at two magnetic fields, in order to investigate the second-order nature of the influence of B_0 with respect to spin-spin interactions. Figure 6.17 shows the DNP results as a function of ω_1/ω_e for both the SE and the CE (with $d/2\pi = 12$ MHz) and of d/ω_e for the CE (with $\omega_1/2\pi = 1$ MHz). Knowing that $\omega_e = \gamma_e B_0$, we rescale $\omega_1/2\pi$ and $d/2\pi$ by B_0 to show the corresponding effects on the SE and the CE mechanism, respectively. Figure 6.17a, b show that the SE ϵ_{ss} and τ'_{DNP} correspondingly depend on the reduced variable ω_1/ω_e , equivalent to ω_1/B_0 . Such a relation between DNP results and ω_1/ω_e is not true for the CE as Figure 6.17c, d show. Instead, Figure 6.17e, f show that the CE ϵ_{ss} and τ'_{DNP} functions depend on the reduced variable d/ω_e , equivalent to d/B_0 . Specifically, the CE ϵ_{ss} function has a maximum at an intermediate d/ω_e .

Note that the quadratic shape of the SE ϵ_{ss} function at small ω_1/ω_e (Figure 6.17a) indicates that the SE ϵ_{ss} is proportional to B_0^{-2} at constant small ω_1 . Meanwhile, the SE τ'_{DNP} decreases with increasing ω_1/ω_e (Figure 6.17b), which is a result of stronger transition moments for the SE process at lower B_0 . On the other hand, ω_1/ω_e does not correspondingly determine the CE results (Figure 6.17c, d), since the rate-determining step of the CE is the three-spin process which has stronger relationship with the electron–electron interaction (Figure 6.17e, f) and electron–nucleus interaction. Note that a change of the CE results due to changed B_0 can be recovered by a proportional change of $d/2\pi$ (by the electron–electron distance) with respect to B_0 . Therefore, the effect of B_0 on the three-spin process in the CE can be compensated by varying the inter-electron distance or the electron concentration. However, there is another effect of B_0 on the overall CE DNP which occurs with randomly orientated radicals.

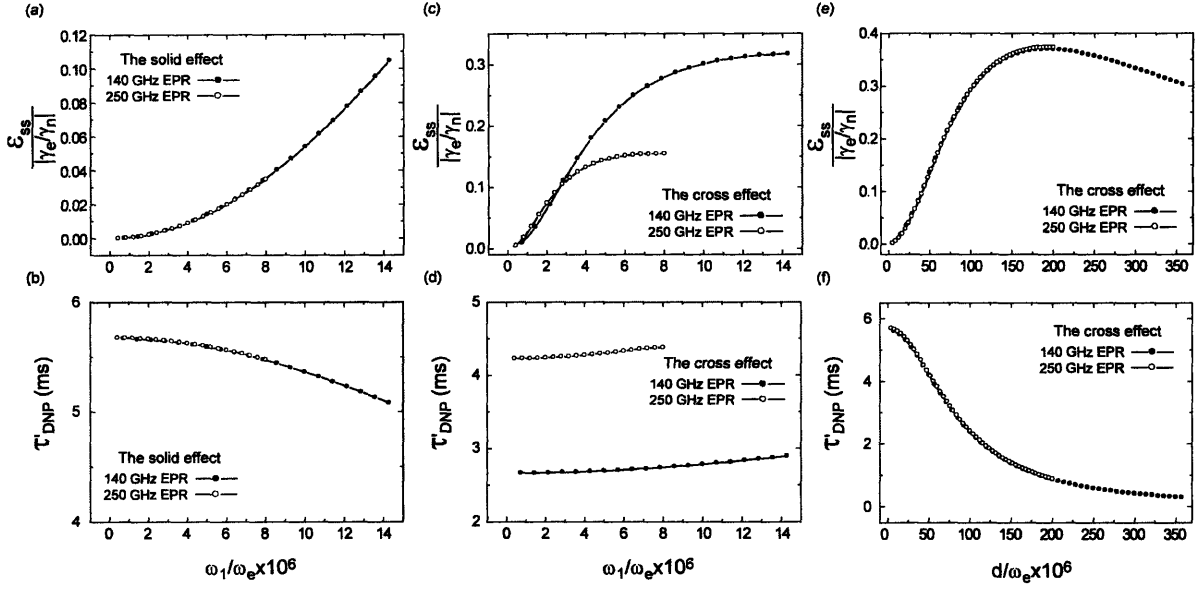


Figure 6.17. Simulations showing influences of the static magnetic field B_0 on ϵ_{ss} and τ'_{DNP} functions of reduced variables ω_1/ω_e (the SE and the CE) and d/ω_e (the CE). Note that $\omega_e = \gamma_e B_0$. (a, b) Corresponding effects of ω_1/ω_e on the SE ϵ_{ss} and τ'_{DNP} . (c, d) No corresponding effects of ω_1/ω_e on the CE ϵ_{ss} and τ'_{DNP} . Note that the used $d/2\pi = 12.4$ MHz represents the average electron-electron dipole interaction in the BT2E biradical. (e, f) Corresponding effects of d/ω_e on the CE ϵ_{ss} and τ'_{DNP} . All other simulation parameters are listed in Table 6.2.

As a constant d/ω_e can be always maintained by an easy adjustment of $d/2\pi$, B_0 affects the CE through the frequency matching which is an essential condition for the effective three-spin process. First, we verify the range of frequency matching in the CE as is shown in Figure 6.18 where a constant matching bandwidth can be maintained at various B_0 (5 and 9 T) and $\omega_1/2\pi$ (1, 0.4 and 0.1 MHz), when constant d/B_0 and the remaining parameters (Table 6.2) are provided. A larger ω_1 leads to a higher intensity of the enhancement profile, but leaves the shape of the profile unchanged. Subsequently, this unchanged matching bandwidth at different B_0 permits the DNP enhancement to depend on the probability of the correct EPR frequency separation ($\sim\omega_n$). In a powder

sample, the matching probability is inversely proportional to the EPR linewidth at a certain microwave frequency, so that DNP enhancement is proportional to B_0^{-1} as long as the line broadening is primarily contributed by g -anisotropies, which is true in higher magnetic fields. As a brief summary, the simulated DNP results on the influence of external magnetic field are consistent with the conclusion of classical DNP theories^{58, 67} that predict that the DNP enhancement is proportional to B_0^{-2} and to B_0^{-1} in the SE and the CE, respectively.

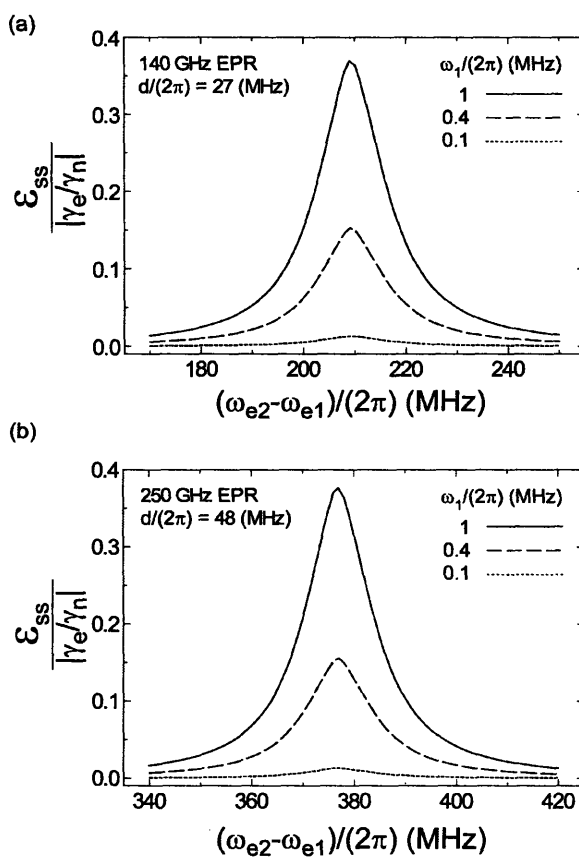


Figure 6.18. Simulated matching bandwidths for the EPR frequency separation ($\omega_{e2} - \omega_{e1}$) in the CE using (a) 140 and (b) 250 GHz microwave irradiation. The electron-electron dipole interaction $d/2\pi$ was chosen by the corresponding effect of d/ω_e and optimized with respect to the simulation parameters (Table 6.2). In addition, various microwave field ω_1 was used for the simulations.

6.2.3.6. Improvement of DNP using designer biradicals

The CE produces larger enhancements than the SE in high-field DNP experiments because the efficiency of CE is generally higher at moderated microwave field strengths and impeded less by high magnetic fields. To compensate for the negative impact of the magnetic field on both the SE and the CE, a general strategy is to increase ω_1 using a stronger microwave power and to elongate T_{1n} by using lower experimental temperatures. According to current simulations and previous experiments discussed in Chapters 3-5, a further improvement of the CE is feasible through preparation of the optimal electron–electron interaction and the correct EPR frequency separation. While improving DNP by those two parameters was demonstrated by experiments that used biradicals and radical mixtures, our theoretical model provides a background for explaining and advancing those developments. Specifically, the improvement of the DNP enhancements observed using TEMPO and trityl radical mixtures probably arises not only from matching the correct EPR frequency separation, but also from the different T_{1e} 's for the pair of radicals as was verified by our simulations.

In designing novel polarizing agents for high-field DNP, it is crucial to predict the enhancement and the buildup time constant of the enhanced nuclear polarization. Predicting DNP results from randomly-oriented biradicals is possible using our three-spin model with the appropriate spectral parameters and considering the anisotropies of the parameters if necessary. The orientation-dependent parameters can be derived from the simulation of a biradical's powder EPR lineshape¹⁶⁴. Attempted simulations of realistic DNP processes (in a powder system with relaxation) should reproduce the enhancement profile as B_0 is swept through the EPR spectrum and indicates the optimal magnetic field

for DNP using a certain paramagnetic species. The simulations should also predict the enhancement buildup during the microwave irradiation period. Our theoretical models of DNP have been verified by previous DNP and EPR measurements on known designer biradicals, and should assist us in rationalizing novel designs of biradical polarizing agents for high-field DNP.

6.2.4. Conclusions

A stochastic Liouville equation treatment of three spin electron–electron–nucleus systems was implemented to account for relaxation effects observed in two DNP polarizing mechanisms, the solid effect and the cross effect. Simulation results were compared to experimental data by which the relaxation parameters for the quantum mechanical calculations are justified. Our numerical model provides a new theoretical foundation for understanding polarizing mechanisms for high-field DNP. In addition to consistencies with classical DNP theories, in terms of frequency matching and magnetic field dependence, our model provides insights into the influence of other parameters, such as the electron–electron dipolar interactions and relaxation time constants. This new model of polarization transfer in a three-spin system can be extended for complete simulations of realistic DNP experiments using any paramagnetic species containing two unpaired electrons.

According to the simulations, the CE is found to be a potent mechanism for high-field DNP. Based on the basic polarizing mechanism with one electron and one nucleus, the second electron resonating with microwave irradiation can facilitate the polarization transfer by producing polarization difference between two electrons. The EPR absorption

spectrum, the relaxation parameters of the electrons and the nuclei, and the electron–electron dipolar interaction associate with the second electron provide new parameters for optimizing the efficiency of the DNP experiment.

6.2.5 Supporting Materials

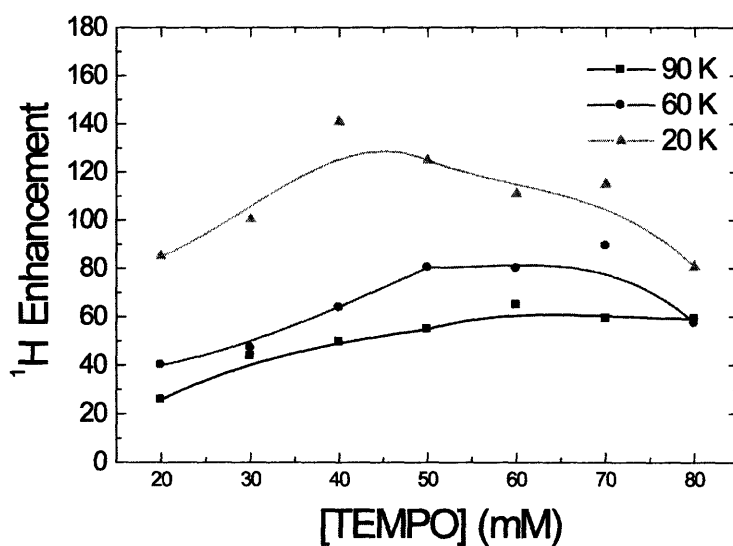


Figure S1. Concentration dependence of DNP enhancement at 90, 60 and 20 K. The optimal concentration that maximizes the DNP enhancement shifts to smaller values at lower temperatures.

Chapter 7 Applications of DNP using TOTAPOL

Part of the works in this chapter is summarized in the publications:

Patrick Van Der Wel, Kan-Nian Hu, Jozef Lewandowski, Robert G. Griffin, “*Dynamic Nuclear Polarization of Amyloidogenic Peptide Nanocrystals: GNNQQNY, a Core Segment of the Yeast Prion Protein Sup35p*,” J. Am. Chem. Soc. (2006) **in print**.

Chan-Gyu Joo, Kan-Nian Hu, Jeffrey A. Bryant, and Robert G. Griffin, “*In situ Temperature Jump-High Frequency Dynamic Nuclear Polarization Experiments: Enhanced Sensitivity in Liquid State NMR*,” accepted by J. Am. Chem. Soc., **128**, 9428-9432 (2006).

7.1. Dynamic Nuclear Polarization of Amyloidogenic Peptide Nanocrystals: GNNQQNY, a Core Segment of the Yeast Prion Protein Sup35p

7.1.1. Introduction

In several previous DNP experiments the nitroxide polarizing agent, 4-amino-TEMPO (4-amino-2,2,6,6-tetramethylpiperidine-1-oxyl) (4AT), was in intimate contact with the solute to be polarized. However, experiments on many macromolecular assemblies require that we consider the possibility that the paramagnet is excluded from close contact with the solute, and thus the question arises if DNP experiments will be applicable to this type of system. In particular, will bulky biradical polarizing agents such as TOTAPOL, consisting of two TEMPO moieties tethered by a three carbon chain (4-oxy-TEMPO-4-amino-TEMPO-2-propanol), be useful in polarizing for example virus particles, membrane proteins, amyloid fibrils, and peptide and protein nanocrystals. In these cases the sample domains are potentially macroscopically separated from solvent domains containing the polarizing agents. This question was initially addressed by

Schaefer, et al. when they attempted to transfer enhanced nuclear polarization across a polymer interface ^{123, 157} with the result that they observed no significant enhancements correlated to internuclear spin diffusion. This may partly be ascribed to the fact that the DNP process was based on the solid effect polarizing mechanism using BDPA radicals, which is known to have an inherently low efficiency. In addition, the short nuclear T_1 of the polymer material observed at room temperature may have limited the extent of the spin diffusion. Subsequently, Rosay, et. al.¹⁰⁵ successfully demonstrated the homogenous distribution of enhanced polarization in experiments that compared the size of the ^{31}P and ^{15}N signal enhancements from the DNA on the inside and the ^{15}N -labeled coat protein on the outside of bacteriophage, which is ~6.5 nm in diameter. In these experiments, which were performed at ~20 K and employed the more efficient cross effect DNP polarization mechanism, the ^{31}P and ^{15}N signal enhancements were identical, suggesting that spin diffusion distributed the polarization uniformly throughout the solute – the bacteriophage particle. However, the polarizing agent employed was 4AT and it could have diffused into the phage particles. Further, the phage particles are much smaller than most of the macromolecular assemblies mentioned above (6.5 nm diameter as opposed to >100 nm). We therefore decided to address this question again with studies of another system, nanocrystals of the amyloidogenic peptide GNNQQNY₇₋₁₃ and the improved, but bulky, biradical polarizing agent, TOTAPOL ¹²⁷.

GNNQQNY is an excellent system to use in the investigations presented here. The peptide corresponds to the residues 7-13 of the prion-forming protein Sup35p ^{165, 166} found in yeast and the protein is seen as a model system for an important class of prion-based diseases characterized by a preponderance of Gln and Asn residues in the prion-

forming protein domains. The GNNQQNY₇₋₁₃ peptide itself resembles the short Gln- and Asn-rich repeats found throughout the Sup35p N-terminal domain and constitutes one of the shortest segments shown to form prion-like fibril aggregates¹⁶⁷. Upon dissolution in water it also forms nanocrystals on a short timescale with a width varying from 20 nm to 1 μm^{167, 168}, and a structure of these species was recently determined with microcrystal X-ray diffraction⁴. Once formed these crystals, like many amyloid fibrils, resist dissolution and it is therefore easy to disperse them in cryoprotectants and polarizing agents for DNP experiments. Thus, GNNQQNY₇₋₁₃ is an excellent system to test the applicability of the DNP technique to amyloid peptides, proteins and other macromolecular assemblies.

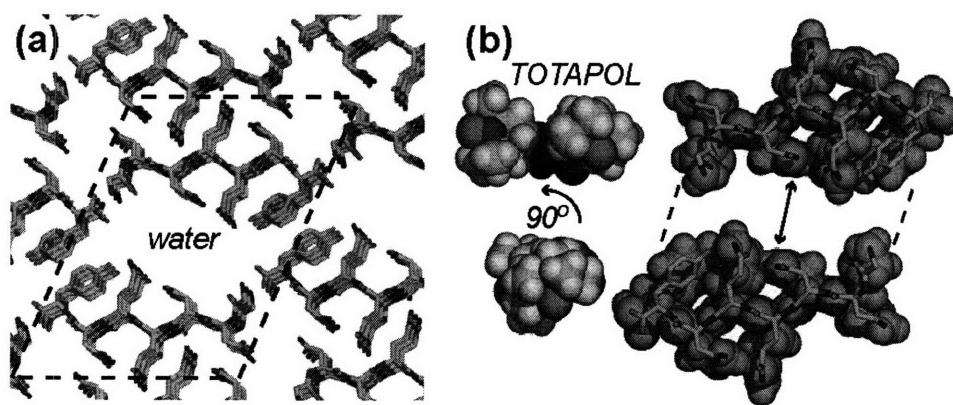


Figure 7.1. (a) Illustration of the crystal lattice of the GNNQQNY X-ray structure⁴, where the dashed lines delineate two monomers surrounding the largest opening in the lattice, containing a network of hydrogen bonded water molecules. (b) Space filling models of the GNNQQNY monomers, the spacing between them (~0.7 nm maximum width), together with two views of an approximate space filling model of the TOTAPOL biradical showing its size relative to the water opening. The plane of the figure is perpendicular to the longest dimension of the crystallites.

Figure 7.1 is an illustration of the crystal lattice ⁴ and shows the presence of (a) a water channel with a width of ~0.7 nm, together with (b) a space filling models of the lattice and a potential average conformation of TOTAPOL, which has limited flexibility in its short linker. An examination of this figure suggests that it is unlikely that the bulky biradical will diffuse into the channel and that the peptide molecules inside the crystallites are in intimate contact with the paramagnetic center. Nevertheless, we observe a substantial enhancement in the nuclear spin polarization ($\epsilon \sim 120$) as opposed to the full enhancement ($\epsilon \sim 160$) observed from the solvent (*vide infra*). This observation is explained quantitatively by considering the size of the crystals, the nuclear T_1 , the ^1H - ^1H spin diffusion constants, and the initial polarization enhancement of the solvent. In addition, we demonstrate that the enhanced ^1H polarization can be readily transferred to ^{13}C and ^{15}N in the peptide and multidimensional spectra acquired with reduced acquisition periods. Thus, DNP experiments will likely evolve to an important spectroscopic ingredient in determining structures of amyloid peptides and proteins in the form of macroscopic nanocrystals and fibrils.

7.1.2. Theory

We begin with a brief discussion of the processes involved in the application of DNP to insulating solids, involving bulk nuclei doped with dilute concentrations of paramagnets. The DNP process involves transfer of spin polarization from electrons to nuclei, which can occur through at least three different mechanisms, the solid effect (SE) ⁵⁰, the cross effect (CE) ^{51-55, 67, 106} and thermal mixing (TM) ^{56, 58}. The relative importance of these mechanisms is determined by the relationship between the

homogeneous EPR linewidth (δ) and the nuclear Larmor frequency (ω_n). When the EPR linewidth is smaller than the nuclear Larmor frequency ($\delta < \omega_n$) only the SE is possible, while the CE and TM are operative when $\delta > \omega_n$. The spin dynamics associated with the SE, CE and TM involve single, pairwise and multiple electron spins, respectively. While an increase in the applied external magnetic field tends to reduce the efficiency of the polarization, the extent of this reduction is dependent on the type of polarization mechanism involved. In the case of the CE and TM, the impact of higher magnetic fields on the polarization transfer efficiency can be compensated by optimizing of the EPR spectral parameters, e.g. the electron-electron dipole interaction and the EPR frequency separation of the paramagnetic species ¹¹⁴, for the desired field strength.

The resulting locally enhanced nuclear polarization is distributed to the bulk nuclei via ¹H nuclear spin diffusion. In a homogeneous sample, the efficiency of this process depends on the density and possibly orientations of nuclear spins. However, the presence of a diffusion barrier ^{169, 170}, for instance resulting from the proximity of a paramagnetic center or two domains characterized by large differences in nuclear spin characteristics, can reduce the efficiency of spin diffusion. The nuclear spin diffusion barrier near a paramagnetic species arises from a strong electron-nuclear dipolar field at the nucleus that isolates the surrounding nuclei in terms of resonance frequency. Similarly, a diffusion barrier can be caused by gaps in resonance frequency between two domains that have different magnetic susceptibilities in response to the external magnetic field ¹⁷¹⁻¹⁷³. This might be a concern for dehydrated nanocrystals embedded in a frozen aqueous solvent matrix. Note that the latter boundary is less intrusive when the domain size is smaller (e.g., in nanometer range).

For simplicity of our discussion, we assume the bulk solvent nuclear spins surrounding the crystals are uniformly polarized with an enhancement factor ϵ_0 . The magnitude of this factor is characteristic of the bulk solvent/radical composition and the experimental and instrumental details^{114, 127}. In our analysis we assume that penetration of enhanced nuclear polarization into a nanocrystal is dominated by uniform nuclear spin diffusion along the smallest dimension of the crystal. This pseudo-1D spin diffusion depends on the width of the smallest crystal dimension, the nuclear T_1 , and the nuclear spin diffusion constant, D , of the nanocrystal.

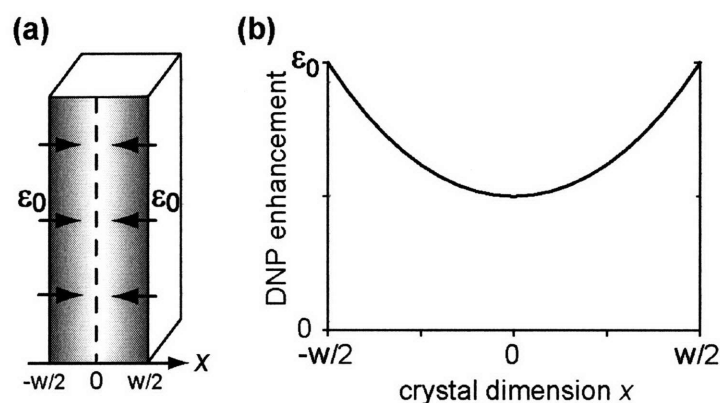


Figure 7.2. (a) Model for an individual peptide crystallite, showing polarization transfer into the core along the narrowest crystal dimension x . (b) Predicted enhanced polarization profile along the dimension x of the nanocrystal.

To illustrate our description of the polarization transfer into uniformly sized crystals, we show the model depicted in Figure 7.2a. A steady-state enhanced polarization of the glass matrix results from microwave irradiation and diffuses into the nanocrystals through the crystal surface. Within the crystal, the enhanced polarization, ϵ_0 , diffuses into the core, following a process that is assumed to be dominated by one-dimensional nuclear spin diffusion along crystal x -axis⁴ and described by Fick's law^{157, 174}:

$$\frac{\partial P}{\partial t} = D \frac{\partial^2 P}{\partial x^2} - \frac{P}{T_{1n}}, \quad (1)$$

where $P(x,t)$ is the polarization, after subtraction of the Boltzmann polarization, at a time t and a distance x from the center of the crystal; D is the diffusion constant, and T_{1n} is nuclear spin-lattice relaxation time. In the steady-state $\partial P / \partial t = 0$, and we obtain

$$D \frac{\partial^2 P}{\partial x^2} = \frac{P}{T_{1n}}. \quad (2)$$

If we assume that the nuclei in the nanocrystal reach a steady-state and that their enhanced polarization is evenly-distributed, then we have the boundary condition for the surfaces of the crystals:

$$P\left(\frac{w}{2}\right) = P\left(-\frac{w}{2}\right) = \varepsilon_0 P_0, \quad (3)$$

where w is the crystal width along the x axis; ε_0 is the steady state enhancement factor for the solvent nuclear polarization and P_0 is the nuclear Boltzmann polarization at thermal equilibrium. As illustrated in Figure 7.2b, the solution to Eq. 2 in the region $-w/2 \leq x \leq w/2$ with the boundary condition in Eq. 5 is

$$P(x) = \varepsilon_0 P_0 \cosh^{-1}\left(\frac{w}{2\sqrt{DT_{1n}}}\right) \cosh\left(\frac{x}{\sqrt{DT_{1n}}}\right), \quad (4)$$

Experimentally one observes the average polarization across the whole crystal ($-w/2 \leq x \leq w/2$), as given by

$$\frac{1}{w} \int_{-w/2}^{w/2} P(x) dx = \frac{2\sqrt{DT_{1n}}}{w} \varepsilon_0 P_0 \tanh\left(\frac{w}{2\sqrt{DT_{1n}}}\right), \quad (5)$$

which dictates that the measured enhancement factor ε of the crystals is

$$\varepsilon = \varepsilon_0 \frac{2\sqrt{DT_{1n}}}{w} \tanh\left(\frac{w}{2\sqrt{DT_{1n}}}\right). \quad (6)$$

The spin diffusion constant D in a proton rich solid can be estimated as $D = \lambda^2 \pi B_L$, where B_L is the average dipolar interaction at a characteristic ^1H - ^1H distance λ . At room temperature, the average dipolar interaction depends on molecular dynamics affecting the proton coordinates¹⁵⁷. These dynamics are mostly quenched at cryogenic temperatures, except for the threefold hopping of methyl groups. Nonetheless, the application of sample rotation in solid state MAS NMR to the frozen sample can significantly modulate the dipolar interaction. Once the ^1H - ^1H dipolar coupling constant ω_d is smaller than the spinning frequency ω_r , Average Hamiltonian Theory¹⁷⁵ suggests $B_L \propto (\omega_d)^2/\omega_r$. Based on the published crystal structure⁴ combined with computational modeling, the ^1H - ^1H distances along the two shortest crystal axes range from 2.0 to 3.2 Å for a continuous trajectory throughout the crystal, resulting in $\omega_d/2\pi$ of 15 to 3.5 kHz. Notice that the magic angle spinning at $\omega_r/2\pi \sim 5$ kHz has little effect for these magnitudes of the ^1H - ^1H dipolar interaction. In other words, the corresponding spin diffusion constant D should approximate 1×10^5 to 2×10^5 Å²/s. Typical experimental values that were previously obtained for a variety of organic polymers ranged from $2-8 \times 10^4$ Å²/s¹⁷⁶⁻¹⁷⁹, but these are likely to reflect the presence of more molecular dynamics than are present in our system, related to higher temperatures and more mobile moieties including methyl groups. Using

the estimated diffusion coefficients D and measured T_{1n} (~ 17 s, *vide infra*) with Eq. 6, we can predict the theoretical enhancement factor of the ^1H polarization in GNNQQNY₇₋₁₃ as a function of crystal size, as illustrated in Figure 7.3. These predicted DNP enhancements in nanocrystals will be compared to experimental results from DNP measurements and TEM observations.

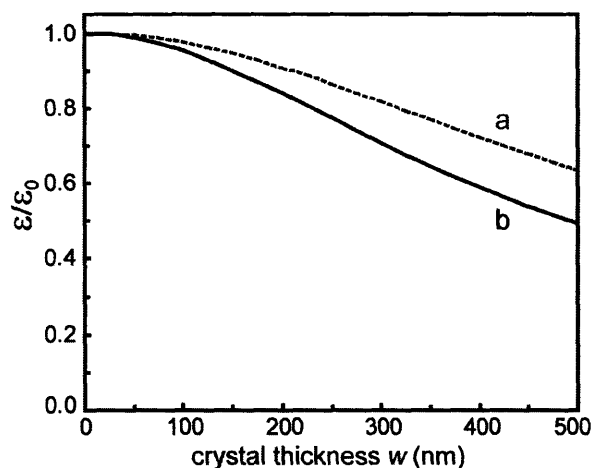


Figure 7.3. The theoretical enhancement ϵ , compared to the homogeneous enhancement ϵ_0 in the glassy matrix, of proton polarization in a nanocrystal of width w . The calculation uses a proton $T_{1n}=17$ s, and the calculated values of the diffusion constant (a) $D=2\times 10^5$ and (b) $1\times 10^5 \text{ \AA}^2/\text{s}$.

7.1.3. Experimental Section

7.1.3.1. Peptide nanocrystal samples

The peptide GNNQQNY was synthesized using solid phase synthesis methods in both a natural abundance form, and a segmentally, isotopically labeled form [$U\text{-}^{13}\text{C}, ^{15}\text{N}$ -GNNQIQNY by CS Bio Co. (Menlo Park, CA). A mixture of 20% labeled and 80% unlabeled material was mixed and then crystallized as follows. A solution of 10 mg/ml in

de-ionized water was filtered through a 0.2 μm filter to remove residual particles and then crystallized for at least 24 hours at 4°C. This protocol yields homogenous monoclinic nanocrystals.

7.1.3.2. DNP experiments

The DNP samples were prepared by washing the fully crystallized sample several times with 80/20 $\text{D}_2\text{O}/\text{H}_2\text{O}$, then mixed with 60/30/10 glycerol- $\text{d}_8/\text{D}_2\text{O}/\text{H}_2\text{O}$, containing 10mM of biradical polarizing agent. The deuterated solvents were obtained from Cambridge Isotope Laboratories (Andover, MA). The biradical TOTAPOL, composed of two TEMPO moieties tethered by a 5-atom linker, was synthesized as described elsewhere¹²⁷. The resulting heterogeneous mixture, containing a total of ~20 mg peptide, was center-packed into a 4 mm sapphire MAS rotor. A similarly-prepared, undiluted sample consisting of 100% $[\text{U-}^{13}\text{C}, ^{15}\text{N-GNNQ}]\text{QNY}$ crystals hydrated in de-ionized water was used as a reference sample.

All DNP enhanced CP-MAS experiments were performed in a 5 Tesla superconducting magnet (^1H frequency of 212 MHz) with a superconducting sweep coil capable of changing the magnetic field by ± 750 G. A custom-designed probe was used to perform triple resonance experiments -- two rf frequencies (^1H , ^{13}C) and a waveguide provided for irradiation of the 4 mm sample with microwaves -- during MAS (~4-6 kHz) at ~90 K⁶³. High-power, 139.66 GHz microwaves were obtained from a gyrotron (~10 W output power) delivering ~1.5 W to the sample. Since there is not a resonant microwave structure in the probe, the quality factor is low ($Q \sim 1$) for the microwave radiation. The Q of the RF circuit is not perturbed by the microwave waveguide. The pulse sequence¹¹⁴ begins with saturation of ^1H polarization by a series of 90° pulses and

delays (10 ms) followed by a period of polarization recovery (1-75 s). Application of microwaves during the recovery period leads to a buildup of enhanced ^1H polarization that is subsequently transferred to the ^{13}C or ^{15}N spins through ramped cross-polarization (CP) (spin-lock for 1.2 ms with a constant 30 kHz ^1H field and a ramped 26-30 kHz ^{13}C field). The resulting ^{13}C and ^{15}N CP-signals were detected using ~ 70 kHz TPPM ^1H decoupling¹¹⁶. The two-dimensional ^{13}C - ^{13}C correlation experiments involved ^{13}C - ^{13}C mixing with 6 ms of ^1H -driven spin diffusion (PDSD) with R^3 ^1H irradiation¹⁸⁰, and was executed in the absence of the saturating proton pulses with the following experimental details: 5 s recycle delay, 56 t_1 points of four scans each, resulting approximately 20 minutes of acquisition time. The data were processed using NMRPipe¹⁸¹.

7.1.3.3. Transmission Electron Microscopy

A Philips EM410 electron microscope was used to examine the peptide crystals by transmission electron microscopy (TEM) before and after the DNP measurements. TEM micrographs were obtained after negative staining with aqueous uranyl acetate. The dimensions of numerous peptide nanocrystals were measured by comparison to calibration micrographs of reference grid samples (Electron Microscope Sciences, Hatfield PA).

7.1.4. Results and Discussion

7.1.4.1. Enhanced NMR signal intensities of peptide nanocrystals

One-dimensional CP/MAS NMR data recorded for the 20% labeled peptide nanocrystal sample in the absence of DNP yielded relatively poor signal-to-noise spectra.

The measurements were repeated in the presence of microwave irradiation, which resulted in a dramatic increase in the signal intensity, as illustrated in Figure 7.4. The signal-to-noise without microwave irradiation was insufficient to observe well resolved spectral lines for the (20%) isotopically labeled ^{13}C . However, in the presence of microwaves even the natural abundance ^{13}C signals could be seen (from the unlabeled residues in the segmentally labeled peptide and the glycerol in the frozen solvent matrix). The same enhancement effect is observed for the ^{15}N spectrum, where the signals were undetectable in the absence of DNP, but are rather intense with DNP enhancement. The maximum observed enhancement was quantified to be $\epsilon \sim 120 \pm 10$ after 75 s of microwave irradiation, relative to the ^{13}C spectrum without DNP. Note that the NMR signals of the solute (e.g. the glycerol carbons) in the glass matrix are also strongly enhanced, with an estimated enhancement $\epsilon_0 \sim 160$, based on previous measurements. The intensity of the ^{15}N signals without microwave irradiation was too weak to allow an accurate measurement of the enhancement, but its enhancement should be similar to that measured for the peptide ^{13}C 's since both are determined by the polarization enhancement of the ^1H spins.

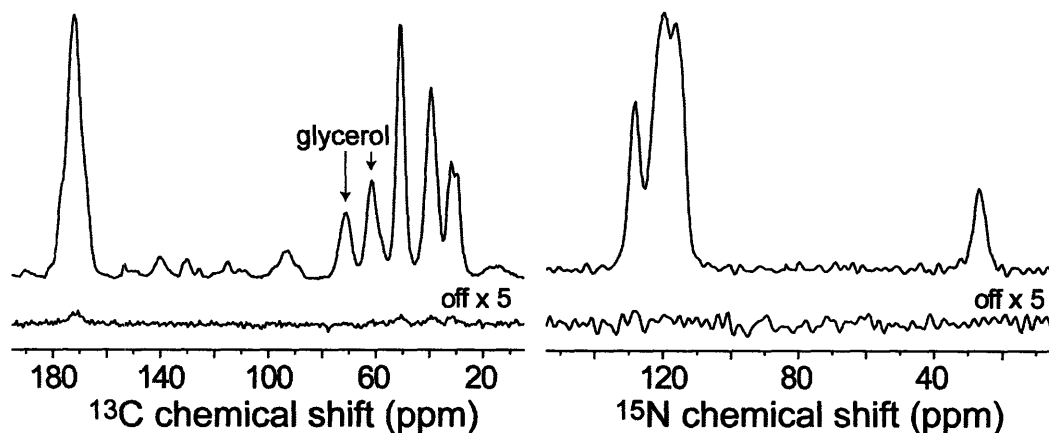


Figure 7.4. DNP enhanced ^{13}C (a) and ^{15}N (b) CP-MAS spectra of [20% $\text{U-}^{13}\text{C}$, ^{15}N -GNNQ]QNY in d_8 -glycerol/ $\text{D}_2\text{O}/\text{H}_2\text{O}$ (60/30/10) with 10 mM TOTAPOL biradical at 90 K and 5 T, with (top trace) and without (bottom trace) DNP. The microwave power was 1.5 W and irradiation time was 75 s for both spectra.

While the signal intensity in the absence of DNP was too low for a two dimensional NMR experiment to be practical, the observed DNP enhancement stimulated us to perform a 2D experiment to evaluate the applicability of DNP to this and other amyloid samples. This involves a two-dimensional ^{13}C - ^{13}C homonuclear correlation experiment with 6 ms spin diffusion mixing. The results are shown in Figure 7.5 and the combined acquisition time of entire experiment required approximately 20 minutes. This of course compares extremely favorably with the anticipated acquisition time in the absence of DNP. Note that one can discern several signals from the natural abundance Tyr side chain further highlighting the high enhancement factor resulting from the microwave irradiation.

The assignments of the cross peaks in the spectrum are indicated in the figure, and were based on experiments performed at higher fields to be described in a separate publication. As mentioned we observe the natural abundance glycerol peaks on the

diagonal, which are broadened because of the amorphous nature of the frozen glass matrix and the proximity of the biradical species. The presence of a substantial radical concentration in a solution is known to cause significant broadening in any co-dissolved solute. Especially when using high concentrations of less efficient polarizing agents, this is also seen in DNP experiments on frozen solutions. In contrast, the crystalline nature of the sample shields the molecules on the interior of the crystals from both the glassy solvent and the direct interaction with the radicals (except for narrow regions near the crystal surface), resulting in peptide peaks that are narrower than the glycerol signals. However, the peptide signals are significantly broader than observed in our assignment experiments mentioned above, where the spectra were recorded on a 500 MHz instrument. To evaluate whether any broadening is due to the experimental DNP conditions and examine whether it could be indicative of the radical having direct access to a significant portion of the peptide, we performed a number of tests. In room temperature spectra comparing the glycerol and TOTAPOL-containing DNP sample to a non-DNP reference sample (lacking glycerol and radicals) we observe the same line width for both samples, which also matches the line widths at low temperature. This fact, plus the observation that the spectra narrow at high fields, suggest that the additional linewidth arises from $n = 0$ rotational resonance effects^{175, 182}. These effects are important when the shift separation is comparable to the dipolar coupling and the spinning frequency is low as was the case in these experiments. For a more sensitive test for the penetration of TOTAPOL biradicals into the crystals, we performed room temperature measurements at higher field (700 MHz ¹H frequency) and faster spinning (15 kHz MAS) comparing GNNQQNY nanocrystals before and after the addition of

biradical. The line widths in these data are significantly smaller (approximately 100 ± 2 Hz for the various labeled ^{13}C carbons and as low as 35 ± 2 Hz for the N-terminal glycine- ^{15}N) and should be sensitive to broadening by nearby radicals. Even at a concentration of 50 mM TOTAPOL, five times the amount used in the DNP experiments, no broadening of the above carbon and nitrogen line widths was observed, confirming the absence of radicals from the inside of the crystals.

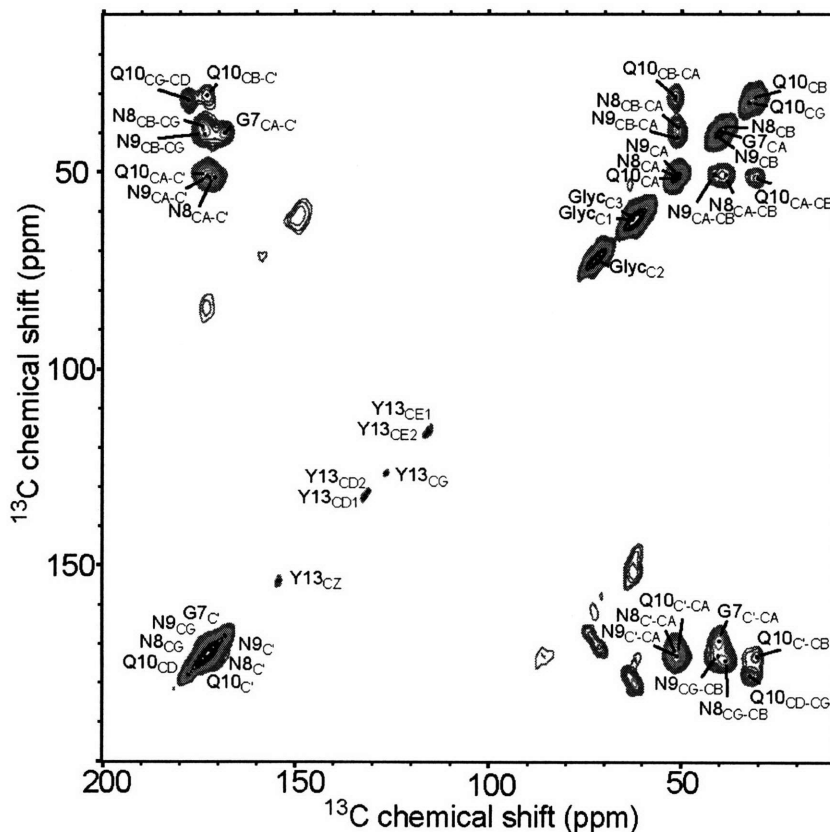


Figure 7.5. DNP-enhanced ^{13}C - ^{13}C R^3 PDS correlation spectrum of [20% $\text{U-}^{13}\text{C}$, ^{15}N -GNNQ]QNY nanocrystals. Indicated assignments are based on previous assignment data, and unmarked cross peaks represent spinning sidebands and experimental artifacts.

The recycle delay for the acquisition of the 2D spectrum was significantly shorter than required for the development of the full DNP enhanced polarization of the ^1H 's in the crystals, and reflects a compromise between a large signal enhancement and the phase cycling requirements of the experiment. The result of this choice of recycle delay is that the relative intensities of the glass-embedded glycerol solvent relative to the peptide signals are shifted in favor of the solvent signals, reflecting a difference in the polarization rate between the crystals and the solvent molecules. This difference is further illustrated in a series of one-dimensional experiments, examining the buildup of magnetization as a function of the microwave irradiation time. These experiments were performed according to the procedure described previously¹¹⁴ and the resulting ^{13}C spectra confirm that the polarization buildup for the glycerol is substantially faster than for the peptide crystal signals (Figure 7.6). The time constants for the glycerol signals, ranging from 7 to 8 s, are shorter than those of the nanocrystal signals which range from 15.5 to 17 s. The presence of the biradicals at 10 mM reduces the ^1H T_{1n} in the glassy solvent, giving a rapid polarization transfer and shorter time constants for polarization. Since the peptide crystals exclude the TOTAPOL, polarization time constants in the crystals reflect the intrinsic ^1H T_{1n} , which is relatively long due to the low temperatures and determines the internuclear spin diffusion within the crystals. Note that, in general, relatively long spin lattice relaxation times are necessary for optimal DNP enhancement. We will now correlate the diffusion constant, T_{1n} , and size of nanocrystals with the observed enhancement using the Fick's law treatment discussed above.

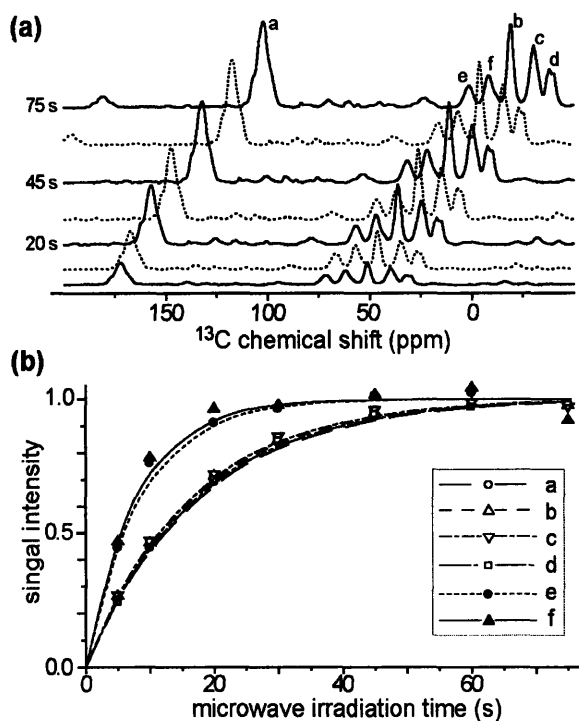


Figure 7.6. Time-dependent growth of the enhancement polarization. (a) Illustration of the 1D ^{13}C spectra as a function of microwave irradiation time, after 5, 10, 20, 30, 45, 60 and 75 s of microwave irradiation. The chemical shift axes are offset for visual clarity. (b) The intensity of the spectral lines normalized to maximum intensity of each signal. Lines indicate calculated fits using growth time constants of 16-17 s for crystal signals (a-d), and 7-8 s for glycerol peaks e and f.

7.1.4.2. Polarized portions of fibril crystals

Based on the TEM micrographs illustrated in Figure 7.7, we were able to measure the dimensions of the nanocrystals in the samples used to record the DNP enhanced spectra. The average width of the crystals approximates 150 nm, with a typical range between 100 and 200 nm. The distribution of crystal sizes in these samples is not entirely uniform, with a few exceptions of significantly thicker or thinner (down to ~50 nm) width. Narrowing of the crystals tends to occur at their ends. These observations correspond well to previously published TEM data and dimensions of GNNQQNY nanocrystals¹⁶⁸.

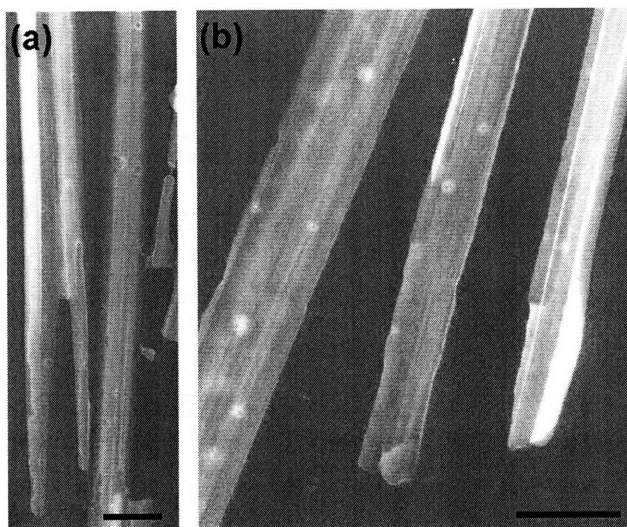


Figure 7.7. Transmission electron micrographs of GNNQQNY nanocrystallites at an approximate magnification of (a) 55,000 and (b) 110,000. The black bars indicate 200 nm.

We will now compare these experimental observations to the predicted relative enhancements in Figure 7.3, obtained using the Fick's law formula in Eq. (6) together with the estimates of the D and measured values of T_{1n} . The central assumption in that calculation was that the biradical TOTAPOL does not penetrate the crystals, an assumption that is supported by the observations mentioned above, involving the size of TOTAPOL relative to the water channel (see Figure 7.1) and the T_{1n} data of the frozen solvent *versus* the crystals (see Figure 7.6).

Assuming the polarizing agent from the crystal core is absent from the crystal core, then direct polarization of the crystal surface layer is unable to explain the observed large crystal signal enhancement. Rather it is due to diffusion into the crystals of the enhanced nuclear polarization $\epsilon_0 P_0$ uniformly present throughout the solvent matrix, and at the surface of the crystals, as described in Section 7.1.2. There, we estimated the ^1H spin diffusion constants as lying in the range $1 \times 10^5 - 2 \times 10^5 \text{ \AA}^2/\text{s}$. Based on these assumptions

and the measured $T_{1n} \sim 17$ s we predicted the enhancements to be observed in crystals with a various characteristic widths (Figure 7.3). In our case we observed an average crystal enhancement ϵ that is ~ 0.75 (120/160) of the enhancement ϵ_0 in the bulk solvent matrix. Combined with the crystal dimensions that were observed in our TEM experiments (100 - 200 nm), this result falls slightly under the curve shown for the lower diffusion constant. Considering the relatively simple nature of the applied model, it is unclear whether very detailed conclusions concerning the exact value of the spin diffusion rate can be drawn on the basis of these results. The lower rate could indicate that the effective diffusion rate is limited by a 'bottleneck' across the direction of transfer that is not apparent in the crystal structure, possibly near the crystal-solvent interface. Inhomogeneity and anisotropy in the crystal packing could affect the effective spin diffusion constant. Furthermore, one could also consider other experimental features such as the distribution of crystal sizes and possible factors affecting the uniformity of the surface polarization and the diffusion pattern.

7.1.5. Conclusions

We have shown that DNP experiments are applicable to enhancing the ^1H polarization of peptide nanocrystals of ~ 100 - 200 nm width, yielding intense NMR signals and significant reductions in acquisition times. The increased signal intensity opens new possibilities for significantly more complex and informative pulse experiments to be performed on relatively dilute samples. Dilution of the isotopically labeled sample is often essential when intermolecular interactions have to be suppressed, as is the case for small molecules like the peptides studied here. DNP enhancement would allow a high

level of dilution while maintaining sufficient signal intensity for accurate and sensitive NMR measurements.

One of the limiting aspects of the data shown here is the limited resolution that can be achieved on this relatively low-field prototype equipment. Ongoing experiments on different instrumentation^{62, 89} in our group have demonstrated the acquisition of higher resolution DNP spectra^{117, 118}. We note that the experiments discussed here show little or no sign of additional broadening due to the presence of the radicals or the cooling to 90 K. These observations could be attributed to the nature of these crystals, which are very tightly packed and exclude both the TOTAPOL radicals and the amorphously freezing solvent system.

The exclusion of the bulky biradical polarizing agent from the crystal lattice highlights the importance of ^1H - ^1H spin diffusion in DNP experiments on heterogeneous samples. We presented a simple calculation based on 1D spin diffusion that explains the observed extent of polarization and correlates it to the observed crystal size. A more detailed evaluation of the exact role of spin diffusion in these experiments, and further quantification, would benefit from further experiments with particles (or crystals) of a carefully controlled size. The theory discussed here (supported by our data) would suggest that nanocrystals with a size up to 1 μm can be efficiently polarized, opening avenues for further applications of DNP to studies of protein microcrystals. Further experiments with a wider variety of crystalline and fibril compounds should provide further insights into the importance of sample features such as the presence of methyl groups, molecular motion and crystal packing for spectral features such as low-temperature resolution, nuclear spin diffusion, and the achievable DNP enhancement.

7.2. In situ Temperature Jump-High Frequency Dynamic Nuclear Polarization Experiments: Enhanced Sensitivity in Liquid State NMR Spectroscopy

7.2.1. Introduction

The last decade has witnessed a renaissance in the development of approaches to prepare samples with high nuclear spin polarizations with the goal of increasing signal intensities in NMR spectra of solids and liquids. These approaches have included high frequency, microwave driven dynamic nuclear polarization (DNP)^{62, 63, 84, 98, 100, 101, 105, 109, 114, 119}, para hydrogen induced polarization (PHIP)^{183, 184}, polarization of noble gases such as He, Xe¹⁸⁵⁻¹⁸⁷ and more recently Kr³⁸, and optically pumped nuclear polarization of semiconductors^{35, 188, 189} and photosynthetic reaction centers and other proteins^{72, 190-192}. All of these approaches successfully yield highly polarized spins, and are studied to elucidate features of the polarization processes or of the material being polarized. However, one of the most appealing aspects of high polarization methods is the possibility of transferring the polarization from the source to a surrounding medium such as a solvent and to subsequently distribute the polarization to chemically, physically or biologically interesting solutes. For this to occur it is necessary that the polarizing agent be strongly coupled to the lattice of nuclear spins, and in this regard paramagnetic polarizing agents are appealing since the large magnetic moment of the electron spin couples effectively to its surrounding nuclei. Accordingly, high frequency microwave (≥ 140 GHz) driven DNP experiments using stable free radicals as polarizing agents^{98, 114} are currently used successfully to polarize a variety of systems including solid polymers

59-61, 100, 123, 157, frozen solutions of small molecules⁹⁸, amino acids^{62, 84}, virus particles¹⁰⁵, soluble and membrane proteins¹⁰⁹ and amyloid nanocrystals¹¹⁹ achieving enhancements, $\epsilon \sim 50-400$, depending on the details of the experiment.

In addition to polarizing solid samples, there is considerable interest in using high frequency DNP to enhance the sensitivity of liquid state NMR experiments. However, the polarization mechanisms operative in dielectric solids at high fields – the solid effect^{58, 68}, the cross effect^{67, 114} and thermal mixing⁵⁸ – are not applicable to liquids. Instead, the Overhauser effect (OE)^{48, 49, 156} is the dominant polarization mechanism, and it is efficient only at low magnetic fields. In particular, for small molecules, the rotational or translational correlation times are $\sim 10^{-12}$ s and at low magnetic fields the condition $\omega_s \tau_c \leq 1$ is satisfied (where ω_s is the electron Larmor frequency and τ_c the correlation time), and the Overhauser effect is effective in transferring polarization. However, in the high field regime commonly employed in contemporary NMR experiments, ω_s is large, the rotational and translational spectral densities are vanishingly small, and the Overhauser enhancements decrease significantly¹²⁴. Thus, to enhance the polarization of liquid samples in high field experiments, an alternative method is required.

In this section we explore one approach that leads to enhancements in the range of 120 - 400 in spectra of low- γ spins such as ^{13}C and ^{15}N . In particular, we polarize the ^1H spins in the sample at low temperatures (~ 90 K) using low concentrations of biradical polarizing agents^{114, 127}. That polarization is transferred to low- γ spins with cross polarization, the sample is melted with an infrared laser pulse, and the enhanced signal observed in the presence of ^1H decoupling. The entire cycle can be repeated *in situ* and signal averaging performed as is customary in contemporary NMR experiments. If the

polarization step were performed at a lower temperature, then a larger enhancement factor would be observed. Because of the freezing and thawing processes, this version of the experiment will find greatest application to studies of systems that can be repeatedly frozen and thawed such as small molecules and to a field such as metabolic screening.

7.2.2. Experimental Section

Samples for the experiments consist of solutions containing high concentrations of ^{13}C labeled small molecules to facilitate observation of signals in the absence of DNP. In particular, the high concentration facilitates observation of the signal intensity in the absence of microwave irradiation and therefore measurement of the enhancement. For example, in the experiments below we used 2 M ^{13}C -urea in 50% $^2\text{H}_6$ -DMSO and 50 % water (80 % $^2\text{H}_2\text{O}/20$ % H_2O). The solution was prepared with 3 - 5 mM TOTAPOL¹²⁷ as the biradical polarizing agent. About 9 μL of sample was placed in a 2.5 mm OD quartz capillary and NMR measurements were conducted in a custom designed probe in a 5 T magnet (211 MHz for ^1H and 53.31 MHz for ^{13}C). Continuous microwave irradiation was generated with a 140 GHz gyrotron⁹. The sample was maintained at ~ 90 K by circulating cold N_2 gas during the experimental cycle. Typically the equilibrium polarization buildup required 15 - 40 s (the ^1H T_1 is typically 5-10 s), and the enhancement in the solid state spectra, ϵ , was ~ 290 at this temperature and magnetic field. The rapid temperature jump (TJ) was performed by irradiating the sample with 10.6 μm radiation from a CO_2 laser transmitted to the sample through a multimode hollow optic fiber. Haw and coworkers^{10, 11} used a similar approach in TJ experiments on polymers with the exception that the sample was larger (5 mm diameter rotors) and

required higher laser power. Thus, it was necessary to use lenses rather than an optic fiber to irradiate the sample. After melting the solution NMR spectrum was recorded in the presence of decoupling, and the sample was refrozen and polarized again for another experimental cycle. With our current experimental apparatus the freezing typically required 60-90 s, and the melting < 1 s. Figure 7.8 illustrates the cycle used in the TJ-DNP experiments – cooling, polarization with microwaves, melting with IR radiation, and observation of the liquid state spectrum. Figure 7.9 shows the pulse sequence associated with these steps and it incorporates storage/retrieval pulses prior to and following the melting step of the experiment.

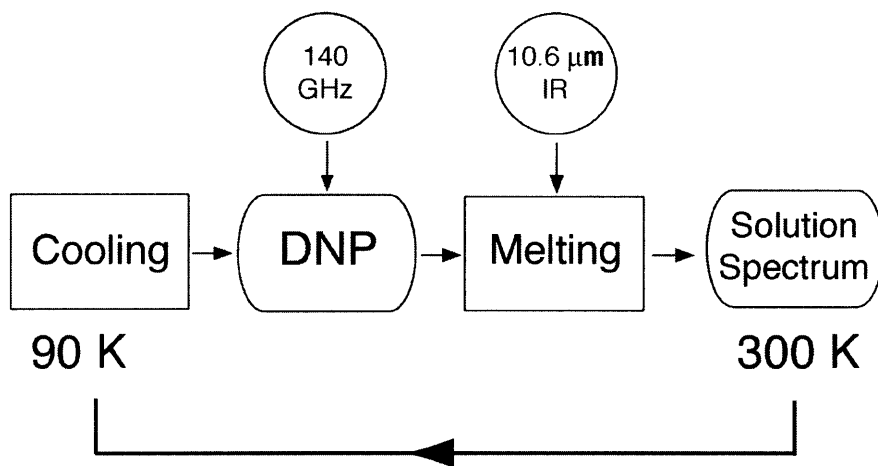


Figure 7.8. TJ-DNP cycle consisting of cooling, polarization, melting and acquisition employed in the experiments described here. The microwaves for the DNP process were supplied by a 140 GHz gyrotron²² and the melting was accomplished with at 10.6 μm CO₂ laser^{10, 11}. With the current configuration of the apparatus the experiment can be recycled every 60 to 90 s.

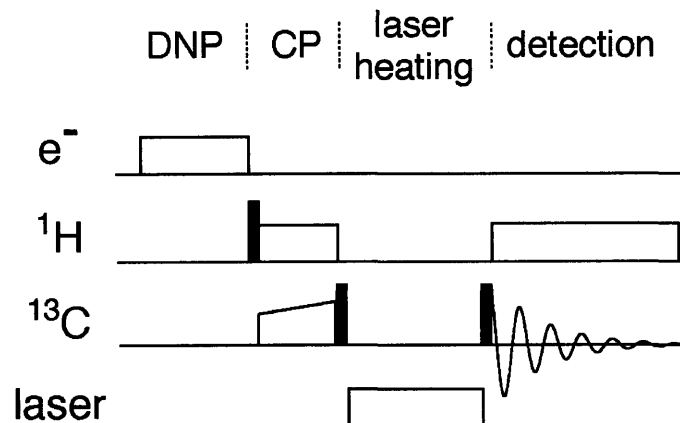


Figure 7.9. Experimental scheme for observation of sensitivity enhanced liquid state NMR using temperature jump-DNP. 140 GHz microwaves irradiate the sample at ~ 90 K, polarizing the ^1H spins in the sample. Enhanced ^1H polarization is then transferred to ^{13}C via cross polarization. During the laser heating, the ^{13}C magnetization is stored along the z-axis of the rotating frame. The ^{13}C spectrum is detected following a 90° pulse in the presence of WALTZ ^1H decoupling.

Enhancements, ϵ^\dagger , (*vide infra*) were determined by comparing the signal intensities of the DNP enhanced ^{13}C signal intensities obtained in the melting experiment with those obtained from room temperature solution NMR experiments. The room temperature liquid state spectra were directly detected and typically acquired by averaging 128 to 512 scans with a long recycle delay (60-120 s) to ensure that we reached the equilibrium Boltzmann polarization. Note that in generating the ^{13}C DNP enhance signals, we transfer polarization from electrons to ^1H and then to ^{13}C via CP since this is the most time efficient manner to move polarization from the electrons to the ^{13}C . In principle we could polarize ^{13}C directly but the process is slower since spin diffusion in the ^{13}C reservoir is slow. It should also be possible to detect the ^{13}C signals indirectly via observation of ^1H as is customary in many solution NMR experiments ³¹.

7.2.3. Results and Discussion

In Figure 7.10 we illustrate a series of spectra of ^{13}C -urea obtained with a magic angle spinning experiment as a function of the microwave irradiation period. The spectra illustrate the growth of the ^{13}C polarization to a value 290 ± 30 times that of the Boltzmann polarization. The initial trace in the series shows the spectrum without microwaves expanded by a factor of 20. For ^{13}C -urea in water/glycerol the polarization process reaches equilibrium in ~ 40 s. In the case of ^{13}C -urea we achieve $\epsilon = 290 \pm 30$ of ^1H polarization, which implies a larger enhancement of ^{13}C polarization. However in other sample this value is lower since relaxation processes are present.

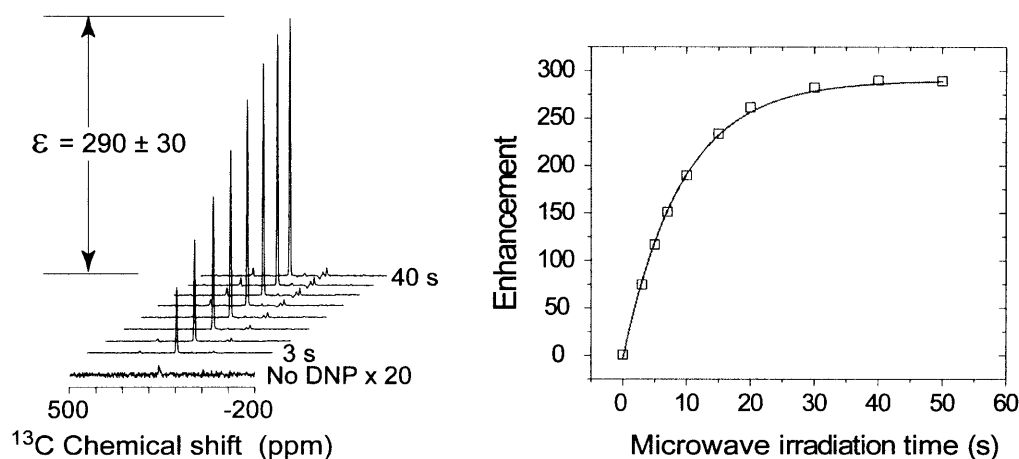


Figure 7.10. (left) MAS-DNP experiment illustrating the growth of the polarization in a ^{13}C -urea sample after microwave irradiation. The irradiation period extends to ~ 40 seconds where an enhancement of 290 ± 30 is achieved. (right) Plot showing the development of the polarization enhancement with time. The growth time constant is ~ 9 s.

Figure 7.11 shows the TJ-DNP enhanced ^{13}C NMR spectra of ^{13}C -urea, $\text{Na}[1,2-^{13}\text{C}_2, ^2\text{H}_3]$ -acetate and $[\text{U}-^{13}\text{C}, ^2\text{H}_7]$ -glucose. In the top trace of each figure is illustrated the TJ-DNP enhanced spectrum and the lower traces show the signal intensity obtained with ^1H

decoupled Bloch decays for comparison. The enhancements observed in the spectra, which we label as ϵ^\dagger , a definition that is discussed below, are included for each compound in the figure and are ~400 for urea, ~290 for sodium acetate, and ~120 for glucose. Note the ^{13}C - ^{13}C J-coupling that is resolved in the acetate spectrum. This clearly establishes that, when the ^{13}C T_1 is long compared to the melting period and is sufficiently long in the solution phase, then it is possible to observe significant signal enhancements in the ^{13}C solution spectra and that the resolution is not degraded by the presence of a paramagnetic polarizing agent.

We noted above that we have labeled the enhancements as ϵ^\dagger , rather than ϵ as is common in solid state MAS experiments^{62, 63, 84, 98, 100, 105, 109, 114, 119}. Thus, there are two conventions in use to report the size of enhancements that deserve explanation.

(1) In solid state MAS experiments it is usual to compare the signal intensity in the presence and absence of microwave irradiation at the temperature where the DNP enhancement is performed. This ratio of signal intensities yields the enhancement ϵ due to the microwave irradiation. The data and enhancements reported in several other publications from our laboratory at $T \leq 90$ K use this convention and are due to the microwave driven enhancement alone^{62, 63, 84, 98, 100, 105, 109, 114, 119}.

(2) In the case of liquids, however, the relevant enhancement, that we define as ϵ^\dagger , is determined by the intensity of the DNP enhanced signal relative to the signal due to the Boltzmann polarization recorded at 300 K. Since the polarization is generated at low temperature, for example 90 K, there is an additional factor of $(T_{\text{obs}}/T_{\mu\text{wave}}) \sim (300 \text{ K}/100 \text{ K}) = 3$ included in the calculation of the enhancement ϵ^\dagger . When the polarization is

performed at 1.2 K and the observation is at 300 K, this number increases to 250. Thus, enhancements reported in the literature for solid state and liquids experiments differ by the factor $(T_{\text{obs}}/T_{\mu\text{wave}})$, which can be substantial. For example, by polarizing at 1.2 K Ardenkjær-Larsen and coworkers¹⁹³ reported $\epsilon^\dagger = 44,400$ which corresponds to $\epsilon = 178$ if we take $(T_{\text{obs}}/T_{\mu\text{wave}}) = 250$. Accordingly, in our discussion we quote two enhancements ϵ^\dagger and ϵ that are related by

$$\epsilon^\dagger = \epsilon(T_{\text{obs}}/T_{\mu\text{wave}})$$

where T_{obs} and $T_{\mu\text{wave}}$ are the temperatures where the signal observation and microwave irradiation occur. Note that, $\epsilon^\dagger = \epsilon$ in the limit where $T_{\text{obs}} = T_{\mu\text{wave}}$.

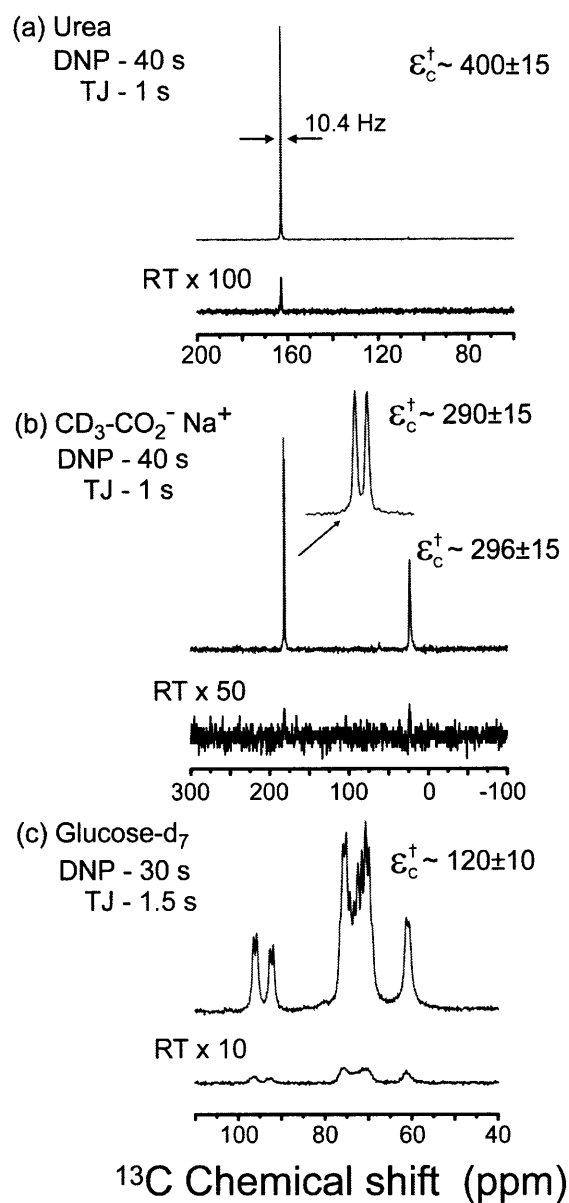


Figure 7.11. ^{13}C TJ-DNP NMR spectra of (a) ^{13}C -urea in 50% $^2\text{H}_6$ -DMSO and 50% water (80% $^2\text{H}_2\text{O}$ / 20% H_2O), (b) $\text{Na}[1,2\text{-}^{13}\text{C}_2, ^2\text{H}_3]$ -acetate in 60% $^2\text{H}_8$ -glycerol and 40% water (80% $^2\text{H}_2\text{O}$ /20% H_2O) and (c) $[\text{U-}^{13}\text{C}, ^2\text{H}_7]$ -glucose in water. Samples contained 3–5 mM TOTAPOL biradical polarizing agent 21 corresponding to 6–10 mM electrons. As explained in the text, deuteration of the samples was employed in order to circumvent the ^1H mediated ^{13}C relaxation in the viscous solution phase. The times required for polarization and melting of the sample are indicated next to each trace. The TJ-DNP spectra (the top trace in each figure) were recorded with a single scan while the room temperature spectra were recorded with (a) 256, (b) 128, and (c) 512 scans, respectively.

In Situ melting and dissolution experiments

In addition, there are several features of the experiments described here that differ in significant ways from the experiments described by Ardenkjær-Larsen, et al ¹⁹³. In particular, while we performed an *in situ* TJ melting experiment, they in contrast utilized an approach involving polarization at low field, “dissolution” of the sample, and transfer to a higher field for observation. The difference in the important experimental details is as follows. First, in the dissolution experiment the polarization step was performed at 1.2 K rather than 90 K. Second, it was performed in a 3.35 T field using a 200 mW, 94 GHz microwave source to drive the DNP process. Third, the triphenylmethyl based trityl radical ⁹⁶ was the polarizing agent, and the ¹³C spins in the sample were polarized directly ($\epsilon \sim 178$) rather than through the ¹H’s. Because of the low temperature, the low microwave power, the long T_{1e} of the trityl radical and the fact that they polarized ¹³C directly, their polarization times were ~ 80 minutes. In contrast, we are able to achieve enhancements $\epsilon \sim 290$ in ~ 40 s at ~ 90 K at 5 T using our 140 GHz microwave source and biradical polarizing agents. Finally, in the “dissolution” experiment the sample, consisting of 40-50 mg of frozen polarized pellets, is melted and dissolved in ~ 7 mL of hot water, diluting it by a factor of ~ 150 . If the polarized solute is used in imaging experiments, then dilution of the sample with solvent may not be a concern. However, for the analytical experiments that are the focus of our intension, it is clearly undesirable. Following dissolution, the sample was manually shuttled to a 400 MHz liquids spectrometer where the solution NMR spectrum was recorded. Because of the requirement of shuttling to a second magnet, it is not possible to rapidly repolarize the sample. In the results illustrated in Figure 7.11, the melting and spectroscopy are performed *in situ*. Further, the sample is

not diluted since the melting is performed with a 10.6 μm laser light. Finally, since the polarization and observation is performed *in situ*, it can be refrozen, repolarized, etc. and the experiment recycled in the manner that is customary in analytical NMR experiments. The point is illustrated in Figure 7.12 where we show a series of 16 spectra acquired over a period of ~40 minutes from a sample of ^{13}C -proline that was cycled through the steps

[Polarization (40 s) – Melting (1 s) – Acquisition (100 ms) – Refreezing (90 s)]_n

This result illustrates that even at this early stage in the development of the experiments the apparatus is sufficiently stable to reproduce the intensities in the spectra to ~5%. We also mentioned above that in the spectra of the samples that normally contain protons, the ^1H 's were substituted with ^2H . The reason for this is that in the liquid phase, the glassy glycerol mixtures used to polarize the samples are viscous. Consequently, the ^1H relaxation times are very short (milliseconds) ¹⁹⁴ and the short ^1H T_1 leads to relaxation of the ^{13}C and loss of the ^{13}C signal. However, we can recover the lost signal-to-noise of protonated carbons, such as those in protonated L-proline and sodium acetate, from signal average through recycled TJ-DNP experiments (Figure 7.12, right). Moreover, preliminary experiments with solvent systems that exhibit lower viscosity in the liquid phase, and still form low-temperature glasses that disperse the biradical, suggest possible circumvention of relaxation problems with employing protonated molecules in the TJ-DNP experiments.

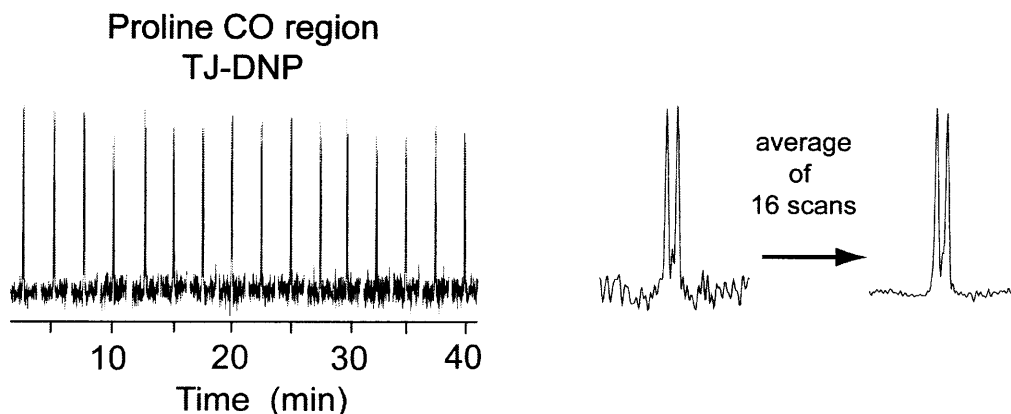


Figure 7.12. (left) Sixteen spectra of the carbonyl resonance in $U\text{-}^{13}\text{C}\text{-}^{15}\text{N}$ -proline resulting from a series of TJ-DNP experiments employing the sequence: DNP (40 s) - Melting (1 s) - Acquisition (100 ms) - refreezing (90 s). The spectra illustrate that following melting the sample can be refrozen, repolarized and another spectrum recorded in order to perform signal averaging. (right) The sixteen spectra can be averaged to show improved signal-to-noise.

Applications of TJ-DNP

The results shown in Figure 7.11 clearly indicate that, in its present form, TJ-DNP is capable of providing substantial enhancements in sensitivity in ^{13}C and other spectra of small molecules. Thus, when the quantity of sample is small and it can be repeatedly frozen, polarized and melted, then TJ-DNP experiments could provide a means to acquire ^{13}C spectra with excellent signal-to-noise in relatively short periods of time. An area where the current experimental protocol might find wide application is in metabolic screening, a subject that is of intense interest in the pharmaceutical industry.

Future Refinements

Our purpose here is to demonstrate the feasibility of using TJ-DNP for observing spectra of liquids with enhanced sensitivity. However, at this point the TJ-DNP is at an early stage of development and there remain many possible technical improvements that

could be implemented. Some of the most obvious and potentially significant are to perform the polarization at lower temperatures, to improve the efficiency of the melting process, and to perform the experiments in glassy solvents that have a lower viscosity at room temperature. For example, the spectra displayed in Figure 7.11 were the result of polarizing at ~90 K and if biradical electron T_1 's are not too long then it might be possible to polarize rapidly in the 2K regime and to achieve even larger enhancements. In addition, once the sensitivity is optimized, the TJ-DNP experiment could be integrated with experiments designed to acquire multidimensional spectra rapidly¹⁹⁵⁻¹⁹⁸ or in a single scan¹⁹⁹ to obtain high sensitivity multidimensional experiments in a few seconds or a fraction of a second.

Finally, we should comment on the applicability of the TJ-DNP approach to solution spectroscopy of proteins and nucleic acids, etc. Clearly, for proteins and nucleic acids the limiting feature of the present experimental protocol is the freezing and thawing process. If the protein or nucleic acid is robust, then the experiment could be quite useful, and we anticipate that this will be the case for some systems, which are presently under investigation.

7.2.4. Conclusions

In summary, we have demonstrated the possibility of observing sensitivity enhanced ^{13}C spectra of small molecules by first polarizing the sample and then melting it with laser radiation followed by observation of the solution NMR spectrum. Currently, we utilize biradical polarizing agents and gyrotron microwave sources for the DNP process. The latter enables the experiment to be performed *in situ* and to be recycled for signal

averaging as is customary in conventional time domain NMR spectroscopy. The sensitivity enhancements at room temperature where the spectra are observed are presently ~120-400, but they could be improved by performing the polarization step at lower temperature, and by further refining the experiment in the aspects of melting procedures and solvent compositions. In its present form the experiment is most readily applicable to small molecules and may find application in metabolic screening.

References

- (1) Rosay, M. Sensitivity-Enhanced Nuclear Magnetic Resonance of Biological Solids. PhD Thesis, Massachusetts Institute of Technology, 2001.
- (2) Hall, D. A. Dynamic Nuclear Polarization of Biological Systems at High Magnetic Field. PhD Thesis, Massachusetts Institute of Technology, 1998.
- (3) Note, G-values and A-values of trityl and 4-hydroxy-TEMPO in frozen glycerol/water solutions are obtained from measurements of the powder EPR spectrum on a house-designed 140 GHz EPR spectrometer.
- (4) Nelson, R.; Sawaya, M. R.; Balbirnie, M.; Madsen, A. O.; Riekel, C.; Grothe, R.; Eisenberg, D. *Nature* **2005**, *435*, 773-778.
- (5) Rose, M. E. *Elementary Theory of Angular Momentum*; Wiley: New York, **1957**.
- (6) Allen, P. J.; Creuzet, F.; Degroot, H. J. M.; Griffin, R. G. *J. Magn. Reson.* **1991**, *92*, 614-617.
- (7) Edmonds, A. R. *Angular Momentum in Quantum Mechanics*; Princeton University Press: Princeton, NJ, **1974**.
- (8) Grinberg, O. Y.; Dubinskii, A. A.; Lebedev, Y. S. *Usp. Khim.* **1983**, *52*, 1490-1513.
- (9) Joye, C. D.; Griffin, R. G.; Hornstein, M. K.; Hu, K.-N.; Kreischer, K. E.; Rosay, M.; Shapiro, M. A.; Sirigiri, J. R.; Temkin, R. J.; Woskov, P. P. *IEEE Transactions on Plasma Science* **2006**, *34*, 518-523.
- (10) Ferguson, D. B.; Haw, J. F. *Anal. Chem.* **1995**, *67*, 3342-3348.
- (11) Ferguson, D. B.; Krawietz, T. R.; Haw, J. F. *J. Magn. Reson. A.* **1994**, *109*, 273-275.
- (12) Hustedt, E. J.; Smirnov, A. I.; Laub, C. F.; Cobb, C. E.; Beth, A. H. *Biophys. J.* **1997**, *72*, 1861-1877.
- (13) Slichter, C. P. *Principles of Magnetic Resonance*; Springer-Verlag: Berlin, **1990**.
- (14) Eaton, S. S.; Eaton, G. R.; Berliner, L. J. *Biological Magnetic Resonance*; Springer: New York, **2004**, Vol. 24.
- (15) Atherton, N. M. *Principles of Electron Spin Resonance*; Ellis Horwood: PTR Prentice Hall, **1993**.
- (16) Jeschke, G.; Schweiger, A. *Principles of Pulse Electron Paramagnetic Resonance*; Oxford University Press: Oxford, **2001**.
- (17) Bar, G. High-Field / High-Frequency Time Domain Electron Paramagnetic Resonance: Methods and Applications. Massachusetts Institute of Technology, 2004.
- (18) Duer, M. J. *Solid-State NMR Spectroscopy: Principles and Applications*; Blackwell Publishing: **2002**.
- (19) Kihne, S. R.; de Groot, H. J. M. *Perspectives on Solid State NMR in Biology*; Kluwer Academic Publishers: Dordrecht, The Netherlands, **2001**.
- (20) Sattler, M.; Schleucher, J.; Griesinger, C. *Prog. Nucl. Magn. Reson. Spectrosc.* **1999**, *34*, 93-158.
- (21) Andrew, E. R.; Bradbury, A.; Eades, R. G. *Nature* **1958**, *182*, 1659.
- (22) Lowe, I. J. *Phys. Rev. Lett.* **1959**, *2*, 285-287.
- (23) Waugh, J. S., Average Hamiltonian Theory. In *Encyclopedia of NMR*, Grant, D. M.; Harris, R. K., Eds. Wiley: Chichester, 1996; Vol. 2, pp 849-854
- (24) Chmelka, B. F.; Mueller, K. T.; Pines, A.; Stebbins, J.; Wu, Y.; Zwanziger, J. W. *Nature* **1989**, *339*, 42-43.
- (25) Mueller, K. T.; Wu, Y.; Chmelka, B. F.; Stebbins, J.; Pines, A. *J. Am. Chem. Soc.* **1991**, *113*, 32-38.
- (26) Jelinek, R.; Chmelka, B. F.; Wu, Y.; Grandinetti, P. J.; Pines, A.; Barrie, P. J.; Klinowski, J. *J. Am. Chem. Soc.* **1991**, *113*, 4097-4101.
- (27) Frydman, L.; Harwood, J. S. *J. Am. Chem. Soc.* **1995**, *117*, 5367-5368.
- (28) Medek, A.; Harwood, J. S.; Frydman, L. *J. Am. Chem. Soc.* **1995**, *117*, 12779-12787.
- (29) Brinkmann, A.; Levitt, M. H. *J. Chem. Phys.* **2001**, *115*, 357-384.
- (30) Eden, M.; Levitt, M. H. *J. Chem. Phys.* **1999**, *111*, 1511-1519.
- (31) Bodenhausen, G.; Ruben, D. J. *Chem. Phys. Lett.* **1980**, *69*, 185-189.
- (32) Reif, B.; Griffin, R. G. *J. Magn. Reson.* **2003**, *160*, 78-83.
- (33) Tycko, R.; Reimer, J. A. *J. Phys. Chem.* **1996**, *100*, 13240-13250.
- (34) Tycko, R.; Barrett, S. E.; Dabbagh, G.; Pfeiffer, L. N.; West, K. W. *Science* **1995**, *268*, 1460-1463.
- (35) Goto, A.; Hashi, K.; Shimizu, T.; Miyabe, R.; Wen, X. G.; Ohki, S.; Machida, S.; Iijima, T.; Kido, G. *Physical Review B* **2004**, *69*.

- (36) Kober, F.; Koenigsberg, B.; Belle, V.; Viallon, M.; Leviel, J. L.; Delon, A.; Ziegler, A.; Decorps, M. *J. Magn. Reson.* **1999**, *138*, 308-312.
- (37) Stupic, K. F.; Cleveland, Z. I.; Pavlovskaya, G. E.; Meersmann, T. *Solid State Nuclear Magnetic Resonance* **2006**, *29*, 79-84.
- (38) Pavlovskaya, G. E.; Cleveland, Z. I.; Stupic, K. F.; Basaraba, R. J.; Meersmann, T. *Proc. Natl. Acad. Sci. U. S. A.* **2005**, *102*, 18275-18279.
- (39) Raftery, D.; Long, H.; Meersmann, T.; Grandinetti, P. J.; Reven, L.; Pines, A. *Phys. Rev. Lett.* **1991**, *66*, 584-587.
- (40) Pietrass, T.; Seydoux, R.; Pines, A. *J. Magn. Reson.* **1998**, *133*, 299-303.
- (41) Spence, M. M.; Ruiz, E. J.; Rubin, S. M.; Lowery, T. J.; Winssinger, N.; Schultz, P. G.; Wemmer, D. E.; Pines, A. *J. Am. Chem. Soc.* **2004**, *126*, 15287-15294.
- (42) Spence, M. M.; Rubin, S. M.; Dimitrov, I. E.; Ruiz, E. J.; Wemmer, D. E.; Pines, A.; Yao, S. Q.; Tian, F.; Schultz, P. G. *Proc. Natl. Acad. Sci. U. S. A.* **2001**, *98*, 10654-10657.
- (43) Matsumoto, M.; Espenson, J. H. *J. Am. Chem. Soc.* **2005**, *127*, 11447-11453.
- (44) Hubler, P.; Bargon, J.; Glaser, S. J. *J. Chem. Phys.* **2000**, *113*, 2056-2059.
- (45) Tomaselli, M.; Meier, U.; Meier, B. H. *J. Chem. Phys.* **2004**, *120*, 4051-4054.
- (46) Vanriet, B.; Vangerven, L. *Physical Review B* **1982**, *26*, 2442-2449.
- (47) Beckmann, P.; Clough, S.; Hennel, J. W.; Hill, J. R. *Journal of Physics C-Solid State Physics* **1977**, *10*, 729-742.
- (48) Overhauser, A. W. *Phys. Rev.* **1953**, *92*, 411-415.
- (49) Carver, T. R.; Slichter, C. P. *Phys. Rev.* **1953**, *92*, 212-213.
- (50) Abragam, A.; Goldman, M. *Nuclear magnetism: order and disorder*; Clarendon Press: Oxford, **1982**.
- (51) Hwang, C. F.; Hill, D. A. *Phys. Rev. Lett.* **1967**, *18*, 110.
- (52) Hwang, C. F.; Hill, D. A. *Phys. Rev. Lett.* **1967**, *19*, 1011.
- (53) Wollan, D. S. *Physical Review B* **1976**, *13*, 3671-3685.
- (54) Kessenikh, A. V.; Manenkov, A. A.; Pyatnitskii, G. I. *Soviet Physics-Solid State* **1964**, *6*, 641-643.
- (55) Kessenikh, A. V.; Lushchikov, V. I.; Manenkov, A. A.; Taran, Y. V. *Soviet Physics-Solid State* **1963**, *5*, 321-329.
- (56) Goldman, M. *Spin temperature and nuclear magnetic resonance in solids*; Clarendon press: Oxford, **1970**.
- (57) Bunyatova, E. I. *Nuclear Instruments & Methods in Physics Research Section a-Accelerators Spectrometers Detectors and Associated Equipment* **2004**, *526*, 22-27.
- (58) Wind, R. A.; Duijvestijn, M. J.; Vanderlugt, C.; Manenschijn, A.; Vriend, J. *Prog. Nucl. Magn. Reson. Spectrosc.* **1985**, *17*, 33-67.
- (59) Singel, D. J.; Seidel, H.; Kendrick, R. D.; Yannoni, C. S. *J. Magn. Reson.* **1989**, *81*, 145-161.
- (60) Afeworki, M.; Schaefer, J. *Macromolecules* **1992**, *25*, 4097-4099.
- (61) Afeworki, M.; Vega, S.; Schaefer, J. *Macromolecules* **1992**, *25*, 4100-4105.
- (62) Bajaj, V. S.; Farrar, C. T.; Mastovsky, I.; Vieregg, J.; Bryant, J.; Elena, B.; Kreischer, K. E.; Temkin, R. J.; Griffin, R. G. *J. Magn. Reson.* **2003**, *160*, 85-90.
- (63) Rosay, M.; Weis, V.; Kreischer, K. E.; Temkin, R. J.; Griffin, R. G. *J. Am. Chem. Soc.* **2002**, *124*, 3214-3215.
- (64) Hautle, P.; Iinuma, M. *Nuclear Instruments & Methods in Physics Research Section a- Accelerators Spectrometers Detectors and Associated Equipment* **2000**, *440*, 638-642.
- (65) Reynhardt, E. C.; High, G. L. *J. Chem. Phys.* **1998**, *109*, 4090-4099.
- (66) van den Brandt, B.; Bunyatova, E. I.; Hautle, P.; Konter, J. A. *Nuclear Instruments & Methods in Physics Research Section a-Accelerators Spectrometers Detectors and Associated Equipment* **2004**, *526*, 53-55.
- (67) Atsarkin, V. A. *Sov. Phys. Usp.* **1978**, *21*, 725-744.
- (68) Weis, V.; Bennati, M.; Rosay, M.; Griffin, R. G. *J. Chem. Phys.* **2000**, *113*, 6795-6802.
- (69) Kaptein, R.; Frater-Schroder, M.; Oosterhoff, L. *J. Chem. Phys. Lett.* **1971**, *12*, 16.
- (70) Kaptein, R. *J. Am. Chem. Soc.* **1972**, *94*, 6251.
- (71) Meng, Q. X.; Suzuki, K.; Maeda, K.; Terazima, M.; Azumi, T. *J. Phys. Chem.* **1993**, *97*, 1265-1269.
- (72) Polenova, T.; McDermott, A. E. *J. Phys. Chem. B* **1999**, *103*, 535-548.
- (73) Jeschke, G. *J. Am. Chem. Soc.* **1998**, *120*, 4425-4429.
- (74) Deimling, M.; Brunner, H.; Dinse, K. P.; Hausser, K. H.; Colpa, J. P. *J. Magn. Reson.* **1980**, *39*, 185-202.

- (75) Inuma, M.; Takahashi, Y.; Shake, I.; Oda, M.; Masaike, A.; Yabuzaki, T.; Shimizu, H. M. *Phys. Rev. Lett.* **2000**, *84*, 171-174.
- (76) Vieth, H. M.; Yannoni, C. S. *Chem. Phys. Lett.* **1993**, *205*, 153-156.
- (77) Inuma, M.; Takahashi, Y.; Shake, I.; Oda, M.; Masaike, A.; Yabuzaki, T.; Shimizu, H. M. *J. Magn. Reson.* **2005**, *175*, 235-241.
- (78) Henstra, A.; Lin, T. S.; Schmidt, J.; Wenckebach, W. T. *Chem. Phys. Lett.* **1990**, *165*, 6-10.
- (79) Takeda, K.; Takegoshi, K.; Terao, T. *Chem. Phys. Lett.* **2001**, *345*, 166-170.
- (80) Vandenheuvel, D. J.; Schmidt, J.; Wenckebach, W. T. *Chem. Phys.* **1994**, *187*, 365-372.
- (81) Henstra, A.; Dirksen, P.; Schmidt, J.; Wenckebach, W. T. *J. Magn. Reson.* **1988**, *77*, 389-393.
- (82) Strand, J.; Schultz, B. D.; Isakovic, A. F.; Palmstrom, C. J.; Crowell, P. A. *Phys. Rev. Lett.* **2003**, *91*.
- (83) Johnson, M. *Appl. Phys. Lett.* **2000**, *77*, 1680-1682.
- (84) Farrar, C. T.; Hall, D. A.; Gerfen, G. J.; Rosay, M.; Ardenkjaer-Larsen, J. H.; Griffin, R. G. *J. Magn. Reson.* **2000**, *144*, 134-141.
- (85) Hartmann, S. R.; Hahn, E. L. *Phys. Rev.* **1962**, *128*, 2042.
- (86) Weis, V.; Bennati, M.; Rosay, M.; Bryant, J. A.; Griffin, R. G. *J. Magn. Reson.* **1999**, *140*, 293-299.
- (87) Becerra, L. R.; Gerfen, G. J.; Bellew, B. F.; Bryant, J. A.; Hall, D. A.; Inati, S. J.; Weber, R. T.; Un, S.; Prisner, T. F.; McDermott, A. E.; Fishbein, K. W.; Kreisler, K. E.; Temkin, R. J.; Singel, D. J.; Griffin, R. G. *J. Magn. Reson. A.* **1995**, *117*, 28-40.
- (88) Machuzak, J. S.; Woskoboinikow, P.; Mulligan, W. J.; Cohn, D. R.; Gerver, M.; Guss, W.; Mauel, M.; Post, R. S.; Temkin, R. J. *Rev. Sci. Instrum.* **1986**, *57*, 1983-1985.
- (89) Hornstein, M. K.; Bajaj, V. S.; Griffin, R. G.; Kreisler, K. E.; Mastovsky, I.; Shapiro, M. A.; Sirigiri, J. R.; Temkin, R. J. *IEEE Trans. Electron Devices* **2005**, *52*, 798-807.
- (90) Moeller, C. *International Journal of Electronics* **1982**, *53*, 587-593.
- (91) Hornstein, M. K. Design of a 460 GHz Second Harmonic Gyrotron Oscillator for Use in Dynamic Nuclear Polarization. Master's Thesis, Massachusetts Institute of Technology, 2001.
- (92) Hornstein, M. K. A Continuous Wave Second Harmonic Gyrotron Oscillator at 460 GHz. PhD Thesis, Massachusetts Institute of Technology, 2005.
- (93) Woskov, P. P.; Bajaj, V. S.; Hornstein, M. K.; Temkin, R. J.; Griffin, R. G. *Ieee Transactions on Microwave Theory and Techniques* **2005**, *53*, 1863-1869.
- (94) Note, DLH INDUSTRIES INC., P.O. Box 562, San Luis Obispo, California 93406. Tel: (805) 781-3565, FAX: (805) 781-3566, Email: sales@cryocomp.com, Web Site: <http://www.cryocomp.com>.
- (95) Rienstra, C. M. Solid state nuclear magnetic resonance methodology for biomolecular structure determination. PhD Thesis, Massachusetts Institute of Technology, 1999.
- (96) Reddy, T. J.; Iwama, T.; Halpern, H. J.; Rawal, V. H. *J. Org. Chem.* **2002**, *67*, 4635-4639.
- (97) Bowman, M. K.; Mailer, C.; Halpern, H. J. *J. Magn. Reson.* **2005**, *172*, 254-267.
- (98) Gerfen, G. J.; Becerra, L. R.; Hall, D. A.; Griffin, R. G.; Temkin, R. J.; Singel, D. J. *J. Chem. Phys.* **1995**, *102*, 9494-9497.
- (99) Berliner, L. J. *Biological Magnetic Resonance: Volume 14: Spin Labeling*; Springer: Berlin, **1998**.
- (100) Becerra, L. R.; Gerfen, G. J.; Temkin, R. J.; Singel, D. J.; Griffin, R. G. *Phys. Rev. Lett.* **1993**, *71*, 3561-3564.
- (101) Hall, D. A.; Maus, D. C.; Gerfen, G. J.; Inati, S. J.; Becerra, L. R.; Dahlquist, F. W.; Griffin, R. G. *Science* **1997**, *276*, 930-932.
- (102) Baudot, A.; Alger, L.; Boutron, P. *Cryobiology* **2000**, *40*, 151-158.
- (103) Garman, E. F.; Mitchell, E. P. *J. Appl. Crystallogr.* **1996**, *29*, 584-587.
- (104) Kreisler, K. E.; Farrar, C. T.; Griffin, R. G.; Temkin, R. J.; viereg, J. In Proc. 24th Internat'l Conf. Infrared and Millimeter Waves, 1999; 1999; pp IU-A3.
- (105) Rosay, M.; Zeri, A. C.; Astrof, N. S.; Opella, S. J.; Herzfeld, J.; Griffin, R. G. *J. Am. Chem. Soc.* **2001**, *123*, 1010-1011.
- (106) Wollan, D. S. *Physical Review B* **1976**, *13*, 3686-3696.
- (107) Gagnaire, G.; Jeunet, A.; Pierre, J. L. *Tetrahedron Lett.* **1989**, *30*, 6507-6510.
- (108) Luckhurst, G. R., Biradicals as Spin Probes. In *Spin Labeling Theory and Applications*, Berliner, L. J., Ed. Academic Press: New York, 1976; pp 133-181.
- (109) Rosay, M.; Lansing, J. C.; Haddad, K. C.; Bachovchin, W. W.; Herzfeld, J.; Temkin, R. J.; Griffin, R. G. *J. Am. Chem. Soc.* **2003**, *125*, 13626-13627.
- (110) Pfannebecker, V.; Klos, H.; Hubrich, M.; Volkmer, T.; Heuer, A.; Wiesner, U.; Spiess, H. W. *J. Chem. Phys.* **1996**, *100*, 13428-13432.

- (111) Griffith, O. H.; Cornell, D. W.; McConnell, H. M. *J. Chem. Phys.* **1965**, *43*, 2909-2910.
- (112) Libertini, L. J.; Griffith, O. H. *J. Chem. Phys.* **1970**, *53*, 1359-1367.
- (113) Norris, J. R.; Weissman, S. I. *J. Phys. Chem.* **1969**, *73*, 3119-3124.
- (114) Hu, K.-N.; Yu, H.-h.; Swager, T. M.; Griffin, R. G. *J. Am. Chem. Soc.* **2004**, *126*, 10844-10845.
- (115) Joo, C. G.; Hu, K. N.; Bryant, J. A.; Griffin, R. G. *J. Am. Chem. Soc.* **2006**, *128*, 9428-9432.
- (116) Bennett, A. E.; Rienstra, C. M.; Auger, M.; Lakshmi, K. V.; Griffin, R. G. *J. Chem. Phys.* **1995**, *103*, 6951-6958.
- (117) Bajaj, V. S.; Mak, M.; Hornstein, M. K.; Belenky, M.; Herzfeld, J.; Temkin, R. J.; Griffin, R. G. *Biophys. J.* **2005**, *88*, 203A.
- (118) Mak, M. L.; Bajaj, V. S.; Hornstein, M. K.; Belenky, M.; Temkin, R. J.; Griffin, R. G.; Herzfeld, J. *Biophys. J.* **2005**, *88*, 506A.
- (119) Van Der Wel, P.; Hu, K.-N.; Lewandowski, J.; Griffin, R. G. *J. Am. Chem. Soc.* **2006**, *in print*.
- (120) Martin, R. W.; Zilm, K. W. *J. Magn. Reson.* **2003**, *165*, 162-174.
- (121) Igumenova, T. I.; McDermott, A. E.; Zilm, K. W.; Martin, R. W.; Paulson, E. K.; Wand, A. J. *J. Am. Chem. Soc.* **2004**, *126*, 6720-6727.
- (122) Franks, W. T.; Zhou, D. H.; Wylie, B. J.; Money, B. G.; Graesser, D. T.; Frericks, H. L.; Sahota, G.; Rienstra, C. M. *J. Am. Chem. Soc.* **2005**, *127*, 12291-12305.
- (123) Afeworki, M.; McKay, R. A.; Schaefer, J. *Macromolecules* **1992**, *25*, 4084-4091.
- (124) Loening, N. M.; Rosay, M.; Weis, V.; Griffin, R. G. *J. Am. Chem. Soc.* **2002**, *124*, 8808-8809.
- (125) Farrar, C. T.; Hall, D. A.; Gerfen, G. J.; Inati, S. J.; Griffin, R. G. *J. Chem. Phys.* **2001**, *114*, 4922-4933.
- (126) Hu, K.-N.; Bajaj, V. S.; Rosay, M.; Griffin, R. G. *under review* **2006**.
- (127) Song, C.; Hu, K.-N.; Joo, C. G.; Swager, T. M.; Griffin, R. G. *J. Am. Chem. Soc.* **2006**, *in print*.
- (128) Borbat, P. P.; McHaourab, H. S.; Freed, J. H. *J. Am. Chem. Soc.* **2002**, *124*, 5304-5314.
- (129) Jeschke, G.; Pannier, M.; Godt, A.; Spiess, H. W. *Chem. Phys. Lett.* **2000**, *331*, 243-252.
- (130) Saxena, S.; Freed, J. H. *Chem. Phys. Lett.* **1996**, *251*, 102-110.
- (131) Milov, A. D.; Ponomarev, A. B.; Tsvetkov, Y. D. *Chem. Phys. Lett.* **1984**, *110*, 67-72.
- (132) Weber, A.; Schiemann, O.; Bode, B.; Prisner, T. F. *J. Magn. Reson.* **2002**, *157*, 277-285.
- (133) Larsen, R. G.; Singel, D. J. *J. Chem. Phys.* **1993**, *98*, 5134-5146.
- (134) Pannier, M.; Veit, S.; Godt, A.; Jeschke, G.; Spiess, H. W. *J. Magn. Reson.* **2000**, *142*, 331-340.
- (135) Jeschke, G.; Koch, A.; Jonas, U.; Godt, A. *J. Magn. Reson.* **2002**, *155*, 72-82.
- (136) Eaton, G. R.; Eaton, S. S., Spin Labeling Theory and Applications. In *Biological Magnetic Resonance*, B., L. J.; R., J., Eds. Plenum Press: New York, 1989; Vol. 8, p 339.
- (137) Ondar, M. A.; Dubinskii, A. A.; Grinberg, O. Y.; Grigorev, I. A.; Volodarskii, L. B.; Lebedev, Y. S. *Journal of Structural Chemistry* **1981**, *22*, 525-531.
- (138) Capiomon, A.; Lemaire, H.; Chion, B.; Lajzerow. *J. Chem. Phys.* **1974**, *60*, 2530-2535.
- (139) Chen, C. W. *Magnetism and Metallurgy of Soft Magnetic Materials*; Dover Publications: New York, **1986**.
- (140) Brink, D. M.; Satchler, G. R. *Angular Momentum*; Clarendon Press: Oxford, **1979**.
- (141) Calvo, R.; Abresch, E. C.; Bittl, R.; Feher, G.; Hofbauer, W.; Isaacson, R. A.; Lubitz, W.; Okamura, M. Y.; Paddock, M. L. *J. Am. Chem. Soc.* **2000**, *122*, 7327-7341.
- (142) Poole, C. P. *Electron spin resonance: a comprehensive treatise on experimental techniques*; Wiley: New York, **1983**.
- (143) Kirkpatrick, S.; Gelatt, C. D.; Vecchi, M. P. *Science* **1983**, *220*, 671-680.
- (144) Press, W. H.; Teukolsky, S. A.; Vetterling, W. T.; Flannery, B. P. *Numerical Recipes in FORTRAN: The Art of Scientific Computing*; Cambridge University Press: New York, **1992**.
- (145) Hustedt, E. J.; Cobb, C. E.; Beth, A. H.; Beechem, J. M. *Biophys. J.* **1993**, *64*, 614-621.
- (146) Metropolis, N. A.; Rosenbluth, A.; Rosenbluth, M.; Teller, A.; Teller, E. *J. Chem. Phys.* **1953**, *21*, 1087-1092.
- (147) Goffe, W. L.; Ferrier, G. D.; Rogers, J. *Journal of Econometrics* **1994**, *60*, 65-99.
- (148) Parmon, V. N.; Kokorin, A. I.; Zhidomirov, G. M.; Zamaraev, K. I. *Mol. Phys.* **1975**, *30*, 695-701.
- (149) Turro, N. J.; Khudyakov, I. V.; Bossmann, S. H.; Dwyer, D. W. *J. Phys. Chem.* **1993**, *97*, 1138-1146.
- (150) Snipes, W.; Cupp, J.; Cohn, G.; Keith, A. *Biophys. J.* **1974**, *14*, 20-32.
- (151) Berliner, L. J. *Acta Crystallogr., Sect. B: Struct. Sci.* **1970**, *26*, 1198-1202.
- (152) Improta, R.; Kudin, K. N.; Scuseria, G. E.; Barone, V. *J. Am. Chem. Soc.* **2002**, *124*, 113-120.
- (153) Brunger, A. T.; Adams, P. D.; Clore, G. M.; DeLano, W. L.; Gros, P.; Grosse-Kunstleve, R. W.; Jiang,

- J. S.; Kuszewski, J.; Nilges, M.; Pannu, N. S.; Read, R. J.; Rice, L. M.; Simonson, T.; Warren, G. L. *Acta Crystallographica Section D-Biological Crystallography* **1998**, *54*, 905-921.
- (154) Kleywegt, G. J.; Jones, T. A., Model building and refinement practice. In *Macromolecular Crystallography, Pt B*, 1997; Vol. 277, pp 208-230.
- (155) Duijvestijn, M. J.; Vanderlugt, C.; Smidt, J.; Wind, R. A.; Zilm, K. W.; Staplin, D. C. *Chem. Phys. Lett.* **1983**, *102*, 25-28.
- (156) Carver, T. R.; Slichter, C. P. *Phys. Rev.* **1956**, *102*, 975-980.
- (157) Afeworki, M.; Schaefer, J. *Macromolecules* **1992**, *25*, 4092-4096.
- (158) Duijvestijn, M. J.; Wind, R. A.; Smidt, J. *Physica B & C* **1986**, *138*, 147-170.
- (159) Jeschke, G.; Schweiger, A. *Mol. Phys.* **1996**, *88*, 355-383.
- (160) Jeschke, G. *J. Chem. Phys.* **1997**, *106*, 10072-10086.
- (161) Wolfe, J. P. *Phys. Rev. Lett.* **1973**, *31*, 907-910.
- (162) Hansen, A. D. A.; Wolfe, J. P. *Physics Letters* **1978**, *66A*, 320-322.
- (163) Cheng, Y. C.; Silbey, R. J. *Phys. Rev. A* **2004**, *69*, 052325.
- (164) Hu, K.-N.; Song, C.; Yu, H.-h.; Swager, T. M.; Griffin, R. G. *under review* **2006**.
- (165) Liebman, S. W.; Derkatch, I. L. *J. Biol. Chem.* **1999**, *274*, 1181-1184.
- (166) Krishnan, R.; Lindquist, S. L. *Nature* **2005**, *435*, 765-772.
- (167) Balbirnie, M.; Grothe, R.; Eisenberg, D. S. *Proc. Natl. Acad. Sci. U. S. A.* **2001**, *98*, 2375-2380.
- (168) Diaz-Avalos, R.; Long, C.; Fontano, E.; Balbirnie, M.; Grothe, R.; Eisenberg, D.; Caspar, D. L. D. *J. Mol. Biol.* **2003**, *330*, 1165-1175.
- (169) Blumberg, W. E. *Phys. Rev.* **1960**, *119*, 79-84.
- (170) Furman, G. B.; Goren, S. D. *J. Phys.: Condens. Matter* **2002**, *14*, 873-881.
- (171) Hurlimann, M. D. *J. Magn. Reson.* **1998**, *131*, 232-240.
- (172) Sen, P. N.; Axelrod, S. *J. Appl. Phys.* **1999**, *86*, 4548-4554.
- (173) Vasenkov, S.; Galvosas, P.; Geier, O.; Nestle, N.; Stallmach, F.; Karger, J. *J. Magn. Reson.* **2001**, *149*, 228-233.
- (174) Lowe, I. J.; Tse, D. *Phys. Rev.* **1968**, *166*, 279-291.
- (175) Maricq, M. M.; Waugh, J. S. *J. Chem. Phys.* **1979**, *70*, 3300-3316.
- (176) Chen, Q.; Schmidt-Rohr, K. *Solid State Nuclear Magnetic Resonance* **2006**, *29*, 142-152.
- (177) Cheung, T. T. P.; Gerstein, B. C. *J. Appl. Phys.* **1981**, *52*, 5517-5528.
- (178) Clauss, J.; Schmidrohr, K.; Spiess, H. W. *Acta Polym.* **1993**, *44*, 1-17.
- (179) Jia, X.; Wolak, J.; Wang, X. W.; White, J. L. *Macromolecules* **2003**, *36*, 712-718.
- (180) Takegoshi, K.; Nakamura, S.; Terao, T. *Chem. Phys. Lett.* **2001**, *344*, 631-637.
- (181) Delaglio, F.; Grzesiek, S.; Vuister, G. W.; Zhu, G.; Pfeifer, J.; Bax, A. *Journal of Biomolecular NMR* **1995**, *6*, 277-293.
- (182) Levitt, M. H.; Raleigh, D. P.; Cruzet, F.; Griffin, R. G. *J. Chem. Phys.* **1990**, *92*, 6347-6364.
- (183) Duckett, S. B.; Sleight, C. J. *Prog. Nucl. Magn. Reson. Spectrosc.* **1999**, *34*, 71-92.
- (184) Natterer, J.; Bargon, J. *Prog. Nucl. Magn. Reson. Spectrosc.* **1997**, *31*, 293-315.
- (185) Navon, G.; Song, Y. Q.; Room, T.; Appelt, S.; Taylor, R. E.; Pines, A. *Science* **1996**, *271*, 1848-1851.
- (186) Fitzgerald, R. J.; Sauer, K. L.; Happer, W. *Chem. Phys. Lett.* **1998**, *284*, 87-92.
- (187) Cherubini, A.; Payne, G. S.; Leach, M. O.; Bifone, A. *Chem. Phys. Lett.* **2003**, *371*, 640-644.
- (188) Barrett, S. E.; Tycko, R.; Pfeiffer, L. N.; West, K. W. *Phys. Rev. Lett.* **1994**, *72*, 1368-1371.
- (189) Michal, C. A.; Tycko, R. *Phys. Rev. Lett.* **1998**, *81*, 3988-3991.
- (190) Zysmilich, M. G.; McDermott, A. *J. Am. Chem. Soc.* **1996**, *118*, 5867-5873.
- (191) Prakash, S.; Alia, Gast, P.; de Groot, H. J. M.; Jeschke, G.; Matysik, J. *J. Am. Chem. Soc.* **2005**, *127*, 14290-14298.
- (192) Goez, M.; Mok, K. H.; Hore, P. J. *J. Magn. Reson.* **2005**, *177*, 236-246.
- (193) Ardenkjaer-Larsen, J. H.; Fridlund, B.; Gram, A.; Hansson, G.; Hansson, L.; Lerche, M. H.; Servin, R.; Thaning, M.; Golman, K. *Proc. Natl. Acad. Sci. U. S. A.* **2003**, *100*, 10158-10163.
- (194) Bloembergen, N.; Purcell, E. M.; Pound, R. V. *Phys. Rev.* **1948**, *73*, 679-712.
- (195) Kim, S.; Szyperski, T. *J. Am. Chem. Soc.* **2003**, *125*, 1385-1393.
- (196) Atreya, H. S.; Szyperski, T. *Proc. Natl. Acad. Sci. U. S. A.* **2004**, *101*, 9642-9647.
- (197) Kupce, E.; Freeman, R. *J. Am. Chem. Soc.* **2004**, *126*, 6429-6440.
- (198) Bruschiweiler, R.; Zhang, F. L. *J. Chem. Phys.* **2004**, *120*, 5253-5260.
- (199) Frydman, L.; Scherf, T.; Lupulescu, A. *Proc. Natl. Acad. Sci. U. S. A.* **2002**, *99*, 15858-15862.

Curriculum Vitae

Kan-Nian Hu

Honors and Awards (Selected)

1. Cambridge Science Foundation, Graduate Student Travel Grant, 2005
2. MIT Chemistry Department, Morse Travel Grant, 2004
3. The Yens' Award by outstanding Alumni, 1998
4. Research Creativity Award from National Science Council, 1996
5. Scholarship of Dr Yuan-Tseh Lee, 1992-1996

Patent

Robert G. Griffin and Kan-Nian Hu, "Polarizing Agents for Dynamic Nuclear Polarization", Us Patent: US-2005-0107696-A1

Publications

1. Chan-Gyu Joo, Kan-Nian Hu, Jeffrey Bryant, and Robert G. Griffin, "*In situ Temperature Jump-High Frequency Dynamic Nuclear Polarization Experiments: Enhanced Sensitivity in Liquid State NMR*," J. Am. Chem. Soc., **128**, 9428-9432 (2006).
2. Colin D. Joye, Robert G. Griffin, Melissa K. Hornstein, Kan-Nian Hu, Kenneth E. Kreisler, Melanie Rosay, Michael A. Shapiro, Jagadishwar R. Sirigiri, Richard J. Temkin, Paul P. Woskov, "*Operational Characteristics of a 14 Watt, 140 GHz Gyrotron for Dynamic Nuclear Polarization*," IEEE Transactions on Plasma Science, **34**, 518-523 (2006).
3. Kan-Nian Hu, Hsiao-hua Yu, Timothy M. Swager and Robert G. Griffin, "*Dynamic Nuclear Polarization with Biradicals*," J. Am. Chem. Soc., **126**, 10844-10845 (2004).
4. Kan-Nian Hu and Lian-Pin Hwang, "*The Influence of Adsorbed Molecules on Na-Site in NaY Zeolite Investigated by Triple-Quantum ²³Na MAS NMR Spectroscopy*," Solid State Nuclear Magnetic Resonance, **12**, 211-220 (1998).
5. Changsik Song, Kan-Nian Hu, Timothy M. Swager and Robert G. Griffin, "*TOTAPOL—A Biradical Polarizing Agent for Dynamic Nuclear Polarization in Aqueous Media*," J. Am. Chem. Soc. (2006) **in print**.
6. Patrick Van Der Wel, Kan-Nian Hu, Jozef Lewandowski, Robert G. Griffin, "*Dynamic Nuclear Polarization of Amyloidogenic Peptide Nanocrystals: GNNQQNY, a Core Segment of the Yeast Prion Protein Sup35p*," J. Am. Chem. Soc. (2006) **in print**.
7. Kan-Nian Hu and Robert G. Griffin, "*Quantum Mechanical Theory of Dynamic Nuclear Polarization in Solid Dielectrics—An Analytical Approach*," **under review**.
8. Kan-Nian Hu and Robert G. Griffin, "*Quantum Mechanical Theory of Dynamic Nuclear Polarization in Solid Dielectrics—Simulation of Electron-Electron-Nucleus Spin Systems with Relaxation*," **under review**.
9. Kan-Nian Hu, Vikram S. Bajaj, Melanie M. Rosay and Robert G. Griffin, "*High-Frequency Dynamic Nuclear Polarization Using Mixtures of TEMPO and Trityl Radicals*," **under review**.
1. Kan-Nian Hu, Changsik Song, Hsiao-hua Yu, Timothy M. Swager, Robert G. Griffin, "*Improvement of High-Frequency Dynamic Nuclear Polarization Using Biradicals: A Multi-frequency EPR Lineshape Analysis*," **under review**.

Invited Talks

1. Kan-Nian Hu, Changsik Song, Hsiao-hua Yu, Vikram S. Bajaj, Timothy M. Swager and Robert G. Griffin, "*Cross Effect Dynamic Nuclear Polarization Using Biradicals*," 4th Alpine Conference on Solid State NMR, Chamonix Mont-Blanc, France (2005).
2. Kan-Nian Hu, Changsik Song, Timothy M. Swager and Robert G. Griffin, "*Cross Effect Dynamic Nuclear Polarization Using Biradicals*," EUROMAR Conference Proceedings, 27, Veldhoven, The Netherlands (2005).
3. Kan-Nian Hu, Hsiao-hua Yu, Timothy M. Swager and Robert G. Griffin, "*Dynamic Nuclear Polarization with Biradicals*," 45th Experimental NMR Conference Proceedings, 49, Pacific Grove, California (2004).